

# THÈSE

*présenté devant*

**L’Institut National des Sciences Appliquées de Lyon**

*pour obtenir*

## LE GRADE DE DOCTEUR

ÉCOLE DOCTORALE : ÉLECTRONIQUE, ÉLECTROTECHNIQUE, AUTOMATIQUE

FORMATION DOCTORALE : IMAGES ET SYSTÈMES

*par*

**Max LANGER**

## Phase Retrieval in the Fresnel Region for Hard X-ray Tomography

Soutenue le 19 Novembre 2008 devant la commission d'examen

Jury :

|                           |                     |                      |
|---------------------------|---------------------|----------------------|
| <b>Rémy PROST</b>         | Professeur          | Président du Jury    |
| <b>Jérôme IDIER</b>       | Chercheur CNRS      | Rapporteur           |
| <b>Franz PFEIFFER</b>     | Assistant Professor | Rapporteur           |
| <b>Laurent DESBAT</b>     | Professeur          | Examinateur          |
| <b>Jean-Pierre GUIGAY</b> | HDR                 | Invité               |
| <b>Françoise PEYRIN</b>   | DR INSERM           | Directeur de Thèse   |
| <b>Peter CLOETENS</b>     | Chercheur ESRF      | Codirecteur de Thèse |



# Abstract

Phase-based micro-computed tomography ( $\mu$ CT) techniques extend the possibilities of standard, absorption based  $\mu$ CT by offering increased sensitivity. In the hard X-ray region, the increase in sensitivity can be several orders of magnitude. Phase measurements require that the X-ray beam has a defined phase, that is it has a certain degree of coherence. While several phase contrast mechanisms exist, a particularly simple one is to let the beam propagate in free space after interaction with an object. Such an image is called a Fresnel diffraction pattern. The phase in the image plane is lost, but the phase information of the object contributes to the image intensity. Both the object absorption and phase information are entangled in the recorded image.

Such patterns can be used to calculate the phase shift through a process known as phase retrieval. It is a non-linear problem, but the most efficient phase retrieval algorithms so far rely on a linearized contrast model. These are the transport of intensity equation (TIE) and the contrast transfer function (CTF). The TIE is based on linearization in the propagation distance and is valid for short propagation distance only. The CTF is based on linearization of the object function, and is valid for weak absorption and slowly varying phase.

The aim of this work was to extend the validity of phase retrieval from Fresnel diffraction patterns to strongly absorbing objects. To this effect, a new linear contrast model is presented. It is valid for slowly varying objects and unifies the TIE and CTF in that it approaches each in the limit of small propagation distance and weak absorption respectively. Hence, we dub it the mixed approach.

The TIE, CTF and mixed approach, as well as an implementation of the TIE for weak absorption were evaluated using both simulated and experimental data. The mixed approach was shown to perform best in practice, according to the chosen evaluation criteria.

It was noted that, due to how the phase information is propagated to the recorded images, the phase retrieval is sensitive to noise in the low-frequency range and is actually

singular at zero frequency. For this purpose, we propose two regularization schemes, one based on regularization in the Fourier and wavelet domains, and one based on an object prior assuming that the imaged object has homogeneous composition. For the latter, we also develop an algorithm for automatic regularization parameter selection.

The algorithm based on the homogeneous composition prior proves to be useful for a wide range of samples. The application to imaging of a fossil embedded in rock allowed the discovery of the first fossilized brain found. In paleontology, the samples often show a high degree of homogeneity. The algorithm was also applied to the imaging of artificial bone scaffolds grown in vitro with bone cells, for use in tissue engineering. It allows quantitative analysis of scaffold composition and more importantly, 3D analysis of an uncalcified matrix deposited by the cells.

Finally, future directions of phase retrieval in the Fresnel region are considered. No general algorithm exists yet. The possibility of further development of linearized algorithms is discussed briefly. Non-linear algorithms, namely the iterative algorithms used in phase retrieval from a Fraunhofer diffraction pattern, are also considered. Three variants are adapted to the Fresnel case, with several recorded images, and are applied to simulated data. Their adaptation to the Fresnel diffraction at short distance case with multiple images is not trivial. Although three numerical schemes have been proposed and tested on simulated data, we conclude that they are not suitable in their present form.

In conclusion, in this work we developed and validated a phase retrieval algorithm for strongly absorbing object, where the introduction of an object prior proved to be particularly beneficial. The developed method is foreseen to be applied to a wide range of research applications.

# Résumé

Les techniques de micro-tomographie ( $\mu$ CT) basée sur la phase étendent les possibilités des méthodes classiques basées sur l'absorption en offrant une sensibilité accrue. Dans la gamme des rayons X durs, l'augmentation de la sensibilité peut atteindre plusieurs ordres de grandeurs. Afin de pouvoir effectuer des mesures de phase, le faisceau de rayons X doit avoir une phase bien définie, c'est-à-dire un certain degré de cohérence. Bien qu'il existe plusieurs mécanismes permettant d'obtenir du contraste de phase, une technique simple consiste à laisser le faisceau se propager librement dans l'espace après son interaction avec un objet. Ce type de diffraction à distance finie est appelé diffraction de Fresnel. Lorsque l'on enregistre l'image de ce phénomène, la phase elle-même est perdue, mais l'information de phase propre à l'objet contribue à l'intensité de l'image enregistrée. Ainsi, les informations d'absorption et de phase de l'objet sont indirectement enregistrées dans les images.

Ce phénomène peut être utilisé pour calculer le déphasage à travers un processus appelé estimation de la phase (phase retrieval). Bien qu'il s'agisse d'un problème inverse non-linéaire, les algorithmes de reconstruction de phase les plus efficaces sont basés sur des modèles de contraste linéarisés. Ces algorithmes sont l'équation de transport d'intensité (TIE : Transport of Intensity Equation) et la fonction transfert du contraste (CTF : Contrast Transfer Function). La TIE est basée sur la linéarisation de la dependance de l'intensité à fonction de la distance de propagation. Elle n'est valide que pour des distances courtes. La CTF, repose quand à elle sur la linéarisation de la fonction transmittance de l'objet ; elle n'est valide que dans les cas de faible absorption et de variation de phase lente.

Le but de cette étude était d'étendre la validité de l'estimation de phase dans la région de Fresnel au cas de l'objet très absorbant. Nous présentons ici un nouveau modèle linéaire de contraste. Ce modèle est valide pour les objets lentement variables. Il regroupe les modèles TIE et CTF du fait qu'il s'approche de ces modèles respectivement dans la limite des courtes distances et des objets peu absorbants. C'est pourquoi nous

l'appelons l'approche mixte.

La TIE, la CTF et l'approche mixte, ainsi que l'application de la TIE au cas des faibles absorptions ont été évaluées en utilisant à la fois des données simulées et expérimentales. Ces différentes comparaisons ont montré que, dans la pratique, l'approche mixte donnait les meilleurs résultats, d'après les critères d'évaluation choisis.

On peut noter que, étant donné la façon dont la phase est propagée jusqu'aux images enregistrées, la reconstruction de phase est sensible au bruit dans la gamme des basses fréquences et qu'elle est singulière à la fréquence zero. Pour cela, nous proposons deux schémas de régularisation, un basé sur la régularisation dans les domaines de Fourier et des ondelettes, et un second basé sur une connaissance a priori liée à une hypothèse de composition homogène pour l'objet imagé. Pour ce dernier, nous avons aussi développé un algorithme de sélection automatique du paramètre de régularisation.

L'algorithme basé sur l'hypothèse de composition homogène se révèle efficace pour des échantillons très variés. Son application à l'imagerie de fossiles inclus dans la roche a permis la découverte du premier cerveau de poisson fossilisé. En paléontologie, les échantillons montrent souvent un grand degré d'homogénéité. Cet algorithme a également été appliqué à l'imagerie de biomatériaux cultivés *in vitro* avec des cellules osseuses pour l'ingénierie tissulaire. Cela a permis l'analyse quantitative de la composition de la matrice du biomatériau et plus important, l'analyse 3D du tissu non-calcifié déposé par les cellules.

Enfin, les perspectives pour l'estimation de la phase par diffraction de Fresnel sont présentées. Pour le moment, il n'existe aucun algorithme général. La possibilité de développement d'autres algorithmes linéarisés est brièvement abordée. Des algorithmes non-linéaires, à savoir les algorithmes itératifs utilisés dans l'estimation de phase par diffraction de Fraunhofer, sont aussi considérés. Trois variantes de cet algorithme sont adaptées au cas de la diffraction de Fresnel, avec des images enregistrées à différentes distances de propagation et sont appliquées à des données simulées. Leur adaptation à la diffraction de Fresnel pour le cas de courtes distances de propagation avec plusieurs images n'est pas triviale. Bien que trois schémas numériques aient été proposés et testés sur des données simulées, nous concluons qu'ils ne conviennent pas dans leur format actuel.

En conclusion, dans ce travail, nous avons développé et validé un algorithme d'estimation de phase pour les objets très absorbants, où l'introduction de connaissance a priori sur l'objet s'est avérée particulièrement avantageuse. La méthode développée sera appliquée à une vaste gamme de sujets de recherche.

# Résumé étendu

La microtomographie ( $\mu$ CT) par rayons X est une technique de plus en plus utilisée pour la caractérisation en trois dimensions (3D) dans diverses applications allant de la biologie, la médecine, la paléontologie à la science de matériaux (Bonse, 1999, 2002). Elle revient à combiner la tomographie X assistée par ordinateur, largement utilisée en imagerie médicale, à une imagerie à l'échelle microscopique. La microtomographie X 3D repose sur l'acquisition d'images 2D de type projection pour un grand nombre d'angles de vue, puis sur la reconstruction de l'image 3D à partir de ces données. En microtomographie X standard, le principe physique utilisé est l'absorption des rayons X et la reconstruction fournit la distribution du coefficient d'atténuation linéaire dans l'objet.

Une limitation de la microtomographie X par absorption est son manque de sensibilité. On peut montrer que, dans la gamme des rayons X durs, les techniques basées sur le contraste de phase peuvent être trois ordres de grandeur plus sensibles que les techniques basées sur l'absorption (Momose and Fukuda, 1995). Ce mode de contraste peut également être couplé à une acquisition de type tomographique, afin d'augmenter la sensibilité de la méthode.

L'imagerie X par contraste de phase est une technique assez récente. Par rapport à l'imagerie X par absorption, elle nécessite des propriétés spécifiques des faisceaux de rayons X utilisés. Ces propriétés incluent une forte cohérence spatiale, la monochromatique et un flux élevé. De ce fait, la plupart des techniques d'imagerie X par contraste de phase sont développées en utilisant des sources synchrotron. Cela limite actuellement la disponibilité de ces techniques, mais il existe des développements en cours pour l'adapter aux sources X classiques, comme la microscopie X cohérente (Mayo et al., 2003) ou l'imagerie de phase interférométrique basée sur des réseaux de diffraction (Pfeiffer et al., 2006).

Plusieurs mécanismes de contraste de phase ont été explorés dans la gamme des rayons X durs. On peut donc distinguer trois types de techniques : celles basées sur des

cristaux analyseurs (Ingal and Beliaevskaya, 1995; Davis et al., 1995; Chapman et al., 1997), celles basées sur l’interférométrie (Bonse and Hart, 1965; Momose et al., 1996) et celles basées sur la propagation (Snigirev et al., 1995; Cloetens et al., 1996). La coexistence de ces différentes techniques indique qu’elles ont chacune leurs avantages et limitations intrinsèques, ce qui fait que chaque méthode a son propre champ d’applications. Toutefois, peu de comparaisons directes ont été décrites (e.g. Pagot et al. (2005); Kitchen et al. (2005)). Le contraste de phase de Zernike peut aussi être mis en œuvre avec une lentille pour rayons X qui est réalisée avec un réseau zoné (Neuhausler et al., 2003). Il a été couplé à la tomographie (Aoki et al., 2007) mais n’offre qu’un champ de vue très limité ( $\approx 10\mu\text{m}$ ) et la technique n’a pas été utilisée pour la reconstruction quantitative de phase.

Les techniques interférométriques, basées sur la diffraction de Bragg (Bonse and Hart, 1965), ont été les premières méthodes de contraste de phase à être développées pour les rayons X durs. Cette technique a été mise au point par Ando and Hosoya (1972) et couplée à la tomographie dans des études scientifiques (Momose et al., 1995). La principale difficulté de cette technique est qu’elle demande une extrême stabilité mécanique des composants optiques, car leurs positions relatives doivent être stables dans une fraction du paramètre de maille, c’est-à-dire à une échelle sous l’Ångström. Donc, l’interférométrie du type Bonse-Hart est très difficile à mettre en œuvre. Des méthodes de contraste de phase interférométriques à base de réseaux de diffraction ont aussi été développés (David et al., 2002; Pfeiffer et al., 2006). Dans l’absence de diffraction par un réseau cristallin, ces méthodes sont moins sensibles à la stabilité du montage expérimental.

Les techniques basées sur la propagation reposent sur le fait que, si on permet au faisceau de se propager librement dans l’espace après interaction avec l’objet (Fig. 1), l’image enregistrée est un diagramme de diffraction. Un exemple d’objet de phase pur est illustré dans la Fig. 2. Le processus de formation de l’image est bien décrit dans le cadre de la diffraction de Fresnel (Goodman, 2005). Le principe expérimental revient donc à celui de la radiographie X standard, mais avec la possibilité d’éloigner le détecteur par rapport à l’objet. Contrairement aux techniques citées précédemment, cette technique n’exige aucune instrumentation spécifique, ce qui la rend facile à mettre en œuvre et ce qui permet d’éviter la dégradation de la résolution spatiale associée à l’utilisation d’instrumentation supplémentaire. Elle a tout d’abord été démontrée expérimentalement en utilisant un faisceau synchrotron partiellement cohérent ( Snigirev et al. (1995)). En fait, on retrouve un dispositif similaire à celui initialement proposé en holographie Gabor (1948).

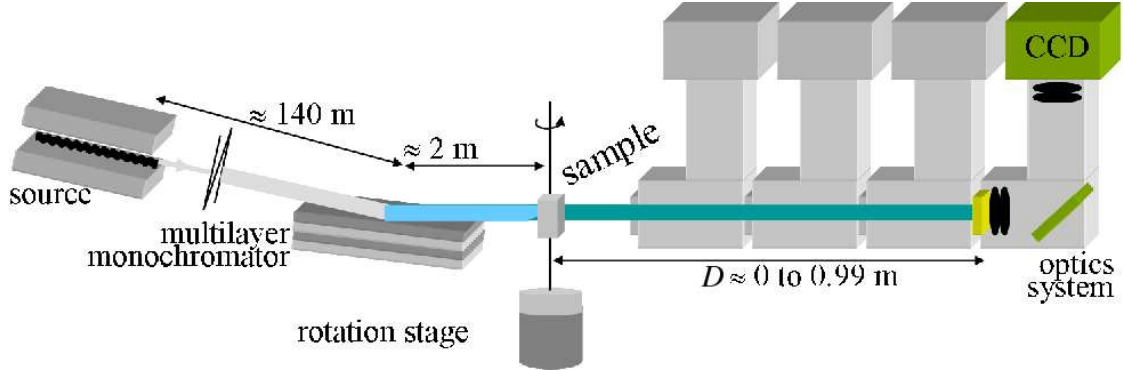


Figure 1: Principe expérimental de la tomographie par contraste de phase basée sur la propagation. Le rayonnement synchrotron, partiellement cohérent et monochromatique, illumine un échantillon monté sur une rotation. Le détecteur, un capteur numérique CCD couplé à un écran scintillateur et à une optique de lumière conventionnelle, est monté sur une translation (en profondeur) pour qu'une série d'images à différentes distances puisse être enregistrée.

Lorsqu'on réalise une acquisition tomographique en positionnant le détecteur à une distance proche de l'objet, on peut montrer que l'image 3D reconstruite correspond à l'image d'absorption à laquelle s'ajoute un terme proportionnel au Laplacien 3D de la partie réelle de l'indice de réfraction (Cloetens et al., 1997). Cette technique, qui n'utilise aucun traitement préalable des radiographies de phase peut être utile en soi et a été utilisée dans plusieurs domaines d'application (notamment en science des matériaux).

Toutefois, le caractère le plus intéressant de l'imagerie X par contraste de phase basée sur la propagation, est qu'on peut aller plus loin en essayant de reconstruire directement la partie réelle de l'indice de réfraction complexe. Ceci va être possible en prenant en compte plusieurs distances de propagation et en utilisant la relation théorique qui existe entre l'objet et l'image enregistrée à une certaine distance. Cette relation fait intervenir le carré de la transformation de Fresnel. En inversant cette relation on pourra déterminer le déphasage introduit par l'objet, ce que, dans ce travail, nous définissons comme *l'estimation de la phase (phase retrieval)*. La phase ainsi estimée sous les différents angles de vue, peut alors être traitée par un algorithme de reconstruction tomographique, comme *l'algorithme par rétroprojection filtrée (filtered back-projection, FBP)*. L'image 3D ainsi reconstruite correspond à la partie réelle de l'indice de réfraction complexe (Cloetens et al., 1999). Comme cette quantité est de un à trois ordres de grandeur plus grande que la partie imaginaire de l'indice de réfraction complexe, ou l'absorption, on voit que l'imagerie de phase a une meilleure sensibilité que

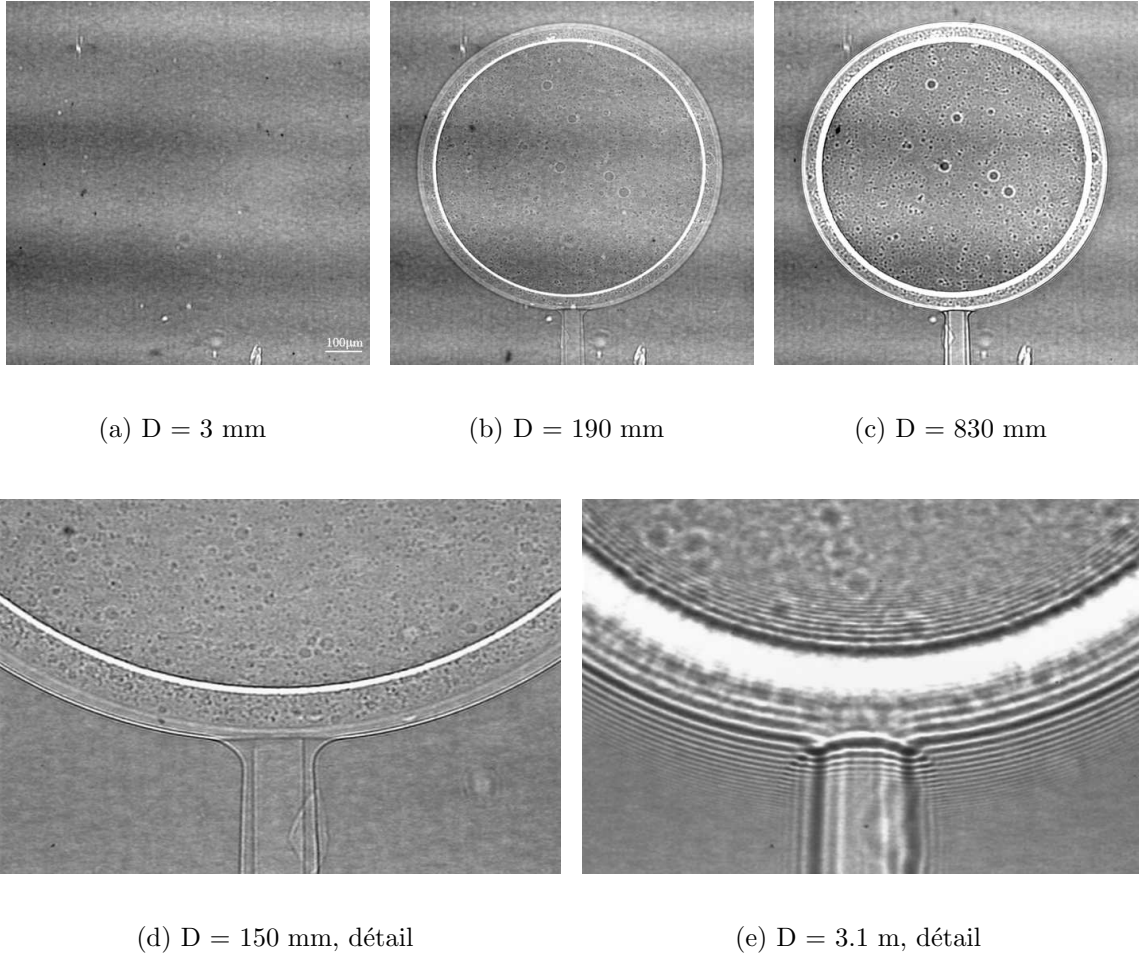


Figure 2: Radiographies en contraste de phase d'une sphère ayant deux couches, une couche de  $30\ \mu\text{m}$  de polystyrène recouverte par une couche de  $15\ \mu\text{m}$  de parylène (Cloetens, 1999).

l'imagerie d'absorption.

L'estimation de la phase est un problème inverse non linéaire pour lequel plusieurs méthodes ont été proposées. La plupart de ces méthodes reposent sur une linéarisation du modèle donnant lieu à des algorithmes d'inversion efficaces (Nugent et al., 1996; Cloetens et al., 1999; Bronnikov, 2002). Toutefois, du fait des approximations introduites lors de la linéarisation, ces méthodes ne sont valables que sous certaines hypothèses, comme le fait de n'utiliser que des distances de propagation faibles ou de supposer que l'objet est peu absorbant.

Dans le cas d'objets faiblement absorbants, des algorithmes efficaces d'estimation de phase ont déjà été développés (Cloetens et al., 1999). Les figures Fig. 3 et 4 illustrent

l'application de cette méthode à l'étude d'une graine d'*Arabidopsis*. La distribution 3D de la partie réelle de l'indice de réfraction complexe a été obtenue après estimation de la phase et reconstruction tomographique (Fig. 4). Cette méthode a permis de mettre en évidence un réseau de canaux d'air à l'intérieur de la graine, jusqu'à présent inconnu. Les graines ont été imitées dans leur état naturel, sans aucune préparation (Cloetens et al., 2006).

Toutefois, beaucoup d'échantillons intéressants présentent une forte absorption. C'est le cas dans le domaine de la recherche sur le tissu osseux, en science des matériaux et en paléontologie, où les échantillons étudiés peuvent être des os, des roches ou des métaux. Des radiographies en contraste d'absorption et de phase d'un objet construit à partir de fibres sont présentées sur la Fig. 5. Le problème est souvent que les structures intérieures ne présentent pas un contraste suffisant pour être différenciées, ou que les parties plus molles ne sont pas correctement résolues en présence de fortes absorptions. On peut essentiellement discerner quatre classes de problèmes :

1. Echantillon ayant un faible contraste d'absorption. Ce cas est courant en imagerie biologique, où l'échantillon peut être composé seulement de tissu mou.
2. Echantillon composé essentiellement de structures faiblement absorbantes avec quelques structures fortement absorbantes. Ce cas peut se trouver, par exemple, dans les applications médicales et en imagerie de petit animal, où il peut y avoir une grande gamme de contraste d'absorption entre l'os et le tissu mou.
3. Echantillon composé essentiellement de structures fortement absorbantes avec quelques structures molles. Ce cas apparaît, par exemple, dans la recherche sur le tissu osseux, où on pourrait souhaiter imager simultanément la microstructure osseuse et la vascularisation.
4. Echantillon composé de différentes structures absorbantes présentant de faibles différences d'absorption. Ce cas peut être rencontré en paléontologie, où le but est de résoudre des petites différences de minéralisation dans un fossile, et en science des matériaux lorsque l'on cherche à observer des phases de composition similaire dans un alliage.

Dans ce contexte, les objectifs de ce travail sont d'évaluer des algorithmes d'estimation de phase existants et d'étendre la validité de la reconstruction de phase aux objets fortement absorbants. Ces développements sont menés dans le cas où l'estimation de la phase est couplée à la tomographie. Une contrainte était donc de développer

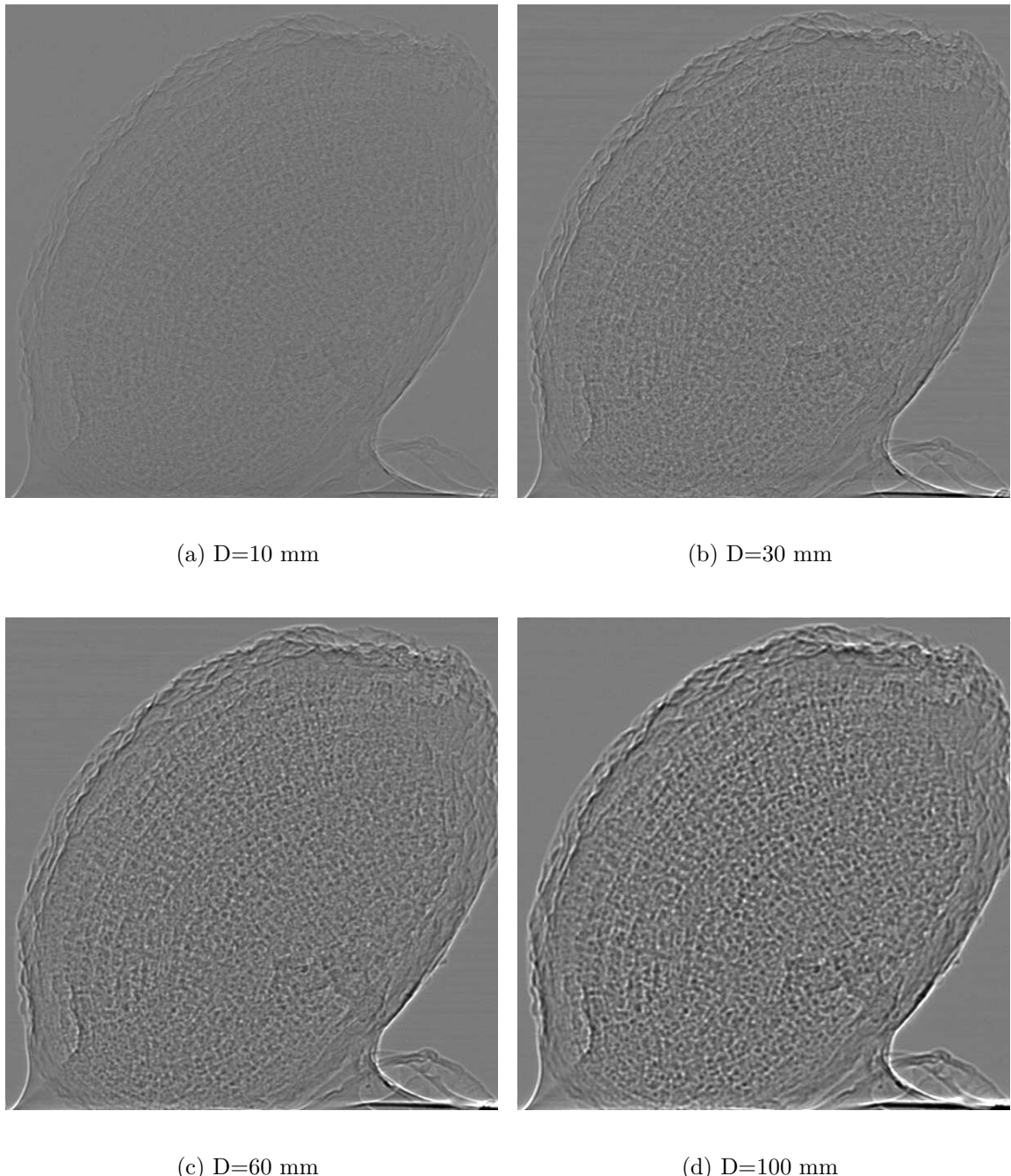
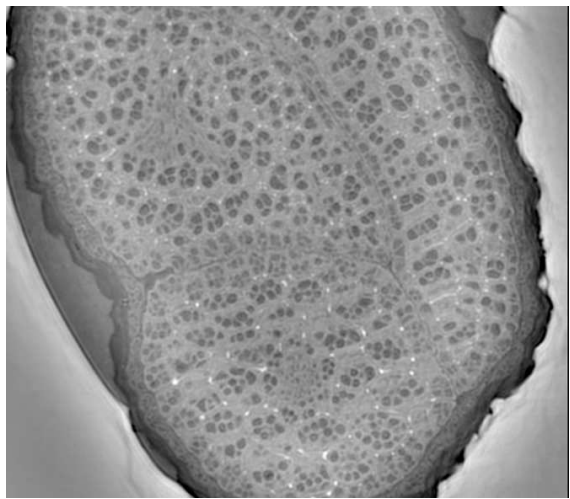
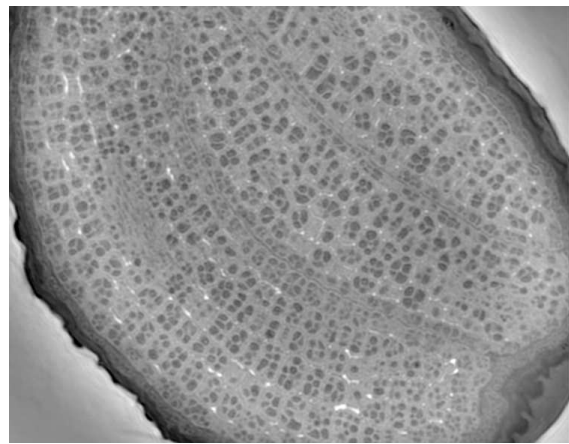


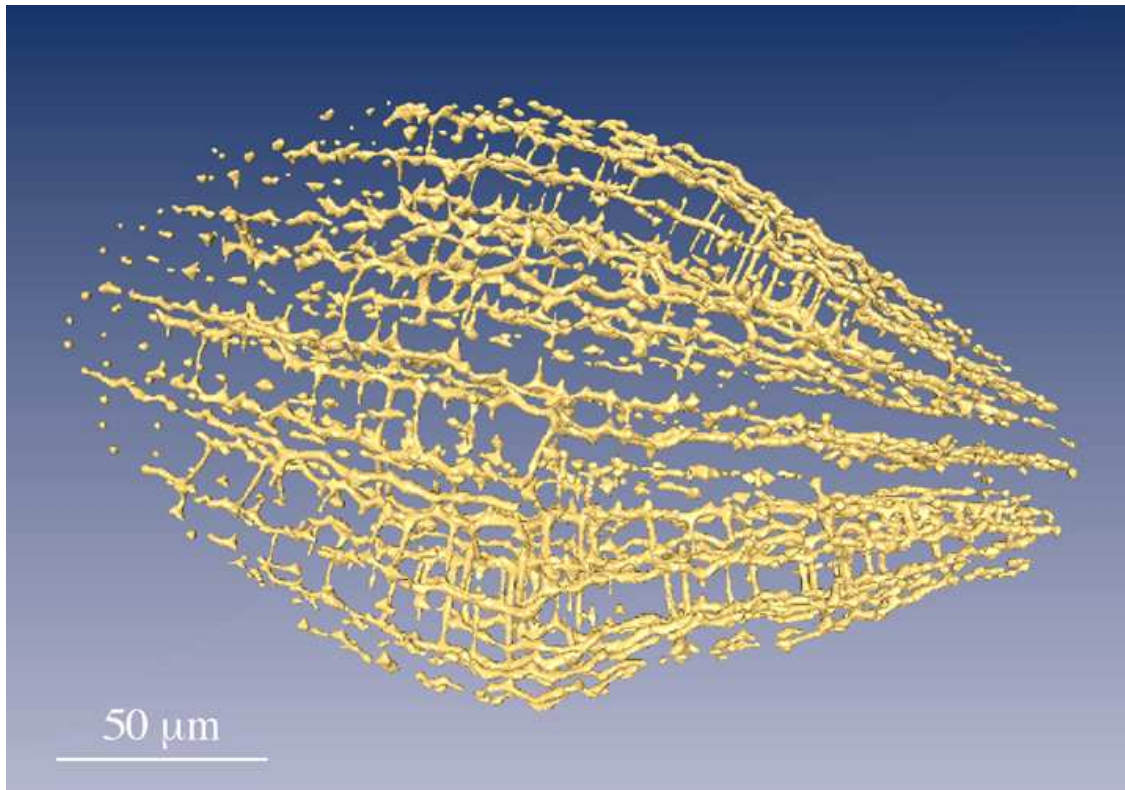
Figure 3: Radiographies en contraste de phase par propagation d'une graine d'Arabidopsis à différentes distances (c.f. Fig 2) (Cloetens et al., 2006).



(a) Axial



(b) Frontal



(c) 3D rendering

Figure 4: Tomographie de phase d'une graine d'Arabidopsis. Les images (a) et (b) sont des sections axiales et frontales. Les parties plus claires correspondent à des vides parsemés entre les cellules. La reconstruction tomographique de la phase permet une analyse quantitative 3D. Le figure (c) montre une interprétation 3D du réseau de vide (Cloetens et al., 2006).

des algorithmes efficaces pouvant facilement être utilisés pour les études scientifiques menées à l'ESRF.

Les contributions de ce travail incluent le développement d'un nouveau modèle mathématique, utilisable pour les objets fortement absorbants et qui unifie un certain nombre de modèles précédemment développés. Nous présentons ensuite une évaluation détaillée des performances de cette méthode sur des fantômes simulés et expérimentaux comparée à d'autres méthodes précédemment développées. Il apparaît que la plupart des méthodes d'estimation de phase fournissent un résultat entaché d'un fort bruit basse fréquence, surtout en présence de forte absorption. Nous nous intéressons donc ensuite à la régularisation du problème en envisageant deux approches originales, la plus prometteuse étant une approche basée sur une connaissance *a priori* sur l'objet, traduisant une composition "homogène". Enfin, un algorithme permettant de sélectionner automatiquement les paramètres de régularisation a été développé. Il permet de réduire considérablement le temps "utilisateur", ce qui rend la méthode plus facilement utilisable dans diverses applications. Finalement, nous présentons deux applications détaillées, l'une concernant la recherche sur le tissu osseux et l'autre la paléontologie.

Le Chapitre 2, présente les bases théoriques nécessaires à cette étude. Tout d'abord, nous rappelons quelques notions sur les problèmes inverses linéaires. Nous décrivons, ensuite, l'interaction des rayons X avec la matière, et montrons l'intérêt d'utiliser des techniques d'imagerie de phase. Nous décrivons la modélisation du processus de formation de l'image pour les techniques de contraste de phase basées sur la propagation à distance finie - *diffraction de Fresnel* - et en champ lointain - *diffraction de Fraunhofer*. Ceci permet la modélisation du *problème direct*, l'estimation de la phase correspondant au problème inverse. Nous présentons ensuite le principe de la tomographie et de la reconstruction tomographique. Nous montrons ensuite que si l'imagerie par contraste de phase est couplée à la tomographie, la distribution 3D de l'indice de réfraction peut être obtenue en appliquant tout d'abord un algorithme d'estimation de phase pour tous les angles de vue, puis un algorithme de reconstruction tomographique. Finalement, nous formulons l'estimation de la phase comme un problème de minimisation.

Le Chapitre 3, présente le développement d'un nouveau modèle linéarisé de l'image radiographique après propagation, dit modèle mixte. Le principal avantage de ce nouveau modèle est qu'il est valide même en cas de forte absorption. Par ailleurs, ce modèle permet d'unifier les deux approches linéarisées principales : l'équation de transport d'intensité (TIE) et l'approche reposant sur les fonctions de transfert de contraste (CTF). Ce chapitre a été publié dans *Optics Letters* (Guigay et al., 2007).

Le Chapitre 4 est consacré à une étude comparative de quatre algorithmes de estimation

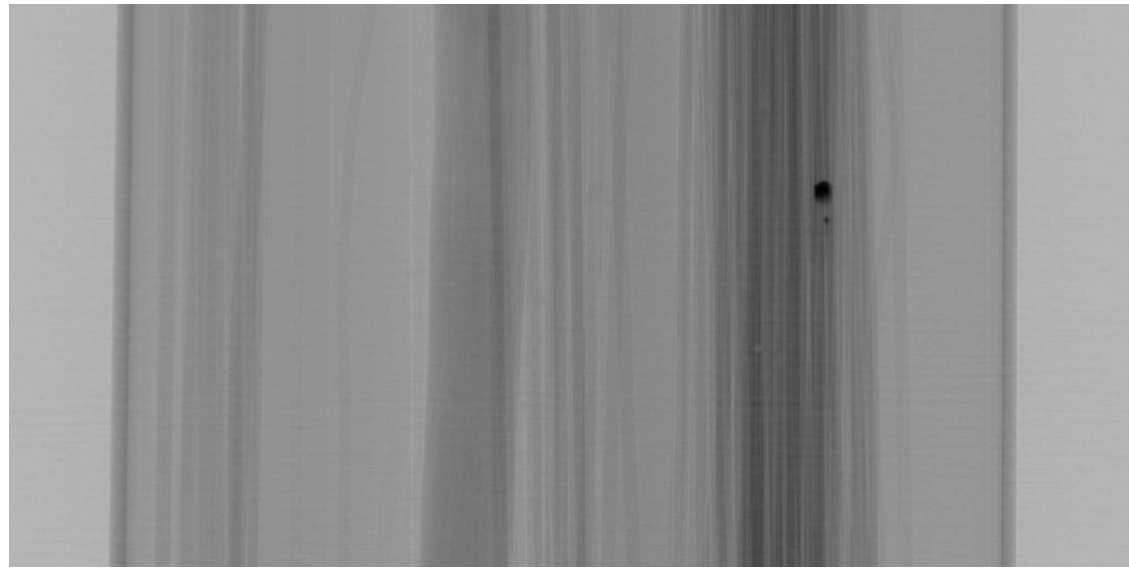
de phase : celui basé sur l'équation de transport d'intensité (TIE), celui basé sur la méthode Bronnikov (TIE dans le cas de faible absorption), celui basé sur les fonctions de transfert de contraste (CTF) et finalement celui basé sur l'approche mixte présentée dans le Chapitre 3. Ce chapitre a été publié dans *Medical Physics* (Langer et al., 2008).

Le Chapitre 5 s'intéresse à la régularisation du problème d'estimation de phase pour lequel deux nouvelles approches sont proposées. La première approche (Section 5.3) s'inspire d'une méthode de déconvolution travaillant dans le domaine de Fourier et des ondelettes. Bien que cette méthode montre une supériorité sur les données simulées, elle se révèle couteuse en temps de calcul et peu efficace dans le cas pratique. La deuxième approche (Section 5.4) est fondée sur un connaissance a priori de composition homogène de l'objet. L'image d'absorption permet de construire un a priori sur l'image de phase, qui est principalement utilisé pour régulariser la partie basse fréquence de l'image, qui du fait du processus de formation de l'image est mal déterminée. Enfin, un algorithme de sélection automatique des paramètres de régularisation, basé sur la méthode de la courbe en L, est mis en œuvre. Il permet de trouver une pondération optimale entre l'écart aux données expérimentales et aux connaissance a priori. La section 5.3, qui décrit la régularisation Fourier-ondelette, est un manuscrit préparé pour le *Journal of the Optical Society of America A*. La section 5.4, a été soumise à *IEEE Transactions on Image Processing*.

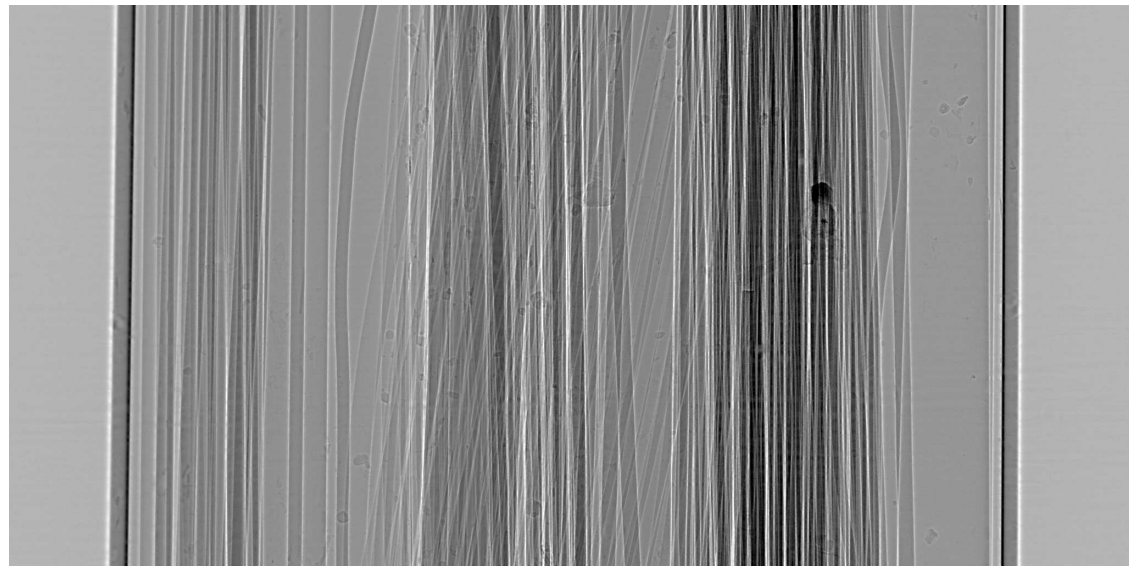
Le Chapitre 6, présente deux applications de la méthode régularisée développée dans la section 5.4. Dans la section 6.1, la méthode est appliquée en paléontologie. Elle a permis la découverte de ce qui semble être le plus ancien cerveau fossilisé à l'intérieur du crâne d'un poisson (sibyrhynchid iniopterygian) datant de 300 millions d'années. Dans la section 6.2, l'algorithme est utilisée en ingénierie du tissu osseux afin d'imager quantitativement la formation osseuse sur des biomatériaux cultivés *in vitro*. Dans ces deux applications, l'hypothèse de composition homogène est adéquate et permet d'améliorer sensiblement la reconstruction des images de phase. La section 6.1 a été soumise au *Proceedings of the National Academy of Science of the United States of America* et la section 6.2 est un manuscrit préparé pour le *Journal of Microscopy*.

Enfin, les perspectives sur de futures directions de recherche sont développées dans le Chapitre 7. En particulier, nous étudions la possibilité d'utiliser les méthodes d'estimation de phase itératives. Nous proposons trois schémas algorithmiques s'inspirant des méthodes itératives utilisées en reconstruction de phase à partir des diagrammes de diffraction de Fraunhofer. La mise en œuvre de ces différentes méthodes nous permet de conclure qu'elles ne conviennent pas dans leur présente forme. Le développement d'une méthode itérative pourrait permettre de directement traiter le problème non linéaire,

et ainsi de s'affranchir des hypothèses parfois restrictives des méthodes linéarisées. Toutefois, ce point est en lui-même un nouveau sujet d'étude.



(a)



(b)

Figure 5: Radiographies d'un fantôme : (a) image d'absorption enregistrée à  $D = 2$  mm et (b) image incluant absorption et contraste de phase enregistrée à  $D = 45$  mm. L'énergie de rayons X est  $E = 20.5$  keV et le champ de vue horizontal couvre 1.4 millimètres.



Refractive index

*This one of the seven forests:  
more light than under water–  
and vast.  
tramping up a frozen rutted road,  
rutted snow,  
toward those shrivelled zinc clouds–  
like a melancholick mailman  
(or Aladdin with his lamp–)  
must I hurry so?*

Kenji Miyazawa



# Contents

|          |  |           |
|----------|--|-----------|
| <b>1</b> | <b>Introduction</b>                                | <b>33</b> |
| 1.1      | Objectives . . . . .                               | 38        |
| 1.2      | Outline . . . . .                                  | 38        |
| <b>2</b> | <b>Theoretical background</b>                      | <b>43</b> |
| 2.1      | Inverse Problems . . . . .                         | 44        |
| 2.1.1    | Linear discrete inverse problems . . . . .         | 44        |
| 2.1.2    | Inversion of linear, discrete problems . . . . .   | 45        |
| 2.1.3    | Conditioning . . . . .                             | 47        |
| 2.1.4    | Regularization . . . . .                           | 47        |
| 2.1.4.1  | Tikhonov regularization . . . . .                  | 48        |
| 2.2      | Direct problem: Image formation . . . . .          | 49        |
| 2.2.1    | Wave-object interaction . . . . .                  | 49        |
| 2.2.2    | Attenuation . . . . .                              | 49        |
| 2.2.2.1  | Absorption . . . . .                               | 50        |
| 2.2.2.2  | Rayleigh scattering . . . . .                      | 50        |
| 2.2.2.3  | Compton scattering . . . . .                       | 51        |
| 2.2.2.4  | Total attenuation coefficient . . . . .            | 51        |
| 2.2.2.5  | Beer-Lambert law . . . . .                         | 52        |
| 2.2.3    | Refractive index decrement . . . . .               | 52        |
| 2.3      | Propagation based phase contrast imaging . . . . . | 54        |
| 2.3.1    | Fresnel diffraction . . . . .                      | 56        |

|          |  |           |
|----------|--|-----------|
| 2.3.1.1  | Spatial domain analysis . . . . .                        | 56        |
| 2.3.1.2  | Fourier space analysis . . . . .                         | 57        |
| 2.3.1.3  | Mixed space-frequency analysis . . . . .                 | 59        |
| 2.3.1.4  | Effect of spherical incident wave front . . . . .        | 59        |
| 2.3.1.5  | Effect of partial coherence . . . . .                    | 60        |
| 2.3.1.6  | Effect of detector . . . . .                             | 61        |
| 2.3.1.7  | Summary . . . . .  | 62        |
| 2.3.2    | Fraunhofer diffraction . . . . .                         | 62        |
| 2.4      | Tomography . . . . .                                     | 65        |
| 2.4.1    | Principle of tomography . . . . .                        | 65        |
| 2.4.2    | Fourier slice theorem . . . . .                          | 65        |
| 2.4.3    | Fourier reconstruction . . . . .                         | 68        |
| 2.4.4    | Filtered back-projection . . . . .                       | 69        |
| 2.5      | Phase contrast tomography . . . . .                      | 72        |
| 2.6      | Phase tomography . . . . .                               | 74        |
| 2.6.1    | Phase Retrieval . . . . .                                | 74        |
| 2.6.1.1  | Phase retrieval from Fraunhofer diffraction patterns . . | 74        |
| 2.6.1.2  | Phase retrieval from Fresnel diffraction patterns . . .  | 76        |
| <b>3</b> | <b>Mixed approach</b>                                    | <b>77</b> |
| 3.1      | Introduction . . . . .                                   | 78        |
| 3.2      | Wave-object interaction . . . . .                        | 78        |
| 3.3      | Linear contrast models . . . . .                         | 79        |
| 3.3.1    | Transport of intensity equation . . . . .                | 79        |
| 3.3.2    | Contrast transfer function . . . . .                     | 80        |
| 3.3.3    | Discussion . . . . .                                     | 81        |
| 3.4      | Mixed approach . . . . .                                 | 81        |
| 3.5      | Phase retrieval . . . . .                                | 83        |
| 3.6      | Experiment . . . . .                                     | 83        |
| 3.7      | Summary . . . . .  | 84        |

|   |            |
|---|------------|
| <b>4 Evaluation of linear phase retrieval algorithms</b>  | <b>87</b>  |
| 4.1 Introduction . . . . .                                | 89         |
| 4.2 Direct problem - image formation . . . . .            | 91         |
| 4.3 Inverse problem - phase retrieval . . . . .           | 93         |
| 4.3.1 Contrast Transfer Function (CTF) . . . . .          | 93         |
| 4.3.2 Transport of Intensity Equation (TIE) . . . . .     | 95         |
| 4.3.3 TIE for weak absorption (WTIE) . . . . .            | 96         |
| 4.3.4 Mixed approach . . . . .                            | 97         |
| 4.4 Simulations and data acquisition . . . . .            | 100        |
| 4.4.1 Simulation of phase contrast . . . . .              | 100        |
| 4.4.2 Experimental data . . . . .                         | 101        |
| 4.4.3 Evaluation criteria . . . . .                       | 102        |
| 4.5 Results . . . . .                                     | 103        |
| 4.5.1 Simulated data . . . . .                            | 103        |
| 4.5.2 Experimental data . . . . .                         | 106        |
| 4.6 Summary and conclusion . . . . .                      | 106        |
| <b>5 Regularization of phase retrieval</b>                | <b>111</b> |
| 5.1 Wavelet transform . . . . .                           | 112        |
| 5.1.1 Discrete wavelet transform (DWT) . . . . .          | 114        |
| 5.1.2 Shift Invariant redundant DWT (srDWT) . . . . .     | 117        |
| 5.2 Splines . . . . .                                     | 119        |
| 5.2.1 Cubic spline interpolation . . . . .                | 119        |
| 5.3 Fourier-Wavelet regularized phase retrieval . . . . . | 123        |
| 5.3.1 Introduction . . . . .                              | 124        |
| 5.3.2 Mathematical model . . . . .                        | 125        |
| 5.3.2.1 Direct problem . . . . .                          | 125        |
| 5.3.2.2 Inverse problem . . . . .                         | 127        |
| 5.3.3 Fourier-wavelet regularized deconvolution . . . . . | 128        |

|          |  |            |
|----------|--|------------|
| 5.3.3.1  | Fourier shrinkage . . . . .                                      | 129        |
| 5.3.3.2  | Wavelet shrinkage . . . . .                                      | 130        |
| 5.3.4    | Implementation . . . . .   | 132        |
| 5.3.5    | Simulation . . . . .   | 132        |
| 5.3.6    | Results . . . . .  | 133        |
| 5.3.7    | Conclusions . . . . .  | 134        |
| 5.4      | Phase retrieval with a homogeneous composition prior . . . . .   | 137        |
| 5.4.1    | Introduction . . . . .   | 138        |
| 5.4.2    | Direct problem: propagation based X-ray phase contrast . . . . . | 140        |
| 5.4.2.1  | Wave-object interaction . . . . .                                | 142        |
| 5.4.2.2  | Contrast formation . . . . .                                     | 143        |
| 5.4.3    | Inverse problem: phase retrieval . . . . .                       | 144        |
| 5.4.3.1  | Linearization of direct problem . . . . .                        | 144        |
| 5.4.3.2  | Inversion of the linearized problem . . . . .                    | 146        |
| 5.4.4    | Regularization . . . . .   | 147        |
| 5.4.4.1  | Phase-attenuation duality as prior . . . . .                     | 147        |
| 5.4.4.2  | Automatic parameter selection . . . . .                          | 148        |
| 5.4.5    | Experimental results . . . . .                                   | 149        |
| 5.4.6    | Discussion and conclusion . . . . .                              | 153        |
| <b>6</b> | <b>Applications</b>  | <b>161</b> |
| 6.1      | Paleontology . . . . .   | 163        |
| 6.1.1    | Introduction . . . . .   | 164        |
| 6.1.2    | Results . . . . .  | 164        |
| 6.1.3    | Discussion . . . . .   | 169        |
| 6.1.4    | Materials and methods . . . . .                                  | 172        |
| 6.1.4.1  | Origin of the material . . . . .                                 | 172        |
| 6.1.4.2  | Methods of SR- $\mu$ CT and holotomography . . . . .             | 172        |
| 6.1.5    | Acknowledgments . . . . .  | 174        |

|                     |   |            |
|---------------------|---|------------|
| 6.2                 | Bone research . . . . .                             | 175        |
| 6.2.1               | Introduction . . . . .                              | 176        |
| 6.2.2               | Materials and methods . . . . .                     | 178        |
| 6.2.2.1             | Sample preparation . . . . .                        | 178        |
| 6.2.2.2             | Holotomography . . . . .                            | 178        |
| 6.2.2.3             | Data acquisition . . . . .                          | 182        |
| 6.2.2.4             | Holotomographic reconstruction . . . . .            | 182        |
| 6.2.2.5             | Quantitative parameter extraction . . . . .         | 182        |
| 6.2.3               | Results . . . . .                                   | 183        |
| 6.2.4               | Discussion . . . . .                                | 188        |
| 6.2.5               | Conclusion . . . . .                                | 190        |
| <b>7</b>            | <b>Perspectives</b>                                 | <b>193</b> |
| 7.1                 | Iterative methods . . . . .                         | 194        |
| 7.1.1               | Error reduction algorithm . . . . .                 | 194        |
| 7.1.2               | Hybrid input-output algorithm . . . . .             | 195        |
| 7.1.3               | Difference map . . . . .                            | 195        |
| 7.1.4               | Constraints in multiple transform domains . . . . . | 197        |
| 7.1.5               | Attempt at adapted algorithms . . . . .             | 197        |
| 7.1.6               | Initial results . . . . .                           | 199        |
| 7.1.7               | Discussion . . . . .                                | 200        |
| 7.2                 | Linear methods . . . . .                            | 203        |
| <b>8</b>            | <b>Conclusion</b>                                   | <b>205</b> |
| <b>References</b>   |   | <b>209</b> |
| <b>Publications</b> |   | <b>225</b> |



# List of Figures

|     |   |    |
|-----|---|----|
| 1.1 | Schematic of the propagation based phase tomography setup . . . . .   | 34 |
| 1.2 | Phase contrast radiographs of a two-layered polymer sphere . . . . .  | 35 |
| 1.3 | Propagation phase contrast radiographs of an Arabidopsis seed . . . . .   | 37 |
| 1.4 | Phase tomography of an Arabidopsis seed . . . . .   | 39 |
| 1.5 | Absorption and mixed absorbtion/phase contrast radiographs of a constructed object . . . . .  | 42 |
| 2.1 | Schematic definition of inverse problems . . . . .  | 45 |
| 2.2 | Geometry of Fresnel diffraction . . . . .   | 55 |
| 2.3 | Summary of the direct problem, calculating image intensity from a known object. . . . .   | 63 |
| 2.4 | The principle of tomography . . . . .   | 66 |
| 2.5 | Coordinate systems used in tomography. $(x_s, y_s)$ are fixed to the sample. The beam propagation and image plane coordinate system $(x, z)$ seems to rotate around the object. . . . . | 67 |
| 2.6 | Illustration of the Fourier slice theorem . . . . .   | 69 |
| 2.7 | Absorption, phase contrast and phase tomography of a constructed phantom . . . . .  | 75 |
| 3.1 | Schematic of the experimental setup . . . . .   | 79 |
| 3.2 | Amplitude and phase contrast factors for the contrast transfer function and transport of intensity equation . . . . .   | 81 |
| 3.3 | Absorption radiograph, phase map, absorption tomogram and phase tomogram of a <i>Crossodactylodes bookermanni</i> frog . . . . .  | 85 |

|      |  |     |
|------|--|-----|
| 4.1  | Schematic of the imaging system . . . . .  | 90  |
| 4.2  | Plot of the square of the phase contrast factor for three different distances and the average . . . . .  | 94  |
| 4.3  | Central slice of the phantom used in the simulations . . . . .   | 102 |
| 4.4  | Central slices of the reconstructed refractive index using simulated, noise-free data . . . . .  | 104 |
| 4.5  | Central slices of the refractive index decrement reconstructed using simulated data with added noise, corresponding to a PPSNR of 12 dB in the first (absorption) distance . . . . . | 105 |
| 4.6  | Phase tomograms of the constructed phantom . . . . .   | 107 |
| 4.7  | Plots of the performance of the different algorithms . . . . .   | 109 |
| 5.1  | Overlapping wavelet bandpass spectra . . . . .   | 116 |
| 5.2  | One stage of an iterated filter bank, implementing the Discrete wavelet transform . . . . .  | 118 |
| 5.3  | Schematic of the experimental setup . . . . .  | 125 |
| 5.4  | Transfer function for the phase in free space propagation . . . . .  | 128 |
| 5.5  | Central slices of the 3D phantom . . . . .   | 133 |
| 5.6  | Reconstructed central slices of the simulated data for different noise levels  | 135 |
| 5.7  | Schematic of the phase tomography setup . . . . .  | 140 |
| 5.8  | Absorption and phase radiographs recorded at different distances . . . . .   | 141 |
| 5.9  | Plot of the normalized combined squared transfer function for in-line phase contrast imaging using four different distances . . . . .  | 143 |
| 5.10 | L-curves and curvatures for the regularized problem . . . . .  | 150 |
| 5.11 | Phase maps reconstructed useing different values for $\delta/\beta$ . . . . .  | 152 |
| 5.12 | Tomographic slice and histogram of $\mu = 4\pi\beta/\lambda$ of the phantom reconstructed using the absorption images . . . . .  | 154 |
| 5.13 | Tomographic slice and histogram of $2\pi\delta_r/\lambda$ of the phantom reconstructed using Tikhonov regularized phase maps . . . . .   | 155 |
| 5.14 | Tomographic slice and histogram of $2\pi\delta_r/\lambda$ of the phantom, reconstructed using the $\delta/\beta$ homogeneous composition prior . . . . .                             | 156 |

|      |   |     |
|------|---|-----|
| 5.15 | Tomographic slice and histogram of $2\pi\delta_r/\lambda$ of the phantom, reconstructed using $\delta/\beta = 1936$ , corresponding to PETE . . . . .                       | 157 |
| 5.16 | Segmented 3D rendering of the phantom, reconstructed using a $\delta/\beta$ -ratio corresponding to alumina . . . . .   | 159 |
| 6.1  | The anatomy of iniopterygians, 300 Myr-old chimaeroid-related cartilaginous fish . . . . .  | 167 |
| 6.2  | Braincase anatomy and exceptional brain preservation in a sibyrhynchid iniopterygian from the Pennsylvanian of Kansas . . . . .   | 171 |
| 6.3  | Schematic of the imaging setup . . . . .  | 177 |
| 6.4  | Phase contrast radiographs and retrieved phase map of the three loaded scaffolds at different distances . . . . .   | 179 |
| 6.5  | Slices through the 3D reconstructions of the absorption and refractive index of the OB+OC scaffold . . . . .  | 184 |
| 6.6  | Zooms on $1 \times 1$ mm regions in the absorption and refractive index reconstructed using the mixed approach regularized with the homogeneous composition prior . . . . . | 185 |
| 6.7  | Histograms of the absorption and refractive index reconstructions . . . . .   | 186 |
| 6.8  | $1 \times 1$ mm closeups of the reconstructed refractive index of the different samples . . . . .   | 187 |
| 6.9  | Histograms of the different reconstructed refractive index volumes . . . . .  | 188 |
| 6.10 | $1 \times 1$ mm close-up of a thresholded slice through the refractive index of the OB+OC scaffold and a virtually cut 3D piece of the OB+OC scaffold                       | 189 |
| 6.11 | Thickness histograms for the scaffolds and matrix . . . . .   | 191 |
| 7.1  | Basic scheme of the iterative transform algorithm . . . . .   | 195 |
| 7.2  | Transform domain projection in the algorithm suggested by Mokso (2006)  | 198 |
| 7.3  | Transform domain projections in the iterative algorithm adapted from Allen and Oxley (2001) . . . . .   | 199 |
| 7.4  | Transform domain projection in the third algorithm in Section 7.1.5 . . . . .   | 200 |
| 7.5  | The unwrapped and wrapped phase of the phantom from Section 4.5.1   | 201 |
| 7.6  | Retrieved phase and error evolution plot with algorithm 1 (Section 7.1.5), using the transform domain projection in Fig. 7.2 . . . . .                                      | 202 |

|     |  |     |
|-----|--|-----|
| 7.7 | Retrieved phase and error plot for algorithm 2 (Section 7.1.5), using the transform domain projection in Fig. 7.3 . . . . .                      | 203 |
| 7.8 | Retrieved phase and error plot for algorithm 3 (Section 7.1.5), using the transform domain projection and iteration scheme in Fig. 7.4 . . . . . | 204 |

# List of Tables

|     |  |     |
|-----|--|-----|
| 2.1 | Complex refractive indices for some representative materials at 20 keV   | 53  |
| 4.1 | Summary of the phase retrieval methods used in this work   | 100 |
| 4.2 | Theoretical values for the absorption coefficient and refractive index at 24 keV for the materials used in the phantom                 | 101 |
| 5.1 | Normalized RMS error for different peak-to-peak signal to noise ratios   | 134 |
| 5.2 | Theoretical values for the absorption coefficient and refractive index at 20.5 keV X-ray energy for the materials used in the phantom. | 146 |
| 6.1 | Volumes and volume filling fractions of the four scaffolds.  | 185 |
| 6.2 | Average thickness of mineral containing fraction and fibrous tissue in $\mu\text{m}$ .   | 186 |



# Chapter 1

## Introduction

X-ray computed micro-tomography ( $\mu$ CT) is an increasingly used technique for three-dimensional (3D) characterization in a wide range of applications, ranging from biology, bone research and medicine to paleontology and materials science (Bonse, 1999, 2002). It combines the from medical imaging now well-known technique of tomography, or cross-sectional imaging, with imaging at the micrometer scale. The technique is based on recording the absorption shadow of an object for several angles of view, which are then used to reconstruct the attenuation coefficient distribution in the object.

One well-known weakness of absorption based  $\mu$ CT is lack of sensitivity. Contrary to most efforts in  $\mu$ CT, development of phase-based techniques do not mainly strive to improve resolution. Instead the main interest of phase contrast is increased sensitivity. It can be shown that, in the hard X-ray range, phase based techniques can be three orders of magnitude more sensitive than absorption based techniques (Momose and Fukuda, 1995). S Phase imaging with X-rays is a fairly recently developed technique. It might not be familiar to some readers, since the requirements on the X-ray beam used are stricter than those delivered from current medical sources. The requirements are, specifically, those of high spatial coherence, monochromaticity and high flux. These combined have led to most X-ray phase imaging techniques having been developed at, or for use at, synchrotron facilities, since synchrotrons currently are the best sources of highly coherent, monochromatic X-rays. This currently makes the availability of such techniques limited, but alternative sources are being developed, which could make X-ray phase imaging techniques more widely available, such as coherent X-ray microscopes (Mayo et al., 2003) or X-ray imaging with grating interferometers (Pfeiffer et al., 2006).

Several phase contrast mechanisms have been explored in the hard X-ray range. They

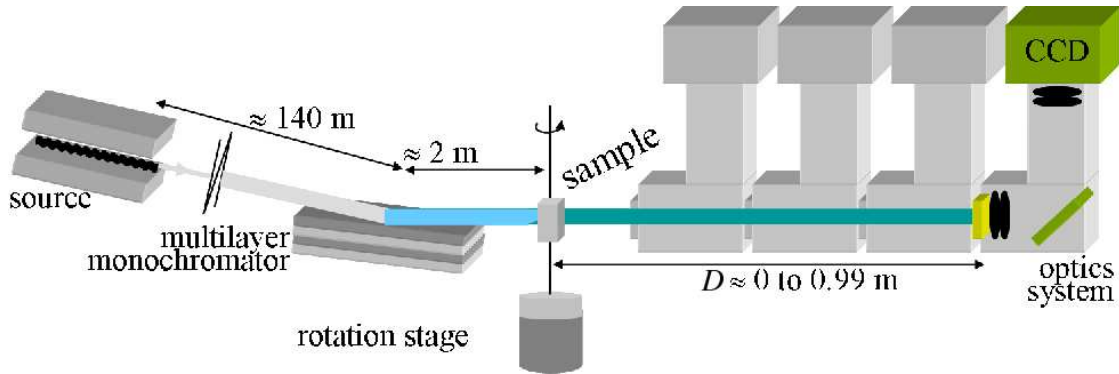


Figure 1.1: Schematic of the propagation based phase tomography setup. Partially coherent, monochromatic synchrotron X-rays are shone on a sample mounted on a rotation stage. The detector, a CCD camera coupled to a scintillating screen with conventional light optics, is mounted on a translation stage so that a series of images at different distances can be recorded.

can roughly be divided into analyzer based (Ingal and Beliaevskaya, 1995; Davis et al., 1995; Chapman et al., 1997), interferometric (Bonse and Hart, 1965; Momose et al., 1996) and propagation based techniques (Snigirev et al., 1995). The continued coexistence of these techniques indicate that the different techniques have their own intrinsic strengths and weaknesses which makes them suitable for different types of studies and classes of samples. Few direct comparisons have been made, however (e.g. (Pagot et al., 2005; Kitchen et al., 2005)). Classical Zernike phase contrast has also been implemented with Fresnel zone plate optics (Neuhausler et al., 2003) and applied to tomography (Aoki et al., 2007), but presently offer very limited field of view ( $\approx 10\mu\text{m}$ ), and the technique has not been used for quantitative phase retrieval.

Interferometric techniques were the first phase contrast methods to be developed for hard X-rays, such as Bragg type interferometry (Bonse and Hart, 1965). This technique was pioneered by Ando and Hosoya (1972), and has been coupled to tomography in scientific investigation (Momose et al., 1995). The main technical difficulty lies in the extreme demands on the mechanical stability of the optical components, as the relative positions of the optical components have to be stable within a fraction of a lattice constant, i.e. to sub-Ångström dimensions. Therefore, Bonse-Hart interferometers are very difficult to handle, especially when made big enough to investigate large samples. Interferometric phase contrast imaging with diffraction gratings has also been developed (David et al., 2002; Pfeiffer et al., 2006). This method is less sensitive to positioning and stability of the setup.

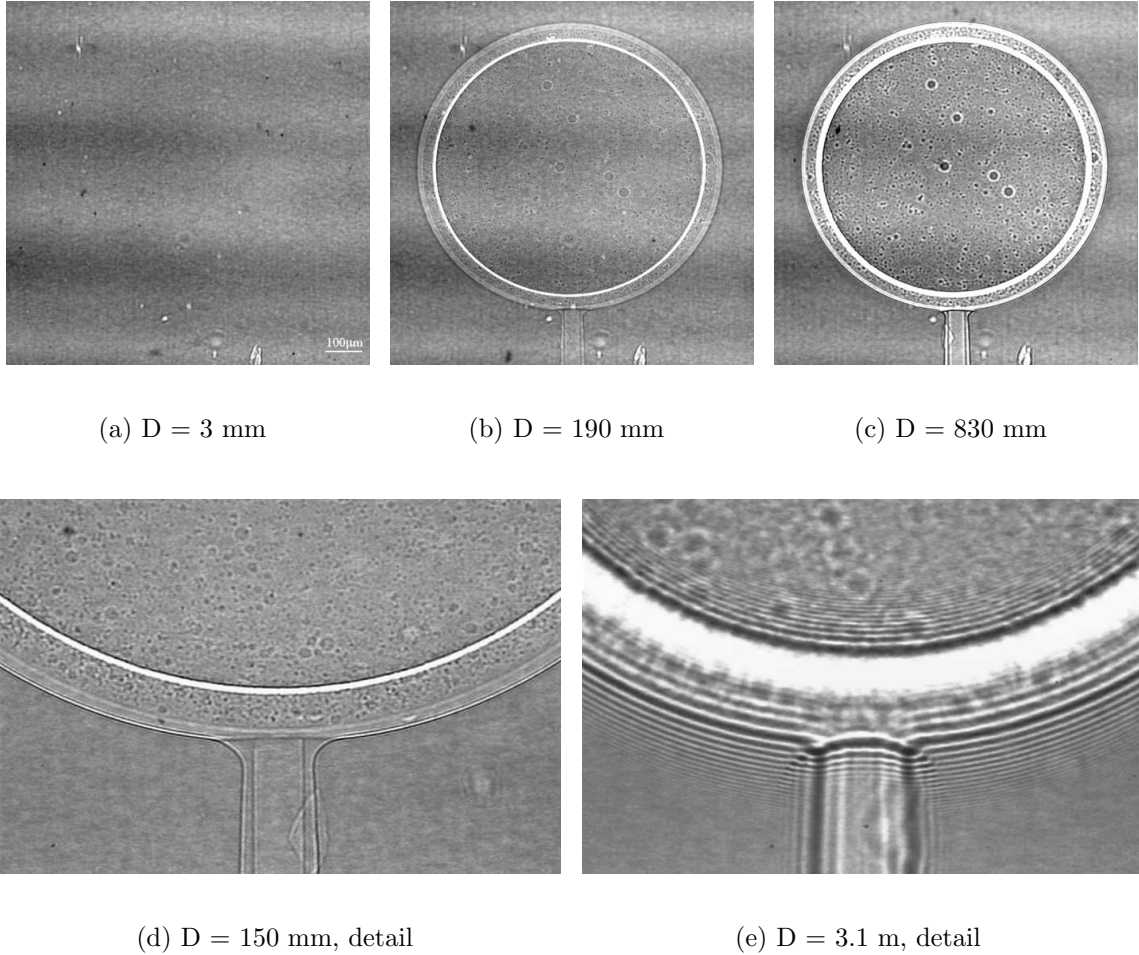


Figure 1.2: Phase contrast radiographs of a two-layered sphere, a  $30 \mu\text{m}$  layer of polystyrene covered by a  $15 \mu\text{m}$  layer parylene, imaged using X-rays with energy close to 18 keV (Cloetens, 1999).

Propagation based techniques are based on the fact that if the beam is allowed to propagate in free space after interaction with the object (Fig. 1.1), the recorded image is a diffraction pattern. An example of such patterns of a pure phase object is given in Fig. 1.2. The image formation process is well described in the framework of Fresnel diffraction (Goodman, 2005). The experimental setup is essentially that of standard X-ray radiography, but with the capability of moving the detector away from the object. It requires no other instrumentation, as opposed to the previously mentioned techniques, which makes it experimentally easy to implement. This technique was first demonstrated experimentally with partially coherent synchrotron radiation by Snigirev et al. (1995), and is actually the same setup as the original in-line holography proposed

## Introduction

by Gabor (1948). If coupled to tomography, the technique provides a reconstruction that is roughly dependent on the 3D Laplacian of the refractive index (Cloetens et al., 1997). This can be useful in its own right, and has been applied to several areas of study.

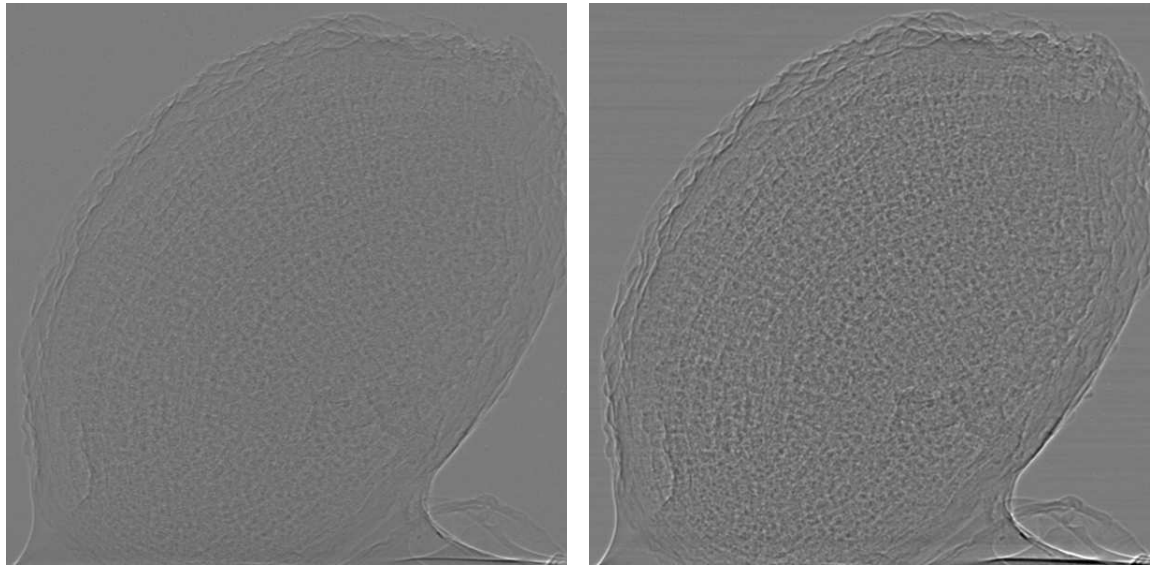
The most interesting feature of propagation based phase contrast imaging is that there exist a quantitative relationship between the object and the recorded image. This can be used to calculate the phase shift that was induced by the object. This is what we in this work define as *phase retrieval*. Several algorithms have been developed, most relying on linearizations of the Fresnel integral to yield efficient reconstruction algorithms (Nugent et al., 1996; Cloetens et al., 1999; Bronnikov, 2002). These algorithms all have limitations, such as being restricted to short propagation distances or to weak absorption.

If phase retrieval is coupled to tomography, by feeding the retrieved phase shift to a tomographic reconstruction algorithm, such as *filtered back-projection* (FBP), the reconstructed quantity is the real part of the complex refractive index (Cloetens et al., 1999). It is from this fact that phase imaging derives its increase in sensitivity, since the real part of the refractive index decrement is one to three orders of magnitude larger than the imaginary, or absorption index, part.

Especially for the weak absorption case, efficient phase retrieval algorithms exist (Cloetens et al., 1999). An example of an application is shown in Fig. 1.3 and 1.4. Phase contrast images of an *Arabidopsis* seed (Fig. 1.3) were used to retrieve the phase, and subsequently by tomographic reconstruction, the 3D refractive index distribution (Fig. 1.4). This allowed to discover channels of air inside the seed, with a presently unknown function. The seeds were imaged in their natural, wet state without staining or any other sample preparation (Cloetens et al., 2006).

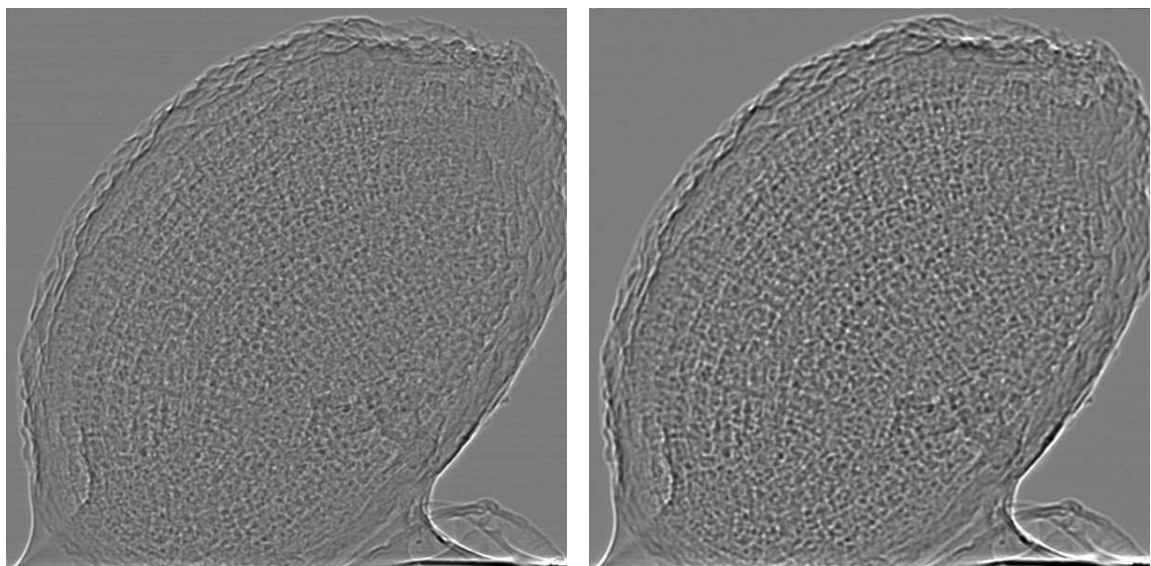
However, many samples interesting to study show strong absorption. This is true in areas such as bone research, materials science and paleontology, where the materials under study often are dense, such as bone, rock or metal. An example of absorption-and-phase contrast radiographs is shown in Fig. 1.5. The problem is often that internal structures do not show sufficient contrast, or that softer parts do not get resolved properly in the presence of strong absorbers. Essentially, four different classes of samples can be discerned:

1. Weak absorption contrast. This case is common in e.g. biological imaging, where the sample might consist only of soft tissue.



(a)  $D=10$  mm

(b)  $D=30$  mm



(c)  $D=60$  mm

(d)  $D=100$  mm

Figure 1.3: Propagation phase contrast radiographs of an *Arabidopsis* seed at different distances  $D$  (cf. Fig. 1.2), imaged using X-rays at 21 keV energy (Cloetens et al., 2006).

2. Mostly weakly absorbing structures, in the presence of strongly absorbing ones. This case is common in e.g. medical applications and small animal imaging, where there can be a large range of absorption contrast between bone and soft tissue.
3. Mostly strongly absorbing structures with some soft ones. This case appears in e.g. bone research, where it might be desirable to resolve both bone microstructure and vascularization simultaneously.
4. Strongly absorbing structures with small relative absorption contrast. This case is common in e.g. paleontology, where the aim is to image small differences in mineralization in a fossil, and in materials science, where the aim might be to resolve grains of similar composition in an alloy.

## 1.1 Objectives

The purpose of this work was to evaluate existing algorithms, and to extend the range of validity of phase retrieval from Fresnel diffraction patterns acquired using hard X-rays, to strongly absorbing objects, that is case 2 to case 4 above. The objective was also to develop practical algorithms that can be used for scientific investigation.

The contributions include the development of a new mathematical model that unifies previously developed models, and also extends validity to objects displaying strong absorption. New regularization techniques were also developed, mainly to deal with problems of low-frequency noise that occurs frequently in phase reconstructions, especially when absorption is strong. The most successful of these is based on an object prior assuming that the sample is homogeneously composed. An algorithm to automatically select the regularization parameter was also developed, which substantially reduces the user time required, thus increasing the practical applicability of the method. Finally, the resulting phase retrieval algorithm was applied to scientific studies in paleontology and bone research.

## 1.2 Outline

In Chapter 2, the foundations of the technique are given. We give the foundations of linear inverse problems. We describe the X-ray interaction with matter, and show why it is advantageous to use phase imaging techniques. We describe the contrast

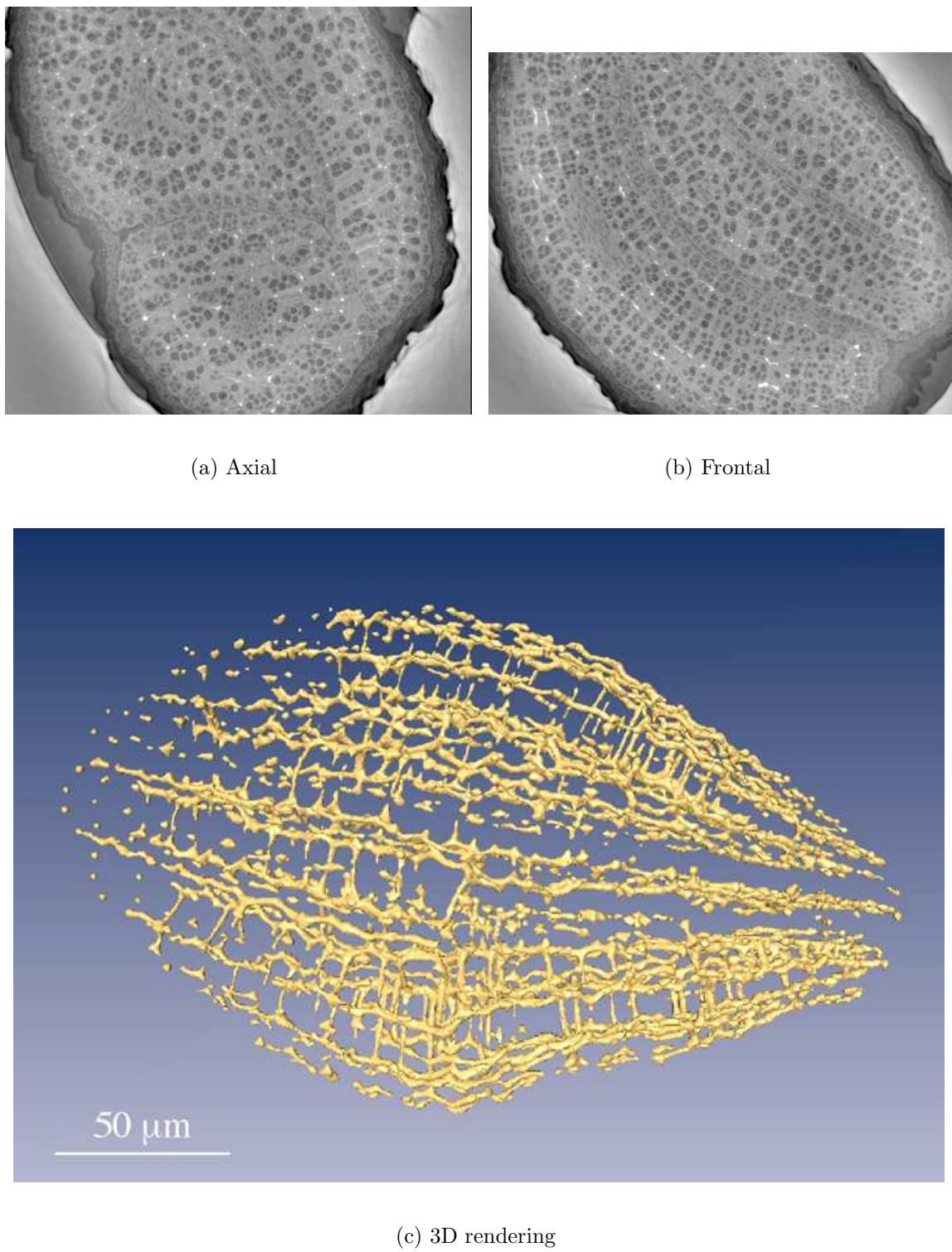


Figure 1.4: Phase tomography of *Arabidopsis* seed. (a) and (b) shows axial and frontal slices. The lighter patches are voids interspersed between the cells. The phase tomography reconstruction enables quantitative analysis in 3D. (c) shows a 3D rendering of the void network. From Cloetens et al. (2006).

## Introduction

formation process for propagation based phase contrast imaging at finite distance - *Fresnel diffraction* - and in the far field - *Fraunhofer diffraction*, which constitutes the *direct problem* for phase retrieval. We then discuss tomography, show the derivations of the main reconstruction techniques, and show that if the phase information is available, it can be used as input to a tomographic reconstruction algorithm to yield the 3D refractive index decrement distribution. We formulate phase retrieval as a minimization problem, which serves as our problem definition.

In Chapter 3, we present a new linearized mathematical model for the contrast formation. It unifies the two main linearized frameworks, the transport of intensity equation (TIE) and contrast transfer functions (CTF), and is also valid for strong absorption. This chapter was published in *Optics Letters* (Guigay et al., 2007).

In Chapter 4, a comparative study of four different phase retrieval algorithms, one based on the contrast transfer functions, one based on the TIE, another one based on the TIE and weak absorption, and finally the mixed approach presented in Chapter 3. This chapter was published in *Medical Physics* (Langer et al., 2008).

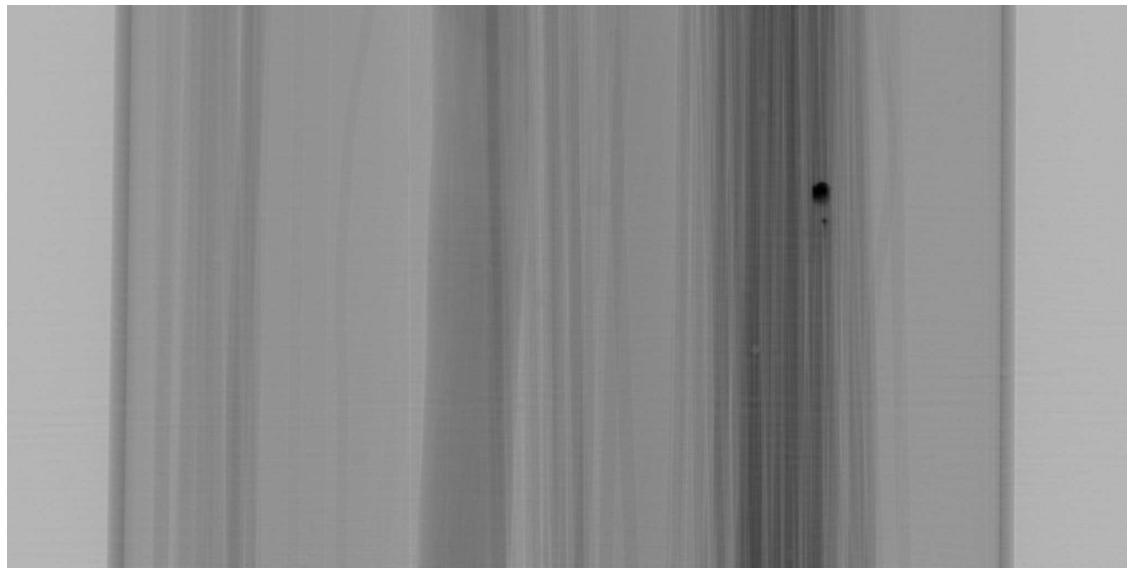
In Chapter 5, we develop two new regularization methods for phase retrieval. The first one (Section 5.3) is based on Fourier-wavelet deconvolution. While it shows some promise on simulated data, it is presently too computationally intensive to be practical. The second one (Section 5.4) is based on a homogeneous composition prior. The absorption image is used as prior knowledge on the phase for the lowest frequencies, where information on the phase is always lost due to the image formation process. An automatic parameter selection algorithm based on the L-curve method was also implemented, which balances the solution's fit to prior knowledge and fit to data. Section 5.3, which describes the Fourier-wavelet regularization scheme, is a manuscript prepared for the *Journal of the Optical Society of America A* and Section 5.4, which describes the homogeneous composition scheme, was submitted to *IEEE Transactions on Image Processing*.

In Chapter 6, the usefulness of the homogeneous composition algorithm presented in Section 5.4 is shown. In Section 6.1, it is applied to paleontology, where its use allowed the discovery of the first ever found fossilized brain. In Section 6.2, the algorithm is used in a tissue engineering study for quantitative imaging of in-vitro cultivated bone scaffolds. Section 6.1 was submitted to the *Proceedings of the National Academy of Science of the United States of America*, and Section 6.2 is a manuscript prepared for the *Journal of Microscopy*.

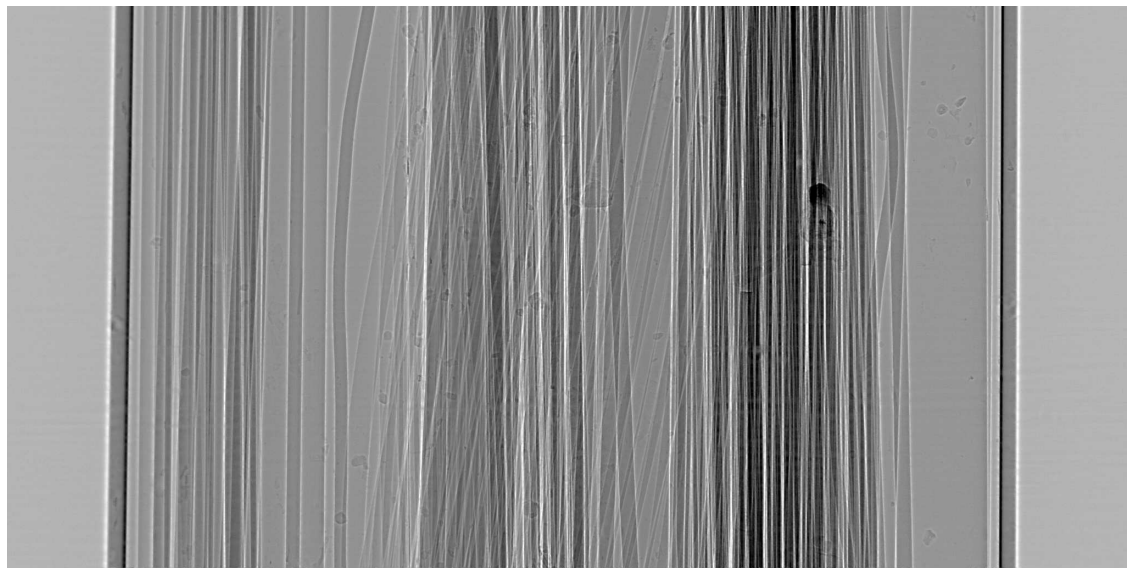
In Chapter 7, we give indications to where future research interests lie. In particular we

investigate the possibility to use iterative phase retrieval methods. We develop three algorithms based on the iterative methods used in phase retrieval from Fraunhofer diffraction patterns. We conclude that they are not suitable in their present form.

## Introduction



(a)



(b)

Figure 1.5: (a) Absorption radiograph recorded at  $D = 2$  mm and (b) mixed absorption and phase radiograph of a constructed object, recorded at  $D = 45$  mm. The X-ray energy was  $E = 20.5$  keV and the horizontal field of view is 1.43 mm.

# Chapter 2

## Theoretical background

Phase retrieval is an example of an inverse problem. We want from a set of measurements of a physical event, in this case Fresnel diffraction, calculate the parameters which give rise to our measurements, that is the 3D composition of our imaged object. Phase tomography actually consists of two inverse problems, phase retrieval and tomography, or cross-sectional imaging. Since tomographic reconstruction is a linear problem, it can be considered separately from the phase retrieval step, creating a two-step process.

In this chapter, we give some basic theory of inverse problems and linear inverse problems. This will be used further on to develop phase retrieval algorithms. The fundamentals of the in-line phase tomography technique is then presented. It is separated in two parts, Fresnel diffraction and tomography. Fresnel diffraction constitutes the direct problem in phase retrieval. We describe a propagating wave's interaction with matter and derive the most important relation, the Fresnel integral (Eq. 2.52), and a form of it due to Guigay (1977) which will prove useful for deriving linear phase retrieval algorithms. We also show the influence of using a partially coherent beam and the influence of the detector in the recorded intensity and note that these influence the problem in a simple way, which makes it possible to consider them separately from the phase retrieval problem.

## 2.1 Inverse Problems

Physical models can be described by mappings  $\mathcal{M}$  of sets of theoretical parameters  $\Gamma$  to sets of results  $R$ .

$$\mathcal{M} : \Gamma \mapsto R \quad (2.1)$$

The mapping  $\mathcal{M}$ , generally a non-linear operator, is called the *forward operator*. The set  $R$  can contain measured, imprecise data, the set of exact, simulated results, as well as many other elements if  $R$  and  $\Gamma$  have been defined in a simple way (Sabatier, 1985).

Solving the *direct problem*, in simple terms (Tarantola, 1987), means using a precise definition of  $\mathcal{M}$  and an element  $p \in \Gamma$  to obtain  $\mathcal{M}(p)$ . That is, in other words, to calculate the output of a known system if the input is known. This is usually less challenging than doing the opposite: solving the *inverse problem*, that is calculating the theoretical parameters  $p$  given some data  $r \in R$ . The direct and inverse problems are summarized in Fig. 2.1. Solving an inverse problem can be seen as interpreting the data  $r$ .

Solving the inverse problem is an easy task if the problem is *well-posed* (Hadamard, 1902), that is

1. A solution exists
2. The solution is unique
3. The solution depends continuously on the data.

This essentially means that  $\mathcal{M}$  has to be bijective, and  $\mathcal{M}^{-1}$  has to be continuous. Problems not satisfying this definition are usually called *ill-posed*.

Well-posedness is rarely the case for physical problems, if nothing else due to that measurements are always finitely many while the parameters are often continuous functions, going through an infinity of values. The ill-posedness can also stem from the mapping  $\mathcal{M}$  itself.

### 2.1.1 Linear discrete inverse problems

If the mapping  $\mathcal{M}$  is linear, that is  $\mathcal{M}(p_1 + p_2) = \mathcal{M}(p_1) + \mathcal{M}(p_2)$  and  $\mathcal{M}(\varsigma p) = \varsigma \mathcal{M}(p)$ , with  $\varsigma \in R$ , the problem is linear. If the problem is discrete or suitably discretized, an instance of the problem can be written as

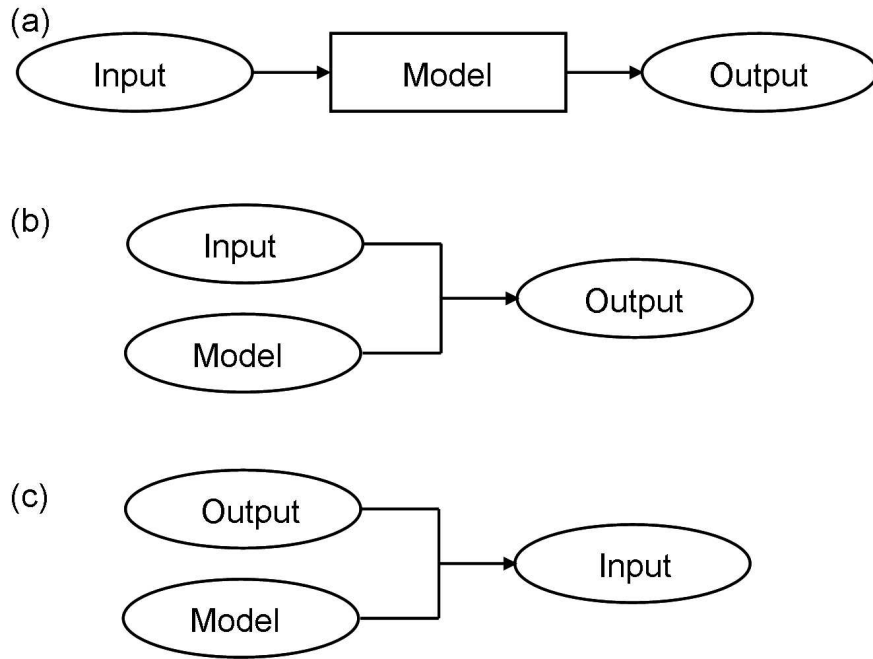


Figure 2.1: (a) A generic system. (b) The direct problem is to calculate the output of a system when the model parameters and the input to the system are known. (c) The inverse problem is to calculate what the input to the system was if the output from the system and the model parameters are known.

$$\mathbf{M}\mathbf{p} = \mathbf{r} \quad (2.2)$$

where  $\mathbf{M}$  is a (complex) matrix, and  $\mathbf{r}$  and  $\mathbf{p}$  are (complex) vectors.

### 2.1.2 Inversion of linear, discrete problems

If the discretized problem is well-posed, that is if  $\mathbf{M}$  is non-singular and has full rank, the inverse  $\mathbf{M}^{-1}$  exist, and  $\mathbf{p}$  is directly given by

$$\mathbf{p} = \mathbf{M}^{-1}\mathbf{r}. \quad (2.3)$$

If the problem is ill-posed, that is  $\mathbf{M}$  is singular or rank deficient, or the matrix  $\mathbf{M}$  is not square, the best we can do is to find an element  $\mathbf{p}$  that is “closest” to  $\mathbf{r}$ , e.g. in the least squares sense

$$\arg \min_{\mathbf{p}} \epsilon^2 = |\mathbf{M}\mathbf{p} - \mathbf{r}|^2, \quad (2.4)$$

## Theoretical background

where  $|\mathbf{x}| = \sqrt{x_1^2 + x_3^2 + \dots + x_n^2}$  is the  $L_2$  norm. The solution to this problem, in analogy to Eq. 2.3, is given by the pseudo-inverse

$$\mathbf{p} = \mathbf{M}^\dagger \mathbf{r}. \quad (2.5)$$

For the least-squares case above, the pseudo-inverse is the Moore-Penrose pseudo-inverse (Moore, 1920; Penrose, 1955, 1956). If the columns of  $\mathbf{M}$  are linearly independent, an explicit formula can be found by premultiplying both sides of Eq. 2.2 with the conjugate transpose  $\mathbf{M}^*$ :

$$\mathbf{M}^* \mathbf{M} \mathbf{p} = \mathbf{M}^* \mathbf{r}. \quad (2.6)$$

The matrix  $\mathbf{M}^* \mathbf{M}$  is a square, and in this case always invertible matrix.  $\mathbf{p}$  is now given by

$$\mathbf{p} = (\mathbf{M}^* \mathbf{M})^{-1} \mathbf{M}^* \mathbf{r} \quad (2.7)$$

and, in this case,

$$\mathbf{M}^\dagger = (\mathbf{M}^* \mathbf{M})^{-1} \mathbf{M}^*. \quad (2.8)$$

This is indeed the solution to Eq. 2.4, as can be shown by finding the extreme point of Eq. 2.4. This is done by calculating the partial derivatives of  $\epsilon^2$  with respect to the real and imaginary part of  $\mathbf{p}$

$$\frac{\partial \epsilon^2}{\partial \mathbf{p}} \equiv \frac{\partial \epsilon^2}{\partial \text{Re}[\mathbf{p}]} + i \frac{\partial \epsilon^2}{\partial \text{Im}[\mathbf{p}]} = 0. \quad (2.9)$$

Calculation of the partial derivatives and reordering of terms gives

$$\begin{cases} \frac{\partial \epsilon^2}{\partial \text{Re}[\mathbf{p}]} &= 2 \text{Re} [\mathbf{M}^* \mathbf{M} \mathbf{p} - \mathbf{M}^* \mathbf{r}] \\ \frac{\partial \epsilon^2}{\partial \text{Im}[\mathbf{p}]} &= 2 \text{Im} [\mathbf{M}^* \mathbf{M} \mathbf{p} - \mathbf{M}^* \mathbf{r}] \end{cases} \quad (2.10)$$

Combining Eq. 2.9 and Eq. 2.10 gives

$$\mathbf{p} = (\mathbf{M}^* \mathbf{M})^{-1} \mathbf{M}^* \mathbf{r}. \quad (2.11)$$

This can be identified directly with Eq. 2.6, which was the desired result.

### 2.1.3 Conditioning

An invertible linear problem can still be problematic. If  $\mathbf{M}$  is close to singular, errors in  $\mathbf{r}$  will be propagated more easily to  $\mathbf{p}$ , since a small error in  $\mathbf{r}$  could cause a large error in  $\mathbf{p}$ . That is there exists an  $\zeta$  which can be arbitrarily small so that

$$\mathbf{M}^{-1}(\mathbf{r} + \zeta) = \mathbf{p} + \xi, \quad (2.12)$$

where  $\xi \gg \zeta$ . i.e.  $\xi$  is not arbitrarily small and is not negligible.

This can be quantified by the *condition number* of a matrix,  $\mathcal{K}(\mathbf{M})$ , which is defined as the maximum ratio of the relative error in  $\mathbf{p}$  divided by the relative error in  $\mathbf{r}$ . If we take  $\mathbf{e}$  to be the error in  $\mathbf{r}$ , then the error in the solution  $\mathbf{M}^{-1}\mathbf{r}$  is  $\mathbf{M}^{-1}\mathbf{e}$ . The ratio of the relative error in the solution to the relative error in  $\mathbf{r}$  can then be written as

$$\frac{|\mathbf{M}^{-1}\mathbf{e}|/|\mathbf{M}^{-1}\mathbf{r}|}{|\mathbf{e}|/|\mathbf{r}|}. \quad (2.13)$$

The maximum of Eq. 2.13 is the condition number, and is found as (Rade and Westergren, 2004)

$$\mathcal{K}(\mathbf{M}) = |\mathbf{M}^{-1}| |\mathbf{M}|. \quad (2.14)$$

If  $\mathbf{M}$  is normal, that is  $\mathbf{M}^*\mathbf{M} = \mathbf{M}\mathbf{M}^*$ , the condition number may be defined as a function of the eigenvalues of  $\mathbf{M}$ . Let  $\{v\}$  be the set of eigenvalues of  $\mathbf{M}$  (Andrews and Hunt, 1977), then

$$\mathcal{K}(\mathbf{M}) = \left( \frac{v_{max}}{v_{min}} \right)^{1/2}. \quad (2.15)$$

It is obvious that if  $v_{min} \rightarrow 0$ , the condition number goes to infinity. This is the case when  $\mathbf{M}$  is singular.

### 2.1.4 Regularization

If  $\mathbf{M}^*\mathbf{M}$  is ill-conditioned or singular, there is generally no unique solution. Instead, some suitable, meaningful solution must be found based on available assumptions, prior knowledge about, or constraints on the solution (Andrews and Hunt, 1977). Additional knowledge about the solution can be e.g. smoothness assumptions or bounds on the

norm (Neumaier, 1998). Introduction of such information in the problem is called *regularization*. The least-squares method can itself be seen as a simple form of regularization, since it introduces an assumption about the solution, namely that  $\mathbf{M}\mathbf{p}$  should minimize the distance to the data  $\mathbf{r}$  in the least squares sense.

#### 2.1.4.1 Tikhonov regularization

The most common ways to regularize a problem is to introduce either a norm of the solution, add a smoothness constraint or introduce some *a priori* knowledge about the solution. These can all be taken into account by *Tikhonov regularization*, which states the minimization problem as

$$\arg \min_{\mathbf{p}} \epsilon^2 = |\mathbf{M}\mathbf{p} - \mathbf{r}|^2 + \alpha |\mathbf{L}(\mathbf{p} - \mathbf{p}_0)|^2, \quad (2.16)$$

where  $\mathbf{p}_0$  is some *a priori* known information about the solution, e.g. an estimate calculated by other means.  $\alpha$  is an arbitrary *regularization parameter* which balances the solution's fit to the measurements and fit to the *a priori* knowledge. The matrix  $\mathbf{L}$  is called the *Tikhonov matrix*, and can be used to enforce smoothness in the solution by choosing it as a high-pass operator, e.g. the difference operator.

It can be shown that the solution to this minimization problem is given by

$$\mathbf{p} = (\mathbf{M}^*\mathbf{M} + \alpha \mathbf{L}^*\mathbf{L})^{-1}(\mathbf{M}^*\mathbf{b} + \alpha \mathbf{L}^*\mathbf{L}\mathbf{p}_0) \quad (2.17)$$

If  $\mathbf{L}_0$  is set to identity and  $\mathbf{p}_0 = 0$ , the effect of Tikhonov regularization is to limit the energy in the solution. We can also note that where  $\mathbf{M}$  approaches zero, the solution will approach the *a priori* solution

$$\lim_{\mathbf{M} \rightarrow 0} \mathbf{p} = \mathbf{p}_0, \quad (2.18)$$

with equality in singular points of  $\mathbf{M}$ , since the measurements will not contain any information about the solution in those points.

## 2.2 Direct problem: Image formation

We now turn our attention to the specific inverse problem at hand. It can be divided into two parts: the phase contrast formation process, which is the direct problem to phase retrieval, and tomographic imaging. We begin by studying the X-ray beam's interaction with matter and how this relates to the contrast formed on the detector. We also show how the phase shift of the X-ray beam induced by the object relates to tomographic imaging, and give the basic results in tomographic reconstruction.

### 2.2.1 Wave-object interaction

When an X-ray beam passes through an object, it may be affected in two ways. It might be absorbed in the object, which changes its amplitude, and it might be retarded in the object, which changes its phase. The effects of a beam encountering an object is usually termed *diffraction*, and can be described by the complex refractive index  $n$ . For X-rays this is usually written as

$$n = 1 - \delta_n + i\beta \quad (2.19)$$

with  $\delta_n$  being the refractive index decrement and  $\beta$  the absorption index. The refractive index is defined so that the wavenumber in vacuum

$$k = 2\pi/\lambda, \quad (2.20)$$

where  $\lambda$  is the X-ray wavelength, and in a material  $k'$  are related by  $k' = nk$ , so that a plane wave is of the form

$$\exp(inkz) = \exp[i(1 - \delta_n)kz] \exp(-\beta kz). \quad (2.21)$$

Thus, the refractive index decrement  $\delta_n$  is related to phase shift and  $\beta$  to absorption.

### 2.2.2 Attenuation

The main processes that contribute to the attenuation of an X-ray beam in the energy range we are concerned with (8-100 keV) are (pure) absorption due to the photoelectric effect, Rayleigh (elastic) and Compton (inelastic) scattering (Michette and Buckley, 1993). Precise formulas for the respective cross sections can be derived (Michette and

## Theoretical background

Buckley, 1993), but we give here instead some rules of thumbs for how they depend on the energy and atomic number (Wang, 2007). In practice, theoretical values for imaged materials are calculated using tabulated values, e.g. by using the XOP software (Dejus and Sanchez del Rio, 1996; Sanchez del Rio and Dejus, 2004) or the NIST XCOM database (Berger et al., 1998).

### 2.2.2.1 Absorption

The absorption part of the total attenuation is due to the photoelectric effect. An incoming X-ray photon with energy  $E$  interacts with a bound atomic electron, whereby it is completely absorbed. The excited atom emits an electron with energy  $E_e = E_p - E_{shell}$ , where  $E_{shell}$  is the binding energy of the electron, and is thereby ionized. Subsequently, the ionized atom returns to the neutral state with the emission of a photon characteristic of the atom. This subsequent emission of lower energy photons is generally absorbed in the material. The atomic photoelectric cross section  $\sigma_{photoelectric}$  is dependent on the X-ray energy  $E$  and the atomic number  $Z$ , and can be shown to depend on them as (Wang, 2007)

$$\sigma_{photoelectric} \propto \frac{Z^5}{E^{3.5}} \quad (2.22)$$

when far from discontinuities associated with the binding energy of the electron, “absorption edges”. Photoelectron absorption is the dominant process for X-ray absorption up to energies of about 500 KeV. Photoelectron absorption is also dominant for atoms of high atomic numbers.

### 2.2.2.2 Rayleigh scattering

Rayleigh scattering, or elastic scattering, refers to the coherent sum of elastic scatterings from all electrons in an atom. Elastically scattered photons maintain their energy and are only deviated from their path by interaction with electrons in the material. The Rayleigh scattering cross section depends on the X-ray energy and atomic number as (Wang, 2007)

$$\sigma_{Rayleigh} \propto \left(\frac{Z}{E}\right)^2. \quad (2.23)$$

Rayleigh scattering is never more than a minor contributor to the attenuation coefficient.

### 2.2.2.3 Compton scattering

The atomic Compton scattering refers to the incoherent sum of scatterings from all electrons in an atom. Here, the photon scatters from an electron which recoils and carries off a fraction of the photon's energy. In this process a photon leaves the interaction (contrary to the photoelectric effect), but with reduced energy (contrary to Rayleigh scattering). The shift in wavelength is

$$\lambda' - \lambda = \frac{\hbar}{m_e c} (1 - \cos \Theta), \quad (2.24)$$

where  $\hbar$  is Planck's constant,  $m_e$  the classical electron mass,  $\Theta$  the scattering angle and  $c$  the speed of light in vacuum. This depends only on the scattering angle and not the nature of the material. The Compton scattering cross section depends on  $Z$  and  $E$  as (Wang, 2007)

$$\sigma_{Compton} \propto \frac{Z m_e c}{E + m_e c^2}, \quad (2.25)$$

where  $m_e c^2 \approx 511\text{keV}$  is the electron rest energy. This means that for our energy range of interest, the Compton scattering cross section is approximately proportional to the atomic number.

### 2.2.2.4 Total attenuation coefficient

The quantity that is measured by recording attenuation projections through an object is the total attenuation coefficient or *linear attenuation coefficient*  $\mu$ . It is based on the total cross section, that is the sum of the contributing processes

$$\sigma_{tot} = \sigma_{photoelectric} + \sigma_{Rayleigh} + \sigma_{Compton}. \quad (2.26)$$

The total linear attenuation coefficient  $\mu$  is then

$$\mu = \frac{N_A \rho \sigma_{tot}}{A} \quad (2.27)$$

where  $\rho$  is the density of the material,  $N_A$  is Avogadro's number and  $A$  is the atomic mass of the material. The attenuation coefficient  $\mu$  is related to the attenuation index  $\beta$  as

$$\mu = \frac{4\pi}{\lambda} \beta. \quad (2.28)$$

### 2.2.2.5 Beer-Lambert law

If we consider an X-ray beam passing through a homogeneous medium, with  $N(z, E)$  the number of photons at a certain energy  $E$ , the number of photons which interact with the medium over a short distance  $dz$  is proportional to the number of incident photons. This is described by the Beer-Lambert law

$$dN = -\mu(z, E)N(z, E)dz. \quad (2.29)$$

The solution to this simple differential equation is given by

$$N(z, E) = N_0(E) \exp[-\mu(z, E)z], \quad (2.30)$$

where  $N_0(E) = N(z_0, E)$  is the number of incident photons. That is, the number of photons passing through a homogeneous medium is dependent on the number of incident photons, the attenuation coefficient and the path length in the medium. The equivalent for heterogeneous objects can be defined by considering infinitesimal sections of the object homogeneous, which yields

$$N(z, E) = N_0(E) \exp \left[ - \int \mu(z, E) dz \right]. \quad (2.31)$$

### 2.2.3 Refractive index decrement

The refractive index decrement  $\delta_n$  describes the wave propagation in the medium. For a pure element it can be written as

$$\delta_n = \frac{r_c \lambda^2}{2\pi V} (Z + f'), \quad (2.32)$$

where  $r_c$  is the classical electron radius and  $f'$  is the real part of the dispersion correction (Henke et al., 1993), which is significant near absorption edges. If we neglect  $f'$ , we can from Eq. 2.32 and Section 2.2.2 see that the dependence of  $\delta_n$  and  $\beta$  on energy and atomic number is approximately

$$\delta_n \propto \frac{Z}{E^2}, \quad \beta \propto \frac{Z^5}{E^{4.5}}. \quad (2.33)$$

For hard X-rays, the absorption index falls off steeply, and  $\delta_n$  can be up to three orders of magnitude larger than  $\beta$  at energies above 10 keV. Values of  $\delta_n$  and  $\beta$  at 20 keV for some representative materials are given in Tab. 2.1. The large difference between  $\delta_n$  and  $\beta$  is the main advantage of phase contrast imaging.

Eq. 2.32 can also be written in terms of the number  $N_j$  of atoms of a certain species  $j$  (Michette and Buckley, 1993)

$$\delta_n = \frac{r_c N_A}{2\pi} \lambda^2 \rho \frac{\sum_j N_j (Z_j + f'_j)}{\sum_j N_j A_j}, \quad (2.34)$$

where  $\rho$  is the mass density of the material. If the composition is known in terms of the mass fractions  $q_j$ , the expression

$$\delta_n = \frac{r_c N_a}{2\pi} \lambda^2 \rho \sum_j q_j (Z_j + f'_j) / A_j \quad (2.35)$$

can be used. The ratios  $Z_j/A_j$  are similar for many atomic species, around 1/2. We can therefore, from Eq. 2.33 and Eq. 2.35, see that  $\delta_n$  is approximately proportional to  $\lambda^2$  and  $\rho$ . It can be determined to be approximately (Guinier, 1994)

$$\delta_n \approx 1.3 \times 10^{-6} \rho \lambda^2, \quad (2.36)$$

with  $\rho$  in  $g/cm^3$  and  $\lambda$  in  $\text{\AA}$ . This shows another interest in phase imaging techniques, especially phase tomography, since the reconstructed quantity is easy to interpret. It corresponds essentially to the electron density, or approximately the mass density.

Table 2.1: Complex refractive indices for some representative materials at 20 keV (Momose, 2005).

| Material    | $\delta_n$           | $\beta$               | $\delta_n/\beta$  |
|-------------|----------------------|-----------------------|-------------------|
| Polystyrene | $5.0 \times 10^{-7}$ | $3.2 \times 10^{-10}$ | $1.6 \times 10^3$ |
| Water       | $5.8 \times 10^{-7}$ | $6.0 \times 10^{-10}$ | $9.7 \times 10^2$ |
| Glass       | $1.3 \times 10^{-6}$ | $2.9 \times 10^{-9}$  | $4.5 \times 10^2$ |
| Silicon     | $1.2 \times 10^{-6}$ | $4.9 \times 10^{-9}$  | $2.4 \times 10^2$ |
| Iron        | $3.8 \times 10^{-6}$ | $9.7 \times 10^{-8}$  | $3.9 \times 10^1$ |

## 2.3 Propagation based phase contrast imaging

For our purposes here, we consider the 3D imaged object completely described by

$$n(x, y, z) = 1 - \delta_n(x, y, z) + i\beta(x, y, z), \quad (2.37)$$

where  $\delta_n(x, y, z)$  is the 3D refractive index decrement distribution in the object,  $\beta(x, y, z)$  the 3D absorption index distribution and  $(x, y, z)$  are the spatial coordinates. Both the attenuation and the phase shift induced by the object can be described as projections through the absorption and refractive index distributions respectively, with

$$B(\mathbf{x}) = (2\pi/\lambda) \int \beta(x, y, z) dz \quad (2.38)$$

and

$$\varphi(\mathbf{x}) = -(2\pi/\lambda) \int \delta_n(x, y, z) dz. \quad (2.39)$$

$\mathbf{x} = (x, y)$  are the spatial coordinates in the plane perpendicular to the propagation direction  $z$  (Fig. 2.2). We assume that the object can be described as a 2D complex transmittance function  $T(\mathbf{x})$ , that is the propagation path inside the object is considered straight and propagation effects that occur inside the sample are neglected. This is often valid in the energy range we are concerned with (Goodman, 2005). This transmittance function can be written as

$$T(\mathbf{x}) = \exp[-B(\mathbf{x})] \exp[i\varphi(\mathbf{x})]. \quad (2.40)$$

This allows us to write the object's influence on the incident wave field  $u_{inc}(\mathbf{x})$  as

$$u_0(\mathbf{x}) = T(\mathbf{x}) u_{inc}(\mathbf{x}), \quad (2.41)$$

where  $u_0(\mathbf{x})$  is the wave field at the exit plane of the object. The *intensity* of the wave at a distance  $D$  downstream of the sample is

$$I_D(\mathbf{x}) = |u_D(\mathbf{x})|^2, \quad (2.42)$$

which is the quantity which can be measured directly. Defining the 2D Fourier transform as

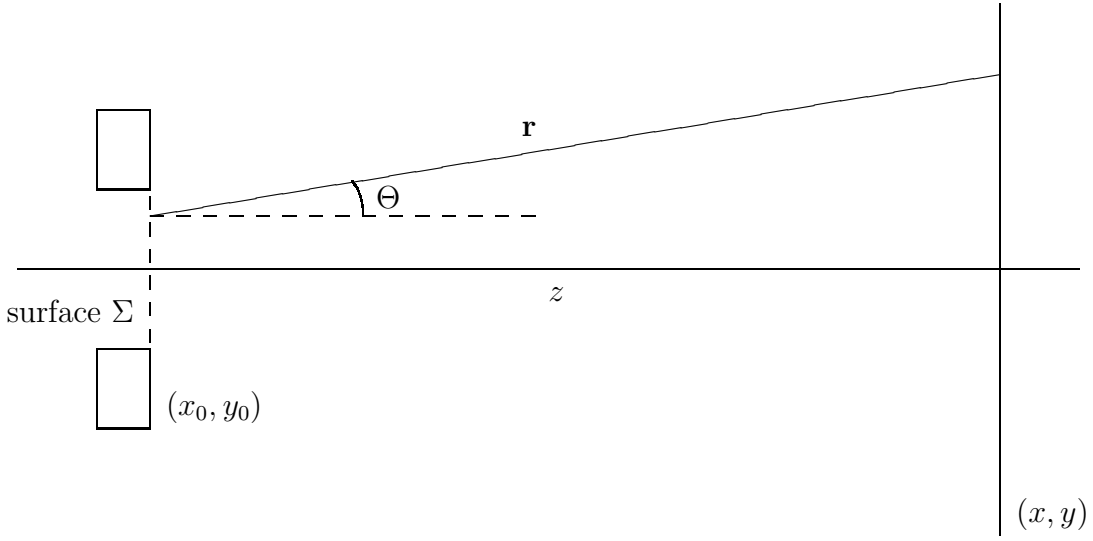


Figure 2.2: Geometry of Fresnel diffraction.  $(x, y)$  are the coordinates in the image plane,  $z$  is the beam propagation direction and  $\Sigma$  is the support of the transmittance function  $T(\mathbf{x})$ . Each point in the object plane contributes to each point in the diffraction plane at distance  $D$ .

$$\tilde{g}(\mathbf{f}) = \mathcal{F}\{g\}(\mathbf{f}) = \int g(\mathbf{x}) \exp(-i2\pi\mathbf{x} \cdot \mathbf{f}) d\mathbf{x}, \quad (2.43)$$

the Fourier transform of the intensity can be written as

$$\tilde{I}_D(\mathbf{f}) = \int \tilde{u}_D(\mathbf{f}') \tilde{u}_D^*(\mathbf{f}' - \mathbf{f}) d\mathbf{f}'. \quad (2.44)$$

This is the autocorrelation of the wave in Fourier space. Calculation of  $I_D(\mathbf{x})$  is simple (Eq. 2.42), compared to the calculation in Fourier space. This makes it preferable to do intensity calculations in real space.

At the exit plane of the sample ( $D = 0$ ), we have

$$I_0(\mathbf{x}) = |T(\mathbf{x})u_{inc}(\mathbf{x})|^2 = \exp[-2B(\mathbf{x})]I_{inc}(\mathbf{x}), \quad (2.45)$$

from which we can see that the attenuation part of the transmittance function can be accessed directly, if the incident intensity  $I_{inc}(\mathbf{x})$  is measured independently. Intensity

measurements are available in essentially every plane, but phase information is lost and has to be retrieved from intensity measurement. Phase modulation turns into amplitude information through free space propagation, and is therefore entangled with the attenuation in the intensity.

### 2.3.1 Fresnel diffraction

It can be shown that the effect on the wave of letting it propagate in free space can be described as a convolution (Goodman, 2005)

$$u_D(\mathbf{x}) = P_D(\mathbf{x}) * u_0(\mathbf{x}). \quad (2.46)$$

$u_D(\mathbf{x})$  is the complex wave function in the diffraction plane, a distance  $D$  from the object and  $P_D(\mathbf{x})$  is called the Fresnel propagator. This can, of course, equivalently be written as a multiplication in the Fourier domain

$$\tilde{u}_D(\mathbf{f}) = \tilde{P}_D(\mathbf{f})\tilde{u}_0(\mathbf{f}). \quad (2.47)$$

These relations can be arrived at through both analysis in the spatial and the Fourier domain.

#### 2.3.1.1 Spatial domain analysis

We start by decomposing the propagating wave into point sources at the exit of the object. These can then be superimposed linearly by summing over all point sources. This yields the Rayleigh-Sommerfield diffraction integral (Goodman, 2005)

$$u_D(\mathbf{x}) = \frac{1}{i\lambda} \iint_{\Sigma} u_0(\mathbf{x}_0) \frac{e^{ik|\mathbf{r}|} \cos \theta}{|\mathbf{r}|} d\mathbf{x}_0. \quad (2.48)$$

The integration is in the object plane,  $|\mathbf{r}|$  is the path length between points in the object and diffraction planes and  $\theta$  is the angle between  $\mathbf{r}$  and the propagation direction (Fig. 2.2).

For X-rays,  $\theta$  is small, so we can make the approximations  $\cos \theta \approx 1$  and  $r \approx D$  in the denominator, moving it outside the integration. In the exponent,

$$|\mathbf{r}| = \sqrt{D^2 + (x - x_0)^2 + (y - y_0)^2} \quad (2.49)$$

can be approximated by the binomial expansion

$$|\mathbf{r}| \approx D \left[ 1 + \frac{1}{2} \left( \frac{x - x_0}{D} \right)^2 + \frac{1}{2} \left( \frac{y - y_0}{D} \right)^2 \right]. \quad (2.50)$$

This is known as the Fresnel approximation. It is valid if the condition

$$D^3 \gg \max \frac{\pi}{4\lambda} [(x - x_0)^2 + (y - y_0)^2]^2 \quad (2.51)$$

holds. This yields the Fresnel integral

$$u_D(\mathbf{x}) = \frac{\exp(i k D)}{i \lambda D} \iint_{\Sigma} u_0(\mathbf{x}_0) \exp \left\{ i \frac{\pi}{\lambda D} [(x - x_0)^2 + (y - y_0)^2] \right\} d\mathbf{x}_0, \quad (2.52)$$

which can be seen as a convolution of the exit wave  $u_0(\mathbf{x})$  and a propagator. We have thus arrived at Eq. 2.46, with the propagator

$$P_D(\mathbf{x}) = \frac{1}{i \lambda D} \exp \left( i \frac{\pi}{\lambda D} |\mathbf{x}|^2 \right), \quad (2.53)$$

where we have dropped the non-relevant phase factor (it disappears on taking the squared modulus for the intensity).

### 2.3.1.2 Fourier space analysis

Propagation of a wave in free space can also be analyzed in the Fourier domain, by decomposing the propagating wave into plane waves (Goodman, 2005). This is done by taking the Fourier transform of  $u_0(\mathbf{x})$  :

$$\tilde{u}_0(\mathbf{f}) = \iint u_0(\mathbf{x}) \exp(-i 2\pi \mathbf{x} \cdot \mathbf{f}) d\mathbf{x}. \quad (2.54)$$

The inverse Fourier transform allows us to write the wave as a superposition of complex exponentials

$$u_0(\mathbf{x}) = \iint \tilde{u}_0(\mathbf{f}) \exp(i 2\pi \mathbf{x} \cdot \mathbf{f}) d\mathbf{f}. \quad (2.55)$$

Each exponential describes a plane wave with wavevector  $\mathbf{k} = (k_x, k_y, k_z)$ , and  $k_x = 2\pi f_x$ ,  $k_y = 2\pi f_y$  and  $k_z = \frac{2\pi}{\lambda} \sqrt{1 - (\lambda f_x)^2 - (\lambda f_y)^2}$ . Propagation to the plane  $z =$

## Theoretical background

$D$  corresponds to a multiplication of a complex exponential with the phase factor  $\exp(ik_z D)$ , which gives

$$u_D(\mathbf{x}) = \iint \tilde{u}_0(\mathbf{f}) \exp \left[ i \frac{2\pi}{\lambda} D \sqrt{1 - (\lambda f_x)^2 - (\lambda f_y)^2} \right] \exp(i2\pi\mathbf{x} \cdot \mathbf{f}) d\mathbf{f}. \quad (2.56)$$

In the Fourier domain, this is

$$\tilde{u}_D(\mathbf{f}) = \tilde{u}_0(\mathbf{f}) \exp \left[ i \frac{2\pi}{\lambda} D \sqrt{1 - (\lambda f_x)^2 - (\lambda f_y)^2} \right]. \quad (2.57)$$

It is seen that free space propagation is described by a multiplication with a frequency-dependent phase term. The angle  $\Theta$  between the wavevector and the incident beam for a given plane wave component is

$$|\sin \Theta| = \lambda |\mathbf{f}|. \quad (2.58)$$

The length scales of interest in the object are much larger than the wavelength  $\lambda$ , which means that  $\theta$  is small and can be approximated as

$$|\sin \Theta| \approx |\Theta|, |\Theta| \ll 1. \quad (2.59)$$

Taylor expansion to the first order of the square root in Eq. 2.57 yields

$$\tilde{u}_D(\mathbf{f}) = \tilde{u}_0(\mathbf{f}) \exp \left( \frac{i2\pi D}{\lambda} \right) \exp(-i\pi\lambda D|\mathbf{f}|^2). \quad (2.60)$$

Second order terms are negligible if

$$\frac{D\lambda^3 |\mathbf{f}|_{\max}^4}{8} \ll 1 \quad (2.61)$$

In Eq. 2.60 we can see that free space propagation is described by a multiplication in the Fourier domain. We have thus arrived at Eq. 2.47, with the Fourier transform of the Fresnel propagator as

$$\tilde{P}_D(\mathbf{f}) = \exp(-i\pi\lambda D|\mathbf{f}|^2), \quad (2.62)$$

again leaving out the phase term. This is, as expected, the Fourier transform of the Fresnel propagator (Eq. 2.53).

### 2.3.1.3 Mixed space-frequency analysis

It is also possible to write the Fourier transform of the intensity  $\tilde{I}_D(\mathbf{f})$  as one double integral on the wave  $u_0(\mathbf{x})$  in the spatial domain (Guigay, 1977). Taking the Fourier transform of Eq. 2.42 and replacing the propagated wave  $u_D(\mathbf{x})$  with the Fresnel integral (Eq. 2.52) gives the intensity spectrum as a sextuple integral. This integral can be simplified to a double integral (Guigay, 1977)

$$\tilde{I}_D(\mathbf{f}) = \iint T\left(\mathbf{x} - \frac{\lambda D \mathbf{f}}{2}\right) T^*\left(\mathbf{x} + \frac{\lambda D \mathbf{f}}{2}\right) \exp(-i2\pi \mathbf{x} \cdot \mathbf{f}) d\mathbf{x}. \quad (2.63)$$

Even though the exponential factor is identical to the one in the Fourier transform, this expression is not a Fourier transform of  $T(\mathbf{x})$ , since the two other terms depend on the frequency  $\mathbf{f}$  in the shifts. This can be seen as a plane through the 4D ambiguity function (Papoulis, 1974; Guigay, 1978; Nugent, 2007)

$$A_T(\eta, \mathbf{f}) = \int T\left(\mathbf{x} - \frac{\eta}{2}\right) T^*\left(\mathbf{x} + \frac{\eta}{2}\right) \exp(-i2\pi \mathbf{x} \cdot \mathbf{f}) d\mathbf{x} \quad (2.64)$$

with  $\eta = \lambda D \mathbf{f}$ . This expression is useful from a theoretical point of view, as it lends itself to the formulation of linearized models, which we will make use of in Chapter 3 and 4.

### 2.3.1.4 Effect of spherical incident wave front

We consider here the case of a spherical incident wave, that is a wave that within the paraxial approximation has a parabolic phase dependency

$$u_{inc}(\mathbf{x}) = \sqrt{I_{inc}(\mathbf{x})} \exp\left\{i\pi \frac{x^2}{\lambda l}\right\}, \quad (2.65)$$

where  $l$  is the source to sample distance. We generalize to a non-homogeneous amplitude  $\sqrt{I_{inc}(\mathbf{x})}$ , that can describe e.g. a Gaussian beam or synchrotron undulator radiation. This will affect the diffraction pattern by modification of the effective propagation distance and magnification, compared to the plane wave case. Inserting this parabolic wave into the Fresnel integral (Eq. 2.52) and using Eq. 2.41 yields

$$u_D(\mathbf{x}) = \frac{1}{i\lambda D} \iint \sqrt{I_{inc}(\mathbf{x}')} \exp\left(i\frac{\pi}{\lambda l} |\mathbf{x}|^2\right) T(\mathbf{x}') \exp\left(i\frac{\pi}{\lambda D} |\mathbf{x} - \mathbf{x}'|^2\right) d\mathbf{x}'. \quad (2.66)$$

Rearranging the complex exponentials gives

$$\begin{aligned}
 u_D(\mathbf{x}) &= \frac{1}{i\lambda D} \exp\left(i\frac{\pi}{\lambda D}|\mathbf{x}|^2\right) \\
 &\times \iint \sqrt{I_{inc}(\mathbf{x}')T(\mathbf{x}')} \exp\left[i\frac{\pi}{\lambda}\left(\frac{1}{l} + \frac{1}{D}\right)|\mathbf{x}'|^2\right] \\
 &\times \exp\left(-i\frac{\pi}{\lambda D}2\mathbf{x}\mathbf{x}'\right) d\mathbf{x}'.
 \end{aligned} \tag{2.67}$$

Based in this, it is convenient to introduce the defocusing distance  $d$  as

$$\frac{1}{d} = \frac{1}{l} + \frac{1}{D}, \tag{2.68}$$

and the magnification  $M$

$$M = \frac{l+D}{l}. \tag{2.69}$$

Eq. 2.67 then becomes

$$u_D(\mathbf{x}) = \frac{1}{M} \exp\left[i\frac{\pi}{\lambda(l+D)}|\mathbf{x}|^2\right] \frac{1}{i\lambda d} \iint \sqrt{I_{inc}(\mathbf{x}')T(\mathbf{x}')} \exp\left[i\frac{\pi}{\lambda d}\left(\frac{\mathbf{x}}{M} - \mathbf{x}'\right)^2\right] d\mathbf{x}'. \tag{2.70}$$

From this, we see that the intensity with spherical wave illumination is a magnified version of the corresponding intensity with plane wave illumination over a propagation distance equal to  $d$ . The non-uniform incident intensity causes the transmission function to be windowed by  $\sqrt{I_{inc}(\mathbf{x})}$ . If the source to sample distance  $l$  is large compared to the sample to detector distance  $D$ , the defocusing distance becomes  $d \approx D$  and the magnification approaches  $M \approx 1$ .

### 2.3.1.5 Effect of partial coherence

In the above description, a perfectly coherent wave is assumed. Any real beam is more likely to show a certain degree of partial coherence. The beam can be decomposed into a superposition of waves that are individually completely coherent, but mutually incoherent. The resulting intensity is an incoherent sum of the contributions from the individual waves  $u_D^{(p)}$ . To quantify the degree of coherence, we introduce first the *mutual intensity* (Born and Wolf, 1997)

$$J_D(\mathbf{x}_1, \mathbf{x}_2) = \sum_p u_D^{(p)}(\mathbf{x}_1) u_D^{(p)*}(\mathbf{x}_2), \quad (2.71)$$

which is the superposition of the waves at point  $\mathbf{x}_1$  and  $\mathbf{x}_2$  in a plane a distance  $l + D$  from the source. When the points coincide, we get the usual intensity

$$J_D(\mathbf{x}, \mathbf{x}) = I_D(\mathbf{x}). \quad (2.72)$$

The degree of coherence is defined as the mutual intensity normalized with the intensity in each point, that is

$$\gamma^c(\mathbf{x}_1, \mathbf{x}_2) = \frac{J(\mathbf{x}_1, \mathbf{x}_2)}{\sqrt{I(\mathbf{x}_1)I(\mathbf{x}_2)}}. \quad (2.73)$$

It describes the coherence that remains between two points separated spatially, and is by definition equal to 1 when the points coincide.

The mutual intensity immediately downstream of the sample is

$$J_0(\mathbf{x}_1, \mathbf{x}_2) = J_{inc}(\mathbf{x}_1, \mathbf{x}_2) T(\mathbf{x}_1) T(\mathbf{x}_2)^*. \quad (2.74)$$

This can, in analogy with Eq. 2.63, be expressed as a double integral (Guigay, 1978)

$$\tilde{I}_D(\mathbf{f}) = \iint J_0\left(\mathbf{x} - \frac{\lambda D \mathbf{f}}{2}, \mathbf{x} + \frac{\lambda D \mathbf{f}}{2}\right) \exp(-i2\pi \mathbf{x} \mathbf{f}) d\mathbf{x}. \quad (2.75)$$

Every factor in the mutual intensity that depends only on the difference  $\mathbf{x}_1 - \mathbf{x}_2$  results in a multiplicative factor to the intensity spectrum.

### 2.3.1.6 Effect of detector

We assume here that the detector constitutes a linear and space-invariant system. Offset, non-linearities and pixel response non-uniformity are considered to be already corrected. If this is the case, the detector will give rise to a point spread function  $R(\mathbf{x})$ , which will induce a blur in the recorded intensity. This is described in the usual way by a convolution of the intensity

$$I_D^{rec}(\mathbf{x}) = R(\mathbf{x}) * I_D(\mathbf{x}), \quad (2.76)$$

or equivalently by a multiplication in the Fourier domain

$$\tilde{I}_D^{rec} = \tilde{R}(\mathbf{f})\tilde{I}_D(\mathbf{f}), \quad (2.77)$$

where  $\tilde{R}(\mathbf{f})$  is the detector transfer function, which is the Fourier transform of the point spread function.

### 2.3.1.7 Summary

As can be seen above, all contributions to the recorded intensity can be described as a multiplication either in the spatial or the Fourier domain. To simulate an image, one has to calculate a series of multiplications with interspersed Fourier transforms. The incident wave and object transmission function are multiplied in real space. Propagation corresponds to a multiplication of the wave with the propagator to distance  $D$  in Fourier space. The intensity is the squared modulus of the wave in real space. Partial coherence and detector response are taken into account by multiplying with the degree of coherence and the detector function in Fourier space. All together, this becomes

$$I_D(M\mathbf{x}) = \mathcal{F}^{-1}[\tilde{R}(\mathbf{f}/M)|\tilde{\gamma}^c(\lambda d\mathbf{f})|\mathcal{F}[|\mathcal{F}^{-1}\{\tilde{P}_d\mathcal{F}[Tu_{inc}]\}|^2](\mathbf{f})](M\mathbf{x}). \quad (2.78)$$

The process of simulating the forward problem is summarized in Fig. 2.3. It requires 4 2D Fourier transforms.

### 2.3.2 Fraunhofer diffraction

If the squares in the exponent of the Fresnel integral (Eq. 2.52) are developed, we get

$$\begin{aligned} u_D(\mathbf{x}) &= \frac{\exp(ikD)}{i\lambda D} \exp\left(\frac{i\pi}{\lambda D}|\mathbf{x}|^2\right) \\ &\times \iint_{\Sigma} u_{inc}(\mathbf{x}_0) T(\mathbf{x}_0) \exp\left(\frac{i\pi}{\lambda D}|\mathbf{x}_0|^2\right) \exp\left[-\frac{i2\pi}{\lambda D}(\mathbf{x}_0 \cdot \mathbf{x})\right] d\mathbf{x}_0 \end{aligned} \quad (2.79)$$

The terms before the integrals, a phase term and a scaling factor, are usually disregarded.  $u_{inc}(\mathbf{x}_0)$  disappears if a flat wavefront is assumed. If the *far-field condition*

$$\frac{\pi(|\mathbf{x}_0|^2)_{\max}}{\lambda D} \ll 1 \quad (2.80)$$

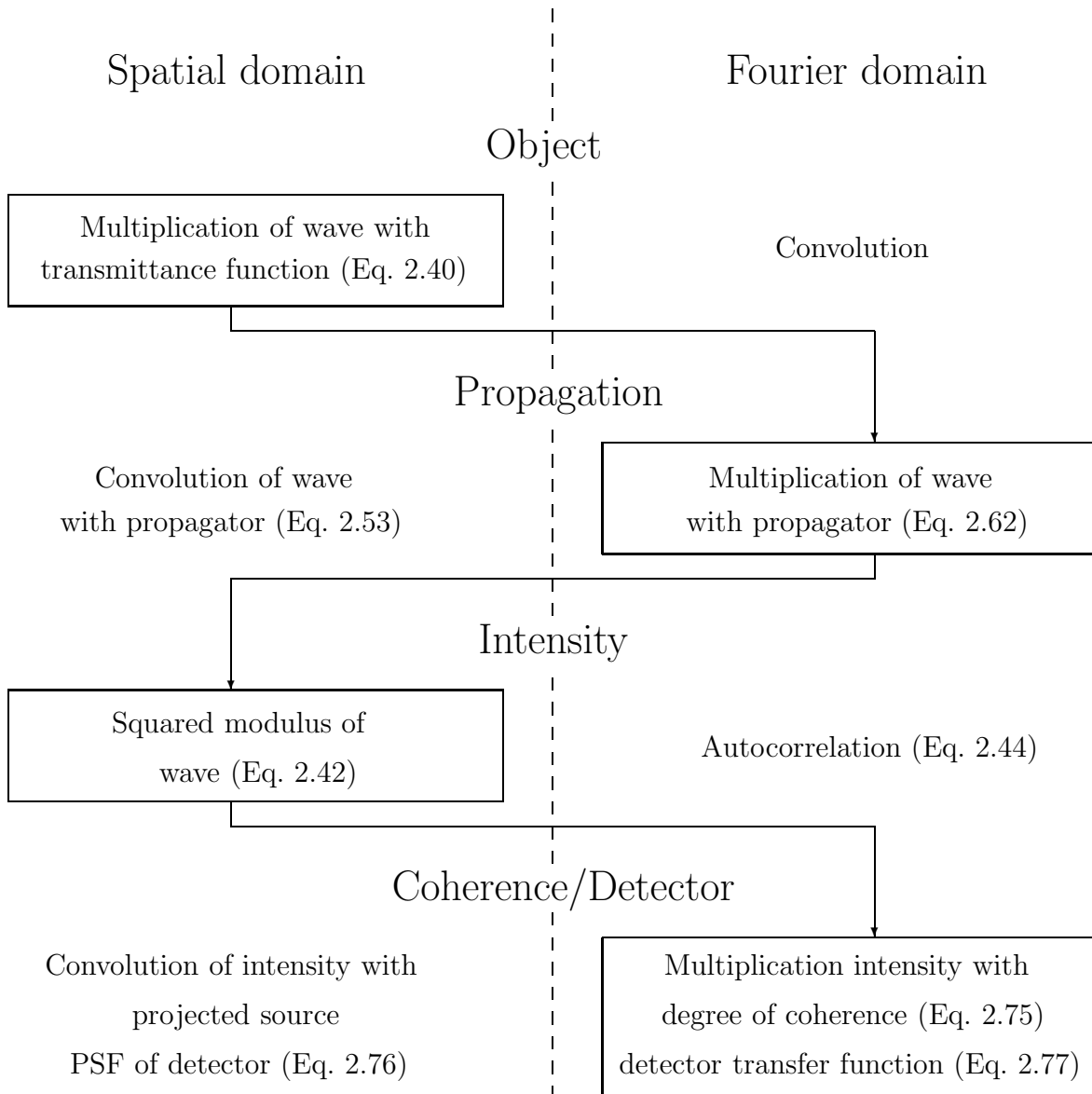


Figure 2.3: Summary of the direct problem, calculating image intensity from a known object.

## Theoretical background

is met, the third term under the integral also vanishes. This leaves

$$u_D(\mathbf{x}) \propto \iint_{\Sigma} T(\mathbf{x}_0) \exp \left[ -\frac{i2\pi}{\lambda D} (\mathbf{x}_0 \cdot \mathbf{x}) \right] d\mathbf{x}_0, \quad (2.81)$$

which is actually a Fourier transform of the transmittance function evaluated at

$$\mathbf{f} = \frac{\mathbf{x}}{\lambda D}, \quad (2.82)$$

so we have

$$u_D(f) \propto \mathcal{F}\{T\} \left( \frac{\mathbf{x}}{\lambda D} \right). \quad (2.83)$$

Finally, recording the intensity of the wave in the diffraction plane gives

$$I_D(\mathbf{x}) = \left| \mathcal{F}\{T\} \left( \frac{\mathbf{x}}{\lambda D} \right) \right|^2 \quad (2.84)$$

i.e. the recorded intensity is the squared modulus of the Fourier transform of the transmittance function.

## 2.4 Tomography

Tomography, or cross-sectional imaging, is now a well-known imaging modality, with applications ranging from the classical medical imaging, for which it was invented (Cormack, 1963; Hounsfield, 1972, 1973), to materials science, paleontology and biology, on scales ranging from macro to nano. It involves the process of recording several radiographs of a sample at different angular positions (Fig. 2.4), which can then be used to reconstruct its inner composition in 3D. It is usually known in the form of Computed Tomography (CT), in which reconstruction of such projection data sets are done by computer processing.

### 2.4.1 Principle of tomography

As seen in Eq. 2.38 and Eq. 2.39, we have projection data both for the absorption and, if it is retrieved, the phase shift. Tomography is described here in 2D, although we always acquire and reconstruct 3D data in this work. This is because we assume a parallel beam geometry (Fig. 2.4), which is well supported by the experimental setup used. This makes generalization to 3D from the 2D formulation trivial, since each slice, that is each row of the detector, can be considered separately as 2D reconstructions.

Choosing the sample as our reference point, the sample cross-sectional coordinate system  $\mathbf{x}_s = (x_s, y_s)$  is fixed relative to the sample. The imaging plane and propagation direction coordinate system  $(x, y, z)$  will appear to rotate relative to the sample, and the relation between the two systems will be dependent on the angle of incidence of the beam relative to  $\mathbf{x}_s$ . (Fig. 2.5). Considering a given row of the absorption (Eq. 2.38) (or, equivalently, the phase), we can now define a projection through the sample along a line in the beam direction  $L_{\theta,x}$  for a fixed angle  $\theta$  and position along  $x$  as

$$B_\theta(x) = (2\pi/\lambda) \int_{L_{\theta,x}} \beta(\mathbf{x}_s) ds. \quad (2.85)$$

It is from this set of projections over the angle  $\theta$  (Fig. 2.4) that we want to reconstruct the 2D absorption index distribution  $\beta(x_s, y_s)$ .

### 2.4.2 Fourier slice theorem

Consider again the  $(x, z)$  coordinate system in Fig. 2.5. Change between the  $(x, z)$  and  $(x_s, y_s)$  systems can be described by a rotation (Kak and Slaney, 1998)

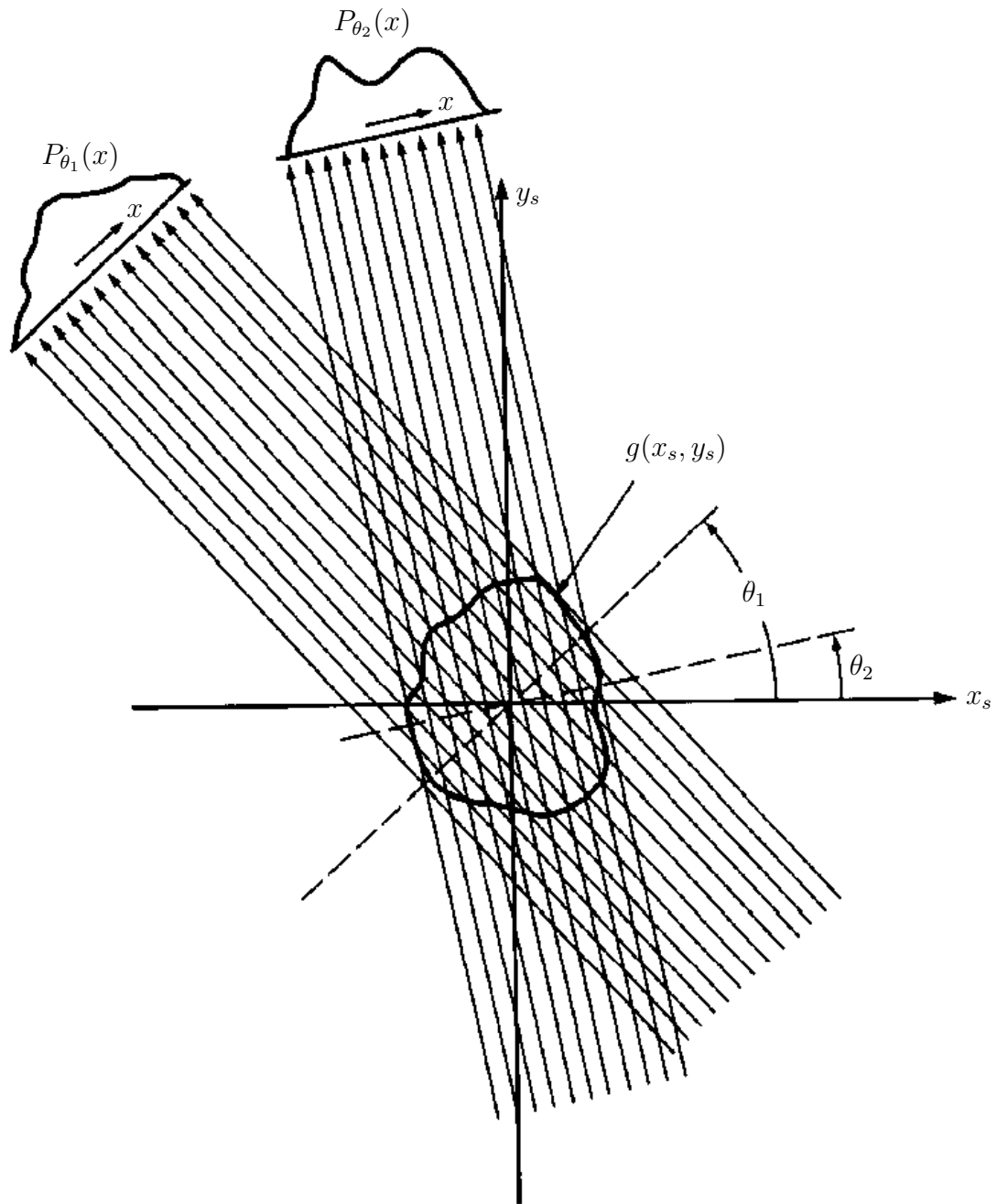


Figure 2.4: The principle of tomography: parallel projections are acquired over a range of angular positions.

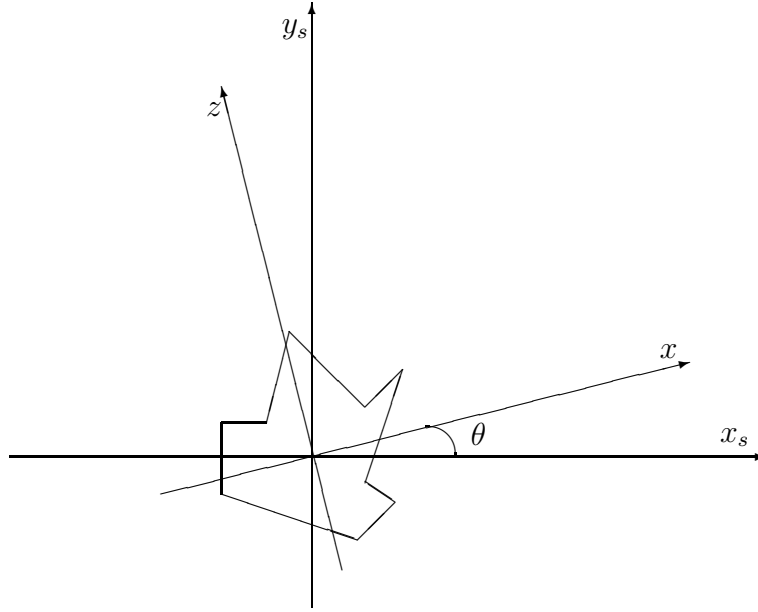


Figure 2.5: Coordinate systems used in tomography.  $(x_s, y_s)$  are fixed to the sample. The beam propagation and image plane coordinate system  $(x, z)$  seems to rotate around the object.

$$\begin{pmatrix} x \\ z \end{pmatrix} = \begin{pmatrix} \cos \theta & \sin \theta \\ -\sin \theta & \cos \theta \end{pmatrix} \begin{pmatrix} x_s \\ y_s \end{pmatrix} \quad (2.86)$$

A projection  $P_\theta(x)$  along lines of constant  $x$  through an arbitrary object function  $g(x_s, y_s)$  is given in the  $(x, z)$  coordinate system as

$$P_\theta(x) = \int_{-\infty}^{\infty} g(x, z) dz. \quad (2.87)$$

Taking the Fourier transform of this projection, we have

$$\tilde{P}_\theta(f_x) = \int P_\theta(x) \exp(-i2\pi f_x x) dx. \quad (2.88)$$

Substitution of Eq. 2.87 into Eq. 2.88 gives

$$\tilde{P}_\theta(f_x) = \iint g(x, z) \exp(-i2\pi f_x x) dx dz. \quad (2.89)$$

## Theoretical background

By using the coordinate transformation in Eq. 2.86, we can transform Eq. 2.89 into the  $(x_s, y_s)$  coordinate system:

$$\tilde{P}_\theta(f_x) = \iint g(\mathbf{x}_s) \exp\{-i2\pi f_x [\mathbf{x}_s \cdot \mathbf{n}(\theta)]\} d\mathbf{x}_s, \quad (2.90)$$

where  $\mathbf{n}(\theta) = (\cos \theta, \sin \theta)$ . This is nothing else than the two-dimensional Fourier transform of the object function at the spatial frequencies ( $u = f_x \cos \theta, v = f_x \sin \theta$ ), which can be written as

$$\tilde{P}_\theta(f_x) = \tilde{g}(f_x \cos \theta, f_x \sin \theta) = \tilde{g}(u, v) \quad (2.91)$$

This is the central result of straight ray tomography: that the Fourier transform of a parallel projection through an object is the 1D Fourier transform along a line through the 2D object Fourier transform (Fig. 2.6). This is usually stated as the *Fourier slice theorem*:

*“The Fourier transform of a parallel projection of an image  $g(x_s, y_s)$  taken at angle  $\theta$  gives a slice of the two-dimensional transform,  $\tilde{g}(u, v)$ , subtending an angle  $\theta$  with the  $u$ -axis. In other words, the Fourier transform of  $P_\theta(x)$  gives the values of  $\tilde{g}(u, v)$  along line BB in Fig. 2.6.”* (Kak and Slaney, 1998, p. 57)

### 2.4.3 Fourier reconstruction

The Fourier slice theorem can be used to devise a conceptually simple tomographic reconstruction algorithm. From a set of projections, we can determine the values of  $\tilde{g}(\mathbf{u})$  on radial lines (Fig. 2.6). If we could take an infinite number of projections, then  $\tilde{g}(\mathbf{u})$  would be known in all points in the frequency domain. The object function could then easily be recovered by the inverse Fourier transform,

$$g(\mathbf{x}_s) = \iint \tilde{g}(\mathbf{u}) \exp(i2\pi \mathbf{u} \cdot \mathbf{x}_s) d\mathbf{u} \quad (2.92)$$

where  $\mathbf{u} = (u, v)$ .

This is a deceptively simple method however. The data obtained by Fourier transforming projections lie on a polar grid, and not an Euclidean one, and to go from one to the other requires advanced interpolation techniques.

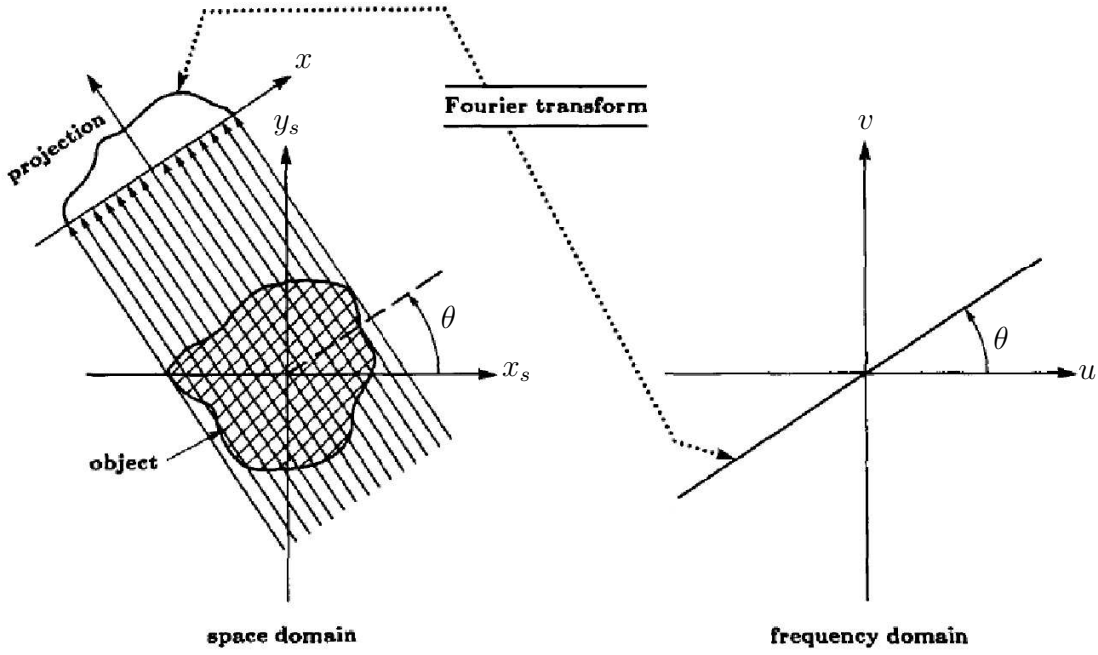


Figure 2.6: Illustration of the Fourier slice theorem. The Fourier transform of a parallel projection through an object at an angle  $\theta$  is equal to the values along a line through the 2D Fourier transform of the object with the same pitch  $\theta$ .

#### 2.4.4 Filtered back-projection

Another reconstruction algorithm can be formulated by considering Eq. 2.92 in a different way. If we change to polar coordinates in Eq. 2.92 and substitute  $u = f_x \cos \theta$  and  $v = f_x \sin \theta$ , we obtain

$$g(\mathbf{x}_s) = \int_0^{2\pi} \int_0^\infty \tilde{g}(f_x, \theta) f_x \exp\{i2\pi f_x [\mathbf{x}_s \cdot \mathbf{n}(\theta)]\} df_x d\theta. \quad (2.93)$$

Since  $\tilde{g}(f_x, \theta + \pi) = \tilde{g}(-f_x, \theta)$ , we can rewrite Eq. 2.93 as

$$g(\mathbf{x}_s) = \int_0^\pi \int \tilde{g}(f_x, \theta) |f_x| \exp\{i2\pi f_x [\mathbf{x}_s \cdot \mathbf{n}(\theta)]\} df_x d\theta. \quad (2.94)$$

Using the Fourier slice theorem (Eq. 2.91), that is substituting  $\tilde{P}_\theta(f_x)$  for  $\tilde{g}(f_x, \theta)$ , we get

$$\begin{aligned} g(\mathbf{x}_s) &= \int_0^\pi \int \tilde{P}_\theta(f_x) |f_x| \exp\{i2\pi[\mathbf{x}_s \cdot \mathbf{n}(\theta)]\} df_x d\theta \\ &= \int_0^\pi \int P_\theta(x) h([\mathbf{x}_s \cdot \mathbf{n}(\theta)] - x) dx d\theta. \end{aligned} \quad (2.95)$$

$h(x)$  is the *reconstruction filter*, and is defined by

$$\begin{aligned} h(x) &= \int_{-f_{x,max}}^{f_{x,max}} |f_x| \exp(i2\pi f_x x) df_x \\ &= \frac{1}{\pi} f_{x,max}^2 \frac{\sin xf_{x,max}}{xf_{x,max}} - \frac{1}{2\pi} f_{x,max}^2 \left( \frac{\sin xf_{x,max}}{xf_{x,max}} \right)^2, \end{aligned} \quad (2.96)$$

where  $2\pi f_{x,max}$  is the bandwidth of the image. Finally, we can observe that Eq. 2.95 can be rewritten as

$$\begin{aligned} g(\mathbf{x}_s) &= \int_0^\pi Q_\theta(\mathbf{x}_s \cdot \mathbf{n}(\theta)) d\theta \\ Q_\theta(x) &= \int P_\theta(x') h(x - x') dx' \end{aligned} \quad (2.97)$$

$Q_\theta(x)$  is the convolution of  $P_\theta(x)$  with  $h(x)$ , the *filtered projection*.  $g(\mathbf{x}_s)$  is the sum of all  $Q_\theta(x)$  over  $\theta$ . For a certain projection angle  $\theta_i$ , each point  $(x_s, y_s)$  in the object function is given the value in  $Q_{\theta_i}(x)$  with  $x = x_s \cos \theta_i + y_s \sin \theta_i$ . It is easy to see that points along lines parallel to the projection direction will be given the same value. Each projection is “smeared” back along the projection direction, or *back-projected*, and the contribution from each projection is added up. This algorithm is known as *filtered back-projection* and can be considered as the standard tomographic reconstruction algorithm (Kak and Slaney, 1998).

The number of projections which have to be acquired is given by the sampling theorem. To achieve sufficient sampling in the Fourier domain, the number of projection angles should be large enough to sample the highest frequency uniformly, that is the same angular rate as radial. If we let  $N$  be the number of picture elements horizontally, along the detector,  $M$  the number of projection angles and  $|f_{max}|$  the maximum radial frequency, the distance  $A$  between two points in the radial direction is

$$A = \frac{4\pi|f_{max}|}{N}. \quad (2.98)$$

The tangential distance between two points is

$$B = 2\pi|f|\Delta\theta = \frac{2\pi^2|f_{max}|}{M}. \quad (2.99)$$

If we require the tangential distance  $B$  to be at least as small as  $A$ , we have

$$\frac{4\pi|f_{max}|}{N} = \frac{2\pi^2|f_{max}|}{M} \Rightarrow M \approx \frac{\pi}{2}N. \quad (2.100)$$

## 2.5 Phase contrast tomography

Phase contrast radiographs can be used directly as input to a tomographic reconstruction algorithm. If we consider weak defocusing conditions (Cloetens et al., 1997)

$$\lambda D|f|^2 \ll 1, \quad (2.101)$$

the intensity (Eq. 2.42) can be approximated by (Cowley, 1995)

$$I_D(\mathbf{x}) = I_0(\mathbf{x}) \left[ 1 - \frac{\lambda D}{2\pi} \nabla^2 \varphi(\mathbf{x}) \right] - \frac{\lambda D}{\pi} \exp[-B(\mathbf{x})] [\nabla \exp[-B(\mathbf{x})] \nabla \varphi(\mathbf{x})]. \quad (2.102)$$

$\nabla$  is the gradient operator in the plane transverse to the beam propagation direction. Since the attenuation usually varies slowly compared the phase term, the last term in Eq 2.102 can be dropped, which leaves

$$I_D(\mathbf{x}) = I_0(\mathbf{x}) \left[ 1 - \frac{\lambda D}{2\pi} \nabla^2 \varphi(\mathbf{x}) \right]. \quad (2.103)$$

The last term is usually much smaller than 1, so we can rewrite Eq. 2.103 as

$$I_D(\mathbf{x}) = I_0(\mathbf{x}) \exp \left[ - \frac{\lambda D}{2\pi} \nabla^2 \varphi(\mathbf{x}) \right] \quad (2.104)$$

If we define a projection as taking the natural logarithm of the intensity in Eq. 2.104, analogously to the pure absorption case, and insert for the absorption and phase shift Eq. 2.38 and Eq. 2.39 respectively, we obtain

$$-\ln[I_D(\mathbf{x})] = (4\pi/\lambda) \int \beta(x, y, z) dz - D \left( \frac{\partial^2}{\partial x^2} + \frac{\partial^2}{\partial y^2} \right) \int \delta_n(x, y, z) dz. \quad (2.105)$$

Since tomographic reconstruction is a linear operation (see section 2.4.4), we can consider the two terms in Eq. 2.105 separately when reconstructing. The first term gives the absorption index, as in Eq. 2.38. The second term is the 2D Laplacian in the image plane of the parallel projection through the real part of the refractive index. Tomographic reconstruction of this term gives the 3D Laplacian of the real part of the refractive index distribution (this is also seen through linearity arguments). The reconstructed 3D distribution is therefore approximately

$$g(x, y, z) = \mu(x, y, z) + D \left( \frac{\partial^2}{\partial x^2} + \frac{\partial^2}{\partial y^2} + \frac{\partial^2}{\partial z^2} \right) \delta_n(x, y, z). \quad (2.106)$$

The second term contributes to  $g(x, y, z)$  in regions of the object where there are strong variations in the refractive index, such as boundaries between different phases. This will act as a form of edge enhancement (Fig. 2.7 (a-c)). In Eq. 2.106, it is seen that an increase in propagation distance should increase the edge enhancement effect.

In most cases, the reconstruction  $g(x, y, z)$  is most easily interpreted if contribution is given only by one term, that is pure absorption contrast or pure phase contrast, for example by making the sample-to-detector distance  $D$  as small as possible to get pure absorption contrast, or to increase the X-ray energy to reduce the absorption contribution and set  $D$  accordingly.

Experimentally, for practical reasons it is hard to completely eliminate phase contrast completely, as it is difficult to get the detector closer to the sample than in the millimeter range. This is especially true when imaging at high spatial resolutions, where even a  $D$  of 1 mm will be relatively large. An example of this effect can be seen in Fig. 2.7 (a), where the light materials are mostly visible due to the slight edge enhancement effect.

Even though the resulting quantity can be difficult to interpret, phase contrast tomography can be a useful imaging technique in its own right. It has been used for several investigations, where it is the enabling technology, when absorption contrast is not sufficient, e.g. imaging of insect inclusions in opaque amber (Lak et al., 2008), foams (Lambert et al., 2005) and mammography (Kotre and Birch, 1999), or where absorption is strong, but internal contrast is not sufficient, such as paleontology (Tafforeau et al., 2006), materials science (Baruchel et al., 2006), and bone research (Weiss et al., 2003; Zabler et al., 2006).

## 2.6 Phase tomography

From Eq. 2.39 and Section 2.4, it is easy to see that if the phase information was available, the refractive index decrement distribution  $\delta_n(x, y, z)$  could be reconstructed by tomographic reconstruction techniques, such as FBP (Section 2.4.4). Phase and amplitude information at the object exit plane will be entangled in intensity measurements downstream of the object, and the process of retrieving the phase information is what we in the context mean by *phase retrieval*. The two problems of phase retrieval and tomographic reconstruction are generally regarded separately, so that it becomes a two-step process (although some suggestions have been made otherwise, see Section 4.3.3 for a discussion).

### 2.6.1 Phase Retrieval

The two different diffraction modes have, due to their different mathematical formulations, given rise to quite different phase retrieval algorithms. In the Fraunhofer, or far-field regime, the diffraction pattern is the squared modulus of the Fourier transform of the transmittance function (Eq. 2.40). This is easy to implement on a computer with the help of the fast Fourier transform (FFT), and has mainly been explored with non-linear iterative methods.

The near-field pattern, however, is the squared modulus of the Fresnel transform with parameter  $D$  of the transmittance function. This is slightly more time-consuming to calculate than the Fourier transform, along with other complications, have made iterative methods seem less appropriate to use for this problem. Instead, most of the body of work in phase retrieval from Fresnel diffraction patterns have been based on linearization of the intensity of the Fresnel integral (Eq. 2.52, 2.63).

#### 2.6.1.1 Phase retrieval from Fraunhofer diffraction patterns

The phase retrieval problem is that of retrieving the phase from intensity measurements of the Fourier transform of the object being imaged. It is the inverse problem to Fraunhofer diffraction. We can formulate phase retrieval from a Fraunhofer diffraction as the minimization problem

$$\arg \min \left| |\tilde{T}(\mathbf{f})|^2 - I_D \right|^2. \quad (2.107)$$

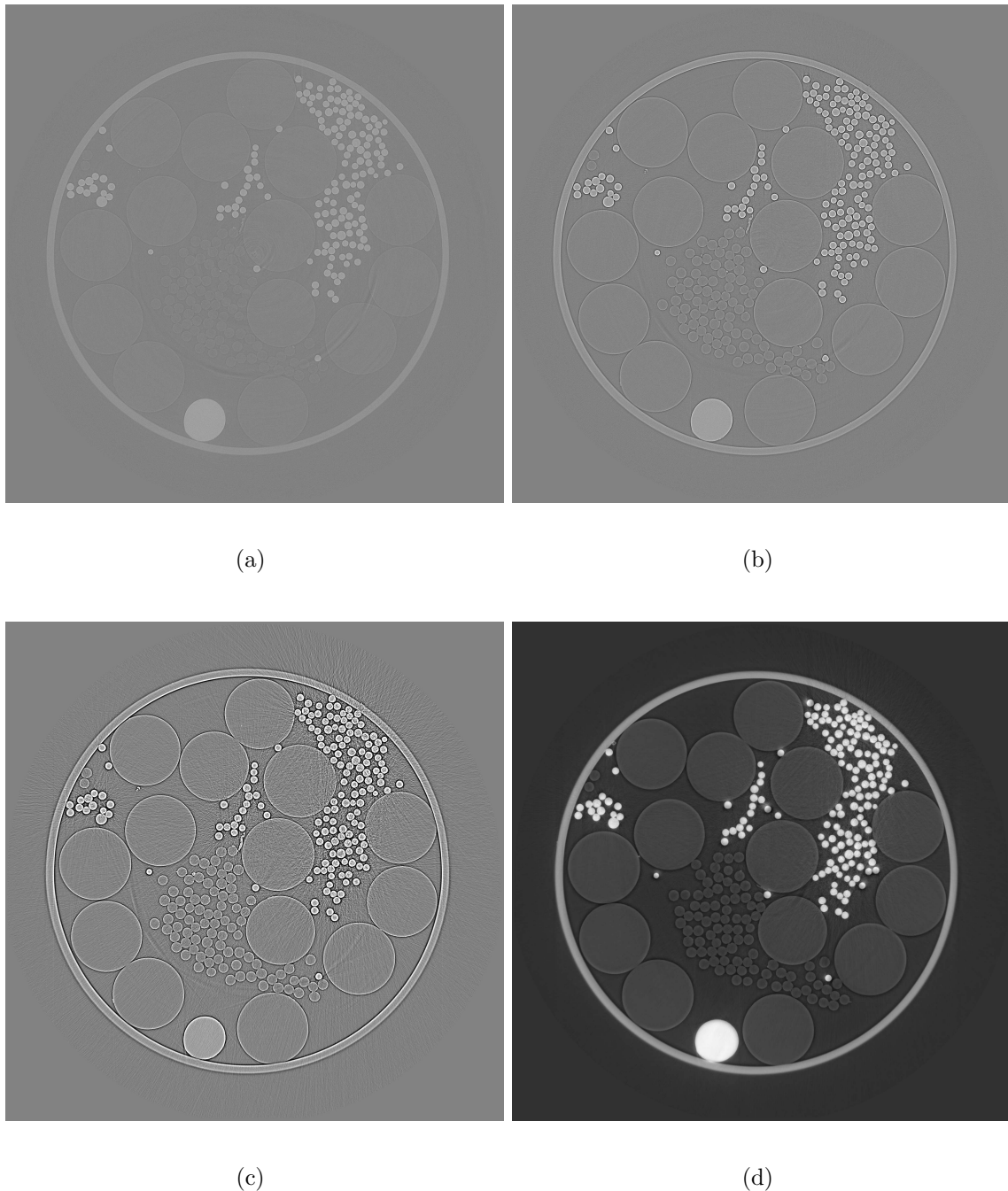


Figure 2.7: Absorption, phase contrast and phase tomography of a phantom constructed from a 1 mm inner diameter Pyrex capillary filled with a single strand of 125  $\mu\text{m}$  Aluminum wire, 20  $\mu\text{m}$  Alumina fibers, 200  $\mu\text{m}$  Polyethylene Terephthalate (PETE) monofilaments and 28  $\mu\text{m}$  Polypropylene (PP) fibers. (a) Absorption ( $D = 2$  mm), (b) phase contrast ( $D = 10$  mm), (c) phase contrast ( $D = 45$  mm), (d) phase (reconstructed with the method described in Section 5.4,  $\delta_n/\beta = 484$ ).

We can see that it is actually more a case of object retrieval. The phase retrieval step in this case is the retrieval of Fourier phase. Once that is known, the complex transmission function would be available as the inverse Fourier transform of the measured Fourier intensity and retrieved Fourier phase.

This is a non-linear inverse problem, which has been under study for some time. Since no linearizations or simplifications of the problem are known, it is usually tackled with iterative methods.

### 2.6.1.2 Phase retrieval from Fresnel diffraction patterns

The relations in Eq. 2.46 and Eq. 2.47 can be used to define the *Fresnel transform* with parameter  $D$  of a function. We can write this in operator form (Paganin, 2006)

$$\mathbf{Fr}_D = \mathcal{F}^{-1} \tilde{P} \mathcal{F}. \quad (2.108)$$

Phase retrieval from one or several Fresnel diffraction patterns can then be defined analogously to the Fraunhofer case as the minimization problem

$$\varphi(\mathbf{x}) = \arg \min_{\varphi} \sum_D ||\mathbf{Fr}_D[T](\mathbf{x})|^2 - I_D(\mathbf{x})|^2, D \in \{D_1, D_2, \dots, D_N\}. \quad (2.109)$$

The reason for including several distances in Eq. 2.109 is that the transfer function to a certain distance in the Fresnel transform (Eq. 2.108) can have zero crossings. This means that information at these frequencies in the Fourier transform of the phase functions will not contribute to the diffraction pattern at that distance. This means that several distances have to be combined to give as good coverage of the Fourier domain as possible. How to incorporate more than one distance is shown in Chapter 3.

The propagator in Eq. 2.108 always goes to zero when  $\mathbf{f} \rightarrow 0$ , so regardless of how many distances are used, information will always be lost around the Fourier domain origin. It is for this reason we introduce different regularization schemes (Chapter 5). This is also the motivation to introduce prior knowledge on the phase in Section 5.4.

# Chapter 3

## Mixed approach

### **Mixed transfer function and transport of intensity approach for phase retrieval in the Fresnel region**

J. P. Guigay, M. Langer, R. Boistel and P. Cloetens

Published in

Optics Letters, Vol. 32, pp. 1617-1619, 2007

We present a method for phase retrieval in propagation based X-ray imaging, based on the contrast transfer and transport of intensity approaches. We show that the contrast transfer model does not coincide with the transport of intensity in the limit of small propagation distances and derive a new model that alleviates this problem. Using this we devise an algorithm to retrieve the phase on slowly varying samples that is valid beyond the limit of small distances. We show its utility by imaging in 3D a biological sample that causes both strong absorption and phase shift.

### 3.1 Introduction

Phase contrast imaging extends the possibilities of absorption imaging. In the hard X-ray energy region the increase in sensitivity can be a factor of  $10^3$  for light elements (Pfeiffer et al., 2006; Momose and Fukuda, 1995). In propagation based imaging techniques, phase contrast is formed by letting the wave-field propagate in free space after interaction with the object, creating a very simple experimental setup (Snigirev et al., 1995) (Fig. 3.1). There is a quantitative correspondence between the object and the recorded images, which can be used to retrieve the phase shift induced by the object. This information can then be used as input to a tomographic reconstruction algorithm to create a 3D reconstruction of the refractive index. Two approaches commonly used in the Fresnel diffraction regime are the Transport of Intensity Equation (TIE) (Teague, 1983; Nugent et al., 1996) which is valid in the limit of small object-to-detector distances, and the Contrast Transfer Function (CTF) (Guigay, 1977; Cloetens et al., 1999; Zabler et al., 2005), which is valid for objects with slowly varying phase and weak absorption. Many interesting samples display both strong amplitude and phase modulation, even in the hard X-ray region. In this letter we show that the CTF does not converge to the TIE solution for small distances in the case of mixed objects. We present an extension to the CTF, similar to the approach considered by Wu and Liu (Wu and Liu, 2003), which is valid for slowly varying objects. We show that it converges to the TIE in the limit of small distances. We then apply the model to a biological imaging problem of tomographically visualizing soft tissues in the case of strong absorption, demonstrating the method's utility.

### 3.2 Wave-object interaction

We consider an object, described by the 3D complex refractive index distribution

$$n(x, y, z) = 1 - \delta_r(x, y, z) + i\beta(x, y, z) \quad (3.1)$$

where  $\beta$  is the absorption coefficient and  $\delta_r$  is the refractive index decrement. When the object is illuminated by a plane monochromatic X-ray beam of wavelength  $\lambda$ , the wave-object interaction can be described as a transmittance function

$$T(\mathbf{x}) = a(\mathbf{x}) \exp[i\varphi(\mathbf{x})] = \exp[-B(\mathbf{x}) + i\varphi(\mathbf{x})] \quad (3.2)$$

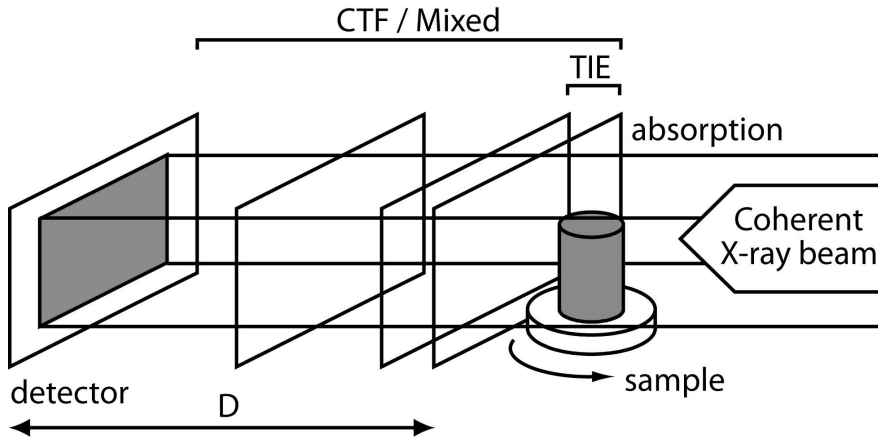


Figure 3.1: Schematic of the experimental setup. Phase contrast is formed by moving the detector away a distance  $D$  from the sample. Tomographic scans are then recorded at several distances, typically 2 using the transport of intensity equation (TIE) and 4 using the contrast transfer function (CTF). Absorption contrast images are recorded by moving the detector to  $D = 0$ .

where  $\mathbf{x}$  are the spatial coordinates in the transverse plane to the propagation direction. The absorption  $a(\mathbf{x})$  and phase shift  $\varphi(\mathbf{x})$  induced by the object are projections through the complex refractive index (Eq. 3.1), with  $B(\mathbf{x}) = (2\pi/\lambda) \int \beta(x, y, z) dz$  and  $\varphi(\mathbf{x}) = (2\pi/\lambda) \int [1 - \delta_r(x, y, z)] dz$  respectively. When images are recorded at a distance  $D$  from the object, the intensity formed on the detector is a diffraction pattern. In the near-field regime the Fourier transform of this intensity can be written as (Guigay, 1977)

$$\tilde{I}_D(\mathbf{f}) = \int T\left(\mathbf{x} - \frac{\lambda D \mathbf{f}}{2}\right) T^*\left(\mathbf{x} + \frac{\lambda D \mathbf{f}}{2}\right) \exp(-i2\pi \mathbf{x} \cdot \mathbf{f}) d\mathbf{x} \quad (3.3)$$

where  $I_D(\mathbf{x})$  is the intensity distribution at distance  $D$  from the object in the propagation direction  $\mathbf{z}$  and  $\mathbf{f}$  are the coordinates in the Fourier domain corresponding to  $\mathbf{x}$ .

### 3.3 Linear contrast models

#### 3.3.1 Transport of intensity equation

The TIE can be derived from Eq. 3.3 by Taylor expanding the transmittance function to the first order with respect to  $D$  (Turner et al., 2004)

$$T(\mathbf{x} + \lambda D\mathbf{f}/2) = T(\mathbf{x}) + \frac{1}{2}\lambda D\mathbf{f} \cdot \nabla T(\mathbf{x}). \quad (3.4)$$

Substituting Eq. 3.4 into Eq. 3.3 and keeping only the terms linear with respect to  $D$  yields

$$I_D = I_0 - \frac{\lambda D}{2\pi} \nabla \cdot [I_0(\mathbf{x}) \nabla \varphi(\mathbf{x})]. \quad (3.5)$$

Due to the Taylor expansion, this expression is only valid in the limit of small distances and is therefore equivalent to the transport of intensity equation:

$$\nabla \cdot [I_0(\mathbf{x}) \nabla \varphi(\mathbf{x})] = -\frac{2\pi}{\lambda} \frac{\partial}{\partial z} I_0(\mathbf{x}) \quad (3.6)$$

### 3.3.2 Contrast transfer function

The CTF is derived by linearizing the transmittance function Eq. 3.2 with respect to the amplitude and phase modulation

$$T(\mathbf{x}) \approx 1 - B(\mathbf{x}) - \varphi(\mathbf{x}) \quad (3.7)$$

Substituting Eq. 3.7 into Eq. 3.3 and retaining first order terms yields

$$\tilde{I}_D(\mathbf{f}) = \delta(\mathbf{f}) - 2 \cos(\pi \lambda D |\mathbf{f}|^2) \tilde{B}(\mathbf{f}) + 2 \sin(\pi \lambda D |\mathbf{f}|^2) \tilde{\varphi}(\mathbf{f}) \quad (3.8)$$

which is valid for weak absorption and slowly varying phase

$$B(\mathbf{x}) \ll 1, \quad |\varphi(\mathbf{x}) - \varphi(\mathbf{x} + \lambda D\mathbf{f})| \ll 1 \quad (3.9)$$

Evaluating Eq. 3.8 for  $D \rightarrow 0$  gives

$$\tilde{I}_{D \rightarrow 0}(\mathbf{f}) = \delta(\mathbf{f}) - 2 \tilde{B}(\mathbf{f}) + 2\pi \lambda D |\mathbf{f}|^2 \tilde{\varphi}(\mathbf{f}) \quad (3.10)$$

which in the spatial domain becomes

$$I_{D \rightarrow 0}(\mathbf{x}) = I_0(\mathbf{x}) - \frac{\lambda D}{2\pi} \nabla^2 \varphi(\mathbf{x}) \quad (3.11)$$

which clearly differs from Eq. 3.6. Fig. 3.2 shows the phase and amplitude contrast factors of the two models at a given propagation distance  $D$ . Note the zero crossings in the CTF contrast factors. These give rise to the need of recording images at several distances to cover the whole Fourier domain.

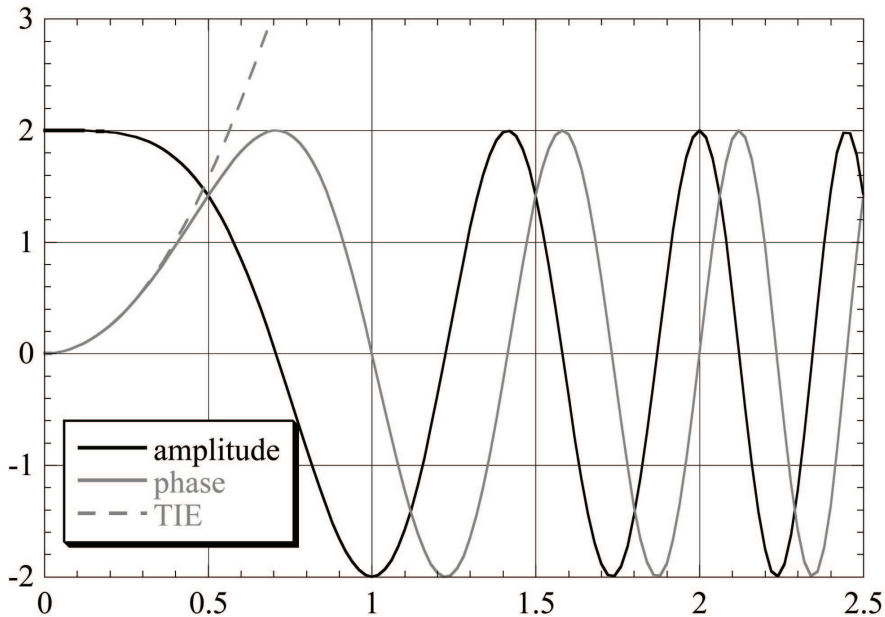


Figure 3.2: Amplitude and phase contrast factors for the contrast transfer function and transport of intensity equation.

### 3.3.3 Discussion

The TIE has a unique solution in most cases, eg. if the intensity distribution is strictly positive.(Paganin, 2006) Experimentally, however, it is difficult to get good enough measurements of the intensity distribution in two planes sufficiently close to fulfill the small distance requirement. The CTF on the other hand does not require images in two closely separated planes. Instead, radiographs are taken at several distances. This is effective in the weak absorption case, but the case of both strong phase and amplitude modulation is still a problem.

## 3.4 Mixed approach

We want a formulation that is valid under strong absorption and approaches the TIE in the limit of small distances. Making only the assumption of slowly varying phase and imposing no restriction on the absorption at this point, the phase can be linearized as before. The basic equation (3.3) then becomes

$$\begin{aligned}\tilde{I}_d(\mathbf{f}) &= \int \exp(-i2\pi\mathbf{x} \cdot \mathbf{f}) a\left(\mathbf{x} - \frac{\lambda D \mathbf{f}}{2}\right) a\left(\mathbf{x} + \frac{\lambda D \mathbf{f}}{2}\right) \\ &\quad \times \left[ 1 + i\varphi\left(\mathbf{x} - \frac{\lambda D \mathbf{f}}{2}\right) - i\varphi\left(\mathbf{x} + \frac{\lambda D \mathbf{f}}{2}\right) \right] d\mathbf{x}\end{aligned}\quad (3.12)$$

Developing the multiplication, we can rewrite Eq. 3.12 as a sum of integrals. Making the variable changes  $= \mathbf{x} - \lambda D \mathbf{f}/2$  and  $= \mathbf{x} + \lambda D \mathbf{f}/2$  respectively and rearranging we obtain

$$\begin{aligned}\tilde{I}_d(\mathbf{f}) &= \tilde{I}_D^{\varphi=0}(\mathbf{f}) + \sin(\pi\lambda D|\mathbf{f}|^2) \int a(\mathbf{x})\varphi(\mathbf{x}) \exp(-i2\pi\mathbf{x} \cdot \mathbf{f}) \\ &\quad \times [a(\mathbf{x} + \lambda D \mathbf{f}) + a(\mathbf{x} - \lambda D \mathbf{f})] d\mathbf{x} \\ &\quad + i \cos(\pi\lambda D|\mathbf{f}|^2) \int a(\mathbf{x})\varphi(\mathbf{x}) \exp(-i2\pi\mathbf{x} \cdot \mathbf{f}) \\ &\quad \times [a(\mathbf{x} + \lambda D \mathbf{f}) - a(\mathbf{x} - \lambda D \mathbf{f})] d\mathbf{x}\end{aligned}\quad (3.13)$$

If we assume a slowly varying object, we can make approximations  $a(\mathbf{x} + \lambda D \mathbf{f}) + a(\mathbf{x} - \lambda D \mathbf{f}) \approx 2a(\mathbf{x})$  and  $a(\mathbf{x} + \lambda D \mathbf{f}) - a(\mathbf{x} - \lambda D \mathbf{f}) \approx 2\lambda D \mathbf{f} \cdot \nabla a(\mathbf{x})$ , which gives

$$\begin{aligned}\tilde{I}_D(\mathbf{f}) &= \tilde{I}_D^{\varphi=0}(\mathbf{f}) + 2 \sin(\pi\lambda D|\mathbf{f}|^2) \\ &\quad \times \int \exp(-i2\pi\mathbf{x} \cdot \mathbf{f}) \varphi(\mathbf{x}) a^2(\mathbf{x}) d\mathbf{x} \\ &\quad + i 2 \cos(\pi\lambda D|\mathbf{f}|^2) \lambda D \mathbf{f} \\ &\quad \cdot \int \exp(-i2\pi\mathbf{x} \cdot \mathbf{f}) \varphi(\mathbf{x}) a(\mathbf{x}) \nabla a(\mathbf{x}) d\mathbf{x}\end{aligned}\quad (3.14)$$

which is

$$\begin{aligned}\tilde{I}_D(\mathbf{f}) &= \tilde{I}_D^{\varphi=0}(\mathbf{f}) + 2 \sin(\pi\lambda D|\mathbf{f}|^2) \mathcal{F}\{I_0\varphi\}(\mathbf{f}) \\ &\quad + \cos(\pi\lambda D|\mathbf{f}|^2) \frac{\lambda D}{2\pi} \mathcal{F}\{\nabla \cdot (\varphi \nabla I_0)\}(\mathbf{f})\end{aligned}\quad (3.15)$$

This is clearly a generalization of the CTF formula Eq. 3.8.  $\tilde{I}_D^{\varphi=0}(\mathbf{f})$  is the Fourier transform of the intensity at distance  $D$  if the phase was zero. This can be either calculated exactly from  $a(\mathbf{x}) = \sqrt{I_0(\mathbf{x})}$  or approximated by  $\tilde{I}_0(\mathbf{f})$ .

We can rewrite the last term in Eq. 3.15 by using the chain rule:

$$\begin{aligned}\tilde{I}_D(\mathbf{f}) &= \tilde{I}_D^{\varphi=0} + 2[\sin(\pi\lambda D|\mathbf{f}|^2) - \pi\lambda D|\mathbf{f}|^2 \cos(\pi\lambda D|\mathbf{f}|^2)] \\ &\quad \times \mathcal{F}\{I_0\varphi\}(\mathbf{f}) - \cos(\pi\lambda D|\mathbf{f}|^2) \frac{\lambda D}{2\pi} \mathcal{F}\{\nabla \cdot (I_0 \nabla \varphi)\}(\mathbf{f})\end{aligned}\quad (3.16)$$

This is a generalization of the TIE formula Eq. 3.5 and approaches it when  $D \rightarrow 0$ : the third term approaches the TIE solution, the second term vanishes as  $D^3|\mathbf{f}|^6$ .

## 3.5 Phase retrieval

Eq (3.15) is solved for the phase by considering the third term as a perturbation term. A first estimate of  $\varphi(\mathbf{x})$  is acquired by neglecting this term and the phase estimate is then iteratively improved. The different distances are taken into account by a linear least squares fitting

$$\mathcal{F}\{I_0\varphi^{(n+1)}\}(\mathbf{f}) = \frac{\sum_D A_D(\mathbf{f}) [\tilde{I}_D(\mathbf{f}) - \tilde{I}_D^{\varphi=0}(\mathbf{f}) - \Delta_D(\mathbf{f})]}{\sum_D A_D^2(\mathbf{f})} \quad (3.17)$$

where  $\Delta_D(\mathbf{f}) = \cos(\pi\lambda D|\mathbf{f}|^2) \frac{\lambda D}{2\pi} \mathcal{F}\{\nabla \cdot (\varphi^{(n)} \nabla I_0)\}(\mathbf{f})$ ,  $A_D(\mathbf{f}) = 2 \sin(\pi\lambda D|\mathbf{f}|^2)$  and  $\varphi^{(n)}(\mathbf{x})$  is the phase at iteration  $n$  with  $\varphi^{(0)} = 0$ . This procedure converges in 3-5 iterations in practical cases.

## 3.6 Experiment

To demonstrate the applicability of Eq. 3.15 the proposed method was used to image a specimen of the frog species *Crossodactylodes bookermanni*. Radiographs were obtained using partially coherent synchrotron radiation X-rays at 17 keV, taken at four different sample to detector distances (18, 83, 283 and 973 mm respectively). In this example 5 iterations of Eq. 3.17 were used. An example retrieved phase map is shown in Fig. 3.3 (b). This procedure was repeated for 900 angles and the retrieved phase maps were used as input to a filtered backprojection (FBP) tomographic reconstruction algorithm. The result is shown in Fig. 3.3 (d). Note that fine details in the soft tissue are visible in the phase tomogram, despite the presence of the strongly absorbing bone.

### 3.7 Summary

We have shown that the CTF and TIE do not coincide in the limit of small distances for general objects. We have derived a new model that approaches the TIE in the limit of small distances and that is valid in the case of strong absorption. Based on this model we have proposed an algorithm to retrieve the phase and demonstrated it's utility in the case of strong absorption by imaging a biological sample.

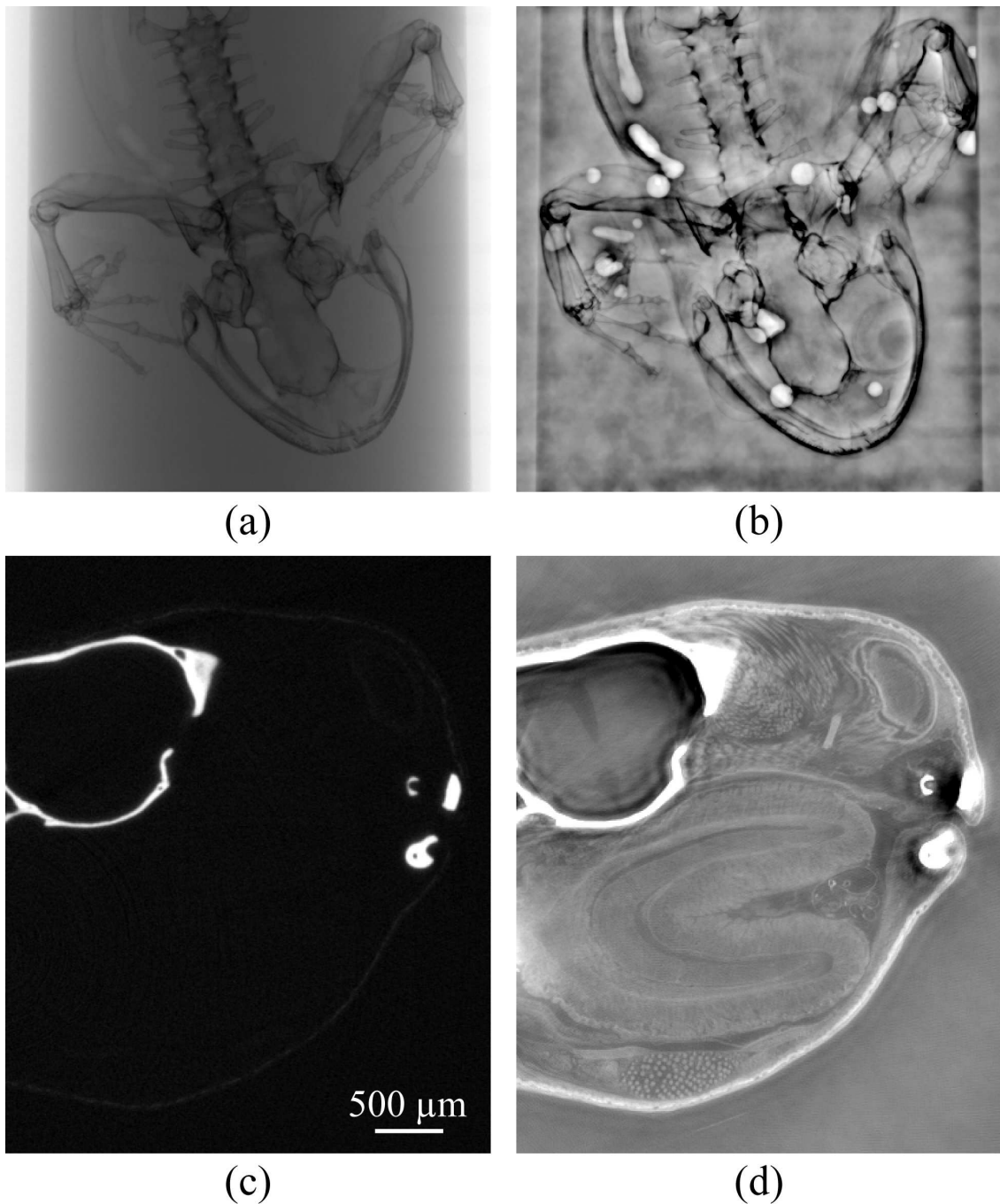


Figure 3.3: (a) Absorption radiograph of a *Crossodactylodes bookermanni* frog embedded in a liquid-filled cylindrical glass sample holder. (b) Phase map retrieved from radiographs at sample-to-detector distances 18, 83, 283 and 973 mm. The bright areas are due to air bubbles in the liquid. (c) Tomographic slice through the frog head using the absorption radiographs and (d) the retrieved phase maps. Fine structures in the soft tissue are visible in (d) despite the presence of strongly absorbing structures (bone).

Mixed approach

# Chapter 4

## Evaluation of linear phase retrieval algorithms

### Quantitative comparison of direct phase retrieval algorithms in in-line phase tomography

M. Langer, P. Cloetens, J. P. Guigay and F. Peyrin

Published in

Medical Physics, Vol. 35, pp. 4556-4566, 2008

A well-known problem in X-ray micro-computed tomography is low sensitivity. Phase contrast imaging offers an increase of sensitivity of up to a factor  $10^3$  in the hard X-ray region, which makes it possible to image soft tissue and small density variations. If a sufficiently coherent X-ray beam, such as that obtained from a 3rd generation synchrotron, is used, phase contrast can be obtained by simply moving the detector downstream of the imaged object. This setup is known as in-line or propagation based phase contrast imaging. A quantitative relationship exists between the phase shift induced by the object and the recorded intensity and inversion of this relationship is called phase retrieval. Since the phase shift is proportional to projections through the 3D refractive index distribution in the object, once the phase is retrieved, the refractive index can be reconstructed by using the phase as input to a tomographic reconstruction algorithm. A comparison between four phase retrieval algorithms is presented.

The algorithms are based on the Transport of Intensity Equation (TIE), Transport of Intensity Equation for Weak absorption (WTIE), the Contrast Transfer Function (CTF) and a Mixed approach between the CTF and TIE, respectively. The compared methods all rely on linearization of the relationship between phase shift and recorded intensity to yield fast phase retrieval algorithms. The phase retrieval algorithms are compared using both simulated and experimental data, acquired at the ESRF 3rd generation synchrotron light source. The algorithms are evaluated in terms of two different reconstruction error metrics. While being slightly less computationally effective, the Mixed approach shows the best performance in terms of the chosen criteria.

## 4.1 Introduction

X-ray micro-tomography ( $\mu$ -CT) is increasingly used in a wide variety of applications, ranging from biological imaging, such as bone (Davis and Wong, 1996; Salomé et al., 1999; Nuzzo et al., 2002; Bayat et al., 2005; Chappard et al., 2006) and small animal imaging (Ford et al., 2003; Badea et al., 2004; Ford et al., 2005), to other fields such as materials science (Baruchel et al., 2000; Maire et al., 2001) and paleontology (Dominguez et al., 2002; Macchiarelli et al., 2006; Tafforeau et al., 2006). A well known problem in  $\mu$ -CT is low sensitivity, which makes it difficult to image soft tissue, especially if dense structures are present. Low sensitivity also makes it difficult to image small variations within dense structures, such as variations in degree of mineralization in bone.

Several techniques to obtain phase contrast exist (Bonse and Hart, 1965; Chapman et al., 1997; David et al., 2002). Here, a particularly simple technique is considered: If the spatial coherence of the X-ray beam is sufficient, phase contrast can be achieved by letting the beam propagate in free space after interaction with the object (Snigirev et al., 1995; Cloetens et al., 1996; Wilkins et al., 1996; Nugent et al., 1996) (Fig. 4.1). This setup is equivalent to in-line holography (Gabor, 1948) and is analogous to the through-focal series method in electron microscopy (Coene et al., 1992).

Phase contrast imaging coupled to tomography can be a useful imaging modality in its own right. The quantity reconstructed in this case is related to the 3D Laplacian of the refractive index distribution (Cloetens et al., 1997). This can usually be seen as a form of edge enhancement, and has been used for qualitative analysis (Cloetens et al., 1997; Monnin et al., 2004; Lewis, 2004; Hwu et al., 2004). A quantitative relationship between the phase shift induced by a sample and the contrast recorded at a sample-to-detector distance  $D$  does exist. Such phase contrast radiographs recorded in the propagation geometry can be used to pose an inverse problem to retrieve the phase shift induced by the object. The phase shift is proportional to a projection through the refractive index distribution in the object, in the same way that absorption in a sample can be considered a projection through the absorption index. Therefore, phase retrieval can be coupled to tomography. The phase shift induced by the object is first retrieved for each projection angle. This is then fed into a tomographic reconstruction algorithm to yield a 3D reconstruction of the refractive index.

The interest in phase contrast imaging is twofold. In the hard X-ray region, phase contrast can give up to a  $10^3$  increase in sensitivity (Momose and Fukuda, 1995). With increasing X-ray energy, absorption will decrease, but phase contrast will still

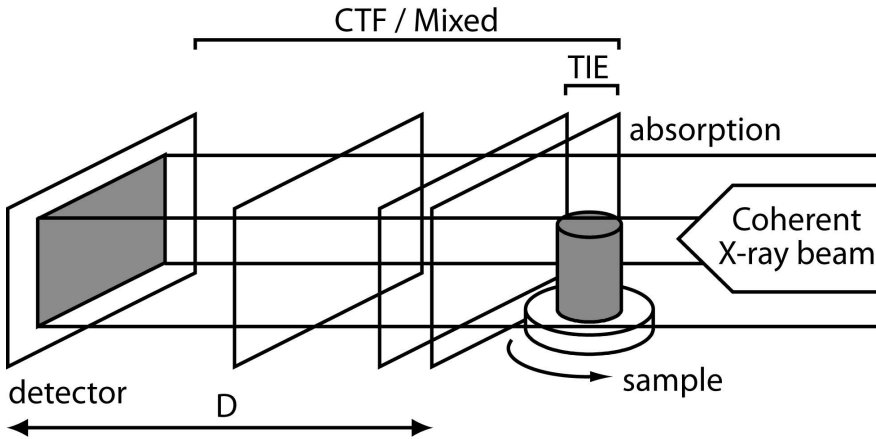


Figure 4.1: Schematic of the imaging system. Phase contrast is formed when the detector is moved a distance  $D$  from the sample. Absorption contrast images are recorded by moving the detector to  $D = 0$ . Tomographic scans are then recorded at several distances, typically 2 using the transport of intensity equation (TIE) and 4 using the contrast transfer function (CTF) and Mixed approach.

be strong, which makes it possible to lower the deposited dose. In several cases however, both dense and soft tissue are present in the imaged object. An example is the imaging of bone biopsies, where both dense structures, such as bone of different levels of mineralization, and soft tissue, such as vessels, are present. Similar conditions can be present in other applications, such as biomaterials engineering and small animal imaging. This means that the X-ray energy has to be chosen so that there will be both strong absorption and phase contrast in the recorded images.

In this work quantitative phase retrieval from in-line phase contrast radiographs recorded at a limited number of propagation distances, in the case of mixed absorption and phase objects, is addressed. Four phase retrieval methods are considered, one based on the transport of intensity equation (TIE) (Teague, 1982, 1983; Gureyev and Nugent, 1996, 1997; Barty et al., 1998; Paganin and Nugent, 1998; Gureyev et al., 1999; Beleggia et al., 2004; Paganin, 2006), one based on the contrast transfer function (CTF)(Guigay, 1977; Cloetens et al., 1999; Zabler et al., 2005), a Mixed approach between the CTF and TIE (Guigay et al., 2007) and a TIE-based approach that aims at combining phase retrieval and the inverse Radon transform (Bronnikov, 2002). We present the methods and show that the latter is equivalent to the TIE method with an additional weak absorption assumption. We also demonstrate that this method also can be considered a two step phase retrieval method. The algorithms are then evaluated in terms of two different reconstruction error metrics using both simulated and experimental data.

## 4.2 Direct problem - image formation

Considering the case of illuminating an object with partially coherent X-rays of wavelength  $\lambda$ , for all practical purposes the object can be described by its 3D complex refractive index distribution. Since the refractive index in the hard X-ray region is generally close to unity, this is usually written as

$$n(x, y, z) = 1 - \delta_r(x, y, z) + i\beta(x, y, z), \quad (4.1)$$

where  $\delta_r$  is the refractive index decrement,  $\beta$  the absorption index and  $(x, y, z)$  are the spatial coordinates.

Due to the weak interaction of X-rays with matter, the propagation path inside the object can be assumed to be straight, that is to say that diffraction within the object is neglected. The wave-object interaction can then be described as a transmittance function (Born and Wolf, 1997)

$$T(\mathbf{x}) = a(\mathbf{x}) \exp[i\varphi(\mathbf{x})] = \exp[-B(\mathbf{x}) + i\varphi(\mathbf{x})], \quad (4.2)$$

where  $\mathbf{x} = (x, y)$  are the spatial coordinates in the plane perpendicular to the propagation direction  $z$ . Both the absorption and phase shift induced by the object can be considered as projections through respectively the absorption and refractive index with

$$B(\mathbf{x}) = (2\pi/\lambda) \int \beta(x, y, z) dz \quad (4.3)$$

and

$$\varphi(\mathbf{x}) = -(2\pi/\lambda) \int \delta_r(x, y, z) dz. \quad (4.4)$$

When moving the detector a relatively short distance downstream from the sample, the intensity formed is called a Fresnel diffraction pattern. In terms of the exit wave, free space propagation can be considered a linear space invariant system. The recorded intensity, however, is the squared modulus of the exit wave (Goodman, 2005)

$$I_D(\mathbf{x}) = |T(\mathbf{x}) * P_D(\mathbf{x})|^2, \quad (4.5)$$

where  $*$  denotes convolution.  $P_D(\mathbf{x})$  is the Fresnel propagator

$$P_D(\mathbf{x}) = \frac{1}{i\lambda D} \exp\left(i\frac{\pi}{\lambda D}|\mathbf{x}|^2\right), \quad (4.6)$$

$D$  being the propagation distance along  $z$ .

Propagation of a wave in free space can also be calculated in the Fourier domain. Defining the Fourier transform of a function  $g(\mathbf{x})$  as

$$\tilde{g}(\mathbf{f}) = \mathcal{F}\{g\}(\mathbf{f}) = \int g(\mathbf{x}) \exp(-i2\pi\mathbf{x} \cdot \mathbf{f}) d\mathbf{x}, \quad (4.7)$$

where  $\mathbf{f} = (f_x, f_y)$  are the spatial frequency coordinates and  $\mathbf{x} \cdot \mathbf{f}$  denotes scalar product, the Fourier transform of the Fresnel propagator (Eq. 4.6) can be written analytically as

$$\tilde{P}_D(\mathbf{f}) = \exp(-i\pi\lambda D|\mathbf{f}|^2). \quad (4.8)$$

The direct problem is then efficiently addressed by calculating the convolution appearing in Eq. 4.5 in the Fourier domain. The simulation of a phase contrast image for an ideal detector response thus requires two two-dimensional Fourier transforms. Alternatively, the Fourier transform of a Fresnel diffraction pattern can be written as (Guigay, 1977)

$$\tilde{I}_D(\mathbf{f}) = \int T\left(\mathbf{x} - \frac{\lambda D \mathbf{f}}{2}\right) T^*\left(\mathbf{x} + \frac{\lambda D \mathbf{f}}{2}\right) \exp(-i2\pi\mathbf{x} \cdot \mathbf{f}) d\mathbf{x}, \quad (4.9)$$

which will be used as the starting point for the inverse problem in the following.

Since both the absorption and phase shift can be described as projections, the absorption index and the refractive index decrement can be reconstructed using a tomographic reconstruction algorithm, such as Filtered Back-Projection (FBP). An absorption image can be acquired directly by moving the detector to  $D = 0$ . This can be seen from Eq. 4.9, where the right hand side becomes the Fourier transform of the squared modulus of  $a(\mathbf{x})$ . Reconstruction of  $\beta(x, y, z)$  can therefore be done by recording radiographs at different angles over a 180 degree range. Reconstructing  $\delta_r(x, y, z)$ , however, requires an intermediate step of first calculating the phase shift  $\varphi(\mathbf{x})$  for each projection angle, a problem known as phase retrieval.

## 4.3 Inverse problem - phase retrieval

To be practically useful, the phase retrieval step has to be efficient, since typical data sets run into thousands by thousands of pixels and thousands of projection angles. Therefore, this work is limited to phase retrieval methods based on linearization of Eq. 4.9, which yield direct solutions of the inverse problem that can be calculated by a series of Fourier filters.

### 4.3.1 Contrast Transfer Function (CTF)

This method is based on an assumption of weak absorption and slowly varying phase shift. The forward model is linearized by Taylor expanding the transmittance function (Eq. 4.2) to the first order (Zabler et al., 2005; Cloetens et al., 1999, 2002)

$$T(\mathbf{x}) \approx 1 - B(\mathbf{x}) + i\varphi(\mathbf{x}). \quad (4.10)$$

Substituting into Eq. 4.9 and again keeping only first order terms gives

$$\tilde{I}_D(\mathbf{f}) = \delta(\mathbf{f}) - 2 \cos(\pi\lambda D|\mathbf{f}|^2)\tilde{B}(\mathbf{f}) + 2 \sin(\pi\lambda D|\mathbf{f}|^2)\tilde{\varphi}(\mathbf{f}), \quad (4.11)$$

where  $\delta(\mathbf{f})$  is the unit impulse function,  $\tilde{B}(\mathbf{f})$  is the Fourier transform of the absorption and  $\tilde{\varphi}(\mathbf{f})$  is the Fourier transform of the phase. Although this expression is arrived at by assuming weak object interaction, it can be shown to be valid for weak absorption and slowly varying phase (Guigay, 1977)

$$B(\mathbf{x}) \ll 1, \quad |\varphi(\mathbf{x}) - \varphi(\mathbf{x} + \lambda D\mathbf{f})| \ll 1. \quad (4.12)$$

Since the phase contrast factor before  $\tilde{\varphi}(\mathbf{f})$  in Eq. 4.11 has zero crossings, several distances have to be used in order to cover as much of the Fourier domain as possible (Fig. 4.2). Eq. 4.11 is used to pose a linear least squares optimization problem, taking the different distances into account:

$$\min \epsilon = \sum_D |2 \sin(\pi\lambda D|\mathbf{f}|^2)\tilde{\varphi}(\mathbf{f}) - 2 \cos(\pi\lambda D|\mathbf{f}|^2)\tilde{B}(\mathbf{f}) - \tilde{I}_D(\mathbf{f})|^2. \quad (4.13)$$

This can be solved simultaneously for  $\tilde{B}(\mathbf{f})$  and  $\tilde{\varphi}(\mathbf{f})$ . The solution for the phase if  $\mathbf{f} \neq (0, 0)$  is

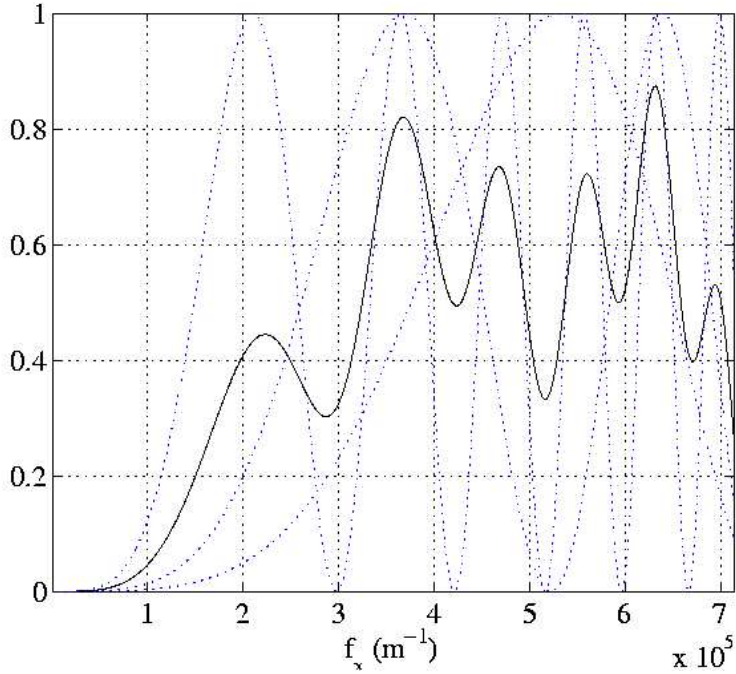


Figure 4.2: Plot of the square of the phase contrast factor (Eqs. 4.11 and 4.27) for three different distances (dashed lines) and the average (solid line). In the CTF and Mixed approach, distances are chosen to avoid zeros in the sum of squared contrast factors. Note that this sum will always go to zero when the frequency variable goes to zero.

$$\tilde{\varphi}(\mathbf{f}) = \frac{1}{2\Delta + \alpha} \left[ C \sum_D \tilde{I}_D \sin(\pi\lambda D \mathbf{f}^2) - A \sum_D \tilde{I}_D \cos(\pi\lambda D \mathbf{f}^2) \right], \quad (4.14)$$

with  $A = \sum_D \sin(\pi\lambda D \mathbf{f}^2) \cos(\pi\lambda D \mathbf{f}^2)$ ,  $B = \sum_D \sin^2(\pi\lambda D \mathbf{f}^2)$ ,  $C = \sum_D \cos^2(\pi\lambda D \mathbf{f}^2)$  and  $\Delta = BC - A^2$ .  $\alpha$  is a regularizing term, introduced by Tikhonov regularization (Tikhonov and Arsenin, 1977) of Eq. 4.13. This is chosen to minimize the standard deviation outside the imaged object at one projection angle, and then used for the whole tomographic data set. From Eq. 4.14 it can be seen that solving for the phase requires  $N + 1$  calculations of 2D FFTs, one forward of each image at each distance ( $N$ ) and one inverse to get the phase. Typically, three or four distances are used.

### 4.3.2 Transport of Intensity Equation (TIE)

If Eq. 4.9 is instead linearized with respect to the propagation distance, by Taylor expanding  $T(\mathbf{x} \pm \lambda D\mathbf{f}/2)$  with respect to  $D$  and retaining only first order terms (Nugent et al., 1996; Paganin, 2006; Barty et al., 1998; Turner et al., 2004):

$$T(\mathbf{x} \pm \lambda D\mathbf{f}/2) \approx T(\mathbf{x}) \pm \frac{1}{2} \lambda D\mathbf{f} \cdot \nabla T(\mathbf{x}), \quad (4.15)$$

substituting back into Eq. 4.9 yields

$$I_D(\mathbf{x}) = I_0(\mathbf{x}) - \frac{\lambda D}{2\pi} \nabla \cdot [I_0(\mathbf{x}) \nabla \varphi(\mathbf{x})]. \quad (4.16)$$

By observing that this expression is only valid for short propagation distances (due to the Taylor expansion), the difference  $[I_D(\mathbf{x}) - I_0(\mathbf{x})]/D$  can be used as an approximation of a partial derivative in the propagation direction  $z$

$$\nabla \cdot [I_0(\mathbf{x}) \nabla \varphi(\mathbf{x})] = -\frac{2\pi}{\lambda} \frac{\partial}{\partial z} I_0(\mathbf{x}), \quad (4.17)$$

which is known as the transport of intensity equation (Teague, 1982).

Different approaches have been proposed to solve the TIE equation, solving either the corresponding two-dimensional linear partial differential equation (Teague, 1983; Gureyev and Nugent, 1996, 1997; Gureyev et al., 1999; Allen and Oxley, 2001) or using Fourier methods (Paganin and Nugent, 1998; Paganin, 2006). A comparison of the different methods for solving the TIE equation goes beyond the scope of the present discussion, however. Here the focus will be on the Fourier solution due to Paganin and Nugent (Paganin and Nugent, 1998; Paganin, 2006), which is similar in implementation to the other phase retrieval approaches presented here.

First, the approximation

$$I_0(\mathbf{x}) \nabla \varphi(\mathbf{x}) \approx \nabla \xi(\mathbf{x}), \quad (4.18)$$

is made, defining the scalar potential  $\xi(\mathbf{x})$ . The validity of this approximation is discussed in detail by Paganin and Nugent (1998). Substituting Eq. 4.18 into Eq. 4.17, this can be solved symbolically for  $\xi(\mathbf{x})$ :

$$\xi(\mathbf{x}) = \nabla^{-2} \left[ -\frac{2\pi}{\lambda} \frac{\partial}{\partial z} I_0(\mathbf{x}) \right]. \quad (4.19)$$

By again using Eq. 4.18, dividing both sides with  $I_0(\mathbf{x})$  and applying the divergence operator  $\nabla \cdot$ , making use of the identity  $\nabla \cdot \nabla = \nabla^2$ , a symbolic expression for the phase can be obtained:

$$\varphi(\mathbf{x}) = -\frac{2\pi}{\lambda} \nabla^{-2} \left( \nabla \cdot \left\{ \frac{1}{I_0(\mathbf{x})} \nabla \left[ \nabla^{-2} \frac{\partial}{\partial z} I(\mathbf{x}) \right] \right\} \right). \quad (4.20)$$

Solving Eq. 4.20 requires the calculation of two inverse Laplacians. This can be done directly by implementing the inverse Laplacian as (Paganin, 2006)

$$\nabla_{\alpha}^{-2} = -\frac{1}{4\pi^2} \mathcal{F}^{-1} \frac{1}{(f_x^2 + f_y^2 + \alpha)} \mathcal{F}. \quad (4.21)$$

The singularity at  $f_x = f_y = 0$  and small values of the Laplacian at low frequencies is handled by replacing  $(f_x^2 + f_y^2)^{-1}$  with zero at the Fourier domain origin  $\mathbf{f} = (0, 0)$  and introducing a regularizing term  $\alpha$ , which is selected as above. This method requires images in two planes, the contact plane to get  $I_0(\mathbf{x})$  and a plane a small distance downstream, to get  $I_D(\mathbf{x})$ . Solving for the phase in this manner thus requires calculation of 6 2D FFTs; one forward for the first inverse Laplacian and gradient operator, two inverse to divide by  $I_0(\mathbf{x})$  (one for each component), two forward to apply the divergence and the last inverse Laplacian and finally one inverse to get the phase. In the experimental case however, the images at different distances have to be aligned. This is usually done in Fourier space, which adds another FFT, making the total 7 2D FFTs. This alignment is already included in the CTF and Mixed approach: since all data processing is done in the Fourier domain, shifts can be directly implemented as multiplications with a phase term. No extra FFTs have to be performed.

### 4.3.3 TIE for weak absorption (WTIE)

A similar method to the TIE has been proposed by Bronnikov (2002), but with the objective to combine the phase retrieval step with the inverse Radon transform into a one-step approach. This method can be derived from Eq. 4.16. If  $B(\mathbf{x})$  is assumed to vary insignificantly, that is if it is close to constant,  $I_0(\mathbf{x})$  can be moved outside the gradient operator. This yields

$$I_D(\mathbf{x}) = I_0(\mathbf{x}) \left[ 1 - \frac{\lambda D}{2\pi} \nabla^2 \varphi(\mathbf{x}) \right]. \quad (4.22)$$

This equation can be solved for the phase, for example by calculating the inverse Laplacian as in Eq. 4.21:

$$\varphi(\mathbf{x}) = -\frac{2\pi}{\lambda D} \nabla_{\alpha}^{-2} \left( \frac{I_D(\mathbf{x})}{I_0(\mathbf{x})} - 1 \right). \quad (4.23)$$

This has been shown to be an effective and accurate algorithm for the weak absorption case, providing the regularization parameter has been chosen correctly (Groso, Abela and Stampanoni, 2006).

It is worth noting that this expression can be arrived at directly from Eq. 4.20. By assuming insignificantly varying absorption, the division by  $I_0(\mathbf{x})$  can be moved inside the gradient and inverse Laplacian. The divergence and gradient will then cancel one of the inverse Laplacians, thus yielding Eq. 4.23. In the following we denote this method as TIE for weak absorption (WTIE).

It has been shown that this solution can be combined with the 3D inverse Radon transform to yield a one step approach. This combination has been shown to be the combination of two convolutions, that is a multiplication in the Fourier space of the inverse Laplacian (Eq. 21) and the reconstruction filter  $|f_x|$  of the inverse Radon transform (Bronnikov, 2002). As the other methods presented here also yield solutions in the Fourier domain, this reconstruction filter could also be incorporated in these methods, which yields a filtered phase function rather than the phase function itself. In practice, it seems more convenient to separate the two steps also in this method. That is, first a phase retrieval step, followed by a 2D FBP slice by slice. This is still the fastest method presented here, requiring 2 FFTs, one forward and one back to calculate the inverse Laplacian. Also here the images have to be aligned before phase retrieval, which in this case adds two FFTs - one forward and one inverse, bringing the total to 4 2D FFTs.

#### 4.3.4 Mixed approach

As can be seen above, the CTF and TIE methods have different strengths and weaknesses. The TIE is efficient in calculations and data, requiring images in two planes, but is only valid for short propagation distances where the contrast is weak. The CTF on the other hand is only valid for weak absorption, but allows the use of more data and is not restricted to short distances. It has been seen as desirable to combine these two approaches to extend the validity of the approximations and several methods have

been proposed along these lines (Gureyev et al., 2004; Wu and Liu, 2003; Guigay et al., 2007; Meng et al., 2007).

It has also been shown that the TIE and the CTF models do not approach the same expression when  $D \rightarrow 0$  (Guigay et al., 2007). To alleviate this, the weak absorption assumption in the CTF and the short propagation distance requirement in the TIE, a mixed approach between the two has been proposed, that directly links the CTF and the TIE (Guigay et al., 2007; Wu and Liu, 2003). The first step is to Taylor expand the phase term only in Eq. 4.9., again retaining only the first order terms

$$\begin{aligned} \tilde{I}_D(\mathbf{f}) &= \int \exp(-i2\pi\mathbf{x} \cdot \mathbf{f}) a\left(\mathbf{x} - \frac{\lambda D \mathbf{f}}{2}\right) a\left(\mathbf{x} + \frac{\lambda D \mathbf{f}}{2}\right) \\ &\quad \times \left[ 1 + i\varphi\left(\mathbf{x} - \frac{\lambda D \mathbf{f}}{2}\right) - i\varphi\left(\mathbf{x} + \frac{\lambda D \mathbf{f}}{2}\right) \right] d\mathbf{x}. \end{aligned} \quad (4.24)$$

The multiplication is then expanded and the result rewritten to a sum of integrals. Making variable changes  $\mathbf{y} = \mathbf{x} + \lambda D \mathbf{f}/2$  and  $\mathbf{y} = \mathbf{x} - \lambda D \mathbf{f}/2$  respectively and recombining terms yields

$$\begin{aligned} \tilde{I}_D(\mathbf{f}) &= \tilde{I}_D^{\varphi=0} + \sin(\pi\lambda D|\mathbf{f}|^2) \int a(\mathbf{x})\varphi(\mathbf{x}) \exp(-i2\pi\mathbf{x} \cdot \mathbf{f}) \\ &\quad \times [a(\mathbf{x} + \lambda D \mathbf{f}) + a(\mathbf{x} - \lambda D \mathbf{f})] d\mathbf{x} \\ &\quad + i \cos(\pi\lambda D|\mathbf{f}|^2) \int a(\mathbf{x})\varphi(\mathbf{x}) \exp(-i2\pi\mathbf{x} \cdot \mathbf{f}) \\ &\quad \times [a(\mathbf{x} + \lambda D \mathbf{f}) - a(\mathbf{x} - \lambda D \mathbf{f})] d\mathbf{x}. \end{aligned} \quad (4.25)$$

$\tilde{I}_D^{\varphi=0}(\mathbf{f})$  is the Fourier transform of the intensity at distance  $D$  if the phase was zero and can be approximated by  $\tilde{I}_0(\mathbf{f})$ . Assuming that the absorption is slowly varying, that is  $|B(\mathbf{x} + \lambda D \mathbf{f}) - B(\mathbf{x} - \lambda D \mathbf{f})| \ll 1$ , this can in turn be linearized, with  $a(\mathbf{x} + \lambda D \mathbf{f}) + a(\mathbf{x} - \lambda D \mathbf{f}) \approx 2a(\mathbf{x})$  and  $a(\mathbf{x} + \lambda D \mathbf{f}) - a(\mathbf{x} - \lambda D \mathbf{f}) \approx 2\lambda D \mathbf{f} \cdot \nabla a(\mathbf{x})$ , which gives

$$\begin{aligned}
\tilde{I}_D(\mathbf{f}) &= \tilde{I}_D^{\varphi=0}(\mathbf{f}) + 2 \sin(\pi \lambda D |\mathbf{f}|^2) \\
&\quad \times \int \exp(-i2\pi \mathbf{x} \cdot \mathbf{f}) \varphi(\mathbf{x}) a^2(\mathbf{x}) d\mathbf{x} \\
&\quad + i2 \cos(\pi \lambda D |\mathbf{f}|^2) \lambda D \mathbf{f} \\
&\quad \cdot \int \exp(-i2\pi \mathbf{x} \cdot \mathbf{f}) \varphi(\mathbf{x}) a(\mathbf{x}) \nabla a(\mathbf{x}) d\mathbf{x}.
\end{aligned} \tag{4.26}$$

The integrals are identified as Fourier transforms, which yields

$$\begin{aligned}
\tilde{I}_D(\mathbf{f}) &= \tilde{I}_D^{\varphi=0}(\mathbf{f}) + 2 \sin(\pi \lambda D |\mathbf{f}|^2) \mathcal{F}\{I_0 \varphi\}(\mathbf{f}) \\
&\quad + \cos(\pi \lambda D |\mathbf{f}|^2) \frac{\lambda D}{2\pi} \mathcal{F}\{\nabla \cdot (\varphi \nabla I_0)\}(\mathbf{f}).
\end{aligned} \tag{4.27}$$

It is interesting to note that Eq. 4.26 generalizes both the CTF and the TIE. If  $D \rightarrow 0$ , the TIE (Eq. 4.17) is recovered and if the absorption is assumed to be weak, the CTF (Eq. 4.11) is recovered. The differential equation in Eq. 4.26 can be solved iteratively by considering the last term as a perturbation term. This term vanishes for homogeneous absorption. Different distances are again taken into account by a linear least squares fitting. Considering  $\mathcal{F}\{I_0 \varphi\}(\mathbf{f})$  as the unknown, the minimization problem

$$\min \sum_D |A_D(\mathbf{f}) \mathcal{F}\{I_0 \varphi^{(n+1)}\}(\mathbf{f}) + \tilde{I}_D^{\varphi=0}(\mathbf{f}) + \Delta_D(\mathbf{f}) - \tilde{I}_D(\mathbf{f})|^2 \tag{4.28}$$

is posed, where  $\Delta_D(\mathbf{f}) = \cos(\pi \lambda D |\mathbf{f}|^2) \frac{\lambda D}{2\pi} \mathcal{F}\{\nabla \cdot (\varphi^{(n)} \nabla I_0)\}(\mathbf{f})$ ,  $A_D(\mathbf{f}) = 2 \sin(\pi \lambda D |\mathbf{f}|^2)$  and  $\varphi^{(n)}(\mathbf{x})$  is the phase at iteration  $n$ . The minimization problem in Eq. 4.28 has the solution

$$\mathcal{F}\{I_0 \varphi^{(n+1)}\}(\mathbf{f}) = \frac{\sum_D A_D(\mathbf{f}) [\tilde{I}_D(\mathbf{f}) - \tilde{I}_D^{\varphi=0}(\mathbf{f}) - \Delta_D(\mathbf{f})]}{\sum_D A_D^2(\mathbf{f}) + \alpha}, \tag{4.29}$$

where the perturbation term  $\Delta_D(\mathbf{f})$  is handled by assuming a zero phase shift in the first iteration:  $\varphi^{(0)} = 0$ , and  $\alpha$  is a regularizing parameter, as above. While this solution lacks an optimality proof, according to our experience the iteration converges in all practical cases after 3-5 iterations. To set up the first iteration,  $N$  2D FFTs have to be calculated. The subsequent iterations require 2 2D FFTs each. Typically three or four distances are used, so in practice between 9 to 14 2D FFTs are required to solve Eq. 4.29 for the phase.

## 4.4 Simulations and data acquisition

### 4.4.1 Simulation of phase contrast

The imaging system was simulated in a deterministic fashion. First, two phantoms were defined, one for the absorption coefficient and one for the refractive index decrement. They were based on the 3D Shepp-Logan phantom (Kak and Slaney, 1998), consisting of a series of ellipsoids (Fig. 4.3). Theoretical values of  $\delta_r$  and  $\beta$  of different materials at 24 keV X-ray energy ( $\lambda = 0.5166 \text{ \AA}$ ) were used in the different regions, listed in table 4.2.

Analytical projections were then calculated in a parallel beam geometry, for 600 projection angles with  $2048 \times 2048$  pixels in each projection image. For each projection angle, the two resulting data sets were combined to form a complex representation of the wave exiting the object (Eq. 4.2). Propagation in free space was simulated in the Fourier domain by using Eq. 4.8. The intensity was then calculated by taking the inverse FFT and calculating the squared modulus in the spatial domain. Four distances were used: 0, 0.1, 0.3 and 0.99 m. Due to the relatively low spatial resolution in the experiment, no zero-crossings of the transfer functions occur in the relevant frequency range, except at zero spatial frequency. The radiographs were then down-sampled to  $512 \times 512$  pixels to account for the fact that the wave function is a continuous function. The intensity in the resulting radiographs at  $D = 0$  varied between 1.0 outside the object and down to 0.71 inside the object and the maximum phase shift was  $124\pi$  rad.

Simulations were also performed with an additive uniformly distributed white noise

Table 4.1: Summary of the phase retrieval methods. This corresponds to the conditions used in this work. The numbers in brackets are for the experimental case, where the different distances have to be aligned (this can be done without extra FFTs in the CTF and Mixed approaches). The values given for the CTF and Mixed approach are typical minima.

|       | Validity                              | Images / angle | FFTs   |
|-------|---------------------------------------|----------------|--------|
| WTIE  | Weak absorption, short propagation    | 2              | 2 (+2) |
| TIE   | Short propagation                     | 2              | 6 (+1) |
| CTF   | Weak absorption, slowly varying phase | 3-             | 4-     |
| Mixed | Slowly varying object                 | 3-             | 9-     |

Table 4.2: Theoretical values for the absorption coefficient and refractive index at 24 keV for the materials used in the phantom. These values were also used in the simulated data.

|          | $4\pi\beta/\lambda$<br>( $cm^{-1}$ ) | $2\pi\delta_r/\lambda$<br>( $\times 100 cm^{-1}$ ) |
|----------|--------------------------------------|--|
| Aluminum | 5.130                                | 11.4   |
| Ethanol  | 0.305                                | 4.00   |
| Oil      | 0.262                                | 4.36   |
| PMMA     | 0.425                                | 5.63   |
| Polymer  | 0.306                                | 5.00   |
| Water    | 0.482                                | 4.87   |

with zero mean. Noise with a certain peak to peak level compared to the first image plane was added to all radiographs. This was done for peak to peak signal to noise ratios (PPSNR)<sup>1</sup> in the range [24, 0] dB.

#### 4.4.2 Experimental data

To evaluate the algorithms under experimental conditions, a phantom object was imaged. This phantom was constructed from a PMMA cylinder with a diameter 7.5 mm, in which five channels were drilled. These were then filled with materials of well known composition: demineralized water, 99.6 % ethanol, a lipid, a 0.125 mm filament of 99.99 % pure aluminum and a mix of 0.1 and 0.2 mm monosized polymer particles. A tomographic slice at detector distance  $D$  close to zero (absorption contrast) is shown in Fig. 4.6(a) and theoretical values for the materials at 24 keV X-ray energy, obtained from the DABAX database (Dejus and Sanchez del Rio, 1996; Sanchez del Rio and Dejus, 2004), are shown in table 4.2.

The image acquisition was performed at the ID19 experimental station at the European Synchrotron Radiation Facility (ESRF), Grenoble, France. ID19 is a long (150 m) imaging beamline, which can produce a beam with very high spatial coherence. X-rays at 24 keV energy were used, selected from the radiation from a wiggler by a double silicon crystal monochromator set to reflect in the vertical plane.

---

<sup>1</sup>PPSNR =  $20 \log_{10} \frac{f_{max}}{n_{max}}$ , where  $f_{max}$  is the maximum signal amplitude and  $n_{max}$  the maximum noise amplitude.

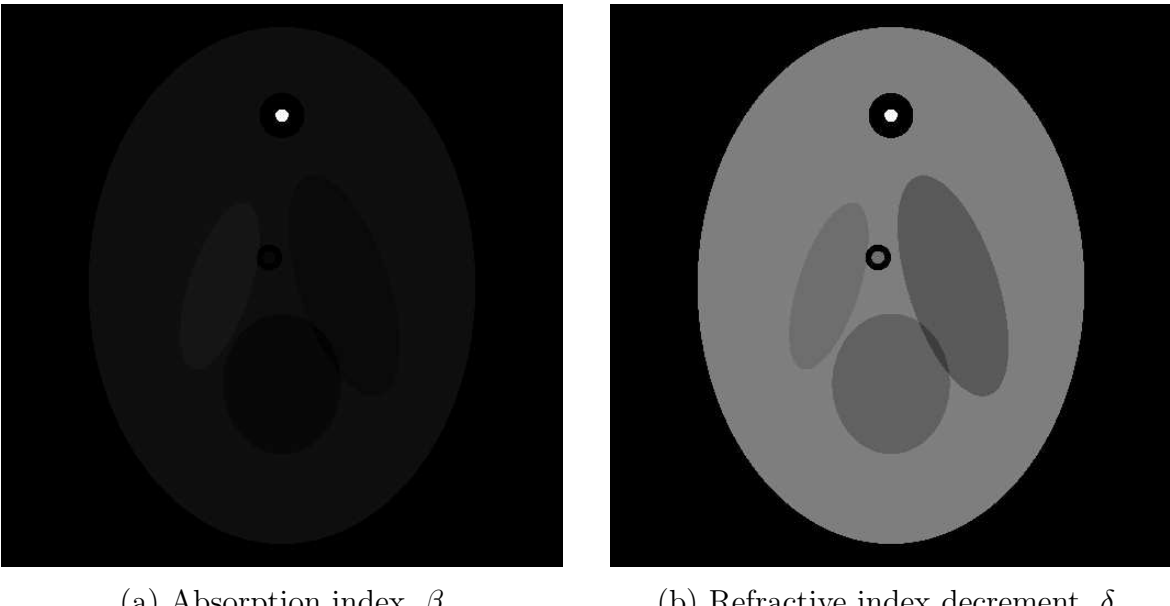


Figure 4.3: Central slice of the phantom used in the simulations. It is based on the 3D Shepp-Logan phantom, modified to the physical values of the materials used in the constructed phantom below. Areas of no material were also added around the parts corresponding to polymer and aluminum to closer emulate the qualitative appearance of the constructed phantom. As can be seen, the contrast is weak in the absorption index, compared to the refractive index decrement.

A FReLoN camera (Labiche et al., 2007) was used for detection, in which visible light, produced by a Gadox scintillator, is imaged onto a cooled charge-coupled device. The effective pixel size was  $7.5 \mu\text{m}$ , giving a field-of-view of  $15.4 \times 15.4 \text{ mm}$ . Four angular scans were recorded, each consisting of 1200 images, at sample-to-detector distances 0.012 m, 0.1 m, 0.3 m and 0.99 m. The intensity in the radiographs recorded at the shortest distance varied between 1.0 and down to 0.67 and the maximum measured phase shift was roughly  $100\pi \text{ rad}$ .

#### 4.4.3 Evaluation criteria

For the simulated data set, the ideal volumes are readily available. The reconstructions can be compared to directly calculated slices of the refractive index phantom. The normalized mean square error

$$NMSE = 100 \times \left( \frac{\sum |f(\mathbf{x}) - g(\mathbf{x})|^2}{\sum |f(\mathbf{x})|^2} \right)^{1/2}, \quad (4.30)$$

expressed as a percentage, is used in this case, where  $f(\mathbf{x})$  is the ideal image and  $g(\mathbf{x})$  is the reconstructed image.

For the experimental data, ideal reconstructions are not available. Theoretical values of the refractive index decrement  $\delta_r$ , however, are known. Comparison in this case is done with the measured average values  $k_i$  in the different regions corresponding to material  $i$ , to the ideal value  $m_i$ . The difference is normalized with the ideal value of the refractive index and the mean error over all materials is used as error measure, also expressed as a percentage:

$$AVGE = 100 \times \frac{1}{M} \sum \frac{|m_i - k_i|}{m_i}. \quad (4.31)$$

The AVGE is also used for the simulated data to allow for comparison with the experimental data and to provide an alternative to Eq. 4.30.

## 4.5 Results

### 4.5.1 Simulated data

Figure 4.4 shows reconstructed tomographic slices of the noise-free data, using the phases retrieved with the respective algorithms. The fourth distance (along with the first for the absorption) was used in the phase retrieval with the TIE since this yielded the best results even for the noiseless data. All four methods yield qualitatively acceptable reconstructions, with some streaking artifacts visible, strongest with the WTIE method. Average reconstructed values of the refractive index decrement in the different regions are shown in Fig. 4.7 (a), where it can be seen that all methods yield values close to the true values, except the CTF which gives too low values due to the weak absorption requirement being violated. By examining the AVGE (Fig. 4.7 (f)), it is seen that the TIE gives the most accurate reconstruction in the noise-free case. In terms of NMSE however, the TIE performs worse than both the WTIE and Mixed approach, due to artifacts close to the material interfaces, hardly visible in Fig. 4.4.

Reconstructed tomographic slices using noisy simulated data is shown in Fig. 4.5. The data set used for these reconstructions had a PPSNR of 12 dB in the first plane.

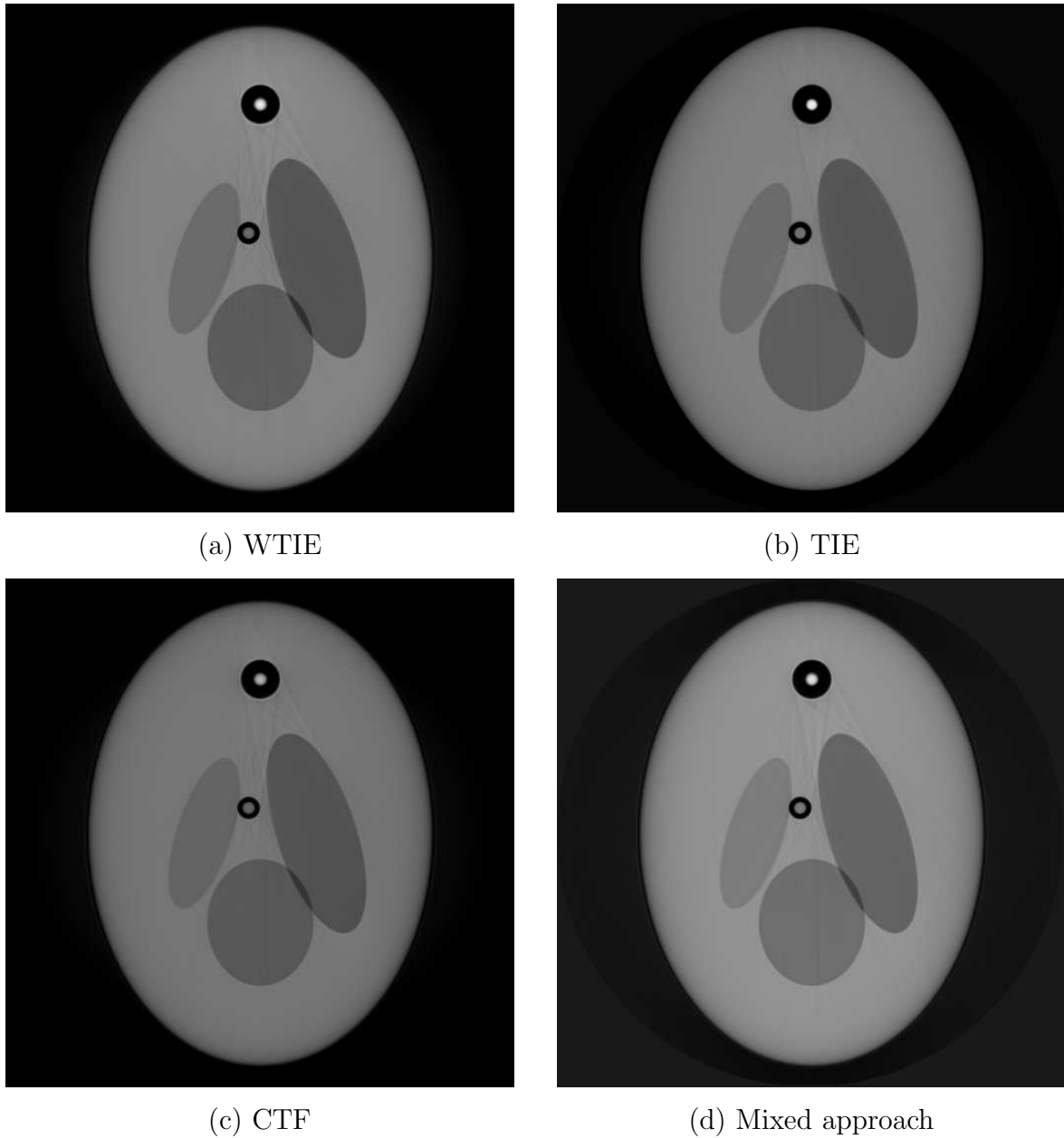


Figure 4.4: Central slices of the reconstructed refractive index using simulated, noise-free data. Reconstruction was done using (a) Transport of Intensity Equation for weakly absorbing objects (WTIE), (b) Transport of Intensity Equation for general objects (TIE), (c) Contrast Transfer Function (CTF) and (d) Mixed approach algorithms. All four reconstructions show some streaking artifacts, most pronounced in the WTIE reconstruction, but qualitative appearance is in all cases good. The field of view is 15.4 mm.

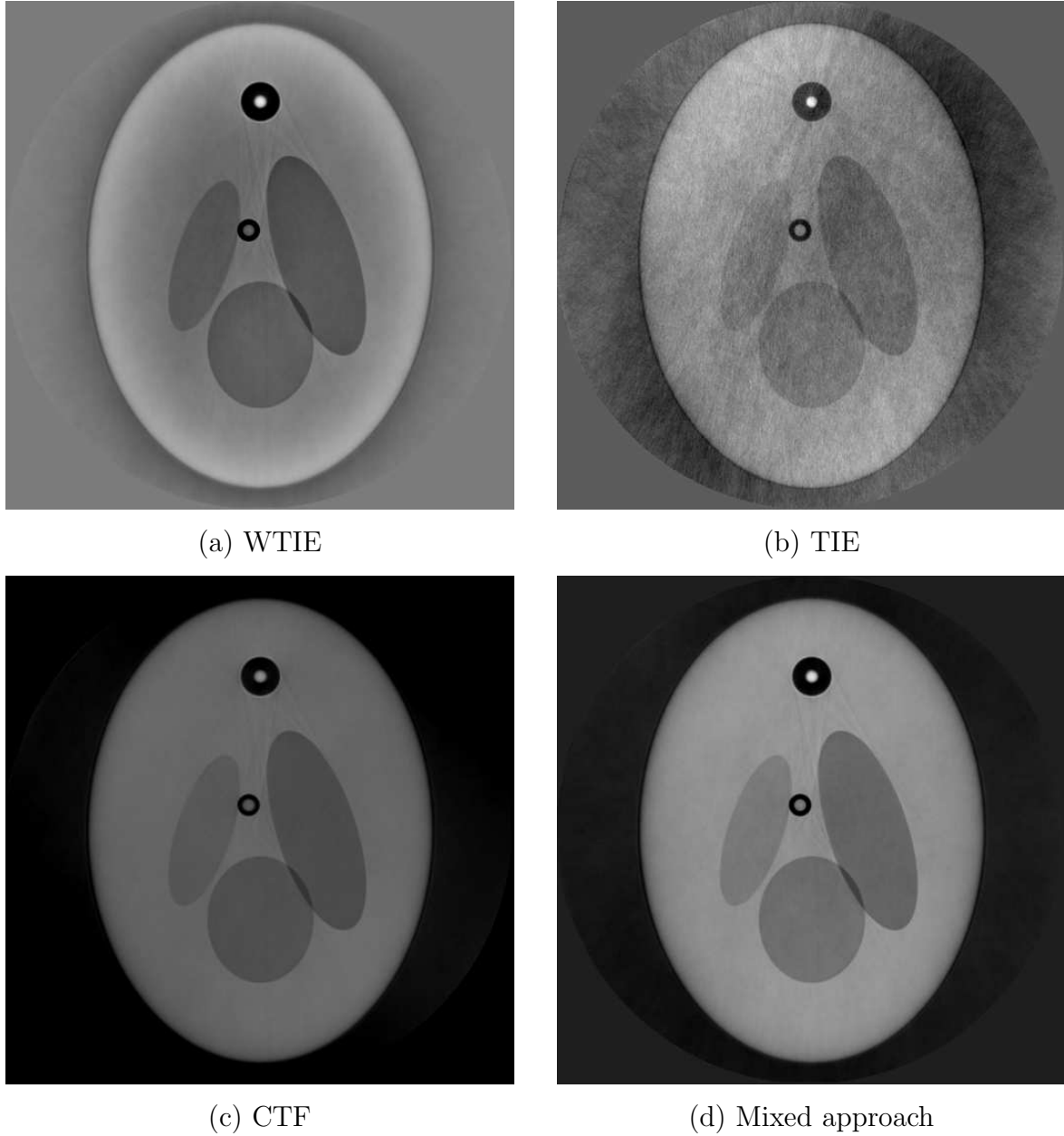


Figure 4.5: Central slices of the refractive index decrement reconstructed using simulated data with added noise, corresponding to a PPSNR of 12 dB in the first (absorption) distance. Reconstruction was done using (a) WTIE (b) TIE, (c) CTF and (d) Mixed approach algorithms. The given numerical implementations of the WTIE and TIE show low-frequency distortions and TIE show high-frequency noise. Both the CTF and Mixed approach yield qualitatively more correct reconstructions.

The TIE and WTIE reconstructions show typical artifacts for noisy data: strong low-frequency noise for the WTIE and some low-frequency noise and higher frequency noise for the TIE. Examining the reconstructed mean values at 24 dB (Fig. 4.7 (b)) and 12 dB (Fig. 4.7 (c)), it is seen that the accuracy of the TIE and WTIE degrades with increased noise, while the results of the CTF and Mixed approaches remain approximately the same. This is confirmed by examining the AVGE at different noise levels (Fig. 4.7 (f)). The Mixed approach yields accurate reconstructions even for low SNR in the data. Also the CTF reconstructions seem less influenced by noise, but remain underestimated. The error in the TIE and WTIE however rises more sharply with increased noise levels. The same can be seen in the NMSE (Fig. 4.7 (e)). This is not only explained by the increased statistics of having multiple images. In the Mixed approach and CTF, the noise does not fit the data model and is filtered out because of the use of images at several distances, while in the TIE and WTIE approaches, noise is propagated more easily to the solution.

#### 4.5.2 Experimental data

Tomographic slices of the test object are shown in Fig. 4.6. As in the simulated case, some low-frequency distortion can be seen, strongest in the TIE and WTIE reconstructions. The CTF seems, like in the simulated case, to yield an underestimation of the refractive index due to the strong absorption. Examining the measured mean values (Fig. 4.7(d)), these observations are confirmed. The results are in good correspondence with the simulations, the Mixed approach yielding the lowest reconstruction error; the AVGE for the different approaches were 17.7 % for the WTIE, 16.8 % for the TIE, 29.7 % for the CTF and 14.2 % for the Mixed approach.

### 4.6 Summary and conclusion

The reconstruction quality of four phase retrieval methods in in-line phase tomography of mixed absorption and phase objects has been quantitatively evaluated. The comparison was performed using a numerical phantom, used to simulate phase contrast tomography data, both with and without noise. A phantom object was also built and imaged to evaluate the performance in an experimental setting. The simulations were set up to reflect the quantitative and qualitative appearance of the constructed phantom, by using the corresponding absorption and refractive indices of the respective materials used. The reconstructions were compared in terms of reconstructed average

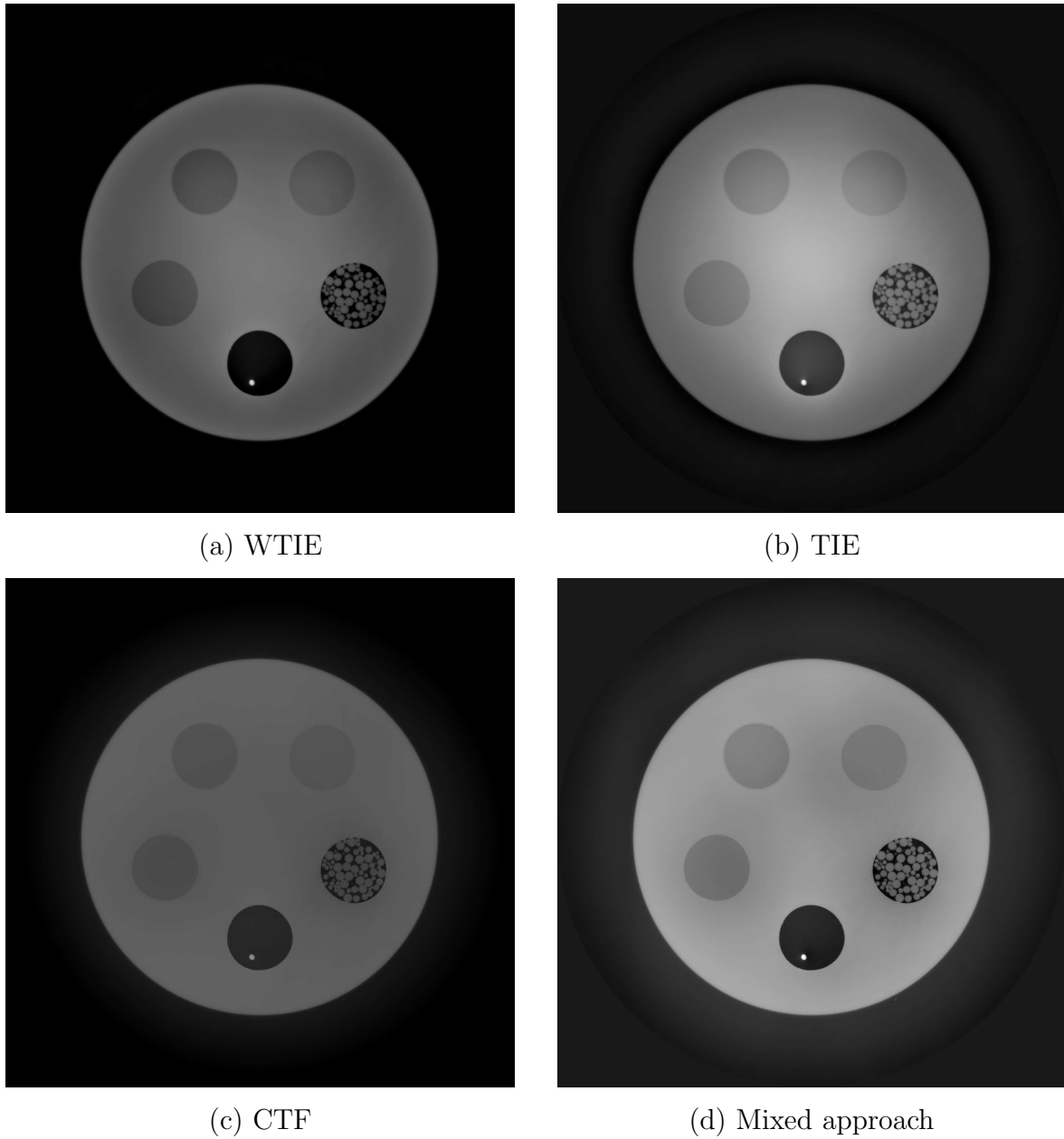


Figure 4.6: Phase tomograms of the constructed phantom, imaged at 24 keV. Reconstruction was done using (a) WTIE (b) TIE (c) CTF and (d) Mixed approach algorithms. The field of view is 15.4 mm. Some low-frequency distortion is present in all four reconstructions, due to the weak sensitivity to low frequencies of the phase contrast method (Fig. 4.2), strongest in the WTIE and TIE reconstructions. The CTF consistently underestimates the refractive index due to the weak absorption criterion being violated, while the Mixed approach seems to yield the most correct reconstruction.

values of the refractive index in regions corresponding to different materials in the phantoms. For the simulated data, the NMSE was also measured.

It can be noted that all four methods perform well in a qualitative sense, the major problem being noise in the low frequency range, due to the transfer function of the image formation process approaching zero for low spatial frequencies (Fig. 4.2). In quantitative terms, the Mixed approach performs best, both on simulated noisy data and experimental data, due to the increased robustness offered by the possibility to include images at several distances. The use of several distances may improve image quality not only because of the improved statistics, but mainly because the model of wave propagation does not include the noise.

It is also worth noting that the TIE performs best for noise free data, due to less restrictions put on the object, but in this implementation is less robust to noise due to the smaller amount of data it uses, without any redundancy. Another thing to note is that in these experiments, there were no zero crossings in the transfer function, except at zero spatial frequency, due to the relatively low spatial resolution. The TIE and WTIE methods could prove to be interesting when low dose deposition is crucial, due to fewer images being required. If quality of reconstructions is the premier goal, especially for quantitative analysis, the Mixed approach would be the method of choice.

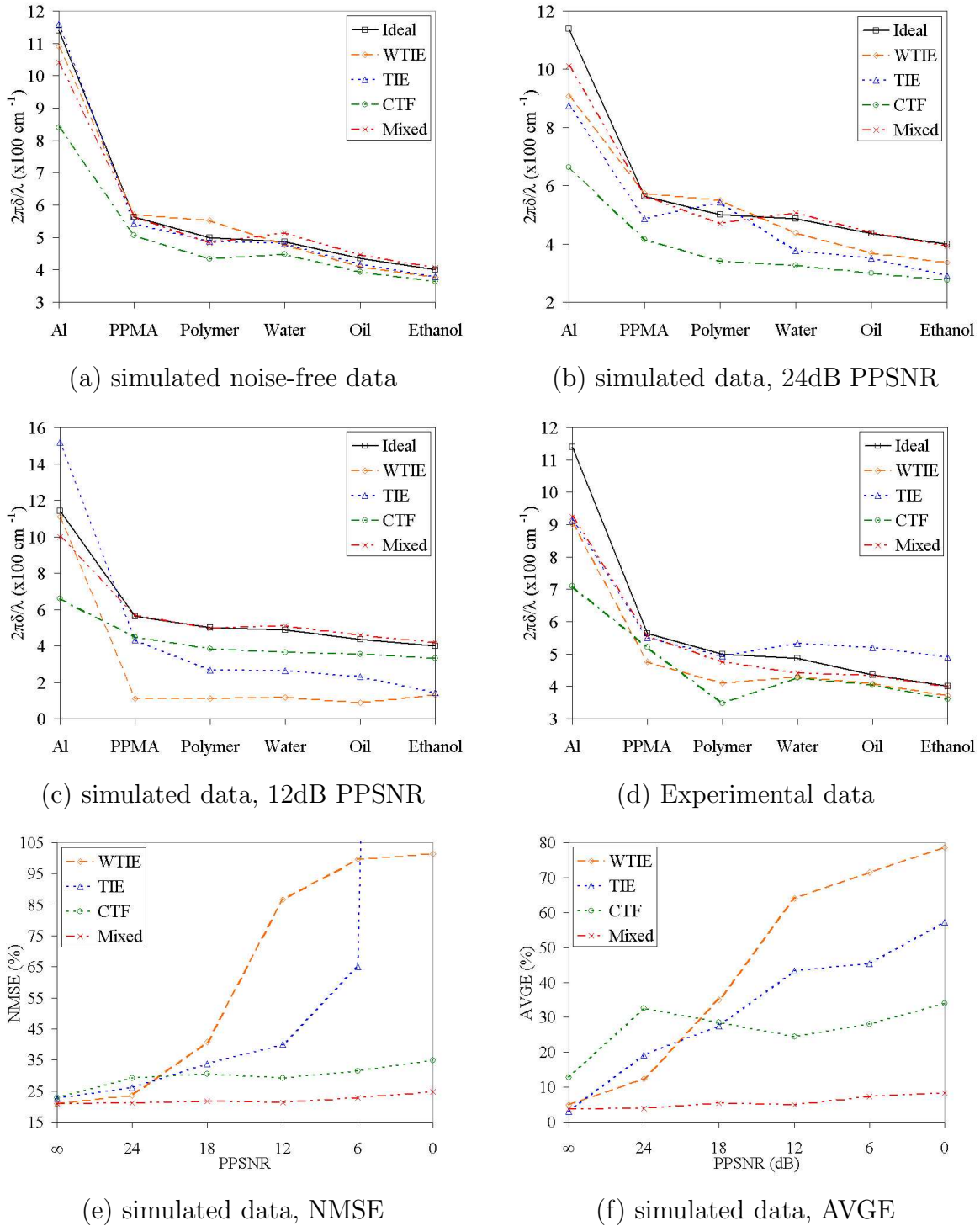


Figure 4.7: Plots of the performance of the different algorithms: Reconstructed average values of  $\delta$  using the (a) simulated, noise-free data, (b) simulated data with 24 dB PPSNR in the first plane, (c) simulated data with 12 dB PPSNR in the first plane, (d) experimental data, (e) normalized mean-square error (NMSE) (Eq. 4.30) for different noise levels and (f) reconstructed mean value average error (AVGE) (Eq. 4.31) for different noise levels.



# Chapter 5

## Regularization of phase retrieval

The mixed approach extends the validity range of phase retrieval to strongly absorbing, slowly varying objects, and unifies the two main mathematical models used for phase retrieval in the Fresnel region (Chapter 3). Some issues remain, however. The main problem being that regardless of how many propagation distances are used, the resulting combined operator  $\sum_D A_D(\mathbf{f})$  (Eq. 5.79) always goes to zero for low spatial frequencies. This makes phase retrieval with the mixed approach, due to the underlying physics, ill-posed due to  $\sum_D A_D(\mathbf{f})$  having a singularity at  $\mathbf{f} = (0, 0)$  and being otherwise ill-conditioned due to very small values around this point. This makes the inverse very sensitive to noise in the low frequency range, giving rise to distortions such as that in Fig. 5.13.

In this chapter we investigate regularization approaches to the low frequency problem. We present two methods, one based on Fourier-Wavelet regularized deconvolution (ForWaRD) (Neelamani et al., 2004) and one based on utilizing prior knowledge to retrieve the low frequency components. We also apply an automatic parameter selection algorithm, based on the L-curve criterion (Hansen, 1992), to this method. It will turn out that the latter is more applicable in practice, and it is the one we use in applied cases in Chapter 6. We begin this chapter by introducing the Wavelet transform (Section 5.1), which we will use in the ForWaRD method, and spline curve fitting (Section 5.2), which will come to use for the parameter selection algorithm.

## 5.1 Wavelet transform

The wavelet transform is similar to the Fourier transform in many ways. Instead of the familiar complex exponentials of the Fourier transform, the wavelet transform decomposes the function  $g(x)$  into a set of basis functions  $\Psi_{j,l}(x)$ , called the *wavelets*. The wavelets are generated by scaling  $j$  and translation  $l$  of a basic wavelet  $\Psi(x)$ , so that

$$\Psi_{j,l}(x) = \frac{1}{\sqrt{j}} \Psi\left(\frac{x-l}{j}\right). \quad (5.1)$$

$\Psi(x)$  is usually called the *mother wavelet*. Some similarities and differences become clear when we look at the definition of the 1D continuous wavelet transform (CWT)

$$g^W(j, l) = \mathbf{W}\{g\}(j, l) = \int g(x) \Psi_{j,l}^*(x) dx. \quad (5.2)$$

The inverse transform is given by

$$g(x) = \iint g^W(j, l) \Psi_{j,l}(x) dj dl. \quad (5.3)$$

We can immediately see one clear distinction to the Fourier transform. The wavelet transform of a one dimensional function is two dimensional. This is due to that the wavelets are localized both in time and frequency, which gives the transform a high degree of redundancy. This is similar to the short-time Fourier transform, where the Fourier transform is calculated in a sliding window of fixed width. In the wavelet transform, the window size is also allowed to vary, which results in a variable resolution in the time-frequency plane (Vetterli and Herley, 1992). Another important difference to the Fourier transform is that the basis functions  $\Phi_{j,l}(x)$  are not specified in the transform, but can be chosen rather freely to best match a certain application, as long as some basic criteria are fulfilled.

The most important properties of wavelets are admissibility and regularity, which are the properties that gave name to wavelets. The admissibility condition can be written as

$$\int \frac{|\tilde{\Psi}(f)|^2}{|f|} df < \infty \quad (5.4)$$

where  $\tilde{\Psi}(f)$  is the Fourier transform of the mother wavelet. It can be shown (Daubechies, 1992) that square integrable functions satisfying the admissibility condition can be used to first analyze and then reconstruct a signal without loss of information. Eq. 5.4 requires that the Fourier transform of  $\Psi(x)$  vanishes at the zero frequency, that is

$$|\tilde{\Psi}(0)|^2 = 0 \quad (5.5)$$

which implies that the wavelet must have a band-pass like spectrum. This also means that the wavelet must have zero average in the spatial domain, that is

$$\int \Psi(x)dx = 0. \quad (5.6)$$

This means that  $\Psi(x)$  must be oscillatory, i.e. a *wave*.

Regularity can be explained in terms of *vanishing moments*. If we Taylor expand the wavelet transform to the  $n$ -th order (setting  $l = 0$  for clarity), we obtain

$$g^W(j, 0) = \frac{1}{\sqrt{j}} \sum_{p=0}^n g^{(p)}(0) \int \frac{x^p}{p!} \Psi\left(\frac{x}{j}\right) dx + O(n+1) \quad (5.7)$$

where  $g^{(n)}$  denotes the  $n$ -th derivative of  $g$ . Defining the *moment* of the wavelet as

$$M_p = \int x^p \Psi(x) dx, \quad (5.8)$$

we can rewrite Eq. 5.7 into a finite development as

$$g^W(j, 0) = \frac{1}{\sqrt{j}} \left[ g(0) M_0 j + \frac{g^{(1)}(0)}{1!} M_1 j^2 + \frac{g^{(2)}(0)}{2!} M_2 j^3 + \dots + \frac{g^{(n)}(0)}{n!} M_n j^{n+1} + O(j^{n+2}) \right]. \quad (5.9)$$

From the admissibility condition we have that the zeroth moment  $M_0$  is equal to zero. If moments up to  $M_n$  are equal to zero, the wavelet decays as  $j^{n+2}$  for a smooth signal  $g(x)$ . This is known as vanishing moments, or *approximation order*. The number of vanishing moments is equal to the approximation order. The number of desired vanishing moments is application dependent (Calderbank et al., 1998). The regularity condition means that the wavelet has to be localized, so we can say that admissibility gives the *wave* and regularity the *let*.

We note that Eq. 5.2 is a convolution integral. Wavelet analysis could then just as well be described as multiplications in the Fourier domain, with the wavelet coefficients at one scaling factor as

$$g_j^W(l) = \mathcal{F}^{-1}\{\tilde{g}\tilde{\Psi}_j\}(l) \quad (5.10)$$

The wavelet transform can, like the Fourier transform, easily be generalized to two (or more) dimensions. The 2D wavelet transform is given by

$$g^W(\mathbf{j}, \mathbf{l}) = \iint g(\mathbf{x}) \frac{1}{\sqrt{j_x j_y}} \Psi^* \left( \frac{x - l_x}{j_x}, \frac{y - l_y}{j_y} \right) d\mathbf{x}, \quad (5.11)$$

with  $\mathbf{j} = (j_x, j_y)$  and  $\mathbf{l} = (l_x, l_y)$ . Note that the wavelet transform of a 1D signal is 2D, the wavelet transform of a 2D signal is 4D and so on.

### 5.1.1 Discrete wavelet transform (DWT)

The DWT is an efficient, non-redundant, discrete implementation of the CWT using orthogonal basis functions. These are important features, as in the CWT, the basis functions are not orthogonal; the transform is redundant as we noted above. The CWT is besides the spatial variable also continuous in the translation and scale, so an infinite number of scales and translations are needed. There is also no analytic solution to the wavelet transform of most functions, so an efficient numerical implementation is important.

The first step to achieve an efficient implementation is to remove the redundancy. This is done by only allowing scaling and translation in discrete steps in Eq. 5.1, which yields the *discrete wavelet* (Daubechies, 1992)

$$\Psi_{j,l}(x) = \frac{1}{\sqrt{s_0^j}} \Psi \left( \frac{x - l\tau_0 s_0^j}{s_0^j} \right). \quad (5.12)$$

$j$  and  $l$  are now integers,  $s_0 > 1$  is a fixed dilation step and  $\tau_0$  the translation factor. Note that the wavelet is still continuous in  $x$ . It is the translation and scale variables that are discretized, and hence the sampling in the space-scale space. Setting  $s_0 = 2$  and  $\tau_0 = 1$ , which is the usual choice, yields dyadic sampling of both translation and scale.

Decomposing a signal using discrete wavelets is called *wavelet series decomposition* (analogous to the Fourier counterpart). It can be shown that a necessary and sufficient condition for reconstruction of a signal from its wavelet series decomposition to be possible, the chosen wavelets must constitute a *frame* (Daubechies, 1992). This means that the energy in the wavelet coefficients must lie between two positive bounds

$$A \int |g(x)|^2 dx \leq \sum_{j,l} |g^W(j,l)|^2 \leq B \int |g(x)|^2 dx. \quad (5.13)$$

If this condition is fulfilled, the discrete wavelet basis functions span a frame with frame bounds  $A$  and  $B$ . If  $A = B$ , the frame is a *tight frame* and the wavelet transform behaves like an orthogonal basis. If  $A \neq B$ , reconstruction has to be made with a different set of functions, the *dual frame*  $\Upsilon_{j,l}(x)$ , which satisfies

$$g(x) = \iint \left[ \int g(x) \Psi_{j,l}^*(x) dx \right] \Upsilon_{j,l}(x) dj dl. \quad (5.14)$$

The final step of removing redundancy in the wavelet transform is to make sure the wavelet basis functions are orthogonal. This is done by choosing a mother wavelet so that

$$\int \Psi_{j,l}(x) \Psi_{j',l'}^*(x) dx = \begin{cases} 1 & j = j', l = l' \\ 0 & \text{otherwise} \end{cases} \quad (5.15)$$

This is only possible with discrete wavelets. With orthogonal basis functions, a signal can be reconstructed from its wavelet coefficients by summing the basis functions, weighted by the coefficients (that is, the basis is its own dual), as

$$g(x) = \sum_{j,l} g^W(j,l) \Psi_{j,l}(x). \quad (5.16)$$

The drawback of using orthogonal wavelets is that it is no longer shift invariant. Differently shifted versions of the same signal will yield different wavelet transforms that are not simply shifted. This can be an undesirable feature in some applications. Some redundancy can also be useful e.g. in denoising applications, to spread noise energy over more basis functions.

This version of the wavelet transform still needs an infinite number of basis functions. To avoid this problem, it is enough to simply use a finite number of basis functions.

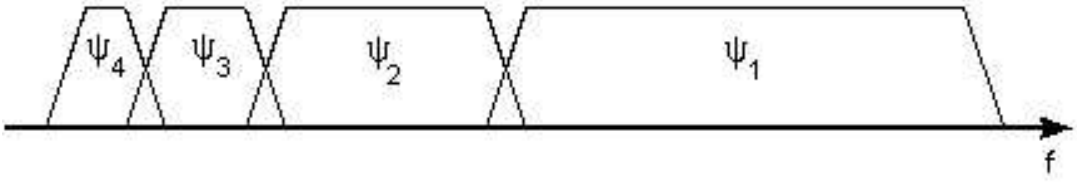


Figure 5.1: Overlapping wavelet bandpass spectra. The wavelets must be chosen to give enough coverage of the frequency domain.

This is acceptable as long as the set of wavelets used give good enough coverage of the frequency domain. This can be seen from the band-pass nature of the wavelet (Fig. 5.1). The most common choice is to also divide the frequency domain in a dyadic manner, that is splitting the frequency domain in two, then splitting these in two. The upper limit is given by the bandwidth of the signal, but an infinite number of wavelets would still be needed to give coverage down to  $f = 0$ . This is handled by introducing a *scaling function*  $\phi(x)$ . The spectrum is divided  $J$  times and the scaling function is then chosen so that its spectrum covers the remaining low part of the frequency domain.

The scaling function can in turn be decomposed into wavelets, and represented by

$$\phi(x) = \sum_{j,l} \phi^W(j, l) \Psi_{j,l}(x). \quad (5.17)$$

This contains components only up to scale  $J$ . If we added one wavelet spectrum to the scaling function, we would get a new scaling function with a spectrum twice as wide as the first. We can express the first scaling function in terms of the second, which is known as the *multiscale formulation* or *two-scale relation* (Chui, 1997):

$$\phi(2^j x) = \sum_l h_{j+1}(l) \phi(2^{j+1} x - l), \quad (5.18)$$

that is the scaling function at a certain scale can be expressed in terms of translated scaling functions at the next smaller scale. The first scaling function was introduced to replace a set of wavelets, which means that we can express the wavelets in terms of translated scaling functions

$$\Psi(2^j x) = \sum_l s_{j+1}(l) \phi(2^{j+1} x - l). \quad (5.19)$$

This is the two-scale relation between the wavelet and the scaling function. Since the signal  $g(x)$  can be expressed in terms of dilated and translated wavelets up to scale

$j - 1$ ,  $g(x)$  can be expressed in terms of dilated and translated scaling functions at scale  $j$  as

$$g_j(x) = \sum_l g_j^L(l) \phi(2^j x - l). \quad (5.20)$$

If we would examine  $g(x)$  at one scale coarser, at  $j - 1$ , we would have to add wavelets in order to keep the same level of detail:

$$g_j(x) = \sum_l g_{j-1}^L(l) \phi(2^{j-1}x - l) + \sum_k g_{j-1}^W(l) \Psi(2^{j-1}x - l). \quad (5.21)$$

Considering only discrete shifts, the coefficients at scale  $j - 1$ ,  $g_{j-1}^L$ , can be calculated as

$$\begin{aligned} g_{j-1}^L(l) &= \int g_j(x) \phi_{j,l}(x) dx \\ g_{j-1}^W(l) &= \int g_j(x) \Psi_{j,l}(x) dx. \end{aligned} \quad (5.22)$$

Substituting Eq. 5.18 and Eq. 5.19 into Eq. 5.22 and rearranging yields

$$\begin{aligned} g_{j-1}^L(l) &= \sum m h(x - 2l) g_j^L(m) \\ g_{j-1}^W(l) &= \sum s(x - 2l) g_j^L(m), \end{aligned} \quad (5.23)$$

where  $x$  only takes integer values, which is the standard definition of the DWT.

The weighting factors  $h(x)$ , the *scaling filter*, must, as we reasoned above, be a low-pass filter and the weighting factors  $s(x)$ , the *wavelet filter*, a high-pass filter. The step size 2 in the  $l$  variable means that only every other point in  $g_{j-1}^L$  is used. This is equivalent of sub-sampling the output  $g_{j-1}^L(x)$  and  $g_{j-1}^W(x)$  by a factor 2 in each step. This follows intuition: as we half the bandwidth in each step, only half the samples are needed to represent the signal. Considering these features together, the DWT can be implemented as an iterated filter bank consisting of filters and downsamplers (Fig. 5.2). The first input is the signal itself, and the filtering can be iterated until the signal at the resulting scale is shorter than the scaling filter or wavelet filter, whichever comes first.

### 5.1.2 Shift Invariant redundant DWT (srDWT)

The downsampling in the DWT makes it no longer shift-invariant. In some applications, this is a more important feature than non-redundancy. A shift invariant,

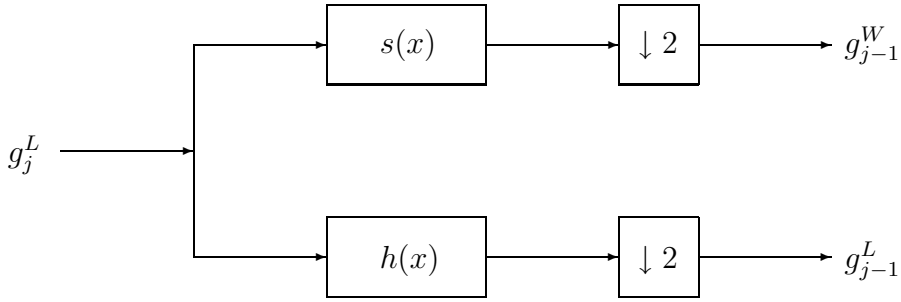


Figure 5.2: One stage of an iterated filter bank, implementing the DWT (Eq. 5.23). The first input is the signal  $g(x)$  to be analyzed and the bank is iterated until the signal at that scale is shorter than the scaling filter  $h(x)$  or the wavelet filter  $s(x)$ .

redundant DWT can be obtained by simply removing the downsampling step in the DWT (Daubechies, 1992; Mallat, 1999). This can also be derived by using directly the definition of the CWT (Eq. 5.2), by filtering discrete signals with discrete filters, directly obtaining a discretized version of the CWT, which avoids the need to iterate the filtering to achieve a lower scale, since each scale can be applied directly. This means that the transform can be implemented as a series of Fourier filters by using the FFT. The srDWT yields sparse, well localized representations of many types of signals. This is especially true around discontinuities. This can be exploited for e.g. compression or denoising applications. We will use this version of the transform in Section 5.3.

## 5.2 Splines

Splines refer to a wide class of functions, mainly used in interpolation. They derive their name from the usually wooden strips, “flat splines”, that were used in engineering to draw curves before the introduction of computer aided design (Ahlberg et al., 1967; Bartels et al., 1987). The strip would be fastened to a set of weights, and would take the shape that minimizes the energy required to bend it, thus adopting the smoothest possible shape.

In the mathematical counterpart, given a set of  $m+1$  points  $\{\mathbf{p}_0, \mathbf{p}_1, \dots, \mathbf{p}_m\}$  in a 2D space, called the *knots*, the spline is a plane curve that “connects the dots” in a way that each segment is a distinct parameterized curve,

$$\mathbf{c}(t) = (X(t), Y(t)). \quad (5.24)$$

The  $i^{th}$  segment  $c_i$  runs from  $\mathbf{p}_i$  to  $\mathbf{p}_{i+1}$ , and we assume that the parameter  $t$  correspondingly runs from knot  $i$ ,  $t_i$ , to knot  $i + 1$ ,  $t_{i+1}$ . Each segment  $\mathbf{c}_i(t)$  is then represented parametrically as  $(X_i(t), Y_i(t))$ . The problem of interpolating the data points  $\mathbf{p}_i$  is then finding out how  $X_i(t)$  and  $Y_i(t)$  are determined by the points

$$\mathbf{p}_i = (x_i, y_i). \quad (5.25)$$

Since the x-coordinates  $X(t)$  of points on a curve generally are determined only by the x-coordinates  $x_0, \dots, x_m$  of the data points, and similarly  $Y(t)$  is determined only by the y-coordinates of the data points, and  $X(t)$  and  $Y(t)$  is treated in the same way, we show only the treatment of  $Y(t)$ .

### 5.2.1 Cubic spline interpolation

If we let the spline be piecewise constructed of third degree polynomials, it is called a *cubic spline*. This often provides a flexible enough representation for many applications, at a reasonable computational cost (Bartels et al., 1987). In a cubic spline, the  $i$ -th element of the spline  $c(t)$  is represented by

$$Y_i(t) = a_i + b_i t + c_i t^2 + d_i t^3. \quad (5.26)$$

Based on the definition of the spline, we already know two things about the segment, namely that

$$Y_i(0) = a_i = y_i \quad (5.27)$$

and

$$Y_i(1) = a_i + b_i + c_i + d_i = y_{i+1}. \quad (5.28)$$

Taking the derivative of  $Y_i(t)$  also gives

$$Y'_i(0) = D_i = b_i \quad (5.29)$$

and

$$Y'_i(1) = D_{i+1} = b_i + 2c_i + 3d_i. \quad (5.30)$$

These four equations can be solved symbolically for the coefficients in  $Y_i(t)$ , yielding

$$\begin{aligned} a_i &= y_i \\ b_i &= D_i \\ c_i &= 3(y_{i+1} - y_i) - 2D_i - D_{i+1} \\ d_i &= 2(y_i - y_{i+1}) + D_i + D_{i+1}. \end{aligned} \quad (5.31)$$

To yield a continuous curve, the first and second derivatives at the end points of each segment has to match with the adjoining intervals. This is done by setting

$$\begin{aligned} Y_{i-1}(1) &= y_i \\ Y_i(0) &= y_i \\ Y'_{i-1}(1) &= Y'_i(0) \\ Y''_{i-1}(1) &= Y''_i(0). \end{aligned} \quad (5.32)$$

Examining Eq. 5.31, we see that if we solved for  $D_i$ , we can obtain the coefficients through their definition. Setting the second derivatives of each polynomial to zero at the endpoints provides a boundary condition which completes a system of  $m + 1$  equations and  $m + 1$  unknowns

$$\begin{pmatrix} 2 & 1 & & & \\ 1 & 4 & 1 & & \\ & 1 & 4 & 1 & \\ & \cdot & \cdot & \cdot & \\ & \cdot & \cdot & \cdot & \\ & & 1 & 4 & 1 \\ & & & 1 & 2 \end{pmatrix} \begin{pmatrix} D_0 \\ D_1 \\ \cdot \\ \cdot \\ \cdot \\ D_m \end{pmatrix} = \begin{pmatrix} 3(y_1 - y_0) \\ 3(y_2 - y_0) \\ \cdot \\ \cdot \\ \cdot \\ 3(y_m - y_{m-2}) \\ 3(y_m - y_{m-1}) \end{pmatrix}. \quad (5.33)$$

This would force the spline to be a straight line outside the interval, and is known as a *natural cubic spline*. Solving Eq. 5.33 yields the desired interpolation.



### 5.3 Fourier-Wavelet regularized phase retrieval

## Fourier-wavelet regularization of phase retrieval in x-ray in-line phase tomography

Manuscript prepared for  
Journal of the Optical Society of America A, JOSA A

Phase sensitive X-ray imaging extends standard X-ray microscopy techniques by offering up to  $10^3$  times higher sensitivity than absorption based techniques. If an object is illuminated with a sufficiently coherent beam, phase contrast is achieved by moving the detector downstream from the object. There is a quantitative relationship between the phase shift induced by the object and the recorded intensity. This relationship can be used to retrieve the phase shift induced by the object through the solution of an inverse problem. Since the phase shift can be considered as a projection through the 3D refractive index, the latter can be reconstructed using standard tomographic inversion techniques. However, the determination of the phase shift from the recorded intensity is an ill-posed inverse problem. In this paper, we investigate the application of Fourier-wavelet regularized deconvolution (ForWaRD) to this problem. The method is evaluated using simulated data and is shown to increase the quality of reconstructions, in terms of normalized RMS error, compared to standard Tikhonov regularization, at a three times increase in computational cost.

### 5.3.1 Introduction

In-line phase tomography is a powerful technique in X-ray microscopy with numerous potential applications ranging from bone research and small animal imaging to materials science and paleontology. The prime interest in phase sensitive X-ray imaging techniques is increased sensitivity, up to a factor  $10^3$  in the hard X-ray region, compared to standard, absorption based computed micro-tomography ( $\mu$ -CT) (Momose et al., 1996), which makes it possible to image soft, biological tissue without staining.

X-ray phase contrast imaging is possible when the X-ray beam has a defined phase, i.e. it is spatially coherent. If the coherence is sufficiently high, a particularly simple mode of phase contrast is enabled (Snigirev et al., 1995), where phase contrast is achieved by moving the detector downstream of the imaged object (Fig. 5.3). Hence, the wavefield is allowed to propagate in free space and the recorded image on the detector is a Fresnel diffraction pattern.

A quantitative relationship exists between such patterns and the complex refractive index distribution in the object, the real and imaginary parts being the refractive and absorption indices respectively. The contrast recorded at a certain distance can be expressed by a non-trivial relationship of both the absorption and the phase shift induced by the object. The phase shift and absorption can be considered as projections through the real and imaginary parts of the 3D complex refractive index distribution respectively.

Reconstruction of the absorption coefficient requires only the images acquired when the detector is located in the contact plane for different rotation angles. These images can be directly used with standard tomographic reconstruction techniques such as filtered backprojection (FBP). This corresponds to standard  $\mu$ -CT. On the other hand, the reconstruction of the refractive index distribution requires first the retrieval of the phase shift for each rotation angle, from one or several images at different distances. The recorded patterns can be analyzed directly in the Fourier domain (Guigay, 1977) and several methods for phase retrieval are based on this Fourier representation (Nugent et al., 1996; Cloetens et al., 1999; Guigay et al., 2007). These methods are based on linearization of some aspect of the Fourier representation, to yield an efficient phase retrieval algorithm. Here, the mixed approach proposed in (Guigay et al., 2007) is considered, which has been shown to have more general validity conditions (Guigay et al., 2007) and be more accurate and robust to noise (Langer et al., 2008). The linearization of the forward problem yields an ordinary differential equation, which is solved iteratively in a minimum least squares sense. However due the ill-posed nature

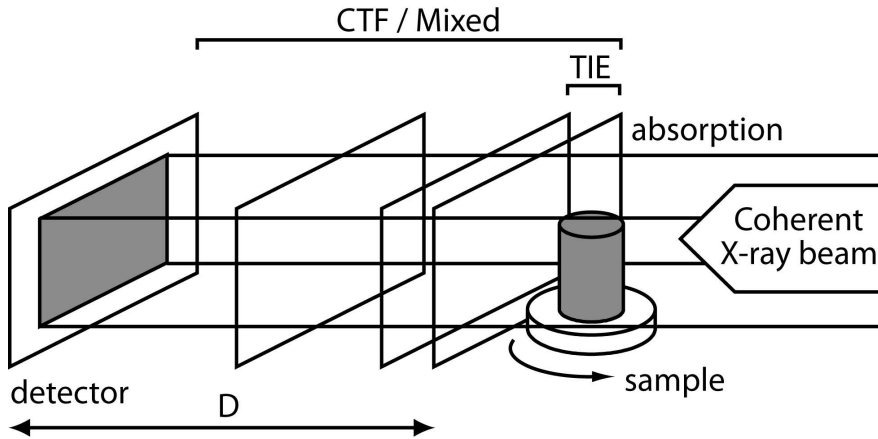


Figure 5.3: Schematic of the experimental setup. The sample is mounted on a rotation stage and the detector on a translation stage. The sample is then illuminated with partially coherent X-rays and tomographic scans are recorded at several (typically 4) sample to detector distances  $D$ .

of the problem some regularization is required.

In this paper, we investigate the application of the Fourier-wavelet regularized deconvolution (ForWaRD) algorithm (Neelamani et al., 2004). This method has the prospect of increased noise reduction with better edge preservation. This is due to the ability of the Fourier transform to efficiently represent the post-deconvolution colored noise and the wavelet transform's ability to economically represent a wide variety of signals. The method is applied to simulated data and the results are compared to standard Tikhonov regularization (Tikhonov and Arsenin, 1977).

### 5.3.2 Mathematical model

#### 5.3.2.1 Direct problem

When an object is illuminated with coherent X-rays, it can be considered to be described by its 3D complex refractive index distribution

$$n(x, y, z) = 1 - \delta_r(x, y, z) + i\beta(x, y, z), \quad (5.34)$$

where  $\delta_r$  is the refractive index decrement (the refractive index is smaller than, but close to, one for hard X-rays),  $\beta$  is the absorption index and  $(x, y, z)$  are the spatial coordinates.

The propagation path inside the object is considered straight, which means that the wave-object interaction can be described as a transmittance function

$$T(\mathbf{x}) = a(\mathbf{x}) \exp[i\varphi(\mathbf{x})] = \exp[-B(\mathbf{x}) + i\varphi(\mathbf{x})], \quad (5.35)$$

where  $a(\mathbf{x})$  is the amplitude modulation,  $\varphi(\mathbf{x})$  is the phase shift and  $\mathbf{x} = (x, y)$  are the coordinates in the plane transverse to the beam propagation direction  $z$ . Both the amplitude and phase modulations are projections through the object, with

$$B(\mathbf{x}) = \frac{2\pi}{\lambda} \int \beta(x, y, z) dz, \quad \varphi(\mathbf{x}) = \varphi_0 - \frac{2\pi}{\lambda} \int \delta_r(x, y, z) dz, \quad (5.36)$$

which means that both can be reconstructed by tomographic inversion.

If the incident beam is considered flat, propagation over distance  $D$  can be written as the Fresnel transform with parameter  $D$  of the object transmittance function. The recorded intensity at distance  $D$  is then the squared modulus of the wavefield, which is

$$I_D(\mathbf{x}) = |\mathbf{Fr}_D[T(\mathbf{x})]|^2. \quad (5.37)$$

The Fresnel transform is calculated as a convolution of the wavefield with the Fresnel propagator

$$\mathbf{Fr}_D[T(\mathbf{x})] = T(\mathbf{x}) * P_D(\mathbf{x}) \quad (5.38)$$

with

$$P_D(\mathbf{x}) = \frac{1}{i\lambda D} \exp\left(i\frac{\pi}{\lambda D}|\mathbf{x}|^2\right). \quad (5.39)$$

The Fresnel transform can therefore also be calculated in Fourier space. If the Fourier transform of a function  $g(\mathbf{x})$  is taken as

$$\tilde{g}(\mathbf{f}) = \mathcal{F}\{g\}(\mathbf{f}) = \int g(\mathbf{x}) \exp(-i2\pi\mathbf{x} \cdot \mathbf{f}) d\mathbf{x}, \quad (5.40)$$

the Fourier transform of the propagator in Eq. 5.38 becomes

$$\tilde{P}_D(\mathbf{f}) = \exp(-i\pi\lambda D|\mathbf{f}|^2) \quad (5.41)$$

The Fourier transform of the intensity at distance  $D$  can also be written directly as (Guigay, 1977)

$$\tilde{I}_D(\mathbf{f}) = \int T\left(\mathbf{x} - \frac{\lambda D \mathbf{f}}{2}\right) T^*\left(\mathbf{x} + \frac{\lambda D \mathbf{f}}{2}\right) \exp(-i2\pi \mathbf{x} \cdot \mathbf{f}) d\mathbf{x}, \quad (5.42)$$

which proves to be a convenient starting point for the derivation of inversion methods for the forward problem.

### 5.3.2.2 Inverse problem

The image formation is a non-linear process. To enable efficient solution for the phase, Eq. 5.42 is linearized. Several such solutions have been proposed. If  $T(\mathbf{x})$  is Taylor expanded with respect to the propagation distance  $D$  and only linear terms are retained, the transport of intensity equation is arrived at (Nugent et al., 1996). If  $T(\mathbf{x})$  is instead Taylor expanded with respect to the absorption and phase, one gets the contrast transfer function (Zabler et al., 2005). Here a mixed approach between the two is considered.  $T(\mathbf{x})$  is Taylor expanded with respect to the phase only in a first step. This yields the linearized forward model (Guigay et al., 2007)

$$\tilde{I}_D(\mathbf{f}) = \tilde{I}_D^{\varphi=0}(\mathbf{f}) + 2 \sin(\pi \lambda D |\mathbf{f}|^2) \mathcal{F}\{I_0 \varphi\}(\mathbf{f}) + \cos(\pi \lambda D |\mathbf{f}|^2) \frac{\lambda D}{2\pi} \mathcal{F}\{\nabla(\varphi \nabla I_0)\}(\mathbf{f}) \quad (5.43)$$

where  $I_D^{\varphi=0}$  is the intensity at distance  $D$  if the phase was zero.

This approach has more general validity conditions and seems more accurate and robust to noise than the two previously mentioned methods for mixed absorption and phase objects (Langer et al., 2008).

Eq. 5.43 can be used to solve for the phase. To include several distances, a least squares minimization procedure is used. Defining the phase-absorption product as  $\psi(\mathbf{x}) = I_0(\mathbf{x}) \varphi(\mathbf{x})$ , the phase retrieval problem can be stated as

$$\tilde{\psi}(\mathbf{f}) = \arg \min_{\tilde{\psi}} \sum_D |A_D(\mathbf{f}) \tilde{\psi}(\mathbf{f}) - [\tilde{I}_D(\mathbf{f}) - \tilde{I}_D^{\varphi=0}(\mathbf{f}) - \Delta_D(\mathbf{f})]|^2, \quad (5.44)$$

with  $A_D(\mathbf{f}) = 2 \sin(\pi \lambda D |\mathbf{f}|^2)$  and  $\Delta_D(\mathbf{f}) = \cos(\pi \lambda D |\mathbf{f}|^2) \frac{\lambda D}{2\pi} \mathcal{F}\{\nabla(\psi \nabla \ln I_0)\}(\mathbf{f})$ . Eq. 5.44 can be solved iteratively, with the solution given as (Guigay et al., 2007)

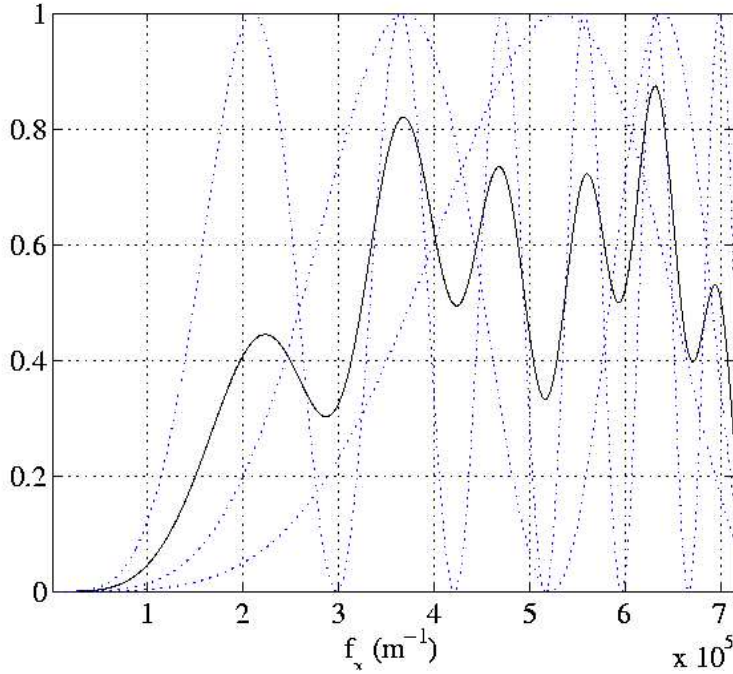


Figure 5.4: Squared modulus of the transfer function. The gray dotted lines are the transfer functions to three different distances ( $A_D^2(\mathbf{f})$ ) and the solid line is the combined transfer function ( $\frac{1}{N} \sum_D A_D(\mathbf{f})$ ) for all three distances. Propagation to a single distance has zeros in the transfer function, which is countered by using several propagation distances. The combined transfer function still goes to zero for low frequencies, which must be handled by regularization.

$$\tilde{\psi}^{(n+1)}(\mathbf{f}) = \frac{\sum_D A_D^*(\mathbf{f}) [\tilde{I}_D(\mathbf{f}) - \tilde{I}_D^{\varphi=0}(\mathbf{f}) - \Delta_D^{(n)}(\mathbf{f})]}{\sum_D |A_D(\mathbf{f})|^2} \quad (5.45)$$

The direct model description  $A_D(\mathbf{f})$  potentially has zero crossings, and goes to zero for small spatial frequencies. By combining several distances, the zero crossings can be eliminated (Cloetens et al., 1999; Zabler et al., 2005), but the zero at  $\mathbf{f} = (0, 0)$  remains and  $A_D(\mathbf{f})$  is also ill-conditioned around this point (Fig. 5.4). To yield stable solutions, regularization is required.

### 5.3.3 Fourier-wavelet regularized deconvolution

Consider the general deconvolution problem of retrieving  $q(\mathbf{x})$  from noisy measurements  $p(\mathbf{x})$  of the system  $h(\mathbf{x})$ :

$$p(\mathbf{x}) = h(\mathbf{x}) * q(\mathbf{x}) + n(\mathbf{x}), \quad (5.46)$$

with additive gaussian white noise  $n(\mathbf{x})$ , which is uncorrelated with the object. It is clear that, if  $h(\mathbf{x})$  is singular or ill-conditioned, straight-forward inversion of  $h(\mathbf{x})$  will not give reasonable results. This is most easily shown by Fourier transforming 5.46, where the convolution becomes a multiplication. An estimate  $\tilde{q}(\mathbf{f})$  is then given by

$$\tilde{q}(\mathbf{f}) = \frac{\tilde{p}(\mathbf{f})}{\tilde{h}(\mathbf{f})} - \frac{\tilde{n}(\mathbf{f})}{\tilde{h}(\mathbf{f})}, \quad (5.47)$$

that is the ideal  $\tilde{q}(\mathbf{f})$  degraded with filtered noise, which can be large or possibly unbounded if  $\tilde{h}(\mathbf{f})$  is singular or ill-conditioned.

Regularization aims at increasing the quality of the solution by introducing some additional information or desired quality of the solution. Least squares minimization in itself can be viewed as a very simple form of regularization. A simple form of regularization is to simultaneously minimize a norm of the solution. This is known as Tikhonov regularization (Tikhonov and Arsenin, 1977) and is often considered the standard regularization method. In this work, we investigate the use of a hybrid Fourier-wavelet deconvolution algorithm (ForWaRD) (Neelamani et al., 2004) to regularize the minimization problem in Eq. 5.44.

The ForWaRD algorithm consists of three steps:

1. Operator inversion
2. Fourier shrinkage
3. Wavelet shrinkage

The operator inversion and Fourier shrinkage is usually combined in one step for better numerical stability. We describe the two shrinkage steps below.

### 5.3.3.1 Fourier shrinkage

Consider again Eq. 5.46. The optimal solution to this problem, in the least squares sense, is given by

$$\tilde{q}(\mathbf{f}) = \tilde{p}(\mathbf{f}) \frac{\tilde{h}^*(\mathbf{f}) |\tilde{q}(\mathbf{f})|^2}{|\tilde{h}(\mathbf{f})|^2 |\tilde{q}(\mathbf{f})|^2 + |\tilde{n}(\mathbf{f})|^2}. \quad (5.48)$$

The second term is the Wiener inverse filter. We can see the action of this filter by examining the componentwise filter  $\lambda(\mathbf{f})$ , by rewriting Eq. 5.48 as

$$\tilde{q}(\mathbf{f}) = \lambda(\mathbf{f}) \frac{\tilde{p}(\mathbf{f})}{\tilde{h}(\mathbf{f})} \quad (5.49)$$

with

$$\lambda(\mathbf{f}) = \frac{|\tilde{h}(\mathbf{f})|^2}{|\tilde{h}(\mathbf{f})|^2 + \frac{|\tilde{n}(\mathbf{f})|^2}{|\tilde{q}(\mathbf{f})|^2}}. \quad (5.50)$$

Since the signal and noise spectra  $|\tilde{q}(\mathbf{f})|^2$  and  $|\tilde{n}(\mathbf{f})|^2$  generally are unknown, the best one can do is often to assume flat signal and noise spectra and introduce a regularizing parameter  $\alpha$ , which is determined empirically. The shrinkage then becomes

$$\lambda(\mathbf{f}) = \frac{|\tilde{h}(\mathbf{f})|^2}{|\tilde{h}(\mathbf{f})|^2 + \alpha}. \quad (5.51)$$

This is the solution to the Tikhonov regularized minimization problem (Tikhonov and Arsenin, 1977)

$$\tilde{q}(\mathbf{f}) = \arg \min_{\tilde{q}} |\tilde{h}(\mathbf{f}) \tilde{q}(\mathbf{f}) - \tilde{p}(\mathbf{f})|^2 + \alpha |\tilde{q}(\mathbf{f})|^2, \quad (5.52)$$

which restricts the energy in the solution. This will be used as the Fourier shrinkage step in the following.

### 5.3.3.2 Wavelet shrinkage

The wavelet transform has proved to be useful for estimating signals from noisy measurements

$$p(\mathbf{x}) = q(\mathbf{x}) + n(\mathbf{x}), \quad (5.53)$$

due to its economical signal representation (Donoho and Johnstone, 1994; Donoho, 1995; Donoho and Johnstone, 1999). The wavelet shrinkage is done by wavelet Wiener filtering (WWF). Taking the wavelet transform as

$$g^W(\mathbf{j}, \mathbf{l}) = \mathbf{W}\{g\}(\mathbf{j}, \mathbf{l}) = \iint g(\mathbf{x}) \frac{1}{\sqrt{j_x j_y}} \Psi^*(\frac{x - l_x}{j_x}, \frac{y - l_y}{j_y}) d\mathbf{x}, \quad (5.54)$$

with  $\Psi(\mathbf{x})$  some suitable wavelet family, the ideal shrinkage of each component is in WWF defined as

$$\lambda_W(\mathbf{j}, \mathbf{l}) = \frac{|q^W(\mathbf{j}, \mathbf{l})|^2}{|q^W(\mathbf{j}, \mathbf{l})|^2 + \sigma_j^2}, \quad (5.55)$$

where  $q^W(\mathbf{j}, \mathbf{l})$  signifies the wavelet transform of  $q(\mathbf{x})$  with the scale  $\mathbf{j} = (j_x, j_y)$  and position  $\mathbf{l} = (l_x, l_y)$ .  $\sigma_j^2$  is the noise variance estimate at scale  $\mathbf{j}$  and can be estimated by wavelet decomposing the Fourier regularized filter and multiplying the overall noise estimate  $\sigma$  with the gain in each sub-band:

$$\sigma_j^2 = \sigma^2 \iint_{\mathbf{l}} \left| \mathbf{W} \left\{ \mathcal{F}^{-1} \left[ \frac{\tilde{h}^*}{|\tilde{h}|^2 + \alpha} \right] \right\} (\mathbf{j}, \mathbf{l}) \right|^2. \quad (5.56)$$

$\sigma^2$  can in turn be estimated using a median estimator on the finest scale of the wavelet decomposition of the Fourier regularized estimate  $\hat{q}(\mathbf{x})$  (Donoho, 1995).

The ideal wavelet coefficients  $q^W(\mathbf{j}, \mathbf{l})$  are of course unavailable. A pilot estimate  $\hat{q}_{pilot}(\mathbf{x})$  can be acquired by hard thresholding the wavelet decomposition of the Fourier regularized solution  $\hat{q}(\mathbf{x})$ . This can then be used in the wavelet Wiener filter (Eq. 5.55), as long as sufficiently different wavelets are used for the hard thresholding and the WWF (Ghael et al., 1997; Neelamani et al., 2004). Considering two wavelet transforms  $\mathbf{W}_1$  and  $\mathbf{W}_2$ , defined using sufficiently different wavelets, applying hard thresholding in the first transform domain shrinks the wavelet components with (Mallat, 1999)

$$\lambda_{W_1}^T(\mathbf{j}, \mathbf{l}) = \begin{cases} 1, & \text{if } \hat{q}^{W_1}(\mathbf{j}, \mathbf{l}) > T_j \sigma_j \\ 0, & \text{if } \hat{q}^{W_1}(\mathbf{j}, \mathbf{l}) \leq T_j \sigma_j \end{cases}, \quad (5.57)$$

where  $T_j$  is a scale dependent threshold factor. The pilot estimate is then given in the second wavelet domain as

$$g_{pilot}^{W_2}(\mathbf{j}, \mathbf{l}) = W_2 \{ W_1^{-1} [\lambda_{W_1}^T \hat{q}^{W_1}] \} (\mathbf{j}, \mathbf{l}). \quad (5.58)$$

The Fourier-wavelet regularized solution is then given by

$$\hat{g}^{W_2}(\mathbf{j}, \mathbf{l}) = \hat{g}^{W_2}(\mathbf{j}, \mathbf{l}) \frac{|q_{pilot}^{W_2}(\mathbf{j}, \mathbf{l})|^2}{|q_{pilot}^{W_2}(\mathbf{j}, \mathbf{l})|^2 + \sigma_j^2}, \quad (5.59)$$

### 5.3.4 Implementation

Applying Tikhonov regularization to Eq. 5.44 yields

$$\tilde{\psi}(\mathbf{f}) = \arg \min_{\tilde{\psi}} \sum_D |A_D(\mathbf{f})\tilde{\psi}(\mathbf{f}) - [\tilde{I}_D(\mathbf{f}) - \tilde{I}_D^{\varphi=0}(\mathbf{f}) - \Delta_D(\mathbf{f})]|^2 + \alpha|\tilde{\psi}(\mathbf{f})|^2, \quad (5.60)$$

which has solution

$$\tilde{\psi}^{(n+1)}(\mathbf{f}) = \frac{\sum_D A_D^*(\mathbf{f})[\tilde{I}_D(\mathbf{f}) - \tilde{I}_D^{\varphi=0}(\mathbf{f}) - \Delta_D^{(n)}(\mathbf{f})]}{\sum_D |A_D(\mathbf{f})|^2 + \alpha} \quad (5.61)$$

The phase is initialized to zero as  $\varphi^{(0)}(\mathbf{x}) = 0$ . In all practical cases, Eq. 5.61 converges in 3-5 iterations.

The wavelet regularization was implemented using the shift-invariant redundant discrete wavelet transform (srDWT), which is essentially the standard DWT without downsampling (Mallat, 1999). It was implemented as filtering in the Fourier domain. Two minimum phase Daubechies wavelet bases (Daubechies, 1992), with two and six vanishing moments respectively, were used. We denote srDWT to the first basis with  $\mathbf{W}_1$  and to the second with  $\mathbf{W}_2$ . Wavelet decomposition was restricted to 5 levels.

The overall noise variance  $\sigma^2$  was estimated from the absorption image  $I_0(\mathbf{x})$  using the first wavelet basis. The level-dependent noise was then estimated as

$$\sigma_j = \sigma \sum_l \left| \mathbf{W}_2 \left\{ \mathcal{F}^{-1} \left[ \frac{\sum_D \tilde{A}_D}{\sum_D \tilde{A}_D^2 + \alpha} \right] \right\} (\mathbf{j}, \mathbf{l}) \right| \quad (5.62)$$

The pilot estimate  $\hat{\psi}_{pilot}(\mathbf{x})$  was obtained by hard thresholding (Eq. 5.57) in the first basis. This was subsequently used in the WWF in the second basis, with shrinkage

$$\lambda_{W_2}(\mathbf{j}, \mathbf{l}) = \frac{|\hat{\psi}_{pilot}^{W_2}(\mathbf{j}, \mathbf{l})|^2}{|\hat{\psi}_{pilot}^{W_2}(\mathbf{j}, \mathbf{l})|^2 + \sigma_j^2} \quad (5.63)$$

### 5.3.5 Simulation

The proposed method was evaluated on simulated data. An analytical phantom, based on the 3D Shepp-Logan phantom, described in (Langer et al., 2007) was used. The real and imaginary parts of the central slice of this phantom, digitized to  $512 \times 512$  pixels, are

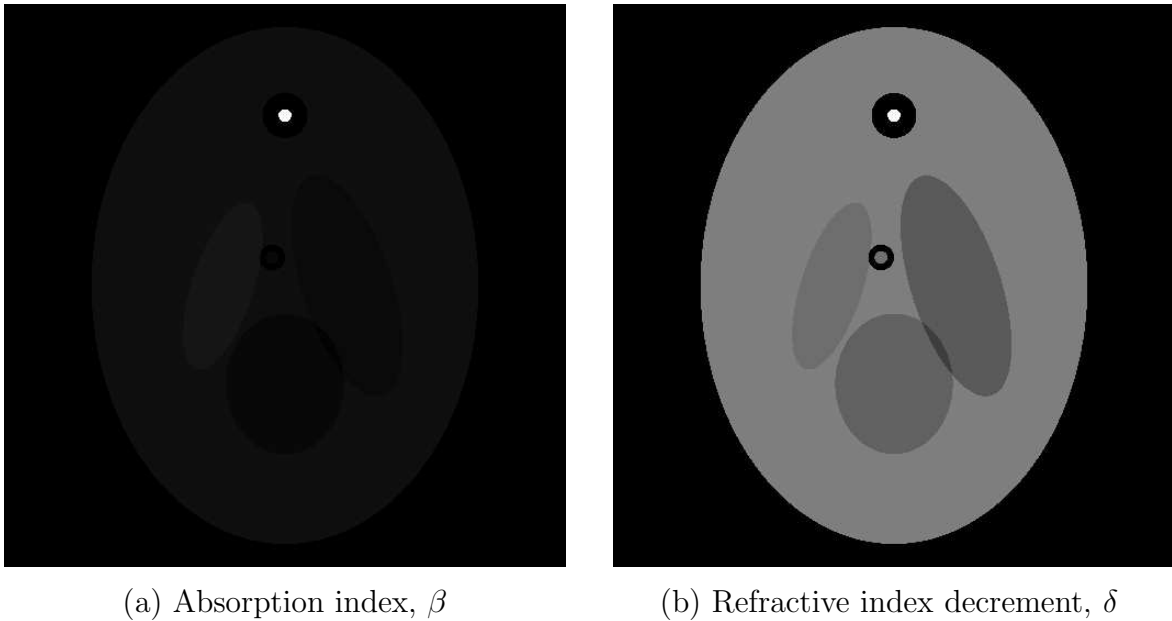


Figure 5.5: Central slices ( $512 \times 512$  pixels) of the 3D phantom used. The images are generated from an analytical definition. Each point is represented by a complex number with the imaginary part shown in (a), which is the absorption index  $\beta$ , and the real part shown in (b), which is the refractive index  $\delta_n$ .

shown in Fig. 5.5. Analytic projections through the absorption and refractive indices were calculated for 600 views, yielding the wavefront at  $D = 0$ , sampled on a  $2048 \times 2048$  grid. Propagation was simulated by calculating Eq. 5.38 in the Fourier domain. The intensities were calculated by taking the squared modulus and then binning the images to  $N = 512 \times 512$  to emulate the effect of the detector. Uniformly distributed zero mean white noise was then added to the images, with a peak to peak signal to noise ratio (PPSNR) of 12 dB, 0 dB and -12 dB respectively. The X-ray energy was 24 keV and distances  $D = \{0, 0.1, 0.3, 0.99\}$  m were used. The corresponding pixel size was  $7.5 \mu\text{m}$ , the minimum value of the absorption image intensity was 0.75 (the maximum 1.0 outside the object) and the maximum value of the phase modulation was 300 rad.

### 5.3.6 Results

Reconstructed tomographic slices at the different noise levels are shown in Fig. 5.3.6. Both Tikhonov (left) and ForWaRD (right) regularization yield qualitative reconstructions at high noise levels. Taking the normalized RMS error as

$$\epsilon = \left( \frac{\sum |f_i(\mathbf{x}) - f(\mathbf{x})|^2}{\sum |f_i(\mathbf{x})|^2} \right)^{1/2} \quad (5.64)$$

where  $f(\mathbf{x})$  is the reconstructed slice and  $f_i(\mathbf{x})$  the ideal slice (Fig. 5.5b), it is seen that the ForWaRD gives consistently better reconstructions (Tab. 5.1).

Considering the efficiency of the methods; applying only the Tikhonov regularization requires 14 2D FFTs per projection angle, if 5 iterations of Eq. 5.61 are used. Applying the wavelet part of ForWaRD requires an additional computation of 4 shift invariant redundant DWTs (one forward and one inverse for the "pilot" estimate, one forward and one inverse for the WWF), with a cost of  $J+1$  FFTs each. In this case, the computational cost for the ForWaRD is 44 2D FFTs per projection angle.

Table 5.1: Normalized RMS error (Eq. 5.64) for different peak-to-peak signal to noise ratios

| PPSNR  | Tikhonov | ForWaRD |
|--------|----------|---------|
| 12 dB  | 3.9 %    | 2.8 %   |
| 0 dB   | 4.0 %    | 3.2 %   |
| -12 dB | 6.8 %    | 5.5 %   |

### 5.3.7 Conclusions

Fourier-wavelet regularized deconvolution (ForWaRD) was applied to the problem of phase retrieval in X-ray in-line phase tomography. The method improves the normalized RMS error (Eq. 5.64) compared to standard Tikhonov regularization on simulated data, at the cost of three times increased computation time. This means that the ForWaRD method show some promise as regularization method in this case, but the increased computational cost might prove limiting in the experimental case, where the typical image size is  $2048 \times 2048$  pixels, and the process has to be applied to approximately 1800 images acquired at different angles.

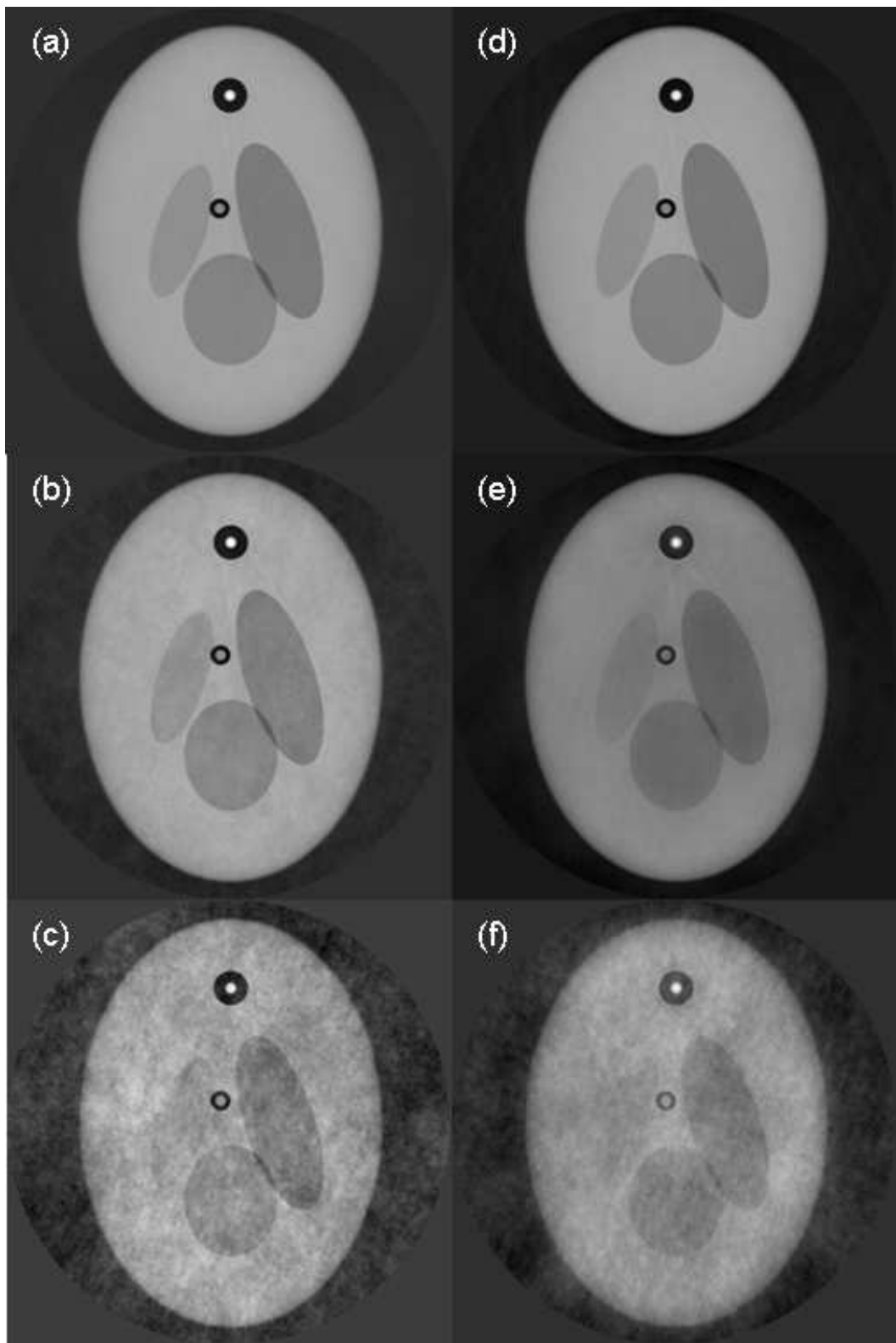


Figure 5.6: Reconstructed central slices of the simulated data. (a)-(c) were reconstructed using Tikhonov regularization. In (a) the PPSNR was 12 dB, (b) 0 dB and (c) -12 dB. (d)-(f) were reconstructed using Fourier-Wavelet regularization (ForWaRD), with the same noise levels as above.



## 5.4 Phase retrieval with a homogeneous composition prior

# Regularization of Phase Retrieval with Phase-Attenuation Duality Prior for 3D Holotomography

M. Langer, P. Cloetens and F. Peyrin

Submitted to:

IEEE Transactions on Image Processing

31 July 2008

We propose a new automatic regularized phase retrieval algorithm for in-line X-ray phase contrast imaging. Phase retrieval in the Fresnel region is a non-linear inverse problem, which is here solved by using a linearization of the forward problem. The retrieved phase is regularized using prior knowledge on the solution, based on the assumption that the object is homogeneous in composition. The regularization parameter is selected automatically using the L-curve corner criterion. The algorithm is applied to data acquired at the ESRF third generation synchrotron and the utility of the method, both for homogeneous and inhomogeneous objects, is shown.

### 5.4.1 Introduction

Three dimensional X-ray computed tomography (3D  $\mu$ -CT) is increasingly used in a wide range of applications, such as materials science, biomedical imaging and paleontology. In standard  $\mu$ -CT, images of the absorption shadow of an object are recorded for a number of projection angles, which are then used to reconstruct the 3D absorption index. However, many interesting samples cannot be imaged successfully using this modality, due to the lack of contrast.

It is known that X-ray phase contrast is up to  $10^3$  times more sensitive than absorption contrast in the hard X-ray region (Momose and Fukuda, 1995). With an X-ray beam of sufficient spatial coherency, a particularly simple phase contrast mechanism becomes available (Snigirev et al., 1995): when the X-ray detector is moved downstream from the imaged object (Fig. 5.7), a fringe pattern is formed on the detector. This pattern is due both to the phase shift and amplitude modulation induced by the object on the incident wave. Such patterns can be analyzed in the Fresnel diffraction formalism (Guigay, 1977), which establishes a quantitative relationship between both amplitude modulation and phase shift, and the recorded pattern, as the squared modulus of the Fresnel transform of the exit wave field.

Estimating the phase shift from recorded data is called phase retrieval. The retrieved phase shift can be used in conjunction with tomography to reconstruct the 3D refractive index. This process is called 3D phase contrast tomography or holotomography. In this case, the phase retrieval process is applied to a large number of projections acquired at different rotation angles, prior to standard tomographic reconstruction. Phase retrieval is a non-linear, ill-posed inverse problem. The non-linearity stems from the squared modulus and the ill-posedness from zero crossings in the transfer function associated with the Fresnel transform. The problem is similar to that which arises in coherent X-ray diffraction imaging (Miao et al., 1999; Marchesini et al., 2003), where a Fraunhofer diffraction pattern is recorded. There, it is instead the squared modulus of a Fourier transform which is recorded, and the non-linear inverse problem is generally solved iteratively (Gerchberg and Saxton, 1972; Fienup, 1982; Elser, 2003). This inversion technique is usually time consuming, requiring hundreds of iterations to converge, which could prove limiting in a tomographic setting, where the phase has to be retrieved at several, typically thousands, projection angles. This type of algorithms has also been adapted to Fresnel region phase retrieval but suffers from slow convergence and, due to the computational load, limited input image size (Allen and Oxley, 2001; Allen et al., 2004).

In the imaging problem considered here, the objective is to perform 3D holotomography, usually with large detector sizes, typically  $2048 \times 2048$  pixels. The methods to solve the Fresnel diffraction phase retrieval problem have therefore mainly been focused on achieving efficient algorithms, taking advantage of properties of the Fresnel transform to linearize the inverse problem. If the imaged object is strongly absorbing, if no additional assumptions are made (Turner et al., 2004), at least two images are needed for each projection angle, one in the contact plane to get the absorption, and one or several phase contrast images recorded at different distances. Notable algorithms designed in this way include the contrast transfer function (CTF) (Cloetens et al., 1999, 2002; Zabler et al., 2005), the transport of intensity (TIE) approach (Teague, 1982; Nugent et al., 1996; Paganin and Nugent, 1998; Gureyev et al., 1999; Paganin, 2006; Bronnikov, 2002) and mixed approaches between the two (Gureyev et al., 2004; Wu and Liu, 2003; Guigay et al., 2007). These assume either weak absorption (Cloetens et al., 1999, 2002; Zabler et al., 2005), weak and homogeneous absorption (Arhatari et al., 2007) or short propagation distances (Teague, 1982; Nugent et al., 1996; Paganin and Nugent, 1998; Gureyev et al., 1999; Turner et al., 2004; Paganin, 2006), however. The Mixed approach (Guigay et al., 2007) was developed to unify the TIE and CTF approaches, and requires less assumptions about the imaged object, namely that both the absorption and phase shift be slowly varying. While it is slightly more data and computation intensive, it has been shown to be more accurate and robust to noise (Langer et al., 2008).

Due to the ill-posedness of the problem, all the methods mentioned above require some form of regularization. Little has previously been mentioned about this problem in phase contrast tomography. A simple approach with a semi-empirical determination of the regularization parameter for the weak absorption case of the TIE (Bronnikov, 2002) was described in (Groso, Abela and Stampanoni, 2006).

In this paper we investigate regularization of the mixed approach described in (Guigay et al., 2007). We present the usual Tikhonov regularization (Tikhonov and Arsenin, 1977) and its limitations in this problem, and propose the use of the absorption contrast image as a prior based on a homogeneous composition assumption. Such assumptions have previously been introduced (Paganin et al., 2002; Turner et al., 2004; Arhatari et al., 2007; Wu et al., 2005), where it was included as a constraint on the refractive index, effectively reducing the number of unknowns to one. This is true for strictly homogeneously composed objects, and for heterogeneous objects if it is composed exclusively of light materials and the X-ray energy is in the range of 60-500 keV (Wu et al., 2005). Here it is included as prior knowledge on the phase shift, and introduced

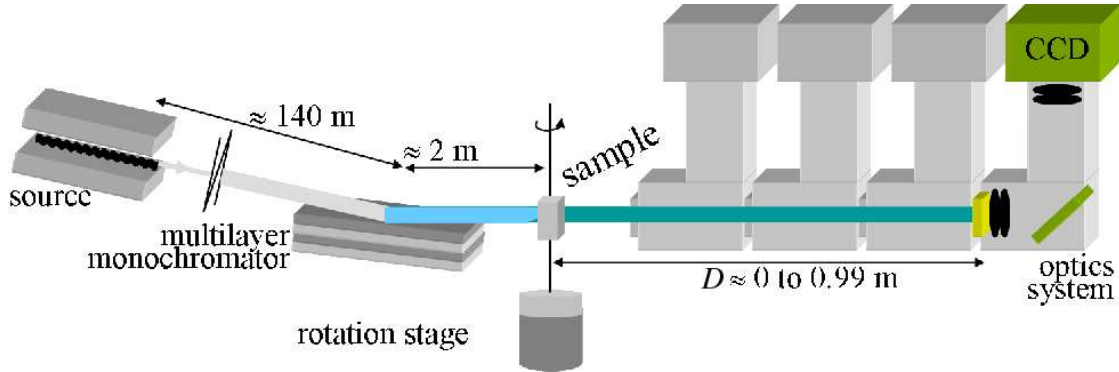


Figure 5.7: Schematic of the phase tomography setup. Partially coherent, monochromatic synchrotron X-rays are shone on a sample mounted on a rotation stage. The detector, a CCD camera coupled to a scintillating screen with conventional light optics, is mounted on a translation stage so that a series of images at different distances can be recorded.

as a regularization term in the minimization problem. We present a method for the automatic selection of the regularization parameter, based on the L-curve corner criterion (Hansen, 1992; Hansen and O’Leary, 1993). Other automatic schemes for finding optimal regularization parameters exist, most notably generalized cross-validation (GCV) (Golub et al., 1979). The L-curve criterion seems more robust however, both numerically and to the type of noise (Hansen, 1992; Hansen and O’Leary, 1993). The resulting phase retrieval algorithm is validated on experimental data, acquired using the  $\mu$ -CT setup at the ID19 beamline at the European Synchrotron Radiation Facility (ESRF), of a constructed phantom designed to evaluate the method.

#### 5.4.2 Direct problem: propagation based X-ray phase contrast

The image formation process in propagation based phase contrast imaging is well described in the framework of Fourier optics. If sufficiently coherent X-rays are used, when the detector is moved downstream of the object (Fig. 5.7), the image formed on the detector is not only due to absorption of X-rays in the object but also the phase shift induced by the object. This setup is known as propagation-based phase contrast or in-line holography (Gabor, 1948).

If the interaction between the wave and object is strong, the recorded intensity will contain both absorption and phase contrast (Fig. 5.8). The analysis of such images is

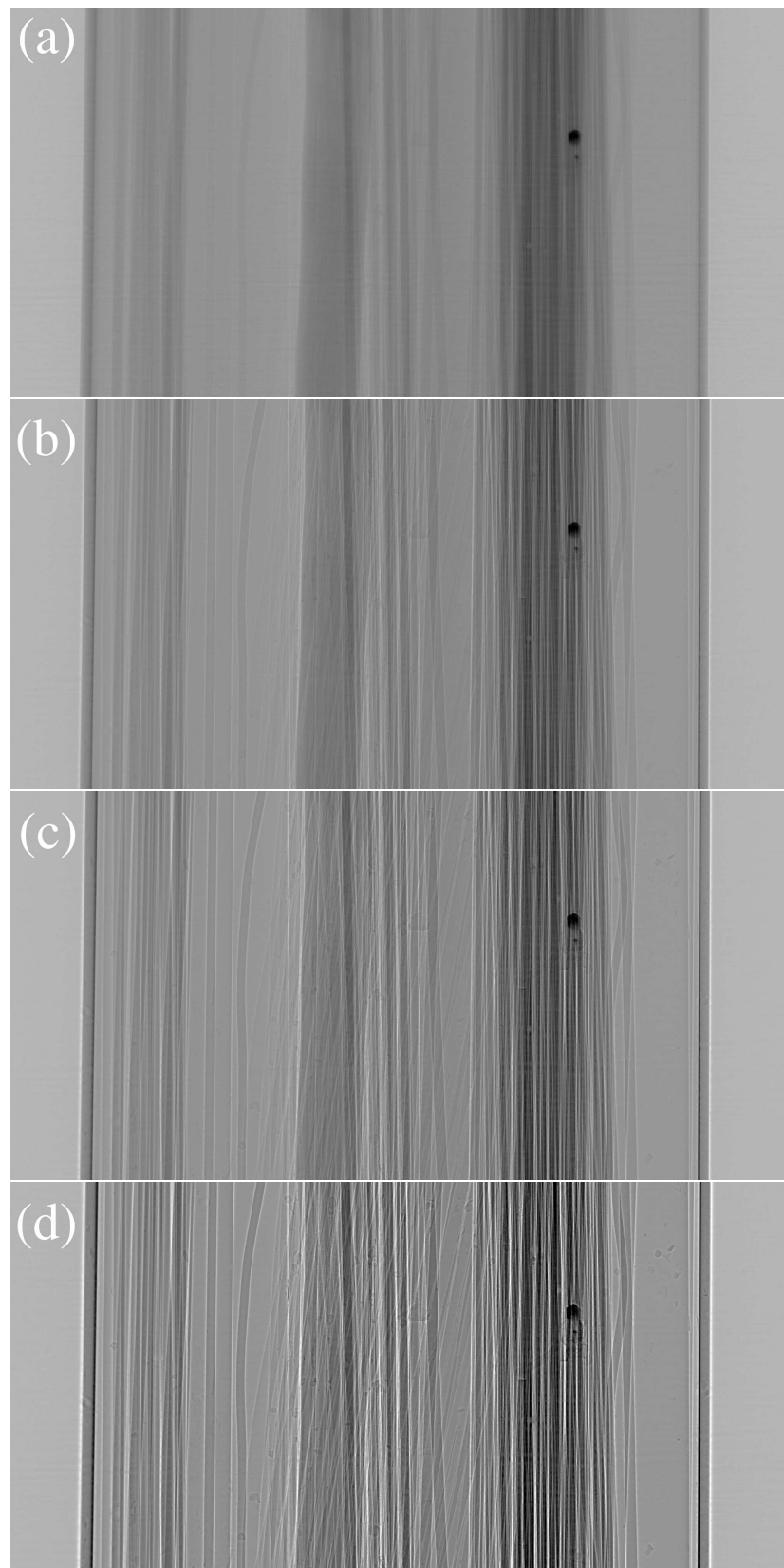


Figure 5.8: Absorption and phase radiographs recorded at different distances  $D$ . (a)  $D \approx 2$  mm (absorption contrast), (b)  $D = 10$  mm (absorption and phase contrast), (c)  $D = 20$  mm and (d)  $D = 45$  mm. The horizontal field of view is 1.43 mm.

described below.

#### 5.4.2.1 Wave-object interaction

The illuminated object is considered to be completely defined by its 3D complex refractive index distribution

$$n(x, y, z) = 1 - \delta_r(x, y, z) + i\beta(x, y, z), \quad (5.65)$$

where  $\delta_r(x, y, z)$  is the refractive index decrement,  $\beta(x, y, z)$  the absorption index and  $(x, y, z)$  the spatial coordinates. If beam propagation inside the object is not taken into account, which is the same as assuming a flat object (Born and Wolf, 1997), the wave-object interaction can be described by a transmittance function

$$u_0(\mathbf{x}) = T(\mathbf{x})u_{inc}(\mathbf{x}) \quad (5.66)$$

where

$$T(\mathbf{x}) = a(\mathbf{x}) \exp[i\varphi(\mathbf{x})] = \exp[-B(\mathbf{x}) + i\varphi(\mathbf{x})], \quad (5.67)$$

$u_{inc}(\mathbf{x})$  is the incident wave field,  $u_0(\mathbf{x})$  is the wave field at the exit plane of the object and  $\mathbf{x} = (x, y)$  is the spatial coordinate vector in the plane transverse to the beam propagation direction  $z$ . In the practical case, the recorded images have to be corrected for  $u_{inc}(\mathbf{x})$  by flat field correction. In the following however, the assumption  $u_{inc}(\mathbf{x}) = 1$  is made.

The absorption  $B(\mathbf{x})$  can be considered a projection through the absorption index

$$B(\mathbf{x}) = (2\pi/\lambda) \int \beta(x, y, z) dz \quad (5.68)$$

and the phase shift  $\varphi(\mathbf{x})$  is a projection through the refractive index decrement

$$\varphi(\mathbf{x}) = -(2\pi/\lambda) \int \delta_r(x, y, z) dz, \quad (5.69)$$

where  $\lambda$  is the wavelength. This means that if  $B(\mathbf{x})$  and  $\varphi(\mathbf{x})$  can be determined at a large number of projection angles,  $\beta(x, y, z)$  and  $\delta_r(x, y, z)$  can be reconstructed by a standard tomographic reconstruction algorithm such as filtered backprojection (FBP).

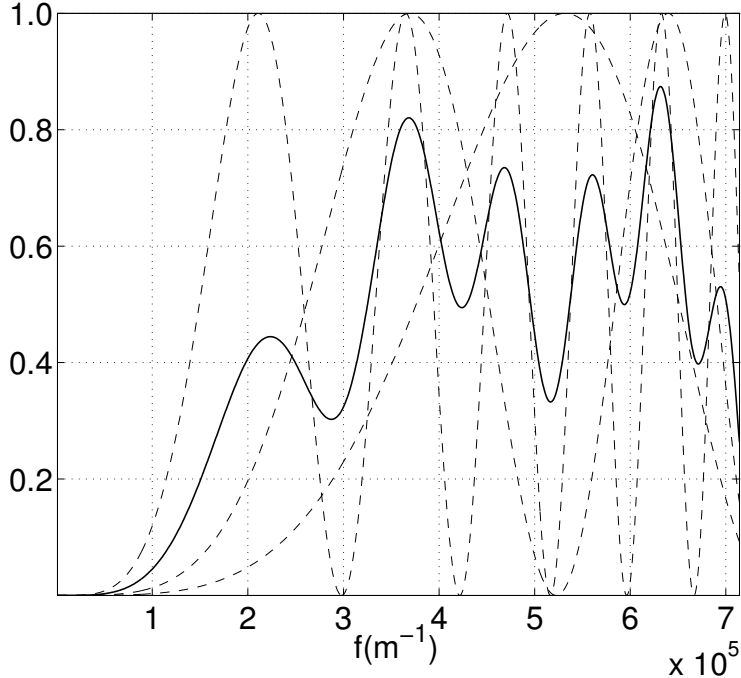


Figure 5.9: Plot of the normalized combined squared transfer function for in-line phase contrast imaging using four different distances (three propagation distances). The normalized squared transfer function  $A_D^2(\mathbf{f})$  to each distance is shown in dashed lines and the average is shown in solid. Note that the combined transfer function does not contain zeros, except at zero spatial frequency. Shown here is the optimal transfer function for the experimental conditions (wavelength and pixel size) presented.

#### 5.4.2.2 Contrast formation

If the wave field is allowed to propagate a distance  $D$  in free space after interaction with the object, the image formed on the detector is a diffraction pattern (Fig. 5.8). Since the propagation distances are small, the Fresnel approximation can be used. The recorded intensity at distance  $D$ ,  $I_D(\mathbf{x})$ , can therefore be written as the squared modulus of the Fresnel transform (Goodman, 2005)

$$I_D(\mathbf{x}) = |\mathbf{Fr}[\varphi, B, D](\mathbf{x})|^2 = |u_0(\mathbf{x}) * P_D(\mathbf{x})|^2 = |T(\mathbf{x}) * P_D(\mathbf{x})|^2, \quad (5.70)$$

where  $P_D(\mathbf{x})$  is the Fresnel propagator

$$P_D(\mathbf{x}) = \frac{1}{i\lambda D} \exp \left( i \frac{\pi}{\lambda D} |\mathbf{x}|^2 \right) \quad (5.71)$$

and  $*$  denotes convolution.

### 5.4.3 Inverse problem: phase retrieval

The problem of phase retrieval from  $N$  Fresnel diffraction images taken at different distances  $\{D_1, D_2, \dots, D_N\}$  can thus be written as

$$\varphi(\mathbf{x}) = \arg \min_{\varphi} \sum_D \|\mathbf{Fr}[\varphi, B, D](\mathbf{x})|^2 - I_D(\mathbf{x})|^2, D \in \{D_1, D_2, \dots, D_N\}. \quad (5.72)$$

The absorption is considered directly available in the object contact plane as

$$B(\mathbf{x}) = -\frac{1}{2} \ln(I_0(\mathbf{x})). \quad (5.73)$$

Defining the Fourier transform as

$$\tilde{g}(\mathbf{f}) = \mathcal{F}\{g\}(\mathbf{f}) = \int g(\mathbf{x}) \exp(-i2\pi\mathbf{x} \cdot \mathbf{f}) d\mathbf{x}, \quad (5.74)$$

where  $\mathbf{f} = (f_x, f_y)$  are the spatial frequency coordinates and  $\mathbf{x} \cdot \mathbf{f}$  denotes scalar product, the Fourier transform of Eq. 5.70 can also be written as (Guigay, 1977)

$$\tilde{I}_D(\mathbf{f}) = \int T\left(\mathbf{x} - \frac{\lambda D \mathbf{f}}{2}\right) T^*\left(\mathbf{x} + \frac{\lambda D \mathbf{f}}{2}\right) \exp(-i2\pi\mathbf{x} \cdot \mathbf{f}) d\mathbf{x}, \quad (5.75)$$

which will be used in the following.

#### 5.4.3.1 Linearization of direct problem

The Mixed approach (Guigay et al., 2007) is derived by first Taylor expanding  $T(\mathbf{x})$  with respect to the phase modulation only in the first step, which gives

$$\begin{aligned} \tilde{I}_D(\mathbf{f}) &= \int \exp(-i2\pi\mathbf{x} \cdot \mathbf{f}) a\left(\mathbf{x} - \frac{\lambda D \mathbf{f}}{2}\right) a\left(\mathbf{x} + \frac{\lambda D \mathbf{f}}{2}\right) \\ &\quad \times \left[ 1 + i\varphi\left(\mathbf{x} - \frac{\lambda D \mathbf{f}}{2}\right) - i\varphi\left(\mathbf{x} + \frac{\lambda D \mathbf{f}}{2}\right) \right] d\mathbf{x}. \end{aligned} \quad (5.76)$$

By developing the multiplication, Eq. (5.76) can be rewritten as a sum of integrals. Making the variable changes  $\mathbf{y} = \mathbf{x} - \lambda D\mathbf{f}/2$  and  $\mathbf{y} = \mathbf{x} + \lambda D\mathbf{f}/2$  respectively and rearranging yields

$$\begin{aligned}\tilde{I}_D(\mathbf{f}) &= \tilde{I}_D^{\varphi=0} + \sin(\pi\lambda D|\mathbf{f}|^2) \int a(\mathbf{x})\varphi(\mathbf{x}) \exp(-i2\pi\mathbf{x} \cdot \mathbf{f}) \\ &\quad \times [a(\mathbf{x} + \lambda D\mathbf{f}) + a(\mathbf{x} - \lambda D\mathbf{f})] d\mathbf{x} \\ &\quad + i \cos(\pi\lambda D|\mathbf{f}|^2) \int a(\mathbf{x})\varphi(\mathbf{x}) \exp(-i2\pi\mathbf{x} \cdot \mathbf{f}) \\ &\quad \times [a(\mathbf{x} + \lambda D\mathbf{f}) - a(\mathbf{x} - \lambda D\mathbf{f})] d\mathbf{x},\end{aligned}\tag{5.77}$$

where  $\tilde{I}_D^{\varphi=0}(\mathbf{f})$  is the intensity at distance  $D$  if there was no phase shift.

Assuming a slowly varying object, the approximations  $a(\mathbf{x} + \lambda D\mathbf{f}) + a(\mathbf{x} - \lambda D\mathbf{f}) \approx 2a(\mathbf{x})$  and  $a(\mathbf{x} + \lambda D\mathbf{f}) - a(\mathbf{x} - \lambda D\mathbf{f}) \approx 2\lambda D\mathbf{f} \cdot \nabla a(\mathbf{x})$  are made, which gives

$$\begin{aligned}\tilde{I}_D(\mathbf{f}) &= \tilde{I}_D^{\varphi=0}(\mathbf{f}) + 2 \sin(\pi\lambda D|\mathbf{f}|^2) \\ &\quad \times \int \exp(-i2\pi\mathbf{x} \cdot \mathbf{f}) \varphi(\mathbf{x}) a^2(\mathbf{x}) d\mathbf{x} \\ &\quad + i 2 \cos(\pi\lambda D|\mathbf{f}|^2) \lambda D\mathbf{f} \\ &\quad \cdot \int \exp(-i2\pi\mathbf{x} \cdot \mathbf{f}) \varphi(\mathbf{x}) a(\mathbf{x}) \nabla a(\mathbf{x}) d\mathbf{x}.\end{aligned}\tag{5.78}$$

This can be identified as

$$\begin{aligned}\tilde{I}_D(\mathbf{f}) &= \tilde{I}_D^{\varphi=0}(\mathbf{f}) + 2 \sin(\pi\lambda D|\mathbf{f}|^2) \mathcal{F}\{I_0\varphi\}(\mathbf{f}) \\ &\quad + \cos(\pi\lambda D|\mathbf{f}|^2) \frac{\lambda D}{2\pi} \mathcal{F}\{\nabla(\varphi \nabla I_0)\}(\mathbf{f}),\end{aligned}\tag{5.79}$$

which is valid for slowly varying objects. The advantage of this model is that it is valid for extended propagation distances and strong absorption, thus alleviating both the short propagation distance requirement of the TIE and the weak absorption requirement of the CTF. It also unifies these two approaches, as it approaches the TIE in the limit of small distances and the CTF in the limit of weak absorption (Guigay et al., 2007).

### 5.4.3.2 Inversion of the linearized problem

To solve Eq. 5.79 for the phase from images recorded at several distances, it is first observed that the term  $\varphi(\mathbf{x})\nabla I_0(\mathbf{x})$  can be rewritten as  $I_0(\mathbf{x})\varphi(\mathbf{x})\nabla \ln[I_0(\mathbf{x})]$ . By defining  $\psi(\mathbf{x}) = I_0(\mathbf{x})\varphi(\mathbf{x})$ , the Fourier transform of the intensity at distance  $D$  can be written as

$$\tilde{I}_D(\mathbf{f}) = \tilde{I}_D^{\varphi=0}(\mathbf{f}) + A_D(\mathbf{f})\tilde{\psi}(\mathbf{f}) + \Delta_D(\mathbf{f}) \quad (5.80)$$

with  $A_D(\mathbf{f}) = 2 \sin(\pi\lambda D|\mathbf{f}|^2)$  and  $\Delta_D(\mathbf{f}) = \cos(\pi\lambda D|\mathbf{f}|^2) \frac{\lambda D}{2\pi} \mathcal{F}\{\nabla[\psi\nabla \ln(I_0)]\}(\mathbf{f})$ .

To take several distances into account, Eq. 5.80 can be used to pose a linear least squares minimization problem

$$\tilde{\psi}(\mathbf{f}) = \arg \min_{\tilde{\psi}} \sum_D |A_D(\mathbf{f})\tilde{\psi}(\mathbf{f}) - [\tilde{I}_D(\mathbf{f}) - \tilde{I}_D^{\varphi=0}(\mathbf{f}) - \Delta_D(\mathbf{f})]|^2. \quad (5.81)$$

Due to the fact that  $A_D(\mathbf{f})$  goes to zero for small spatial frequencies, and the possibility of values close to zero at high spatial frequencies, the solution has to be regularized. Normally, standard Tikhonov regularization is used, where a term limiting the energy of the solution is added to the minimization problem. Eq. 5.81 then becomes

$$\begin{aligned} \tilde{\psi}(\mathbf{f}) = \arg \min_{\tilde{\psi}} \epsilon = & \sum_D |A_D(\mathbf{f})\tilde{\psi}(\mathbf{f}) - [\tilde{I}_D(\mathbf{f}) - \tilde{I}_D^{\varphi=0}(\mathbf{f}) - \Delta_D(\mathbf{f})]|^2 \\ & + \alpha |\tilde{\psi}(\mathbf{f})|^2. \end{aligned} \quad (5.82)$$

with  $\alpha$  a regularizing parameter. This minimization problem can be solved in an iterative fashion by considering  $\Delta_D(\mathbf{f})$  as a perturbation term, initializing the phase to

Table 5.2: Theoretical values for the absorption coefficient and refractive index at 20.5 keV X-ray energy for the materials used in the phantom.

|          | $4\pi\beta/\lambda$<br>( $cm^{-1}$ ) | $2\pi\delta_r/\lambda$<br>( $\times 100 cm^{-1}$ ) | $\delta/\beta$ |
|----------|--------------------------------------|--|----------------|
| Aluminum | 8.66                                 | 13.4   | 309            |
| Alumina  | 8.26                                 | 20.0   | 484            |
| PETE     | 0.761                                | 7.37   | 1936           |
| PP       | 0.353                                | 4.97   | 2817           |

zero and solving the linear least squares minimization problem in each iteration. This gives the solution as

$$\tilde{\psi}^{(n+1)}(\mathbf{f}) = \frac{\sum_D A_D(\mathbf{f}) [\tilde{I}_D(\mathbf{f}) - \tilde{I}_D^{\varphi=0}(\mathbf{f}) - \Delta_D^{(n)}(\mathbf{f})]}{\sum_D A_D^2(\mathbf{f}) + \alpha} \quad (5.83)$$

where  $\tilde{\psi}^{(n)}(\mathbf{f})$  is the phase-absorption intensity product at iteration  $n$  with  $\tilde{\psi}^{(0)}(\mathbf{f}) = 0$ .

Examining the denominator of Eq. 5.83, it is seen that the term  $\sum_D A_D^2(\mathbf{f})$  goes to zero for small spatial frequencies. When the propagation distance is increased, a number of zero crossings are also introduced (Fig. 5.9). It is the latter aspect of the direct problem that motivates the use of several propagation distances. The distances are chosen so that the sum of the squared sine factors give as good coverage in the Fourier domain as possible (Zabler et al., 2005).

## 5.4.4 Regularization

### 5.4.4.1 Phase-attenuation duality as prior

It has been observed that phase retrieval using Eq. 5.83 suffers from distortion in the low spatial frequency components. This is due to the fact that the transfer function is always small in the low spatial frequency range, even when several distances are combined (Fig. 5.9), thus making the phase retrieval sensitive to noise in the small spatial frequencies. This type of low frequency artifacts, usually visible as a varying background (Fig. 5.13), can be seen in X-ray phase retrieval (Allen and Oxley, 2001; Groso, Abela and Stampanoni, 2006; Groso, Stampanoni, Abela, Schneider, Linga and Müller, 2006; Arhatari et al., 2007; Langer et al., 2008) as well as in related fields such as transmission electron microscopy (Beleggia et al., 2004) and brightfield microscopy (Ali et al., 2008), where the same formalism can be applied.

To alleviate this problem, we propose the introduction of a prior on the retrieved phase, namely that the retrieved phase should be proportional to the absorption. This prior is based on the assumption that the object is homogeneously composed, that is made up of one or several materials with the same  $\delta/\beta$ -ratio. Since the absorption  $B(\mathbf{x})$  is available from the contact plane image (Eq. 5.73), this prior can be formulated as follows. First, a prior image is defined by multiplying a scaled version of the absorption with the absorption image. This is then low-pass filtered, eg. with a complementary error function ( $\text{erfc}(x) = \frac{1}{\sqrt{\pi}} \int_x^\infty \exp(-t^2) dt$ ), with a cut-off frequency  $f_c$  corresponding to the first maximum of the transfer function to the longest distance (Fig. 5.9). This

is to introduce the homogeneous object assumption only in the low frequency range. This gives

$$\tilde{\psi}_0(\mathbf{f}) = \operatorname{erfc}(f_r - f_c) \mathcal{F} \left\{ \frac{\delta}{2\beta} I_0 \ln(I_0) \right\}(\mathbf{f}). \quad (5.84)$$

with  $f_r = \sqrt{f_x^2 + f_y^2}$ .

We can now formulate the new minimization problem

$$\begin{aligned} \tilde{\psi}(\mathbf{f}) = \arg \min_{\tilde{\psi}} \sum_D & |A_D(\mathbf{f})\tilde{\psi}(\mathbf{f}) - [\tilde{I}_D(\mathbf{f}) - \tilde{I}_D^{\varphi=0}(\mathbf{f}) - \Delta_D(\mathbf{f})]|^2 \\ & + \alpha |\tilde{\psi}(\mathbf{f}) - \tilde{\psi}_0(\mathbf{f})|^2, \end{aligned} \quad (5.85)$$

which has the solution

$$\tilde{\psi}^{(n+1)}(\mathbf{f}) = \frac{\sum_D A_D(\mathbf{f})[\tilde{I}_D(\mathbf{f}) - \tilde{I}_D^{\varphi=0}(\mathbf{f}) - \Delta_D^{(n)}(\mathbf{f})] + \alpha \tilde{\psi}_0(\mathbf{f})}{\sum_D A_D^2(\mathbf{f}) + \alpha}. \quad (5.86)$$

This is solved iteratively in the same manner as above.

#### 5.4.4.2 Automatic parameter selection

To perform the inversion, two parameters have to be selected: the ratio  $\delta/\beta$  and the regularizing parameter  $\alpha$ . The  $\delta/\beta$  can usually be deduced from the main component of the sample, by knowing the composition either a priori or from chemical analysis. The regularization parameter  $\alpha$  has to be selected in a way to obtain a good trade off in the solution between fit to the data and fit to the prior knowledge.

For a general linear least squares problem  $x = \arg \min |Ax - b|^2 + \alpha|(x - x_0)|^2$ , where  $x_0$  is some a priori knowledge of the solution, the L-curve is defined as the log-log plot of the norm of the regularized solution  $x_\alpha$  to the prior,  $R(\alpha) = |(x_\alpha - x_0)|$ , against the corresponding residual norm  $M(\alpha) = |Ax_\alpha - b|$  as a function of all possible values of the regularizing parameter  $\alpha$ , yielding the parameterized plane curve

$$c(\alpha) = (\log_{10} |M(\alpha)|, \log_{10} |R(\alpha)|). \quad (5.87)$$

This curve gives information about the trade off in the regularized solution between the two quantities. The curve draws its name from the characteristic L-shaped corner

usually present in the curve, around which a small decrease in  $\alpha$  will increase  $R(\alpha)$  but not cause a significant change in  $M(\alpha)$  while a small increase in  $\alpha$  will increase  $M(\alpha)$  but will leave  $R(\alpha)$  unchanged. Finding the parameter value that yields the optimal trade-off between the two quantities is associated with finding the corner of the L-curve (Hansen, 1992), which can be defined as the point of maximum curvature. The curvature of a plane curve is defined as

$$\kappa(\alpha) = \frac{R'(\alpha)M''(\alpha) - M'(\alpha)R''(\alpha)}{(R'(\alpha)^2 + M'(\alpha)^2)^{3/2}}. \quad (5.88)$$

The L-curve for Eq. 5.85, then, is defined by taking the residual as

$$M(\alpha) = \sum_D |A_D(\mathbf{f})\tilde{\psi}_\alpha(\mathbf{f}) - [\tilde{I}_D(\mathbf{f}) - \tilde{I}_D^{\varphi=0}(\mathbf{f}) - \Delta_D(\mathbf{f})]| \quad (5.89)$$

and the regularizing term as

$$R(\alpha) = |\tilde{\psi}_\alpha(\mathbf{f}) - \tilde{\psi}_0(\mathbf{f})| \quad (5.90)$$

The curve is sampled at a set of parameter values  $\alpha_1 \alpha_2 \dots \alpha_n$ , which are fitted with a cubic spline plane curve. The curve is oversampled 10 times, and the regularization parameter is chosen corresponding to the point of maximum curvature according to Eq. 5.88.

#### 5.4.5 Experimental results

A constructed phantom was imaged at the ID19 long beamline at the European Synchrotron Radiation Facility. The small source size ( $25 \mu\text{m}$  vertical  $\times$   $135 \mu\text{m}$  horizontal, nominally) and long source to sample distance (145m) deliver a highly parallel beam with high spatial coherence. The images were acquired using 20.5 keV X-rays, produced by a wiggler and selected with a multilayer monochromator. Images were recorded using a FREION CCD camera (Labiche et al., 2007) with a  $2048 \times 2048$  pixels imaging chip. The effective pixel size was  $0.7 \mu\text{m}$  giving a field of view of 1.4 mm. Images were recorded at four sample to detector distances,  $D = (2, 10, 20, 45)$  mm.

The phantom was constructed from a glass capillary with a 1 mm inner diameter, filled with a single strand of  $125 \mu\text{m}$  Aluminum wire,  $20 \mu\text{m}$  Alumina fibers,  $200 \mu\text{m}$  Polyethylene Terephthalate (PETE) monofilaments and  $28 \mu\text{m}$  Polypropylene (PP)

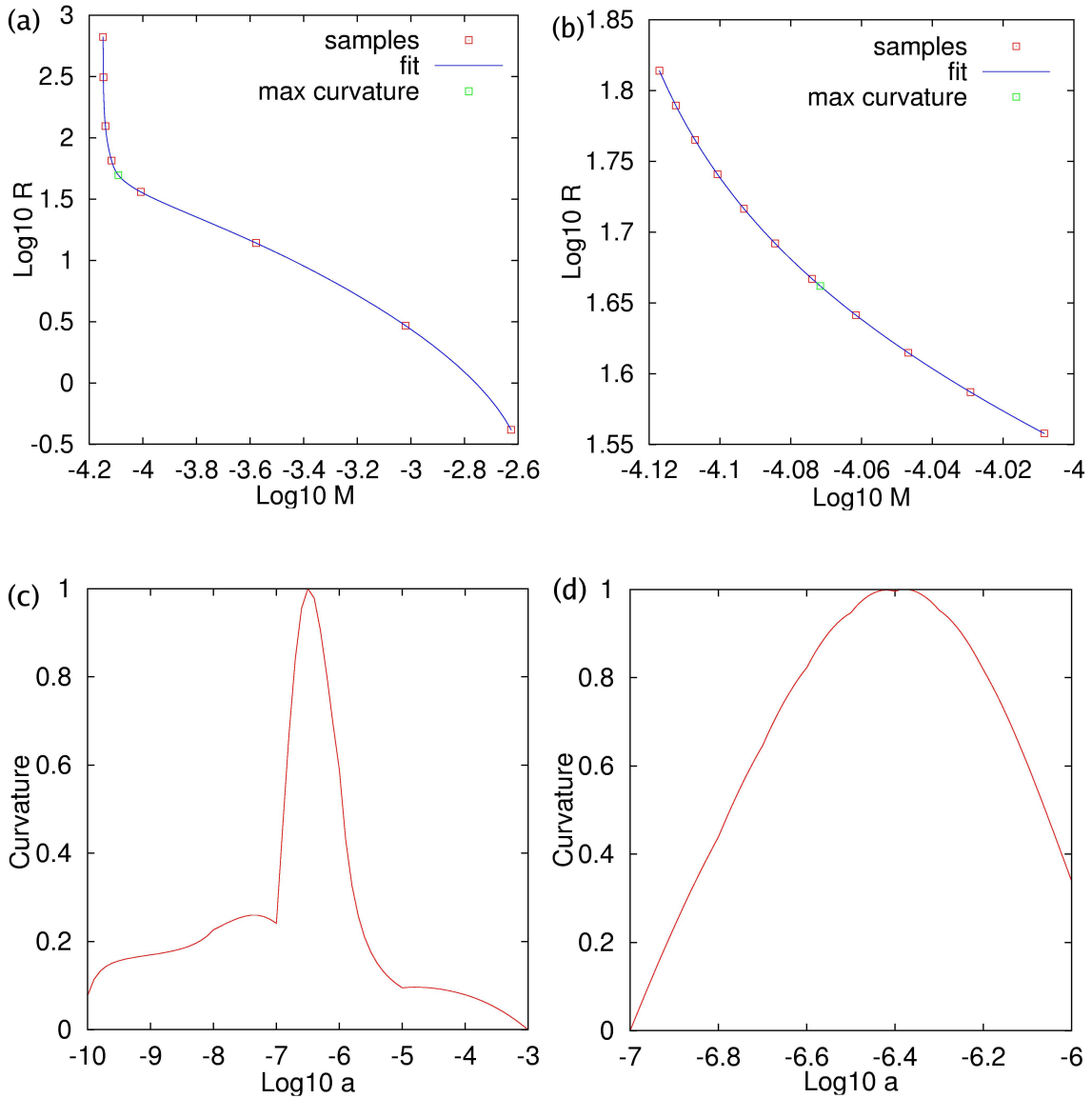


Figure 5.10: (a) L-curve for the regularized problem with  $\delta/\beta = 1936$ , corresponding to PETE. The L-curve was sampled for  $\alpha$ -values ( $10^{-10}, 10^{-9}, \dots, 10^{-3}$ ) and fitted with a cubic spline plane curve. The characteristic L-shape is clearly visible. The value of  $\alpha$  yielding the best trade off between fit to data and fit to prior corresponds to the corner of the curve, defined as the point of maximum curvature. (b) L-curve sampled around the corner, in the range ( $10^{-7}, 10^{-6.9}, \dots, 10^{-6.0}$ ). The point of maximum curvature is less obvious to the eye but is easily found numerically. (c) Plot of the normalized curvature to the regularizing parameter  $\alpha$  for the L-curve in (a). The apparent break in the curve is due to sampling the curve too sparsely. (d) Normalized curvature of the L-curve in (b).

fibers. The materials were chosen to have two strong absorbers with similar absorption coefficients and two light materials with similar absorption coefficients (Tab. 5.2). There is strong absorption contrast in the images (Fig. 5.8), 25% in the first plane, making the phase retrieval challenging.

The phase is retrieved using three different values of  $\delta/\beta$ : 0 (corresponding to the case in Eq. 5.82), the value corresponding to alumina and the value corresponding to PETE (Tab. 5.2). Reconstructed phases at one projection angle using these three values are shown in Fig. 5.11. This process is repeated for each projection angle. The  $\alpha$  parameter is determined as described in section 5.4.4.2 and is used for all projection angles. The L-curves and curvatures for the  $\delta/\beta = 1936$  case are shown in Fig. 5.10. The phase images are then used as input to the FBP algorithm to reconstruct the 3D refractive index decrement  $\delta_r$ .

Fig. 5.12 shows a tomographic slice reconstructed using the absorption images. The light materials are just about visible (they are visually enhanced by phase contrast due to the slight propagation over 2 mm in the first plane), and no contrast between aluminum and alumina is distinguishable. This is confirmed in the histogram, where there is only one peak corresponding to background and light materials, and one peak corresponding to the dense materials.

In Fig. 5.13, a tomographic slice reconstructed using phase maps retrieved with Tikhonov regularization (Eq. 5.82) is shown. The reconstruction shows strong low frequency noise. Note that the propagation distances were chosen purposefully (too short) to exaggerate this effect. While the different components are visible by eye, they are not well separated in the histogram, indicating that quantitative analysis would hardly be possible.

A tomographic slice reconstructed using the homogeneous object prior (Eq. 5.85) is shown in Fig. 5.14. The  $\delta/\beta$  ratio was set corresponding to alumina (Tab. 5.2). The low frequency noise is remedied, and values in the areas corresponding to alumina are correctly reconstructed. The contrast compared to aluminum, however, is inverted, and in the lighter materials, where the  $\delta/\beta$  ratio is chosen too low, there are ringing artifacts. In the histogram, two peaks for the denser materials are now visible. The lighter materials are now also visible in the histogram, but not distinguishable from each other.

Another slice reconstructed using the homogeneous object prior is shown in Fig 5.15.  $\delta/\beta$  was this time set to correspond to PETE (Tab. 5.2). The values in the regions corresponding to the PETE filaments are correctly reconstructed, while in the denser

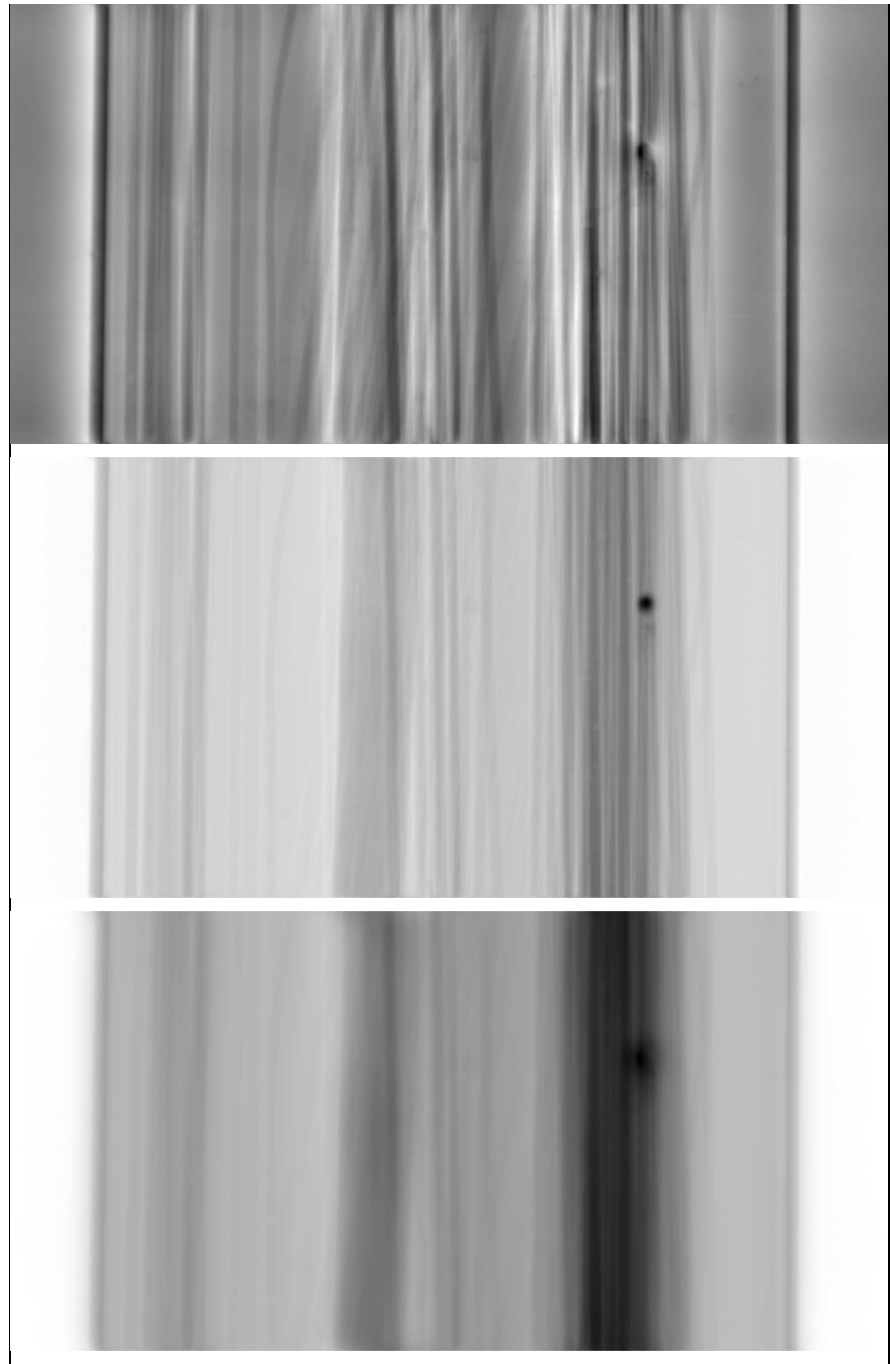


Figure 5.11: Phase maps at  $\theta = 0$  reconstructed using (a)  $\delta/\beta = 0$  (Eq. 5.82) (b)  $\delta/\beta = 484$ , corresponding to Alumina (Eq. 5.86, and (c)  $\delta/\beta = 1936$ , corresponding to PETE.

areas, where the  $\delta/\beta$  value is too high, the values are overestimated. In the histogram, two peaks corresponding to the light materials are visible, while the dense parts are stretched out over a wide range.

From these regularized reconstructions, the different materials can be segmented. A 3D display of a segmentation of the reconstructed volume done with a  $\delta/\beta$ -ratio corresponding to alumina is shown in Fig. 5.16.

#### 5.4.6 Discussion and conclusion

In this paper we have proposed a regularized framework for phase retrieval in holotomography. Previous implementations have been shown to suffer from noise in the low frequency range (Fig. 5.13, (Allen and Oxley, 2001; Beleggia et al., 2004; Groso, Stampanoni, Abela, Schneider, Linga and Müller, 2006; Groso, Abela and Stampanoni, 2006; Arhatari et al., 2007; Langer et al., 2008)). To counter this problem, a prior term was introduced, based on the assumption that the imaged object is of homogeneous composition. This term solves the low frequency problem (Fig. 5.14, 5.15), which facilitates quantitative analysis, but is only strictly quantitative if the object is homogeneously composed.

We proposed to use the L-curve for regularization parameter selection. The algorithm is automatic and does not need user input. The general composition of the sample is assumed to be known, however. The utility of the method, both for homogeneous and non-homogeneous objects was demonstrated by imaging a constructed phantom. Due to the high sensitivity, and robustness achieved by the method, several applications ranging from paleontology and materials science to medical imaging, are foreseen.

Modifications for homogeneous objects have previously been introduced for the TIE (Turner et al., 2004; Paganin et al., 2002; Arhatari et al., 2007) and CTF (Turner et al., 2004) methods. There, the homogeneous object assumption was introduced directly in the contrast formation model as a constraint on the phase, effectively reducing the number of unknowns to one. Here, the homogeneous composition assumption is instead seen as prior knowledge on the low-frequency content of the phase solution. This is a less strict condition, in the sense that the retrieved phase is allowed to differ from strict proportionality to the absorption.

The reconstructions obtained with the proposed method are better than the ones obtained with standard Tikhonov regularization, in the sense that the strong low-frequency noise (Fig. 5.13) is alleviated. However, in the reconstructed volumes, the

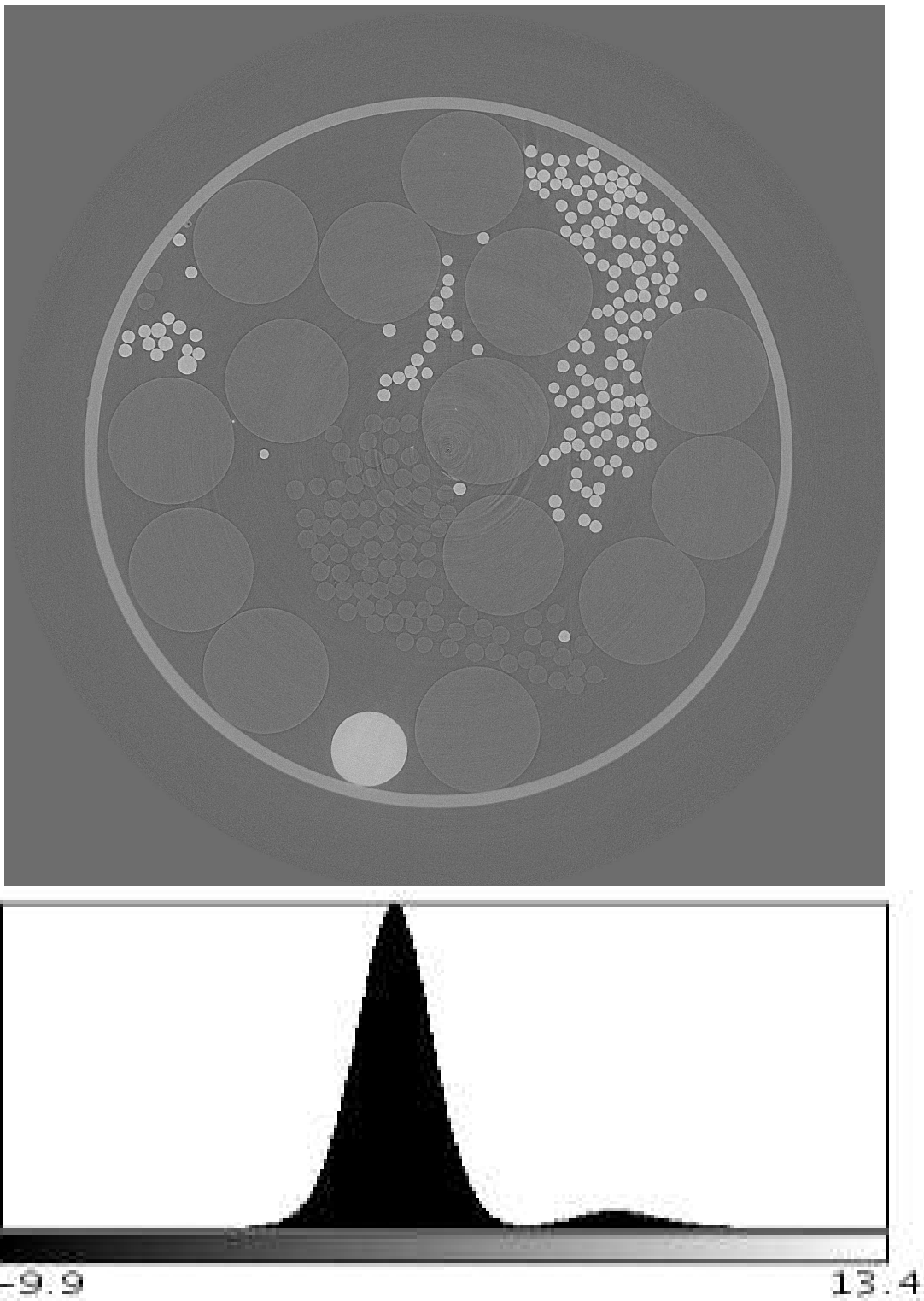


Figure 5.12: Tomographic slice and histogram of  $\mu = \frac{4\pi\beta}{\lambda}$  of the phantom reconstructed using the absorption images. The dense materials are not distinguishable from each other and the contrast in the light materials is weak. The negative values are due to noise and phase contrast present because of the short propagation in the first distance ( $D = 2$  mm). The peak corresponding to the denser materials is at  $6.24 \text{ cm}^{-1}$ . The theoretical values are given in Tab. 5.2.

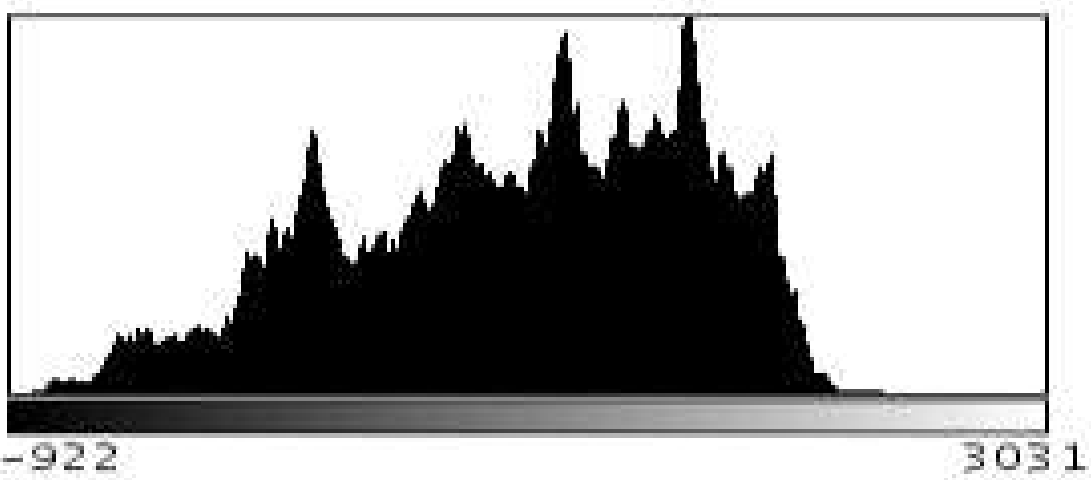
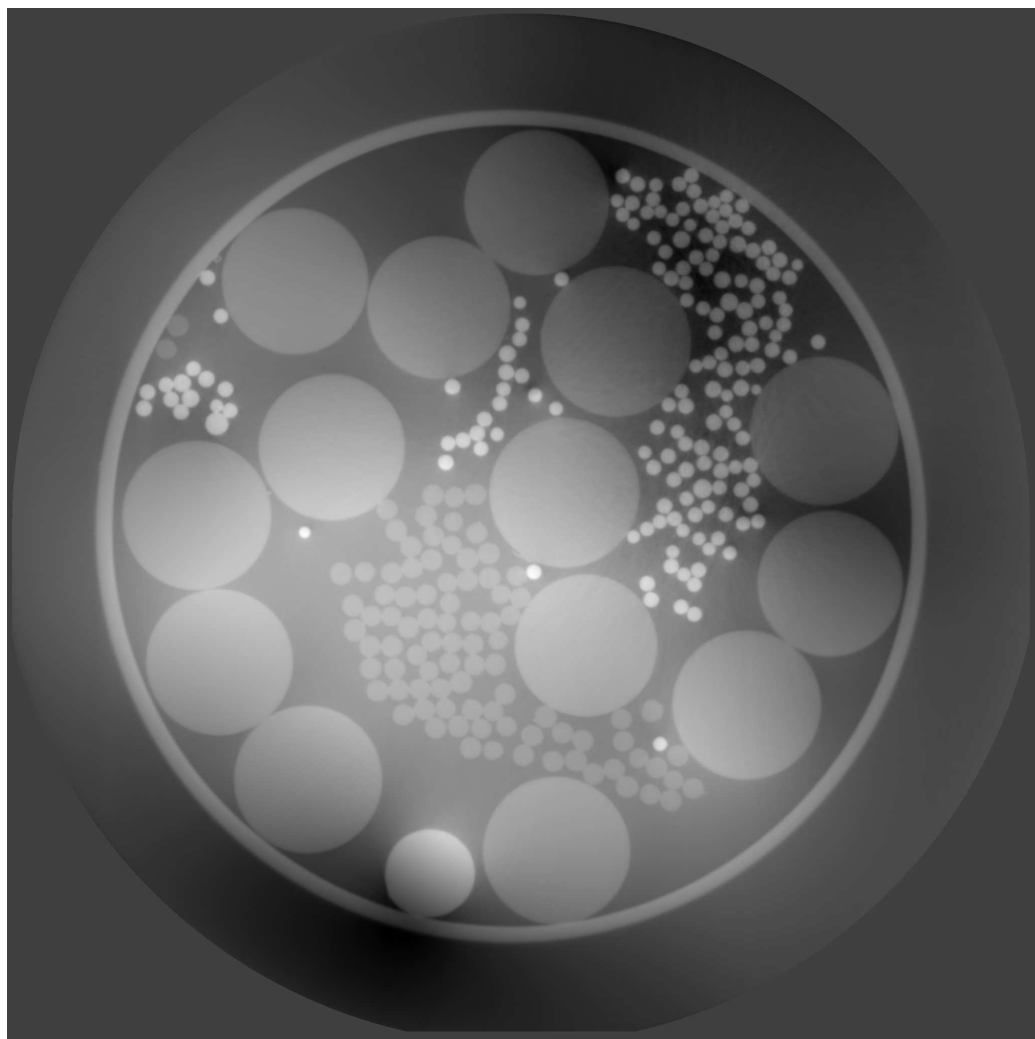


Figure 5.13: Tomographic slice and histogram of  $\frac{2\pi\delta_r}{\lambda}$  of the phantom reconstructed using Tikhonov regularized phase maps. Low-frequency noise makes quantitative analysis and segmentation difficult.

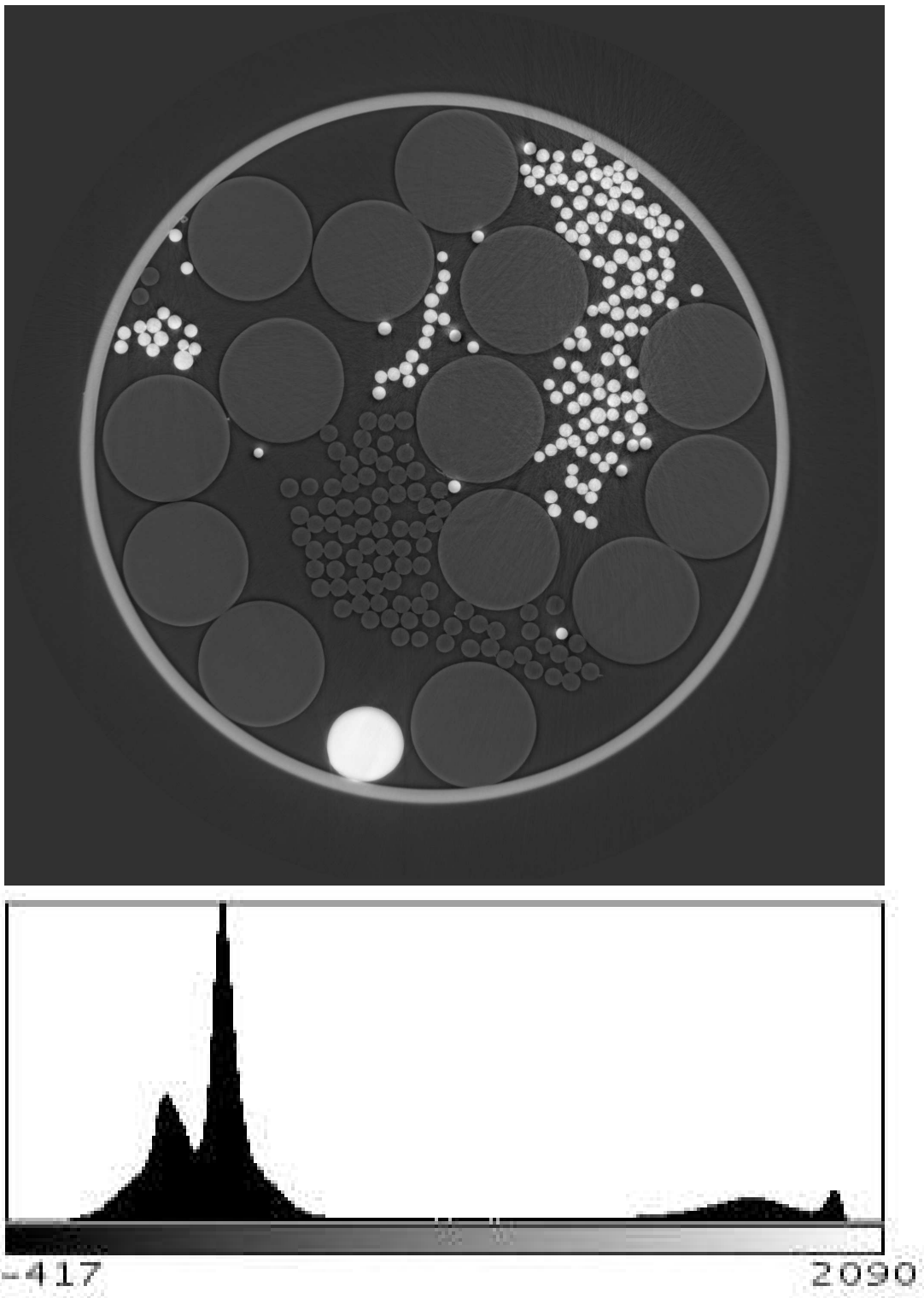


Figure 5.14: Tomographic slice and histogram of  $\frac{2\pi\delta_r}{\lambda}$  of the phantom, reconstructed using the  $\delta/\beta$  homogeneous composition prior. A ratio  $\delta/\beta = 484$ , corresponding to alumina was chosen. The low frequency noise is alleviated and values corresponding to alumina are well reconstructed. There is also sufficient contrast in the light materials to distinguish them from the background, but not from each other. The peaks are at 2050 (in the Aluminum), 1747 (Alumina) and 1028 (soft parts).

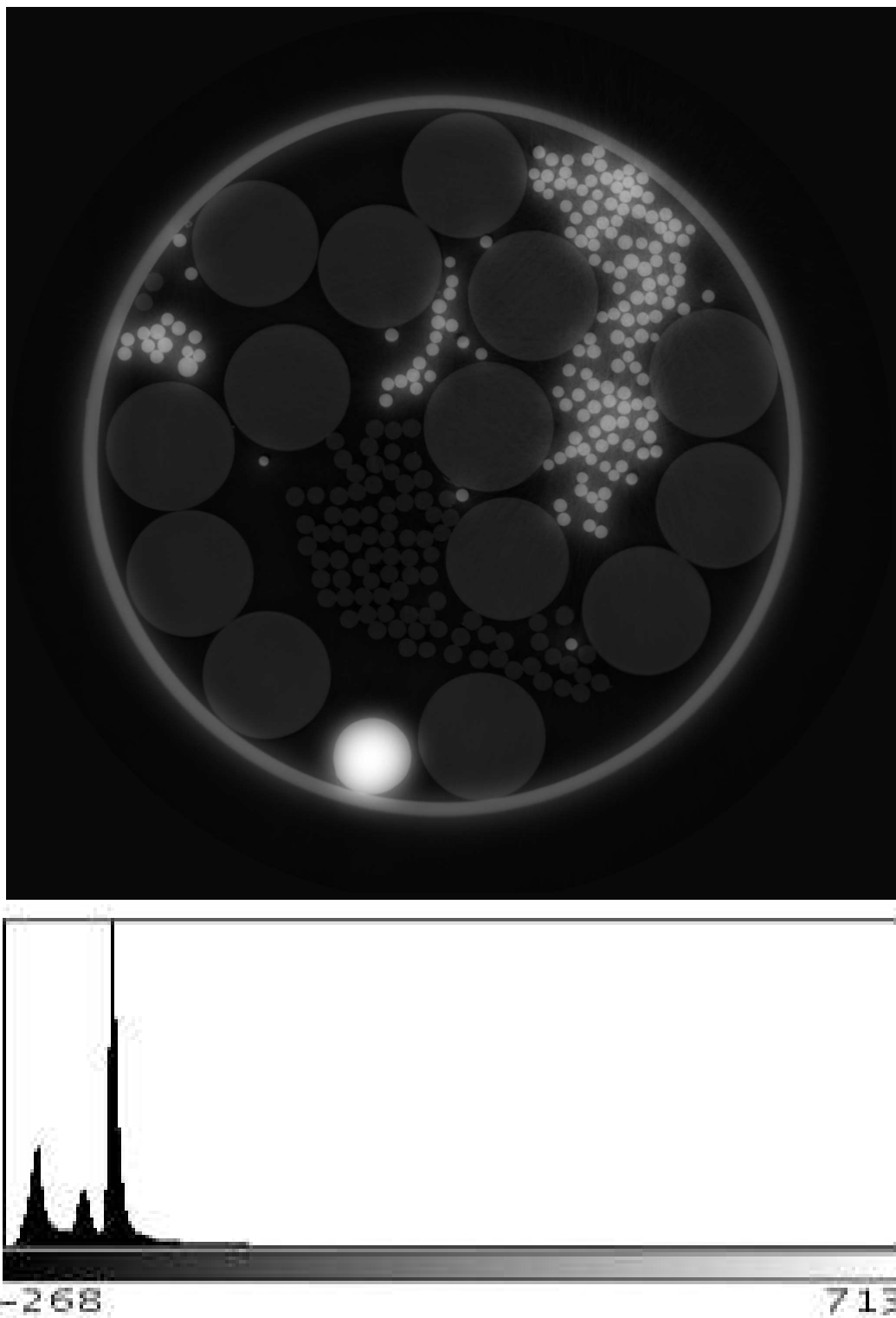


Figure 5.15: Tomographic slice and histogram of  $\frac{2\pi\delta_r}{\lambda}$  of the phantom, reconstructed using  $\delta/\beta = 1936$ , corresponding to PETE. Values corresponding to PETE are correctly reconstructed and the two materials are clearly distinguishable in the histogram. The peaks are at 387 (PP) and 617 (PETE).

values seem always underestimated. This is observed in the absorption tomogram as well, however, and the reconstruction errors are in the same range for the both techniques. This is probably due to the detector point spread function. The presented reconstructions suggest several ways to apply the present algorithm. In the case of a dense, homogeneous or nearly homogeneous object, the algorithm provides accurate, quantifiable reconstructions. In the case of an object consisting both of dense and light materials, two options are available. In many cases it would be enough to resolve the lighter parts, such as soft tissue, without distinguishing small density variations.  $\delta/\beta$  would then be chosen to correspond to the denser structures. If it is desirable to resolve contrast in several density regions, two or more reconstructions could be done, with different values of  $\delta/\beta$ . The different parts of the object could then be analyzed separately. Priors could also be applied to the reconstructed volume, but would require iterative forward and back-projection, since only projection images are available.

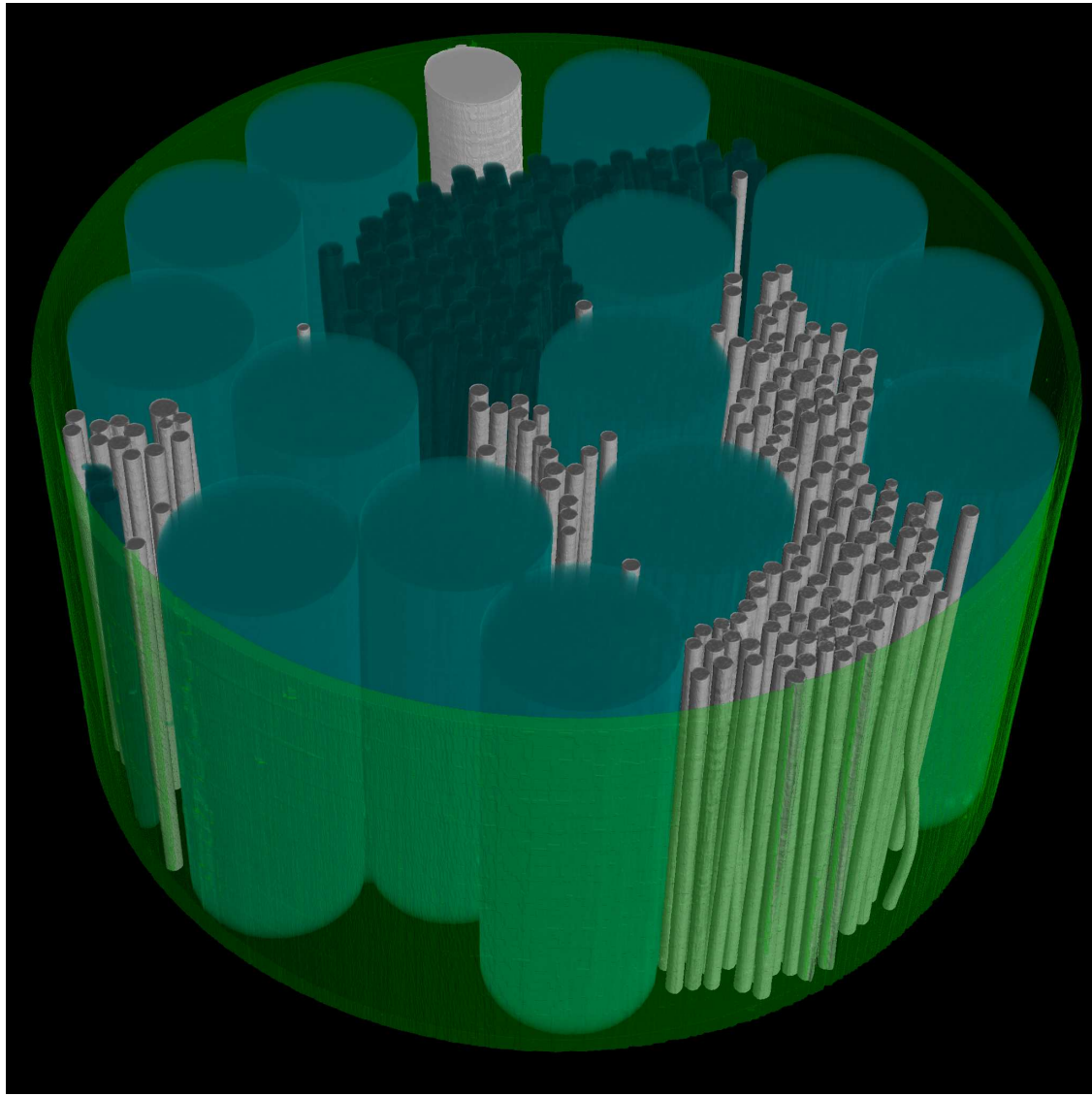


Figure 5.16: Segmented 3D rendering of the phantom, reconstructed using a  $\delta/\beta$ -ratio corresponding to alumina. Aluminium is shown in white, alumina in grey, PETE in light blue, PP in dark blue and the capillary in green.



# Chapter 6

## Applications

One of the main goals of this work was to develop and implement methods that are truly useful for scientific study. The regularized phase retrieval method presented in Section 5.4 has been applied in biological imaging, bone research, tissue engineering, paleontology and materials science. In these fields, the imaging problem often fits well into the assumptions of our method, namely strong absorption and almost homogeneous composition, and we foresee a continued application in these fields. We present here the two most mature applications. In the first, the application of our method to the study of a fossil allowed the discovery of the first known preserved brain. In the second, it allowed the imaging and quantitative analysis of a lowly mineralized pre-bone deposit in in-vitro grown bone scaffolds for tissue engineering.



## 6.1 Paleontology

### Skull and brain of a 300 million-year-old chimaeroid fish revealed by synchrotron holotomography

Alan Pradel, Max Langer, John G. Maisey, Didier Geffard-Kuriyama, Peter Cloetens,  
Philippe Janvier and Paul Tafforeau

Submitted to:

Proceedings of the National Academy of Sciences of the USA, PNAS

22 July 2008

Living cartilaginous fishes, or chondrichthyans, include numerous elasmobranch (sharks and rays) species, but only few chimaeroid (ratfish) species. The early history of chimaeroids and the modalities of their divergence from elasmobranchs are much debated (Zangerl, 1981). During Carboniferous times, 358-300 million years (Myr) ago, they underwent a remarkable evolutionary radiation, with some odd and poorly understood forms, including the enigmatic iniopterygians that were known until now from poorly informative flattened impressions (Zangerl and Case, 1973). Here we report the first iniopterygian skulls found preserved in three dimensions (3D) in about 300 Myr-old concretions from Oklahoma and Kansas. The study was performed using conventional Xray microtomography ( $\mu$ CT) as well as absorption based synchrotron microtomography (SR- $\mu$ CT) (Tafforeau et al., 2006) and a new holotomographic approach, and revealed their peculiar anatomy. Iniopterygians also share unique characters with living chimaeroids, suggesting that the key chimaeroid skull features were already established 300 Myr ago. Moreover, SR- $\mu$ CT of an articulated skull revealed exceptionally preserved parts of the brain itself. This was imaged with exceptional accuracy using holomography, demonstrating its great potential to image preserved soft parts in dense fossils. This is the first evidence of a fossilized vertebrate brain and demonstrates a remarkable size discrepancy between the brain and the surrounding brain cavity in iniopterygians.

### 6.1.1 Introduction

Iniopterygians have been described on the basis of partly articulated specimens preserved as impressions in the 310 Myr-old Carboniferous (Late Pennsylvanian) black shale of northern USA (Zangerl and Case, 1973). These fossils show two main chondrichthyan characteristics: a fragile layer of prismatic calcified cartilage lining the endoskeletal elements, and pelvic claspers (special copulation organs). Iniopterygians display a very odd morphology, such as dorsally inserted pectoral fins and complex tooth setting (Zangerl and Case, 1973; Zangerl, 1981; Stahl, 1999; Grogan and Lund, 2004) (Fig. 6.1A). All iniopterygians described until now were flattened specimens which do not allow 3D reconstructions, although studies based on stereographic radiographs have suggested the presence of chimaeroid-like characteristics (Zangerl and Case, 1973; Stahl, 1999). All other iniopterygians described since then have also been flattened specimens (Zangerl, 1981), and the detailed anatomy of the group has remained largely unknown. However, among the numerous 300 Myr-old fish-bearing concretions from the Pennsylvanian sites of Oklahoma and Kansas (see Materials and methods), most of which yield braincases of palaeonisciforms (ray-finned fishes) (Poplin, 1974), some have turned out to contain chondrichthyan remains. Some three-dimensional (3D) preserved skulls and associated postcranial elements have been attributed to iniopterygians, as evidenced by their jaw shape, characteristic tooth whorls, and star- or horn-shaped scutes covering their head (Fig. 6.1B-E). Mechanical preparation coupled with conventional X-ray microtomography ( $\mu$ CT) (see Supporting online information), absorption based synchrotron microtomography (SR- $\mu$ CT) and SR holotomography (Tafforeau et al., 2006; Cloetens et al., 1999, 2006; Guigay et al., 2007) (see Materials and methods) of the best preserved specimens now provides the first complete reconstructions of the skull of these chondrichthyans and supports previous insights that, despite their very peculiar characters, they are close relatives of living chimaeroids (Figs. 6.1, 6.2, and see supporting online information, Videos 1 and 2).

### 6.1.2 Results

The iniopterygian skulls from Oklahoma and Kansas are very similar to those of *Sibyrhynchus* (Zangerl and Case, 1973) in the shape of the jaw and scutes (Figs. 6.1A, E, 6.2C, D). In dorsal view, they show much the same outline as those of *S. denisoni* from the Indiana black shale (Zangerl and Case, 1973). They have very large orbits, bordered posteriorly and ventrally by an expanded postorbital wall and a suborbital shelf, but the braincase is significantly deeper than previously supposed (Zangerl and

Case, 1973; Zangerl, 1981; Stahl, 1999). Anterior to the orbits is a pair of small, cup-shaped nasal capsules connected to the brain cavity by narrow canals for the olfactory tracts (Figs. 6.1F, 6.2H, L). In front of the olfactory capsules, the braincase is prolonged by a rectangular cartilage plate bearing a transverse series of grooves that housed tooth families or tooth whorls (Figs. 6.1E, 6.2D). Large serrated teeth are also attached directly to the braincase floor, medially to the suborbital shelf (Fig. 6.2D). Posterior to the postorbital wall, the ventral part of the braincase is surprisingly narrow (Figs. 6.1H, 6.2F). It has a deep median ridge containing canals for the spinal cord and the notochord, and is flanked by very deep postorbital depressions that accommodated either jaw musculature or gills (Fig. 6.2F). Dorsal to these depressions are the otic capsules, which are extremely shallow and have small utricular cavities and vertical and horizontal semicircular canals almost in the same plane (Fig. 6.2L, N). Such a condition is otherwise found only in the strongly flattened braincases of certain placoderms (extinct armoured fishes) (Stensiö, 1969; Goujet, 1984). The brain cavity is straight and relatively narrow, but extends all along the braincase floor (Fig. 6.2H). The skull is thus platybasic, as in modern chimaeroids (Jollie, 1962; Briggs, 2003), despite the very large size of the orbits. Some of the canals for cranial nerves can be identified (Figs. 6.1F, 6.2C), notably for the glossopharyngeus and vagus. These exit from the braincase in much the same way as in modern chimaeroids; that is, there is no underlying hypotic lamina, by contrast to elasmobranchs (Briggs, 2003; Coates, 1999; Didier, 1995).

The lower jaw is massive, duck bill-shaped, with a fused symphysis that bears the same ridges (and presumably the same kind of tooth families) as the anterior plate of the braincase. It articulates with the braincase at the level of the posteroventral corner of the orbital margin (Fig. 6.2C, D). There is thus no evidence of an independent palatoquadrate, as in modern chimaeroids. Behind the postorbital wall are a number of elements belonging to the gill skeleton, the shoulder girdle and pectoral fin (Fig. 6.1I).

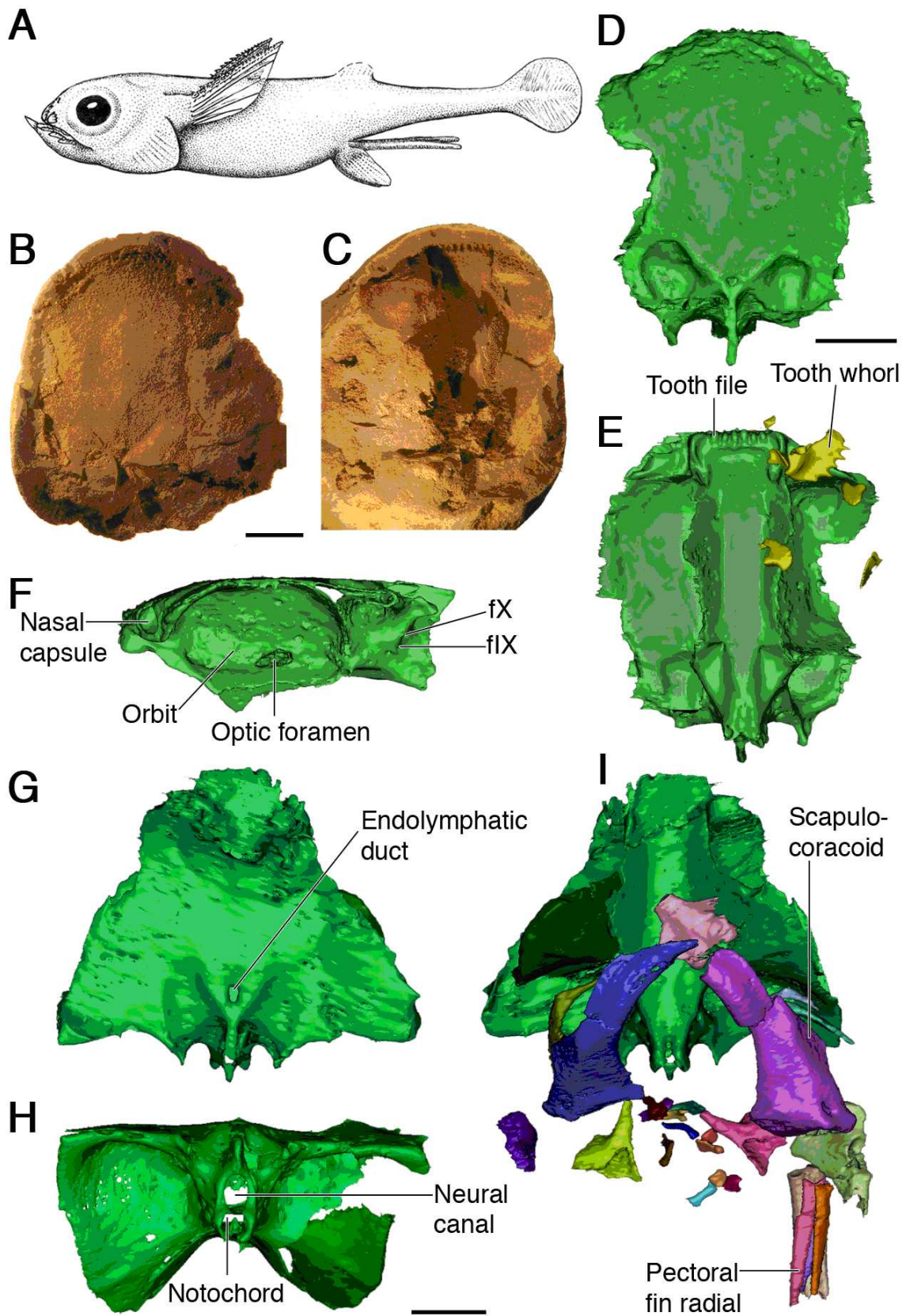


Figure 6.1: The anatomy of iniopterygians, 300 Myr-old chimaeroid-related cartilaginous fish. A, Reconstruction of *Sibyrhynchus denisoni* (not to scale). B,C, Part (B) and counterpart (C) of a phosphatic nodule from the Pennsylvanian of Oklahoma (AMNH OKM38) containing the braincase and shoulder girdle of *Sibyrhynchus* sp. D-F, 3D reconstruction of the same specimen, obtained from conventional X-ray CT images, showing the braincase in dorsal (D), ventral (E) and lateral (F) view, with associated teeth. G-I, 3D reconstruction of the braincase, shoulder girdle and pectoral fin elements of a sibyrhynchid iniopterygian from the Pennsylvanian of Kansas (KUNHM 21894), based on SR- $\mu$ CT images. Braincase in dorsal (G), posterior (H), and ventral views, with articulated shoulder girdles and pectoral fin radials (I). Scale bars = 5 mm. Abbreviations: f.IX, f.X, foramina for glossopharyngeus and vagus nerves.

In one of the articulated iniopterygian skulls, preserved in an unweathered concretion, absorption SR- $\mu$ CT revealed a peculiar structure inside the brain cavity, denser than the surrounding infill of crystalline calcite (Fig. 6.2I-K). We used a new holotomographic approach adapted to absorbing objects (Guigay et al., 2007) in order to resolve this structure in detail. It is a paired, symmetrical and elongated object which projects towards the optic foramina and more posterior foramina, probably for the oculomotorius nerve (Fig. 6.2J, M, N). It also shows two hollow dorsal lobes and, ventrally, a large median swelling (Fig. 6.2J, P, Q). It is continued by an axial posterior prolongation that fades away just before reaching a break through the specimen. The three-dimensional reconstruction of this object is strikingly suggestive of part of an actual brain, showing the optic tectum of the midbrain, the cerebellum, the hypophysial region, the rhombencephalon and spinal chord, the optic tracts, and the oculomotorius nerve (Fig. 6.2O-Q; see Supporting online information and Videos 1 and 2). Yet, there seems to be no trace left of the forebrain, apart from a vague anterior blade-shaped prolongation on one side only. We assume that this was extremely thin and elongated, as in modern chimaeroids (Jollie, 1962). Since the specimen is unique and this brain-like structure remains largely inaccessible, we have only a few hints about its nature. Microprobe analyses in areas where the brain-like structure reaches the surface of the specimen were performed revealed a high concentration of calcium phosphate, whereas the surrounding calcite is almost pure calcium carbonate (see Supporting online information). The object's shape, symmetry and relations to the nerve canals strongly suggest that it is an exceptionally preserved trace of the actual brain rather than a fortuitous artefact. It is possible that the brain underwent microbially induced phosphatization shortly before decay (Briggs, 2003) (the environment being probably saturated with calcium phosphate, hence the concretions). It could have been rapidly surrounded by diagenetic calcite, which preserved it in its almost natural position. Some shrinking of the tissues may have occurred before phosphatization, which is suggested by the position of the cerebellum far anterior to the otic capsule (Briggs, 2003). If our interpretation is correct, it is the first example of an exceptionally preserved Palaeozoic vertebrate brain, apart from an ambiguous case in a Carboniferous ray-finned fish (Coates, 1999). Assuming that the brain is preserved in this specimen, even allowing for post-mortem shrinking, its size and shape probably did not reflect that of the brain cavity, as in many modern elasmobranchs but unlike in living chimaeroids and some early ray-finned fishes (Jollie, 1962). However, the position of the iniopterygian midbrain relative to the olfactory capsules suggests the presence of a very elongate telencephalon, as in chimaeroids (Jollie, 1962; Didier, 1995).

### 6.1.3 Discussion

Iniopterygians were first classified among the Subterbranchialia, corresponding to all chondrichthyans (including living chimaeroids) having gill arches situated beneath the braincase instead of extending behind it, as in sharks (Zangerl, 1981). However, this condition is also observed in osteichthyans (bony fishes) and placoderms (armoured jawed vertebrates) and is thus likely to be a primitive condition for jawed vertebrates (Janvier, 1996). This character alone cannot then support the chimaeroid affinity of iniopterygians. In recent chondrichthyan phylogenies including fossils, iniopterygians are either overlooked, or turn up in unresolved positions, though generally as stem chimaeroids (Stahl, 1999; Grogan and Lund, 2004; Janvier, 1996).

The earliest undisputed chimaeroids are early Triassic (250 Myr) in age (Stahl, 1999), but in addition to iniopterygians a number of Palaeozoic taxa, notably the "bradyodonts" and echinochimaerids are also considered as stem chimaeroids because they share with the latter at least some derived characters (e.g., tubular dentine, prepelvic clasper) (Stahl, 1999; Grogan and Lund, 2004; Patterson, 1965). By contrast, previously described iniopterygian material did not show such characters. The material described here now demonstrates that, despite numerous specializations, iniopterygian skull anatomy is basically chimaeroid-like. No three-dimensionally preserved skull of any fossil chimaeroid (or a supposedly chimaeroid-related taxon) was known to date, and all data used for reconstructing basal chimaeroid relationships were inferred from more or less flattened specimens or from tooth histology (Stahl, 1999; Grogan and Lund, 2004; Patterson, 1965; Maisey, 1984). In contrast, some early elasmobranch and possible stem chondrichthyan skulls are now known in detail, notably thanks to CT-based studies (Maisey, 2007, 2001, 2005). These iniopterygian skulls now provide means for a comparative study of skull anatomy in Palaeozoic representatives of the main two chondrichthyan groups, and hints at an early appearance of chimaeroid specializations, possibly in the early Devonian.

## Applications

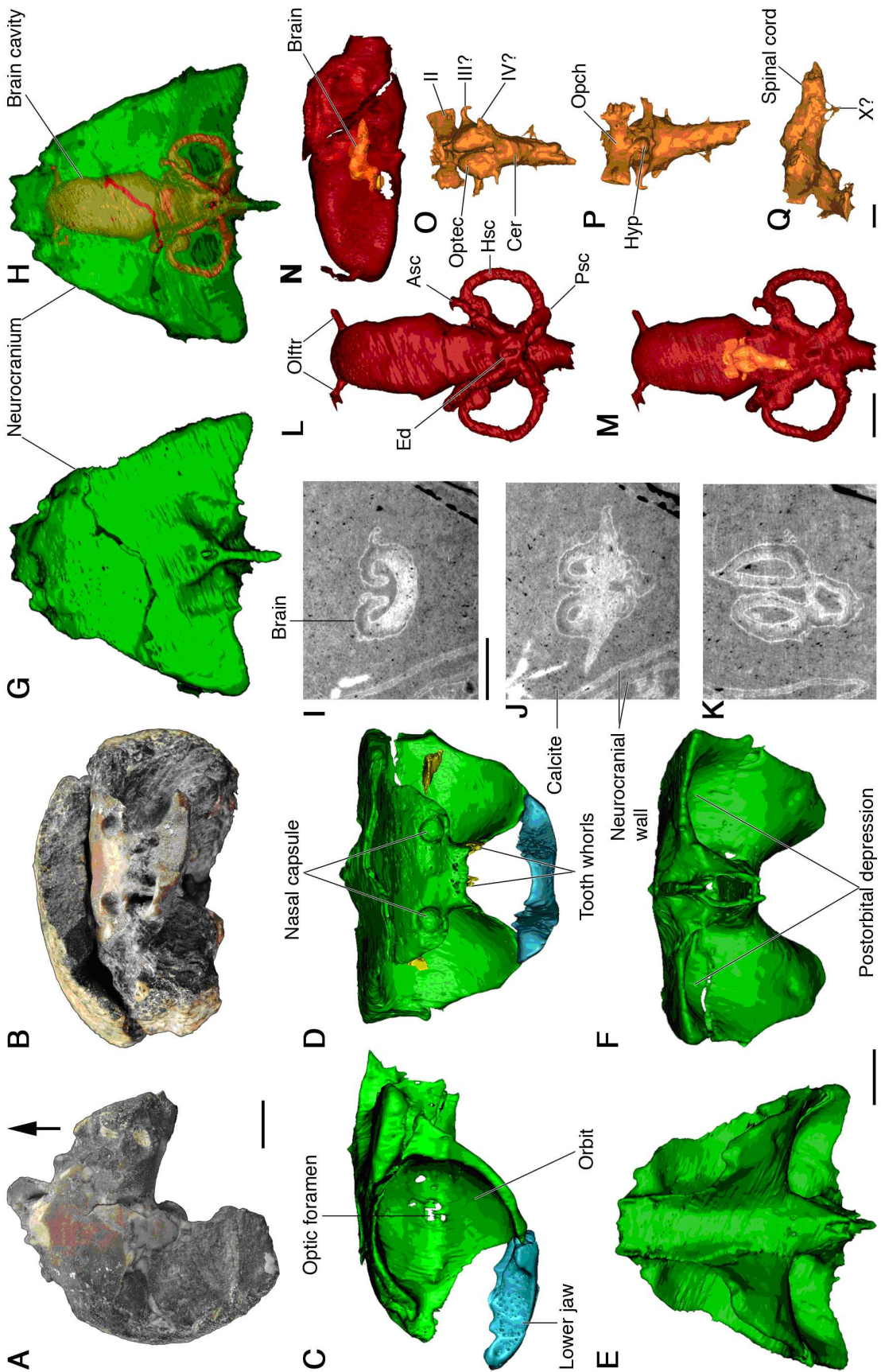


Figure 6.2: Braincase anatomy and exceptional brain preservation in a sibyrhynchid iniopterygian from the Pennsylvanian of Kansas. A, B, Articulated skull preserved in a nodule (KUNHM 22060) in dorsal (A) and anterior (B) view (arrow points forward). C-Q, Threedimensional reconstructions and preserved brain structures of the same specimen, obtained from SR-CT images (and holotomography for brain details). C-H, Braincase, teeth and lower jaw in lateral (C), anterior (D), ventral (E), posterior (F) and dorsal (G) view, showing by transparency the outline of the brain cavity and labyrinth (H). I-K, Selected transverse (I, J) and horizontal (K) SR-CT (holotomography) slices through the calcite-filled brain cavity, showing the probably phosphatized brain at the level of the rhombencephalon (I), hypophysis (J), and roof of the optic tectum and cerebellum (K). L-N, Reconstruction of the brain cavity and otic capsule in dorsal (L, M) and lateral (N) view, showing the brain by transparency (M, N). O-Q, reconstruction of the phosphatized brain in dorsal (O), ventral (P) and lateral (Q) view. Scale bars = 5mm for A-N and 1mm for I-K, O-Q. Abbreviations: Asc, anterior semicircular canal; Cer, cerebellum; Ed, endolymphatic duct; Hsc, horizontal semicircular canal; Hyp, hypophysis; Olftr, canals for olfactory tracts; Opch, optic chiasm; Optec, optic tectum; Psc, posterior

This first evidence of a fossilized vertebrate brain revealed by holotomography also allows the first paleo-neuroanatomical study of a fossil vertebrate based on the actual brain, and not merely the brain cavity. This new application of holotomography confirms the rapidly growing possibilities of X-ray synchrotron phase imaging techniques in palaeontology (Tafforeau et al., 2006; Friis et al., 2007; Feist et al., 2005; Smith et al., 2006) and especially when dealing with the exceptional soft-tissue preservations. It imposes synchrotron radiation as a powerful tool for non-destructive imaging of fossils.

### 6.1.4 Materials and methods

#### 6.1.4.1 Origin of the material

The material described comes from the Upper Carboniferous (Pennsylvanian) of Kansas and Oklahoma.

*Material from Kansas:* The Pennsylvanian fish-bearing concretions from Kansas and the paleoniscoid braincases they contain have been known since the early twentieth century and have been extensively studied (Poplin, 1974). They occur at the limit between the Haskell Limestone Member and the overlying Robbins Shale of the Stranger Formation (dated as Late Virgilian; 305–299 Myr), and crop out between the towns of Lawrence and Baldwin, Kansas. The specimens belong to the collection of the Kansas University Natural History Museum, Lawrence (KUNHM 22060 and 21894).

*Material from Oklahoma:* The specimen from Oklahoma (OKM38) was collected by Dr. Royal Mapes (Geology Department, Ohio University, Athens, Ohio) from the Tackett Shale, Coffeyville Formation (dated as Pennsylvanian, Missourian, Ca 307 Myr), at a roadcut in Tulsa County, Oklahoma (Center of NW sec. 2, T. 18 N, R. 12 E, Sapulpa North 7 1/2 Quadrangle). Numerous paleoniscoid braincases were also recovered from small nodules at this site.

#### 6.1.4.2 Methods of SR- $\mu$ CT and holotomography

Samples were imaged primarily using absorption based X-ray synchrotron microtomography (SR- $\mu$ CT) on the beamline ID19 of the European Synchrotron Radiation Facility. This technique has previously been demonstrated to be a powerful tool for non-destructive imaging of large fossils when conventional X-ray microtomography does not give good enough data quality (Tafforeau et al., 2006). A monochromatic X-ray beam of 60 keV energy was used. The detector was a FReLoN (Fast Readout Low

Noise) (Labiche et al., 2007) CCD camera coupled with an optical magnification system, yielding an isotropic pixel size of 30.3 m. For each tomography, covering a height of 5.6 mm, we used 1200 projections on 180 degrees with 0.4 s of exposure time. Several scans were performed after vertical displacement of the sample in order to image the whole specimen. Data were reconstructed using the filtered backprojection algorithm (PyHST software, ESRF). Reconstructed slices were converted from 32 bits to 8 bits in order to reduce the data size for 3D processing. Successive scans of each sample were then set together by removing the common slices.

Observation of the original absorption scan of the KUNHM 22060 sample revealed a structure that may correspond to a fossilized brain, but the absorption contrast was not good enough to allow satisfactory segmentation of the structure. A new experiment was performed in order to resolve the structure with more details and better contrast. In order to increase the contrast, we decided to use quantitative phase tomography, also called holotomography (Cloetens et al., 1999, 2006). The technique was originally designed to image pure phase objects, but was successfully used to image small fossil samples embedded in a mineral matrix (Tafforeau et al., 2006). It is based on the acquisition of several propagation phase contrast (Snigirev et al., 1995) scans that are then combined to retrieve a phase map of the sample for each angle of the tomographic acquisition. In the case of strongly absorbing objects, this phase retrieval process fails to bring accurate results due to the strong absorption contrast superimposed on the phase contrast, and to the too strong phase shift between the sample and the air that creates false low frequencies in the phase retrieval.

Here, a newly developed approach (Guigay et al., 2007) for strongly absorbing samples is further refined to obtain a robust reconstruction. It involves a first scan in absorption mode, which is available in the contact plane of the sample and the detector. Like all differential phase contrast methods, this technique is sensitive to noise in the low spatial frequency range if the propagation distance is relatively small and the X-ray energy is relatively high. This phenomenon was alleviated by introducing the assumption that the imaged object is roughly homogeneous. If the chemical composition of the sample is roughly known, an estimate of the ratio between absorption and phase shift can be calculated. This combined with the absorption scan is then used to regularize the low frequency content of the phase shift. This allows robust and accurate phase reconstruction on complex, absorbing and roughly homogeneous samples such as fossils. For the holotomography, we used a monochromatic beam at an energy of 60 keV and a detector giving an isotropic pixel size of 14.92  $\mu\text{m}$ . A tomographic scan with 1500 projections, each with an exposure time of 0.3 s, was taken over 180 degrees for each

of the three propagation distances. Two holotomographic acquisitions were necessary to cover the whole structure. The propagation distances were 50 mm (absorption), 400 mm and 950 mm, respectively. After phase retrieval, the slices were reconstructed using the filtered backprojection algorithm, then converted into 8 bits. Finally, the two holotomographic scans were combined to one volume where the common slices were removed. This volume constitutes a quantitative map of the electron density, hence approximately the mass density, through the sample. Due to the high contrast and good resolution provided by the holotomographic approach, it was possible to segment the putative brain in 3D with a good accuracy. The new algorithmic approach opens new possibilities for high quality imaging of dense and complex fossils and can yield impressive results in cases of absorbing, roughly homogeneous samples with small internal variations, such as soft body parts preservation.

Despite a longer acquisition time than single distance phase retrieval protocols (Friis et al., 2007; Paganin et al., 2002; Zabler et al., 2005; Gureyev et al., 2006; Tafforeau et al., 2007), accuracy and sensitivity of this approach to image fossils are clearly higher. Since it does not require the object to be homogeneous and weakly absorbing, it can be applied on a much broader range of samples.

### 6.1.5 Acknowledgments

We thank L. Martin [Kansas University, Natural History Museum (KUNHM)] for the loan of the Kansas specimens and the permission to include them in the present article, and R. Mapes (Geology Department, Ohio University, Athens, Ohio) for donating the Oklahoma specimen to the American Museum of Natural History (AMNH), New York.

## 6.2 Bone research

### 3D SR X-ray Holotomography enables study of fibrous tissue in porous scaffolds for tissue engineering

Manuscript prepared for  
Journal of Microscopy

3D micro-architecture of bone and bone scaffold has previously been studied by micro-computed tomography, synchrotron radiation micro-computed tomography and microdiffraction. However neither of these techniques can resolve the pre-bone fibrous structures. In this paper, we propose an approach based on quantitative phase tomography to image non-calcified pre-bone fibrous matrix in in-vitro cell cultivated porous scaffold samples. We compare the results from a holographic phase tomography approach to synchrotron radiation absorption micro-computed tomography and show that quantitative analysis, such as volume estimation and thickness measurement, of the reconstructed volumes can be performed.

### 6.2.1 Introduction

The use of biodegradable porous scaffolds in conjunction with tissue engineering techniques is emerging as a viable technique for reconstructive bone surgery (Kofron et al., 2004). Desirable characteristics of the scaffolds are that they provide a surface favorable for cell attachment (osteoconductive), that they induce osteoblast precursors to differentiate into mature bone-forming cells (osteoinductive), and that they contribute to bone regeneration (osteogenic). Ideally, they should also be resorbed by the receiving body, and be replaced by new, living bone (Glazer et al., 2001). More precisely, the resorption should not be a random process, but should only occur where new pre-bone matrix is being deposited (Mastrogiacomo et al., 2007).

It has been shown that porous scaffold such as Skelite<sup>TM</sup> (Millenium Biologix, Ontario, CA), based on silicon stabilized tricalcium phosphate (Si-TCP), when loaded with human bone marrow stromal cells induce the formation of mature lamellar bone within 20 weeks when implanted into a soft tissue site in immunodeficient mice (Papadimitropoulos et al., 2007). It has also been shown that Skelite<sup>TM</sup> scaffolds are resorbed when acted upon by osteoclasts (Mastrogiacomo et al., 2006), and that there is a coupling between bone regrowth and scaffold resorption in Skelite<sup>TM</sup> scaffolds (Mastrogiacomo et al., 2007). In vitro, osteoblasts loaded into the scaffold form a fibrous matrix containing calcium deposits, resembling pre-bone structure.

Recently, 3D X-ray microtomography ( $\mu$ CT) has been proposed to study the microarchitecture of bone and scaffolds  $\mu$ CT (Lin et al., 2003; Bernhardt et al., 2004; Thomsen et al., 2005; Ho and Hutmacher, 2006; Bernhardt et al., 2005). In particular, synchrotron radiation  $\mu$ CT (Salomé et al., 1999) has allowed to identify and quantify newly formed bone (Komlev et al., 2006) and has also sucessfully been coupled to microdiffraction to get information about the chemical composition of the scaffolds (Cancedda et al., 2007). However, until now it has not been possible to resolve the fibrous tissue. X-ray phase contrast imaging is a relatively new imaging modality that extends the possibilities of standard  $\mu$ CT. Like all phase imaging techniques, it requires coherent or partially coherent illumination, such as that from a synchrotron source. Phase shift is due to the refractive index distribution in the sample, which can be up to a factor 1000 greater than the absorption index, therefore offering greater sensitivity than absorption based techniques (Momose and Fukuda, 1995). With coherent illumination, phase contrast is formed by propagating the X-ray beam in free space, through Fresnel diffraction (Snigirev et al., 1995; Cloetens et al., 1996; Wilkins et al., 1996; Nugent et al., 1996).

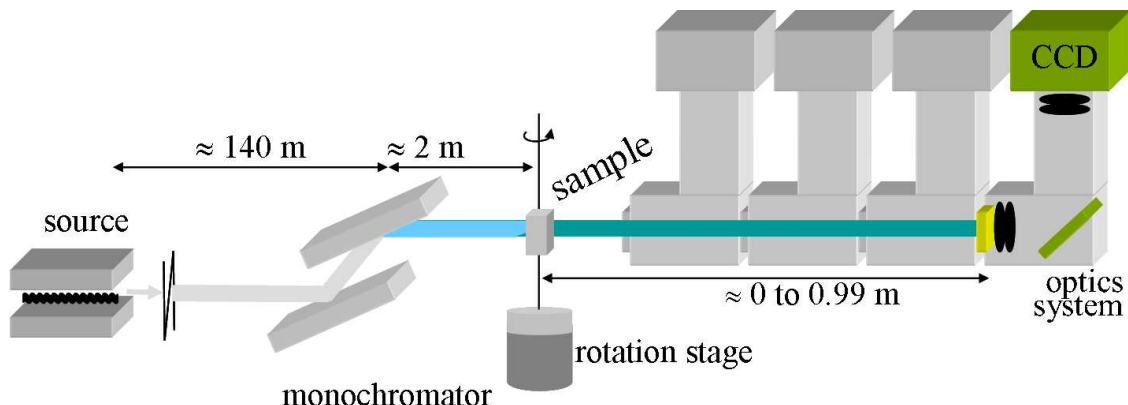


Figure 6.3: Schematic of the imaging setup. X-rays are produced from an undulator synchrotron insertion device and monochromatized by a double silica crystal monochromator set to reflect in the vertical plane. The sample is mounted on a rotation stage to perform tomography. The imaging detector, a scintillator screen mounted in front of a mirror, ordinary light optics and a FReLoN CCD camera (Labiche et al., 2007), is mounted on a translation stage to perform propagation based phase contrast imaging. Based on the phase contrast images, the phase shift at each projection angle is then retrieved.

In this work, quantitative phase tomography is used 6.3. A regularized holographic phase retrieval technique (holotomography) for strongly absorbing objects, that retrieves the phase from several Fresnel diffraction patterns is coupled to standard filtered back-projection tomographic reconstruction (Guigay et al., 2007). Due to the ill-posed nature of the phase retrieval problem, we propose the use of a regularized approach which introduces prior knowledge on the phase based on the absorption image. It is strictly valid for homogeneously composed objects. Regularization parameter selection is automated through the use of the L-curve (Langer et al., Submitted). We show that holotomography is a valid tool for imaging of the pre-bone matrix. We acquire 3D reconstructions of scaffolds cultured with different cell complexes. These are possible to segment using simple thresholding. The segmented volumes can be used to extract quantitative parameters such as volume filling of the fibrous tissue and thickness of the fibrous tissue and mineralized fraction including scaffold and mineralized bone . Thus, the present technique would be suitable for comparative studies of different scaffold materials, as well as different cultivation conditions.

## 6.2.2 Materials and methods

### 6.2.2.1 Sample preparation

The scaffolds studied here were Skelite<sup>TM</sup> (Millenium Biologix Corp., Kingston, Canada), a bone graft substitute containing silicon in the form of Si-TCP. It is composed of approximately 67 % Si-TCP and 33 % HA/B-TCP (Sayer et al., 2003; Reid et al., 2005). Skelite<sup>TM</sup> scaffolds have an interconnected, open pore structure which is similar to human cancellous bone. It has a porosity level of around 60 % with a pore size range of approximately 200  $\mu\text{m}$  to 500  $\mu\text{m}$ . The scaffolds used in this study were discs of 1.2 mm height with a diameter of 9 mm.

The Skelite<sup>TM</sup> discs were seeded with osteoblast (OB) and a combination of osteoblast and osteoclast cells (OB+OC). As controls, a scaffold seeded with osteoclasts (OC) only, and an unseeded, empty scaffold (E) were included in the study. The cells were loaded into the scaffolds and cultivated for 8 weeks. The scaffolds were then washed in phosphate buffered saline (PBS), fixed in paraformaldehyde and stored in 70 % ethanol.

The discs were dried of ethanol before imaging and mounted in a 1 cm inner diameter Pyrex holder. The vertical field-of-view of 7 mm allowed to image up to 3 samples simultaneously, by stacking them in the holder and separating them with pieces of fibre tissue. The samples were fixed by lightly compressing them with a foam material. The three seeded scaffolds were imaged together and the E scaffold separately.

### 6.2.2.2 Holotomography

The scaffolds were imaged using a holotomographic approach. It is related to and extends the possibilities of the usual form of X-ray  $\mu\text{CT}$ . The effect of a sample on an X-ray beam passing through it is described by the complex refractive index

$$n(x, y, z) = 1 - \delta_n(x, y, z) - i\beta(x, y, z). \quad (6.1)$$

Both the absorption and phase shift can be described as projections through the refractive index, the absorption being

$$B(\mathbf{x}) = (2\pi/\lambda) \int \beta(x, y, z) dz \quad (6.2)$$

and the phase shift

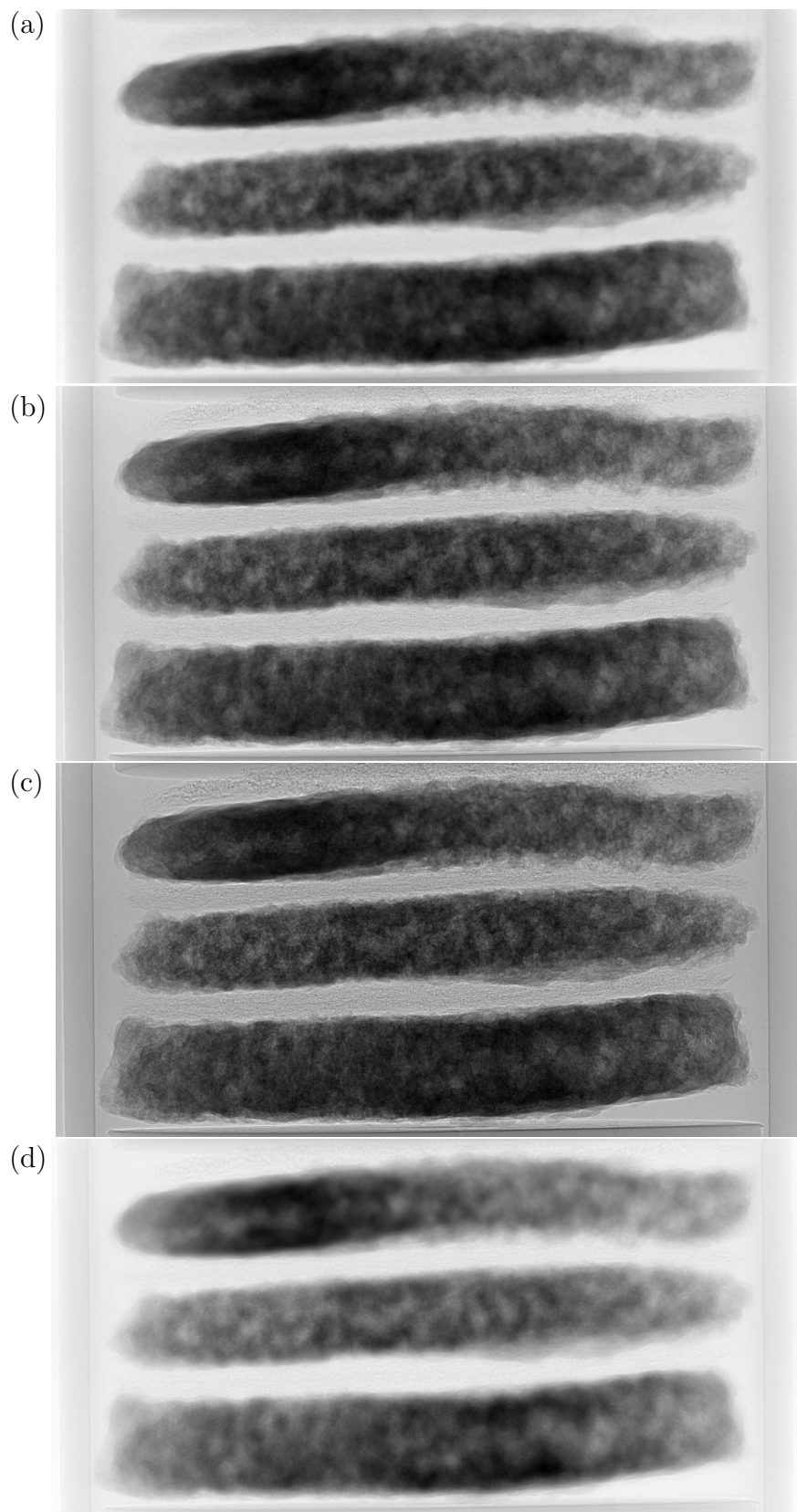


Figure 6.4: Phase contrast radiographs of the three loaded scaffolds at (a)  $D=0.01$  m (absorption), (b)  $D=0.33$  m, (c)  $D=0.99$  m. (b)-(c) shows a mix of strong absorption and phase contrast. (d) Retrieved phase map.)

$$\varphi(\mathbf{x}) = -(2\pi/\lambda) \int \delta_n(x, y, z) dz. \quad (6.3)$$

This means that both  $\delta_n$  and  $\beta$  can be reconstructed using tomographic reconstruction techniques such as filtered back-projection (FBP) (Kak and Slaney, 1998).

Contrary to absorption, local phase variations in the beam do not produce direct contrast. Sufficiently coherent illumination enables a simple phase contrast imaging technique, variously known as propagation based or in-line phase contrast. Phase contrast is achieved by simply moving the detector away from the sample, by Fresnel diffraction (Snigirev et al., 1995; Cloetens et al., 1996; Wilkins et al., 1996; Nugent et al., 1996). The diffraction patterns can be analyzed directly in the Fourier domain (Guigay, 1977). Taking the 2D Fourier transform as

$$\tilde{g}(\mathbf{f}) = \mathcal{F}\{g\}(\mathbf{f}) = \int g(\mathbf{x}) \exp(-i2\pi\mathbf{x} \cdot \mathbf{f}) d\mathbf{x}, \quad (6.4)$$

the intensity of the pattern can be written as

$$\tilde{I}_D(\mathbf{f}) = \int T\left(\mathbf{x} - \frac{\lambda D \mathbf{f}}{2}\right) T^*\left(\mathbf{x} + \frac{\lambda D \mathbf{f}}{2}\right) \exp(-i2\pi\mathbf{x} \cdot \mathbf{f}) d\mathbf{x}. \quad (6.5)$$

$\mathbf{x} = (x, y)$  is the coordinate in the image plane and  $\mathbf{f} = (f_x, f_y)$  the conjugate spatial frequency variable. The intensity is dependent on both absorption and phase shift induced by the object. It can be seen directly from Eq. 6.5 that the absorption is directly available as the contrast at the contact plane (sample-to-detector distance  $D=0$ ). The phase shift has to be inferred from the patterns in an intermediary step by a process known as phase retrieval.

To yield stable phase reconstructions, radiographs taken at several distances are combined using a least-squares optimization procedure (Cloetens et al., 1999). This protocol requires the absorption contrast to be weak. This is the case in many biological imaging problems, and such techniques have been successfully applied in that area (Cloetens et al., 2006). In most bone research, however, there will be significant absorption contrast. Recently, a phase retrieval method adapted to the strong absorption case was developed (Guigay et al., 2007). It is based on linearizations of Eq. 6.5 to yield a simplified contrast model

$$\tilde{I}_D(\mathbf{f}) = \tilde{I}_D^{\varphi=0}(\mathbf{f}) + A_D(\mathbf{f})\tilde{\psi}(\mathbf{f}) + \Delta_D(\mathbf{f}), \quad (6.6)$$

with  $A_D(\mathbf{f}) = 2 \sin(\pi \lambda D |\mathbf{f}|^2)$ ,  $\Delta_D(\mathbf{f}) = \cos(\pi \lambda D |\mathbf{f}|^2) \frac{\lambda D}{2\pi} \mathcal{F}\{[\psi \ln(I_0)]\}(\mathbf{f})$  and  $\psi(\mathbf{x}) = I_0(\mathbf{x})\varphi(\mathbf{x})$ .  $I_D^{\varphi=0}(\mathbf{x})$  is the intensity at distance  $D$  if the phase shift was zero and is usually approximated by  $I_0(\mathbf{x})$ . The model in Eq. 6.6 is referred to as the mixed approach (Guigay et al., 2007).

Eq. 6.6 can be used to solve for the phase in a least squares sense. Because  $A_D(\mathbf{f})$  goes to zero for low frequencies, the solution will be sensitive to noise there and has to be regularized. Due to the term dependent on the gradient of the phase, the retrieval is done iteratively. The solution with standard Tikhonov regularization (Tikhonov and Arsenin, 1977) is

$$\tilde{\psi}^{(n+1)}(\mathbf{f}) = \frac{\sum_D A_D(\mathbf{f}) [\tilde{I}_D(\mathbf{f}) \tilde{I}_D^{\varphi=0}(\mathbf{f}) - \Delta_D^{(n)}(\mathbf{f})]}{\sum_D A_D^2(\mathbf{f}) + \alpha}, \quad (6.7)$$

where  $\alpha$  is the regularization parameter and  $\tilde{\psi}^{(n)}(\mathbf{f})$  signifies the Fourier transform of the phase-absorption product at iteration  $n$ . The solution converges in 3-5 iterations in most cases (Guigay et al., 2007).

A further refinement of this method for homogeneously composed objects has also been reported (Langer et al., Submitted), where the absorption image is included as prior knowledge on the phase. The main motivation was to address the sensitivity to noise in the low frequencies. The low frequencies from the absorption image are used as prior information on the phase to regularize the low frequencies in the phase. This prior term can be written as

$$\tilde{\psi}_0(\mathbf{f}) = \text{erfc}(f_r - f_c) \mathcal{F}\left\{\frac{\delta_n}{2\beta} I_0 \ln(I_0)\right\}(\mathbf{f}), \quad (6.8)$$

where  $\text{erfc}(\mathbf{x}) = \frac{1}{\sqrt{\pi}} \int_x^\infty \exp(-t^2) dt$  is the complementary error function and  $f_r = \sqrt{f_x^2 + f_y^2}$  the radial coordinate in the Fourier domain. The solution is now given by

$$\tilde{\psi}^{(n+1)}(\mathbf{f}) = \frac{\sum_D A_D(\mathbf{f}) [\tilde{I}_D(\mathbf{f}) - \tilde{I}_D^{\varphi=0}(\mathbf{f}) - \Delta_D^{(n)}(\mathbf{f})] + \alpha \tilde{\psi}_0(\mathbf{f})}{\sum_D A_D^2(\mathbf{f}) + \alpha}. \quad (6.9)$$

The parameter  $\alpha$  is selected automatically by balancing model and regularization error through use of the L-curve (Hansen, 1992, 2001; Langer et al., Submitted). The ratio  $\delta_n/\beta$  has to be determined based on the composition of the object. This prior is valid as long as  $\delta_n/\beta$  is constant in the object.

### 6.2.2.3 Data acquisition

All images were acquired at the European Synchrotron Radiation Facility (ESRF), Grenoble, France, on the ID19 beamline. The acquisitions were made in a three-dimensional (3D) parallel beam tomography setup (Salomé et al., 1999). An X-ray beam of 30 keV was selected from undulator radiation using a single Si crystal monochromator set to reflect in the vertical plane. The sample was mounted on a rotation stage to allow for tomography and the camera on a translation stage to allow for phase contrast imaging (Fig. 6.3). The X-rays were converted to visible light by a Gadox scintillating screen, then projected onto a FReLoN charged-coupled device detector (Labiche et al., 2007) using normal light optics. The effective pixel size was 5  $\mu\text{m}$ , giving a field of view of  $10 \times 7 \text{ mm}^2$ , limited in the vertical direction by the monochromator. One data set consisted of three angular scans of 2000 images each, taken at different sample to detector distances: 0.01 m, 0.33 m and 0.99 m. The exposure time was 0.4 s.

### 6.2.2.4 Holotomographic reconstruction

Three iterations of Eq. 6.9 were used in the phase retrieval step. A  $\delta_n/\beta$ -ratio corresponding to the scaffold composition was used. It was calculated, using the XOP software (Sanchez del Rio and Dejus, 2004), to be  $\delta_n/\beta = 380$ . The regularization parameter is sample dependent, and was determined as  $\alpha = 10^{-3.21}$  for the three loaded scaffolds and  $\alpha = 10^{-2.36}$  for the empty scaffold. The tomographic reconstruction was implemented with FBP.

### 6.2.2.5 Quantitative parameter extraction

Due to the high contrast and low noise in the reconstructed 3D volumes, the volumes could be segmented directly by simple thresholding based on the histograms. The thresholds were chosen automatically (Otsu, 1979). No additional filtering or morphological operations were necessary (cf. Mastrogiacomo et al. (2007)). Object volumes (total volume (TV), mineral containing fraction volume (MV) and fibrous tissue volume (FV)), and volume filling fractions (MV/TV and FV/(TV-MV)) of the different phases were then measured simply by counting the number of voxels in each segment. The local thickness (Hildebrand and Rüegsegger, 1997), and based on this the average thickness, of the mineral containing fraction and fibrous tissue were also extracted.

### 6.2.3 Results

In Fig. 6.4 (a-c), absorption and phase contrast radiographs of the three loaded scaffolds at different distances are shown. A phase map, retrieved with the proposed method, is shown in Fig. 6.4 (d). The process is repeated for all projection angles. Fig. 6.5 shows  $2048 \times 2048$  slices through 3D volumes reconstructed with different methods. Fig. 6.5. Fig. 6.5 (a) shows the 3D absorption index, reconstructed from radiographs taken at  $D = 0.01$  m, Fig. 6.5 (b) the refractive index reconstructed with Tikhonov regularization, and Fig 6.5 (c) the refractive index reconstructed using the prior.

Examining complete slices through the absorption index (Fig. 6.5 (a)), refractive index reconstructed with Tikhonov regularization (Eq. 6.7) (Fig. 6.5 (b)) and refractive index reconstructed by using the prior (Eq. 6.9) (Fig. 6.5 (c)) tomograms, the motivation to use the prior can be seen. Low frequency noise can be seen as cloud-like swells in the Tikhonov regularized slice (Fig. 6.5 (b)), which makes further analysis difficult. This is remedied by use of the prior (Fig. 6.5 (c)).

It might not be immediately apparent what is gained in the phase tomogram compared to the absorption. Zooms on  $1 \times 1$  mm regions of the two are more revealing (Fig. 6.6). While a less dense deposit can be seen around the mineral containing fraction in both tomograms, this is close to the noise floor in the absorption tomogram (Fig. 6.6 (a)), whereas the phase tomogram shows more contrast between fibrous tissue and background (Fig. 6.6 (b)). This is also seen in the volume histograms (Fig. 6.7). If brought to the same scale (the linear absorption coefficient runs in the range [0 5.2] and the correspondingly scaled refractive index is in the range [0 890]), a peak is clearly visible in the histogram of the phase tomogram, which is not clearly distinguishable in the histogram of the absorption tomogram.

Examining  $1 \times 1$  mm close-ups of the phase tomography slices of the different prepared scaffolds (Fig. 6.8), little difference can be seen. Obviously, the fibrous tissue is absent in the E and OC scaffolds, whereas it is present in the OB and OB+OC scaffolds. The filling pattern of the fibrous tissue seems to be similar in OB and OB+OC. We can also compare the histograms (Fig. 6.9). Again, the second phase is present in the OB and OB+OC scaffolds. The OB and OB+OC scaffolds seem to contain approximately the same amount of fibrous material, but the mineral containing fraction in the OB sample seems to be less dense (the corresponding peak in the histogram is shifted to the left). In the OB+OC scaffold, there seems to be less material in the mineral containing fraction compared to the others, and it seems to have a bigger range of densities, with more material between the mineral containing fraction and the fibrous tissue.

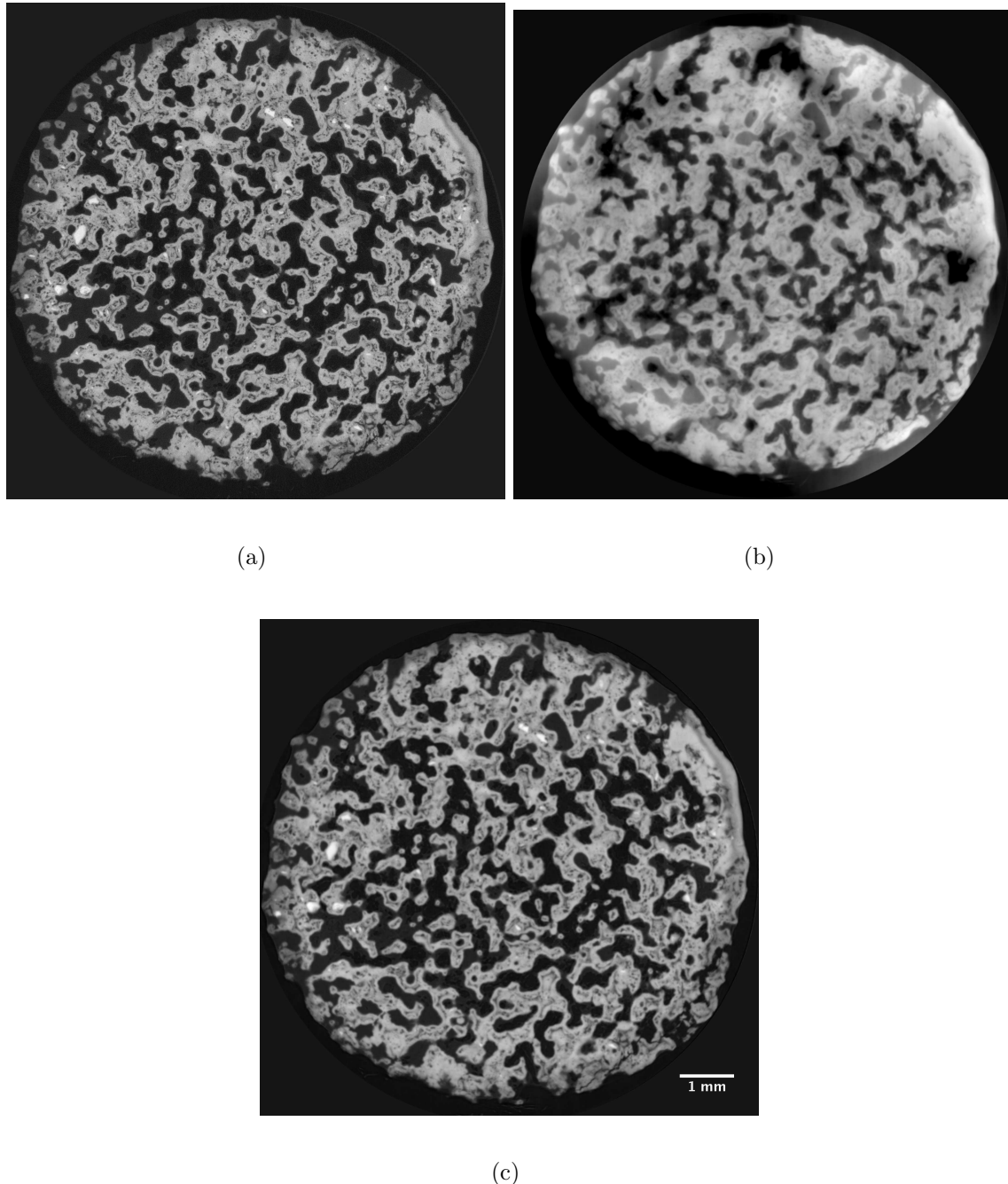


Figure 6.5: Slices through the 3D reconstructions of (a) absorption index, (b) refractive index reconstructed using the Tikhonov regularized mixed approach (Eq. 6.7), and (c) refractive index reconstructed using the mixed approach regularized with the homogeneous composition prior (Eq. 6.9) of the OB+OC scaffold. There are strong swells and uneven background in (b) due to sensitivity to noise in the low frequency range, rendering further analysis problematic. The low frequency noise is improved in (c).

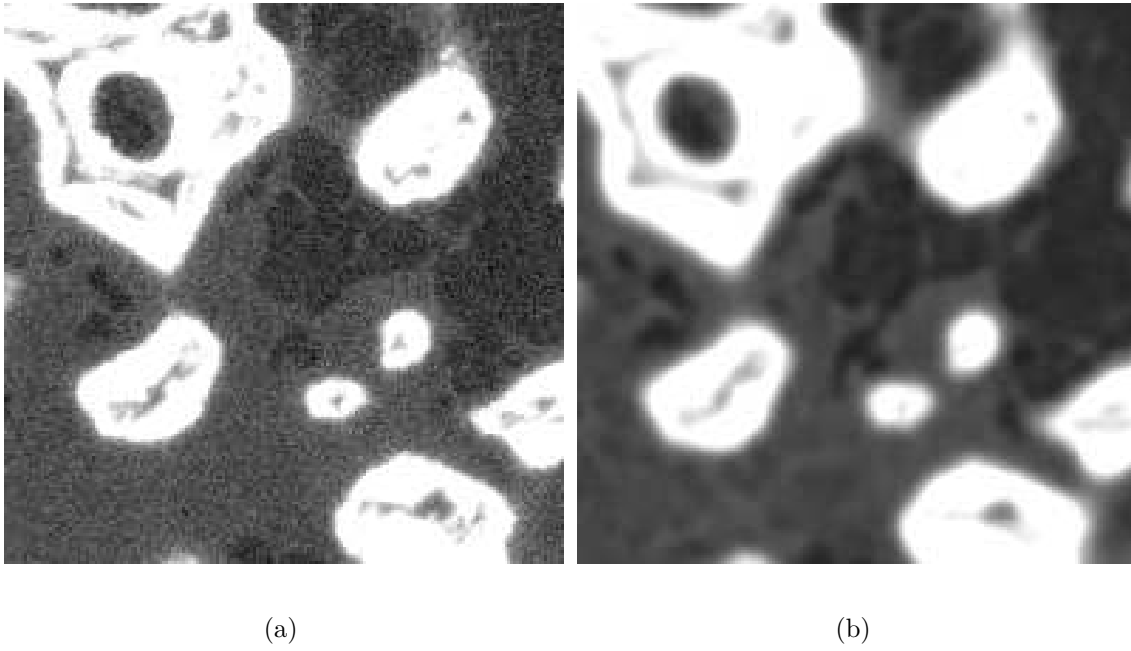


Figure 6.6: Zooms on  $1 \times 1$  mm regions in the (a) absorption and (b) refractive index reconstructed using the mixed approach regularized with the homogeneous composition prior (Eq. 6.9), windowed to show the fibrous tissue. While the fibrous tissue is visible by eye in both slices, in (a) the contrast is low and close to the noise floor.

The clear definition of the peak in the histograms, corresponding to the fibrous tissue, allows segmentation by thresholding based on the histogram of the phase tomograms. We can now analyze the fibrous tissue and mineral containing fraction quantitatively in three dimensions (Fig. 6.10). Total volume (TV), mineral containing fraction volume (MV), fibrous tissue volume (FV), mineral containing volume fraction (MV/TV) and fibrous tissue void filling fraction (FV/(TV-MV)) were measured in a  $25 \text{ mm}^3$  subvolume and presented in Tab. 6.1. FV/(TV-MV) is slightly higher in the OB scaffold, but is consistent with what was observed in the histograms. There is a fairly large

Table 6.1: Volumes and volume filling fractions of the four scaffolds.

|       | (mm <sup>3</sup> ) |       |      | (\%)  |            |
|-------|--------------------|-------|------|-------|------------|
|       | TV                 | MV    | FV   | MV/TV | FV/(TV-MV) |
| E     | 25                 | 12.46 | 0    | 49.84 | 0          |
| OB    | 25                 | 13.93 | 6.46 | 55.72 | 58.33      |
| OC    | 25                 | 15.93 | 0    | 63.70 | 0          |
| OB+OC | 25                 | 14.21 | 6.22 | 56.83 | 57.59      |

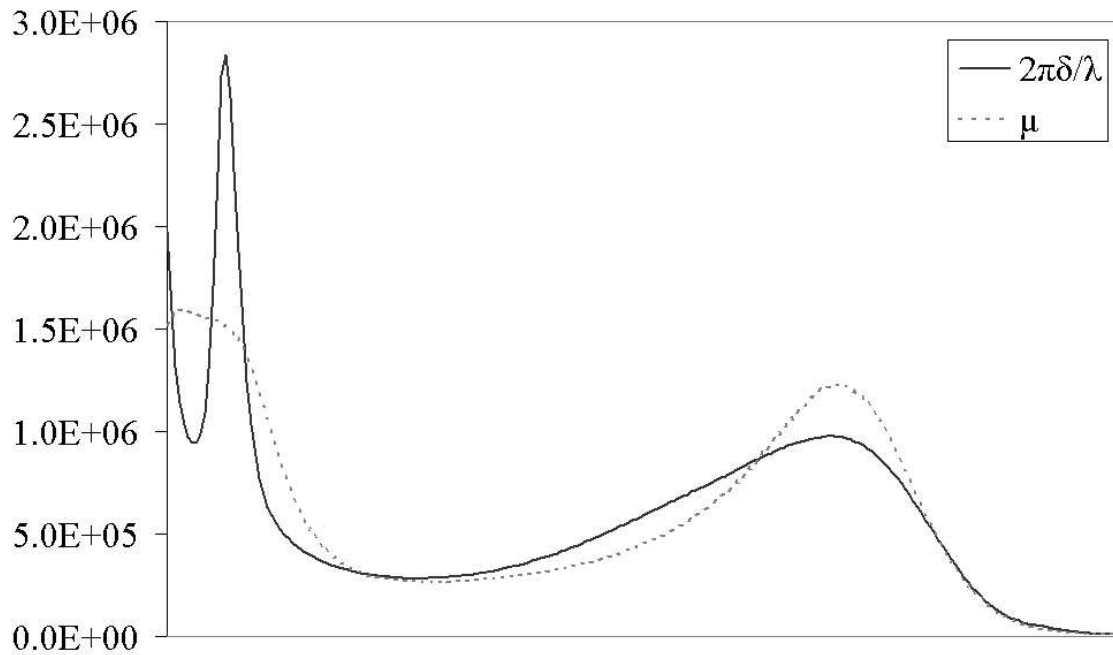


Figure 6.7: Histograms of the absorption and refractive index reconstructions. The histograms were brought to the same range, the linear attenuation coefficient being in the range [0 5.2] and the correspondingly scaled refractive index in the range [0 890]. A peak is clearly visible in the refractive index histogram, corresponding to the fibrous tissue, which is not well defined in the absorption index histogram.

variation in MV/TV between the different samples.

Average thickness measurements in the same subvolume as before (Tab. 6.2) indicates an increase in thickness of the mineral containing fraction (M.Th) in the OB+OC sample. The average thickness of the fibrous tissue (F.th) is also smaller in the OB+OC. Also the M.Th histograms (Fig. 6.11) indicate a shift towards greater thickness of the mineral containing fraction in the OB+OC sample. The mineral containing fraction thickness is lowest in the empty sample E.

Table 6.2: Average thickness of mineral containing fraction and fibrous tissue in  $\mu\text{m}$ .

|       | M.Th  | F.Th  |
|-------|-------|-------|
| E     | 140.4 | -     |
| OB    | 167.1 | 155.2 |
| OC    | 169.4 | -     |
| OB+OC | 197.7 | 122.4 |

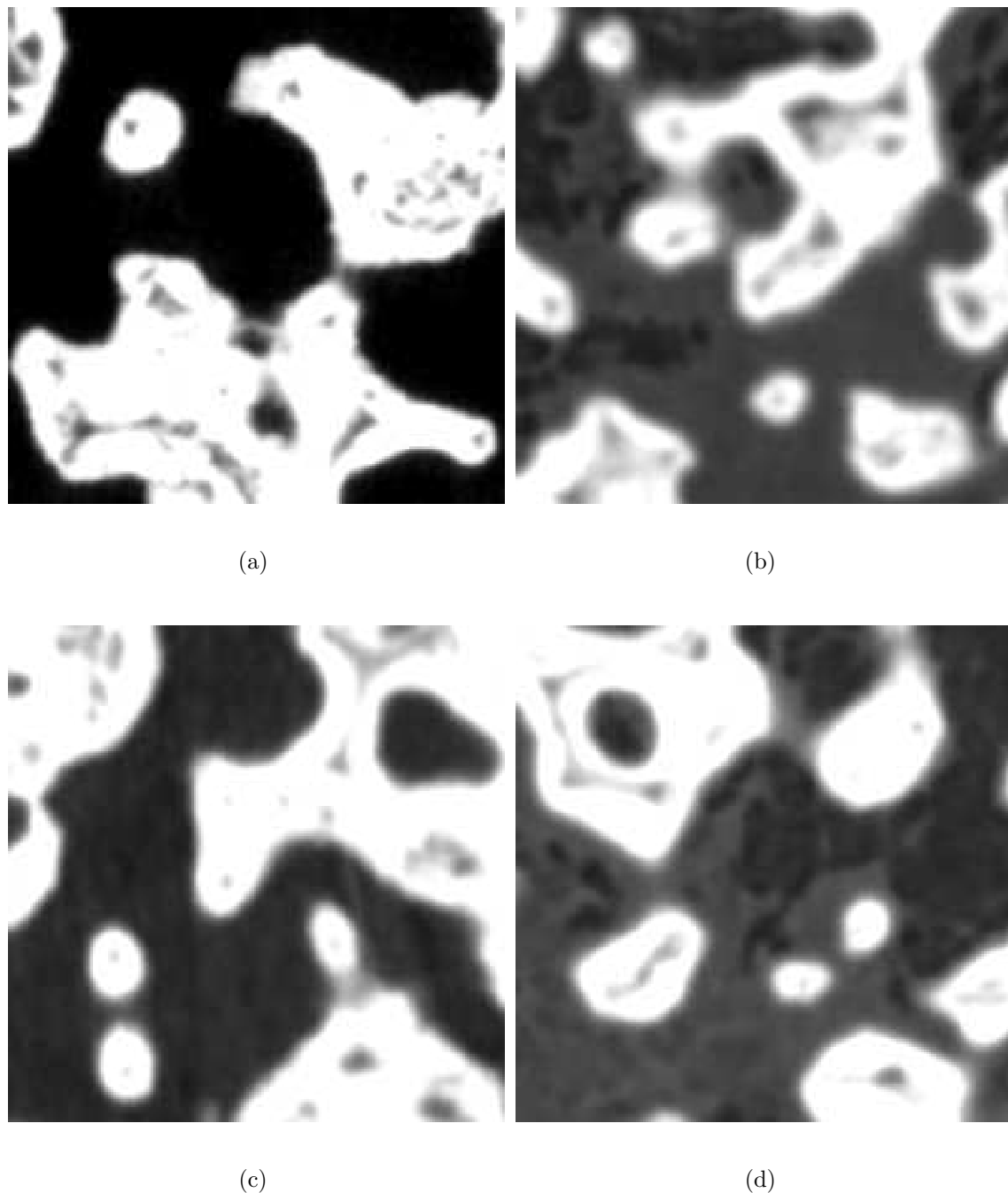


Figure 6.8:  $1 \times 1$  mm close-ups of the reconstructed refractive index of the different samples. (a) E (b) OB (c) OC (d) OB+OC.

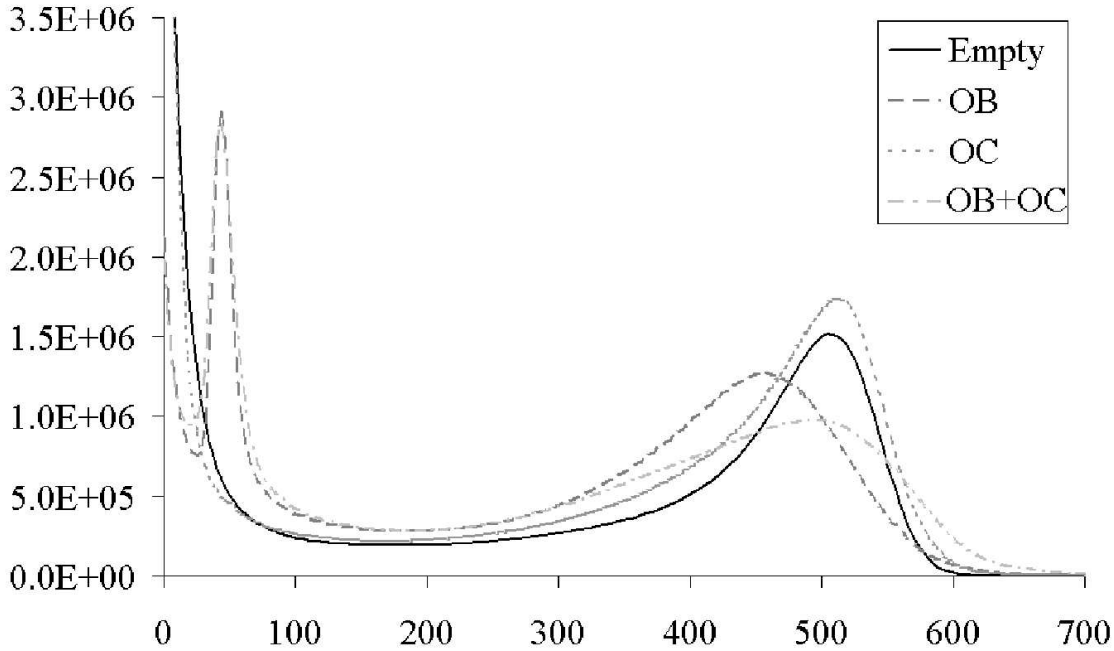


Figure 6.9: Histograms of the different reconstructed refractive index volumes. Note the lower density in the OB sample and the lower counts and more flattened peak in the OB+OC sample.

#### 6.2.4 Discussion

We have shown that holotomography could be an efficient method to resolve fibrous tissue. The proposed regularized scheme greatly improved the phase retrieval process by removing typical low frequency artifacts. The quality of the results show that the prior constraint was appropriate in this context. The value of the refractive index map compared to the absorption was evidenced on the histogram analysis. Segmentation of the fibrous tissue was only possible on the refractive index map. Thus, 3D quantitative parameters could be extracted.

The results indicate that Skelite™ scaffold, while being highly stable in an acellular physiological environment (Langstaff et al., 2001), interacts with the body's bone cells, and is resorbed when acted upon by osteoclasts (Mastrogiacomo et al., 2006), and can be replaced by living bone (Mastrogiacomo et al., 2006, 2007). The lower counts for higher densities in OB+OC, and the increase in material for lower densities, along with an increase in M.Th and decrease in F.Th indicates that the scaffold is beginning to be resorbed by the osteoclasts and mineralization of the fibrous tissue is increasing close to the scaffold walls. Since no change is observed in the OC scaffold, this could

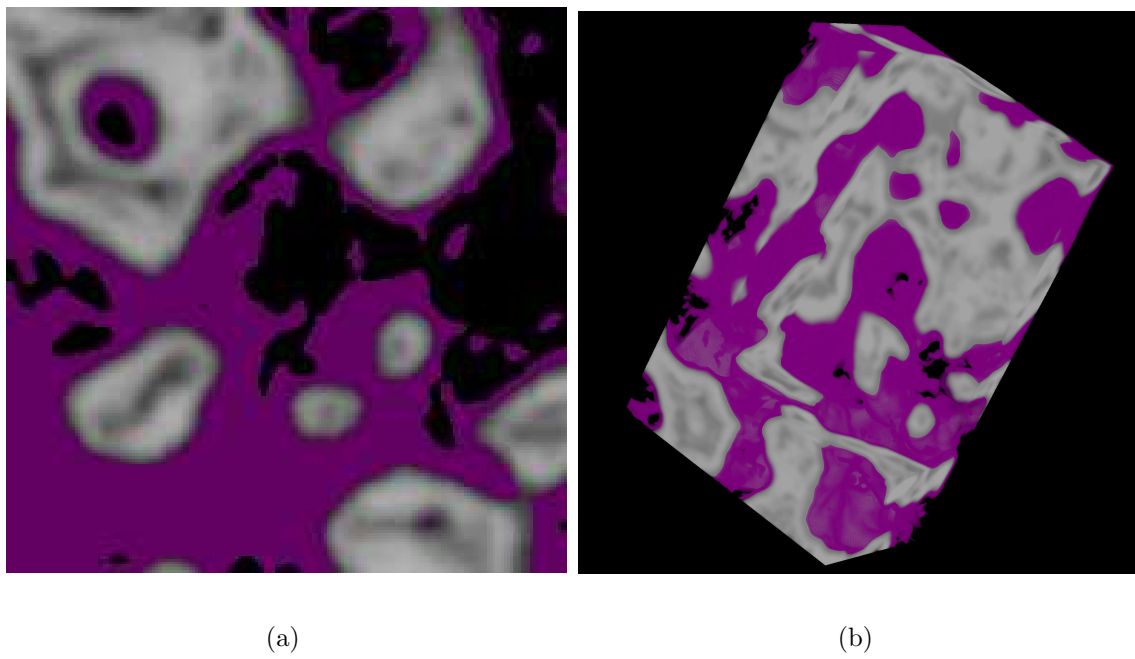


Figure 6.10: (a)  $1 \times 1$  mm close-up of a slice through the refractive index of the OB+OC scaffold, with the fibrous tissue thresholded and shown in magenta. The thresholded volumes clearly show the extent of the fibrous tissue. (b) A virtually cut 3D piece of the OB+OC scaffold, showing a typical fibrous tissue filling pattern with some partially and some fully filled pores.

indicate the proper and desired behaviour of the scaffold being resorbed only where fibrous tissue has been deposited (Mastrogiamomo et al., 2007).

It is not possible to draw definite conclusions from these indications, however. The variation in MV/TV is probably influenced by the appearance of the scaffolds before loading, which we cannot know in this study. Also the indication that the scaffold thickness has increased can not decisively be attributed to the effect of the cell culture. The difference in MT is more reliable, but influence of the original properties of the scaffolds needs to be confirmed. While holotomography enables quantitative analysis of the fibrous tissue, reliable quantification of the effects of the cell cultivation requires to image the scaffolds before and after being subjected to the culture, i.e. to verify the presence of new mineralized bone on the scaffolds.

One of the interests of this study is to create *in vitro* conditions mimicking the physiological bone microenvironment, by cultivating bone forming cells and bone resorption cells together on porous scaffold. Holotomography is proven to be a valid tool to analyze the fibrous tissue, which opens the possibility for more extensive studies of bone

regrowth and scaffold resorption. The continuation of this study is to compare scaffolds before and after being subjected to the in vitro culture, aiming to quantify the formation of fibrous tissue, the resorption of scaffold and the generation of new bone. The study can also be used to optimize cultivation conditions. Analysis of the fibrous tissue could also be used to increase the understanding of scaffold resorption and bone regrowth, and to compare different types of scaffolds

### 6.2.5 Conclusion

Synchrotron X-ray holotomographic imaging coupled to a regularized phase retrieval approach was demonstrated to be a valid imaging modality of in-vitro grown porous bone scaffolds. This is the first application of this technique to the analysis of fibrous tissue deposited by cell culture. The major advantage of reconstructing the refractive index is the improved contrast to noise ratio in the fibrous tissue, which enables 3D quantitative analysis. The findings in this work will be used as background for the design of a larger study to quantify the influence of different cell cultures on porous scaffolds, and to optimize cell culture conditions to mimic the physiological bone microenvironment.

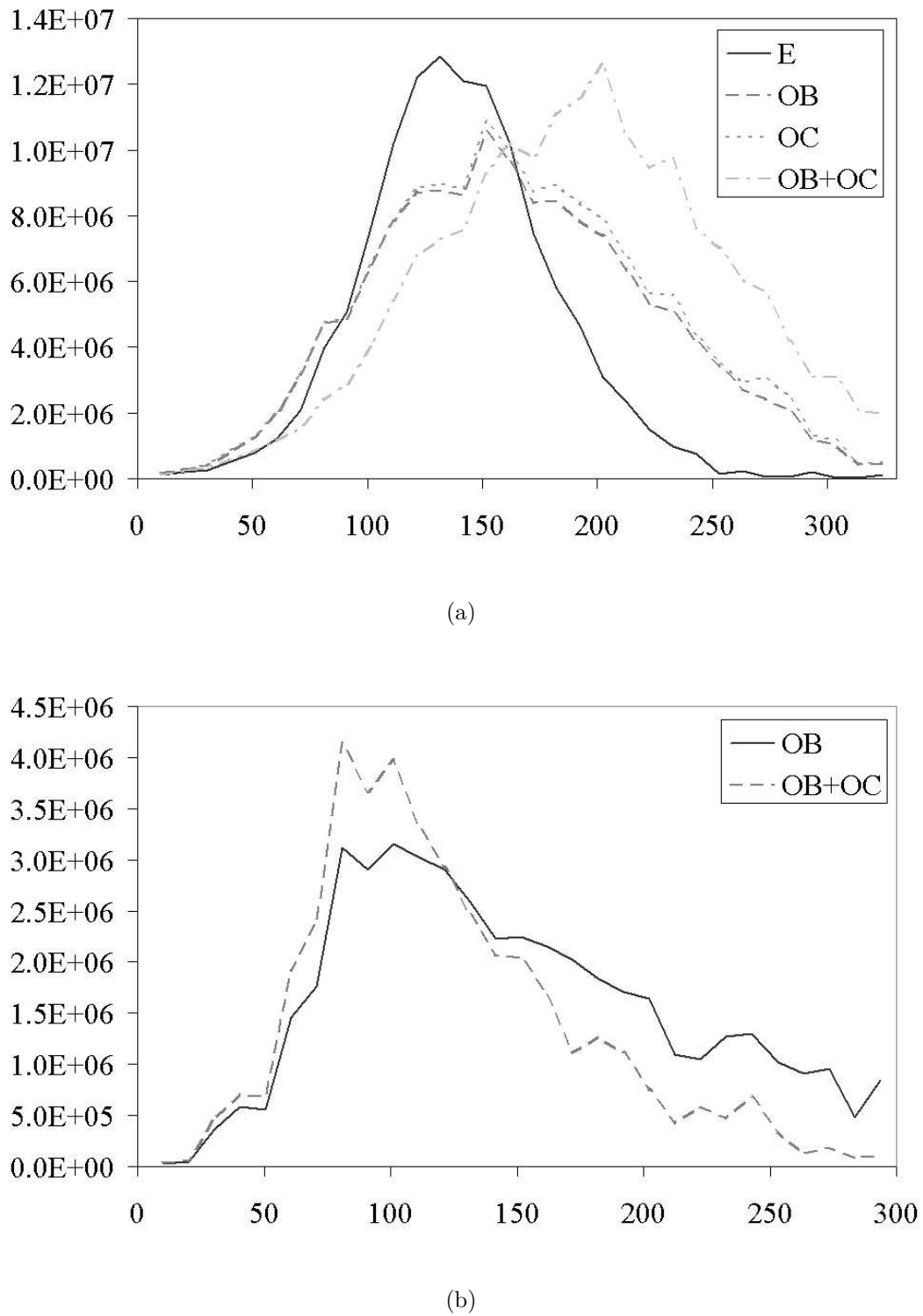


Figure 6.11: Thickness histograms for (a) the mineral containing fraction and (b) the fibrous tissue. The increase in thickness of the mineral containing fraction and decrease of fibrous tissue thickness in the OB+OC sample, together with fewer counts in the mineral containing fraction (Fig. 6.9) suggests scaffold resorption and beginning mineralization of the fibrous tissue close to the scaffold.



# Chapter 7

## Perspectives

Despite the advancements made in recent years, there is still no generally valid phase retrieval algorithm, and none of the existing methods can be dubbed the standard method. This is the ultimate goal, a general algorithm for phase retrieval in the Fresnel region. There seems to be essentially two ways forward, to continue on the current track, based on linearization and regularization, or to use iterative methods, either on their own or in conjunction with linear methods. Iterative methods are the standard in phase retrieval in the Fraunhofer regime, known as coherent diffraction imaging (CDI).

In this chapter we review the theory of iterative methods for phase retrieval, showing the basic algorithms that are in use. We describe two algorithms developed for the Fresnel diffraction case, and also outline a new algorithm for this problem. We then apply these to simulated data and see that they are not effective for Fresnel diffraction data in their standard implementations. We discuss how these algorithms may be adapted to the Fresnel case and also discuss possible directions regarding the linear algorithms.

## 7.1 Iterative methods

The classic method of phase retrieval from Fraunhofer diffraction patterns, now mostly known as the *iterative transform* algorithm (Stark, 1987), is a descendant of an algorithm first proposed by Gerchberg and Saxton (1972). It travels back and forth between the Fourier domain, where the intensity is known, and the object domain, where *a priori* knowledge of the object is applied.

### 7.1.1 Error reduction algorithm

The basic form of this algorithm is known as the *error reduction* (ER) algorithm (Fienup, 1978, 1982). It consists of the following four steps (at iteration  $k$ ):

1. Fourier transform  $T_k(\mathbf{x})$ , the current estimate of the object function  $T(\mathbf{x})$ , yielding  $\tilde{T}_k(\mathbf{f})$
2. Make the smallest possible change in  $\tilde{T}_k(\mathbf{f})$  so that it satisfies the Fourier domain constraints. This yields  $\tilde{T}'_k(\mathbf{f})$ , an estimate of  $\tilde{T}(\mathbf{f})$ .
3. Inverse Fourier transform  $\tilde{T}'_k(\mathbf{f})$  to yield  $T'_k(\mathbf{x})$ , the corresponding object, and
4. make minimum changes in  $T'_k(\mathbf{x})$  so that it satisfies the object domain constraints to form  $T_{k+1}(\mathbf{x})$ , a new estimate of the object transmission function

In the original Gerchberg and Saxton (1972) algorithm, the object domain constraint was the recorded intensity image, but other common constraints may include non-negativity and object support. With  $I_0(\mathbf{x})$  being the recorded intensity in the contact plane and  $I_D(x)$  the recorded intensity in the diffraction plane, the four steps of the ER algorithm are

$$\begin{aligned} \text{Step1 : } & \tilde{T}_k(\mathbf{f}) = \mathcal{F}\{T_k\}(\mathbf{f}) = |\tilde{T}_k(\mathbf{f})| \exp[i\phi_k(\mathbf{f})], \\ \text{Step2 : } & \tilde{T}'_k(\mathbf{f}) = \sqrt{I_D(\lambda D\mathbf{f})} \exp[i\phi_k(\mathbf{f})], \\ \text{Step3 : } & T'_k(\mathbf{x}) = \mathcal{F}^{-1}\{\tilde{T}'_k\}(\mathbf{x}) = |T'_k(\mathbf{x})| \exp[i\varphi_k(\mathbf{x})], \\ \text{Step4 : } & T_{k+1}(\mathbf{x}) = \sqrt{I_0(\mathbf{x})} \exp[i\varphi_k(\mathbf{x})]. \end{aligned} \tag{7.1}$$

The algorithm is typically started by using an array of random numbers for  $T_0(\mathbf{x})$ . A block diagram of the iterative transform algorithm is shown in Fig. 7.1. There are several ways to interpret this algorithm; in terms of the method of successive approximations (Fienup, 1981), as steepest descent gradient search (Fienup, 1982), or as projections onto sets (Bauschke et al., 2002; Elser, 2003).

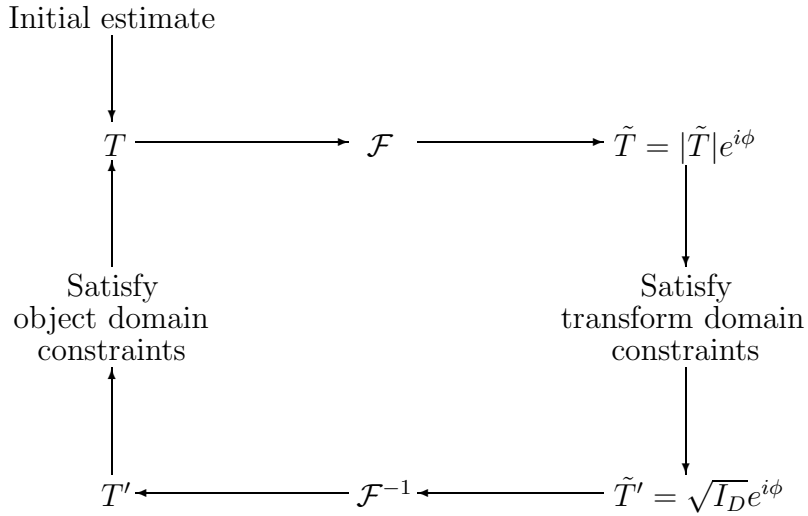


Figure 7.1: Basic scheme of the iterative transform algorithm.

### 7.1.2 Hybrid input-output algorithm

Several modifications of the ER algorithm for use with a single diffraction pattern (where no absorption image is available or desired) have been developed and tested, but the most successful one is the *hybrid input-output* (HIO) algorithm (Fienup, 1982; Stark, 1987). It replaces step 4 of the ER algorithm by

$$T_{k+1}(\mathbf{x}) = \begin{cases} T'_k(\mathbf{x}) & \mathbf{x} \notin \gamma \\ T_k(\mathbf{x}) - \eta T'_k(\mathbf{x}) & \mathbf{x} \in \gamma, \end{cases} \quad (7.2)$$

where  $\eta$  is a constant feedback parameter and  $\gamma$  the set of points where  $T'_k(\mathbf{x})$  violates the object domain constraints. The input  $T_k(\mathbf{x})$  is now no longer an estimate of  $T(\mathbf{x})$ , it is instead an input function that drives the output  $T_{k+1}(\mathbf{x})$  (which is an estimate of  $T(\mathbf{x})$ ). The interesting thing here is the introduction of  $\eta$ , which pushes the solution towards the constraint in a soft manner where it is violated.

### 7.1.3 Difference map

The ER and HIO algorithms can be generalized further. If we view satisfying a constraint as a projection onto a set of solutions fulfilling this constraint, we can consider two arbitrary projections  $\varpi_1(T)$  and  $\varpi_2(T)$ . For example, setting the Fourier modulus to the square root of the recorded intensity can be seen as a projection onto the set

of solutions with that particular Fourier modulus. The *difference map* of these two projections is then defined as (Elser, 2003)

$$D(T) = T + \varepsilon C(T), \quad (7.3)$$

where  $\varepsilon$  is a non-zero real parameter and

$$C(T) = (\varpi_1 \circ q_2)(T) - (\varpi_2 \circ q_1)(T) \quad (7.4)$$

is the difference of the two projection operators. Each of the projections is in turn composed with a map  $q_i(T)$ . The form of these maps is secondary, but the usual choice is

$$q_i(T) = (1 + \nu_i)\varpi_i(T) - \nu_i T, \quad (7.5)$$

which, if  $T$  is seen as a point in the solution space, defines a parameterized line between  $T$  and  $\varpi_i(T)$  with parameter  $\nu_i$ . It turns out that the optimal choice of the parameters  $\nu_i$  is to set  $\nu_1 = -\varepsilon^{-1}$  and  $\nu_2 = \varepsilon^{-1}$ , which yields the one-parameter form of the difference map. One iteration of the algorithm can thus be written as

$$\begin{aligned} T_{k+1} = D(T_k) &= T_k \\ &+ \varepsilon \{ \varpi_1[(1 + \varepsilon^{-1})\varpi_2(T_k) - \varepsilon^{-1}T_k] \\ &- \varpi_2[(1 - \varepsilon^{-1})\varpi_1(T_k) + \varepsilon^{-1}T_k] \}. \end{aligned} \quad (7.6)$$

A suitable progress measure of the difference map is

$$e_k = |C(T_k)|, \quad (7.7)$$

This “error measure” goes to zero when the algorithm reaches a fixed point  $T_f$ , which is characterized by

$$(\varpi_1 \circ q_2)(T_f) = T_{1 \cap 2} = (\varpi_2 \circ q_1)(T_f), \quad (7.8)$$

where  $T_{1 \cap 2}$  lies in the intersection of the constraint subspaces and is a solution to the particular instance of the phase problem.  $T_f$  is generally not a solution. The standard way of applying the difference map is to start with a randomly chosen  $T_0$ , then iterate

until a fixed point is reached. The solution is then found by applying Eq. 7.8. For each iteration, four projections have to be calculated, except if one of  $q_i$  is unity or the corresponding  $\nu_i$  is set to zero, when the number of projections reduces to two. The HIO algorithm can then be seen as a difference map with  $\varpi_1$  the Fourier modulus projection,  $\varpi_2$  the support projection,  $\nu_1 = 1$  and  $\nu_2 = \varepsilon$ .

### 7.1.4 Constraints in multiple transform domains

The question of how to incorporate several intensity measurements has not received a lot of attention. A way of incorporating several measurements was proposed by Mokso (2006), in which the transform domain projection consists of transforming the current estimate to each of the transform domains and imposing the constraint there. These transform domain estimates are then backpropagated and the new estimate is formed by taking the average of the backpropagated estimates (Fig. 7.2). This can be seen as a version of the ER algorithm with a different transform domain projection.

Specific iterative methods for phase retrieval from a series of intensity images (originally from a defocus series) have been developed (Allen and Oxley, 2001; Allen et al., 2004). In Allen and Oxley (2001), the different distances are cycled through in one iteration by forward propagating to the next plane, imposing the intensity constraint there, then propagating the new estimate to each successive plane, and finally backpropagating to the contact plane (Fig. 7.3). This can be seen as an implementation of the ER algorithm with the described projection as the transform domain projection.

### 7.1.5 Attempt at adapted algorithms

Initial development of three algorithms adapted to the Fresnel diffraction case was done. All three were implemented as one-parameter difference maps (Eq. 7.6). The algorithms were implemented as:

**Algorithm 1** uses the transform domain projection in Fig. 7.2 as  $\varpi_1$ . The current estimate  $T_k(\mathbf{x})$  is propagated to each plane (using Eq. 2.47) where the constraint is applied. Each new estimate is then backpropagated to the object plane by using  $-D$  in Eq. 2.62. The intensity projection in the object domain is used as  $\varpi_2$ .

**Algorithm 2** uses the transform projection in Fig. 7.3 as  $\varpi_1$ . The current estimate  $T_k(\mathbf{x})$  is propagated to the first diffraction plane, where the intensity constraint

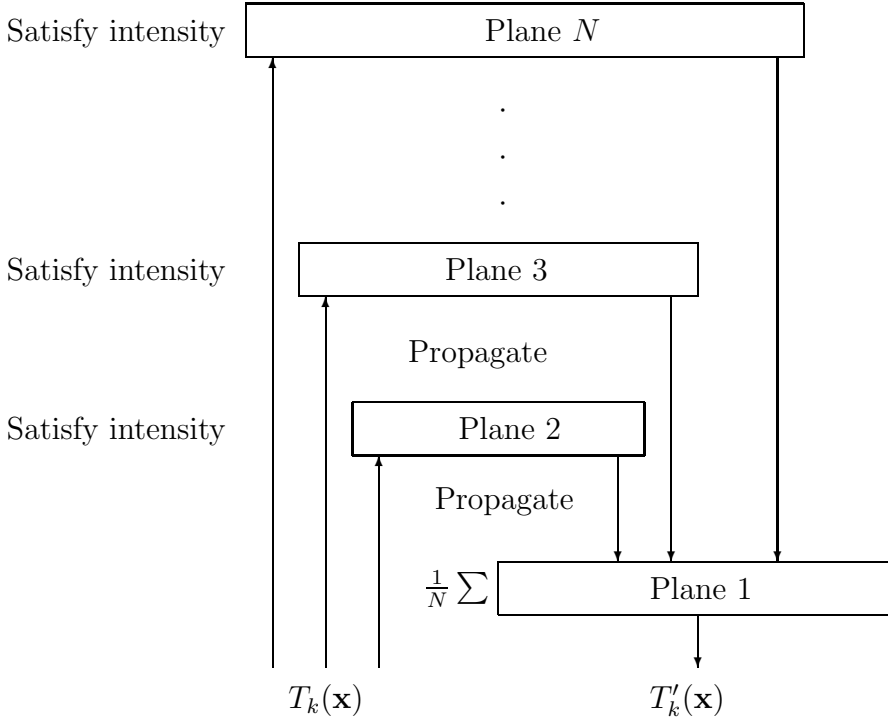


Figure 7.2: Transform domain projection in the algorithm suggested by Mokso (2006). The current estimate  $T_k(\mathbf{x})$  is forward propagated to each distance, the intensity constraints are applied and the resulting estimate is back propagated. The next estimate  $T'_k(\mathbf{x})$  is formed by taking the average of the back propagated estimates. This projection is used in algorithm 1 (Section 7.1.5).

is applied. This new estimate is then propagated to the next plane by using the distance between the two planes as the propagation distance in Eq. 2.62. This is then repeated until the longest distance is reached. The process is then repeated in reverse order by backpropagation until the object plane is reached. The combined intensity and support projection in the object domain is used as  $\varpi_2$ .

**Algorithm 3** uses the transform projection in Fig. 7.4. The intensity images are seen as separate transform projections (the absorption included), so that we have several projections  $\varpi_1, \dots, \varpi_N$ . The support constraint is used in the object domain as  $\varpi_{N+1}$ . One iteration of the algorithm consists of cycling through the transform domain projections  $\varpi_1, \dots, \varpi_N$ , applying the one-parameter difference map (Eq. 7.6) with each intensity constraint paired with the support constraint

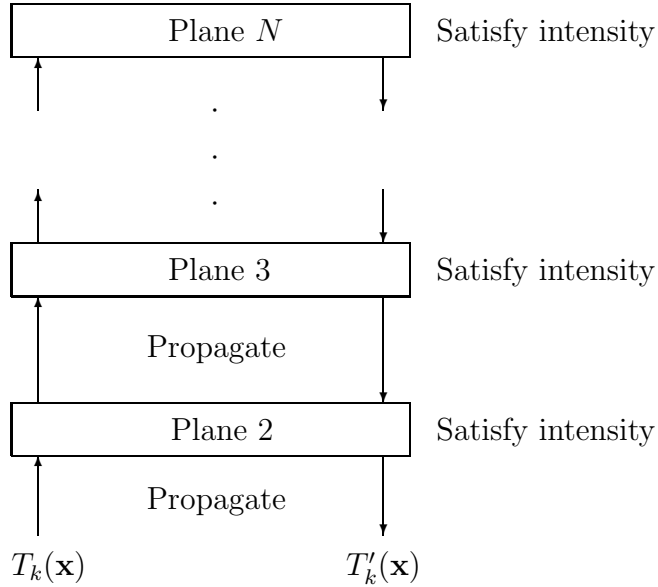


Figure 7.3: Transform domain projection in the iterative algorithm adapted from Allen and Oxley (2001). One projection consists of cycling through the distances by propagating from distance  $n$  to the next distance  $n+1$ , imposing the intensity constraint and then propagating again to the next distance until distance  $N$  is reached. The procedure is then repeated in the opposite direction by backpropagation, until distance 0 is returned to. This projection is used in algorithm 2 (Section 7.1.5)

$\varpi_{N+1}$  in each application.

The ideal support was used as the support constraint. The parameter  $\varepsilon$  was set to 0.75 in all three implementations.

### 7.1.6 Initial results

The algorithms were tested on simulated, noiseless Fresnel diffraction patterns at one projection angle of the phantom described in Section 4.5.1. As can be seen in Fig. 7.5, the phase shift is large and thus wrapped. The algorithms were allowed to run for 1000 iterations. The error measure in Eq. 7.7 was used to monitor the progress. The results of these trials are shown in Figs. 7.6-7.8. As can be seen, algorithm 1 (Fig. 7.6) and 2 (Fig. 7.7) show no convergence in the error plots. The retrieved phases show some structures from the phantom, but contain large amounts of noise. The support is fairly well reconstructed by algorithm 1, where no support projection was used. Algorithm 2 (Fig. 7.7) shows slightly improved results. The support is correctly reconstructed

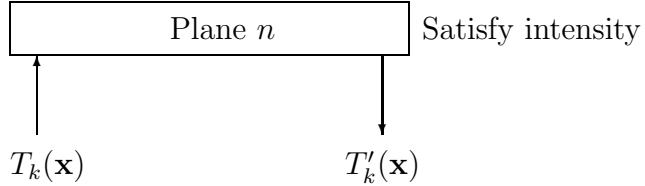


Figure 7.4: Transform domain projection in algorithm 3 (Section 7.1.5). Each intensity image is viewed as a separate constraint (the absorption image included). One iteration of the algorithm consists of cycling through the distances from 1 to  $N$  by applying the difference map (Eq. 7.3) to each distance in turn, paired with a support constraint in the object domain.

due to the support constraint, and slightly more structure is reconstructed inside the object. Algorithm 3 (Fig. 7.8) on the other hand shows a much stronger convergence in the sense that it seems to approach a fixed point. The retrieved phase contains mainly high frequencies, and little noise in regions far from interfaces.

### 7.1.7 Discussion

Despite continuing efforts of applying iterative methods to phase retrieval from Fraunhofer diffraction patterns with X-rays, no truly convincing reconstructions in practical applications have been obtained. Promising results have been shown of binary objects (Miao et al., 1999; Marchesini et al., 2003), and more recently of freeze-dried yeast cells (Shapiro et al., 2005). A problem, certainly in the 3D case, is the number of required iterations, since iterative phase retrieval from Fraunhofer diffraction patterns currently requires hundreds or more iterations (Shapiro et al., 2005).

Iterative methods also introduce the problem of phase unwrapping, since the iterations are done on the object function. The phase now appears in the exponent of a complex exponential function. The phase is therefore insensitive to shifts of multiples of  $2\pi$ . The question is if the iterative methods can retrieve a wrapped phase correctly. In that case, the problem would truly be separable into phase retrieval and phase unwrapping, a scientific area of study in its own right (Ghiglia and Pritt, 1998). This problem has been avoided by imaging very weak objects where the phase shift has been less than  $2\pi$  (Shapiro et al., 2005).

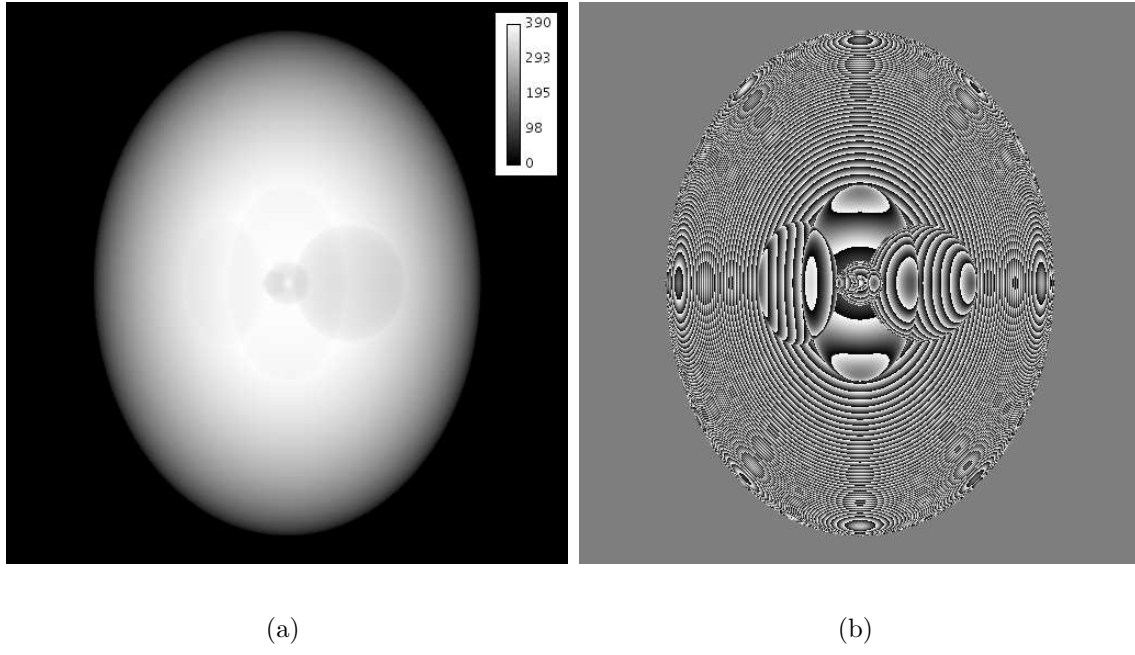


Figure 7.5: (a) The unwrapped and (b) wrapped phase of the phantom from Chapter 4. Note that the phase shift is relatively large, resulting in strong wrapping.

The simulations presented here give some hope of applying iterative methods to Fresnel region phase retrieval. Especially our algorithm 3, an adaptation of the difference map for constraints in several transform domains, gives partial reconstruction of the phase. Better results should be expected if larger propagation distances are used. While the numerical experiments in Section 7.1.6 are not conclusive in any sense, they suggest several roads to improvement. An interesting thing to note is that small changes in parameter selection or projection scheme can produce quite different results. This suggests that different algorithms could be combined to improve convergence. This is standard practice in iterative retrieval (Stark, 1987). Combination of linear and iterative algorithms could be an interesting route, retrieving an initial estimate, mostly in the low frequencies, with a linear algorithm which is then refined with an iterative algorithm. Some attempts have been made to this effect (Gureyev et al., 2004).

Some theoretical aspects could be investigated. An appropriate projection scheme for use with multiple intensity recordings (several distances still have to be used because to the loss of information due to the image formation process) has to be devised. It seems appropriate to consider the different recorded moduli as separate sets. To average the contribution from the different sets, as suggested by Mokso (2006) and used in algorithm 1 (Section 7.1.5), seems undesirable, since it does not minimize the distance

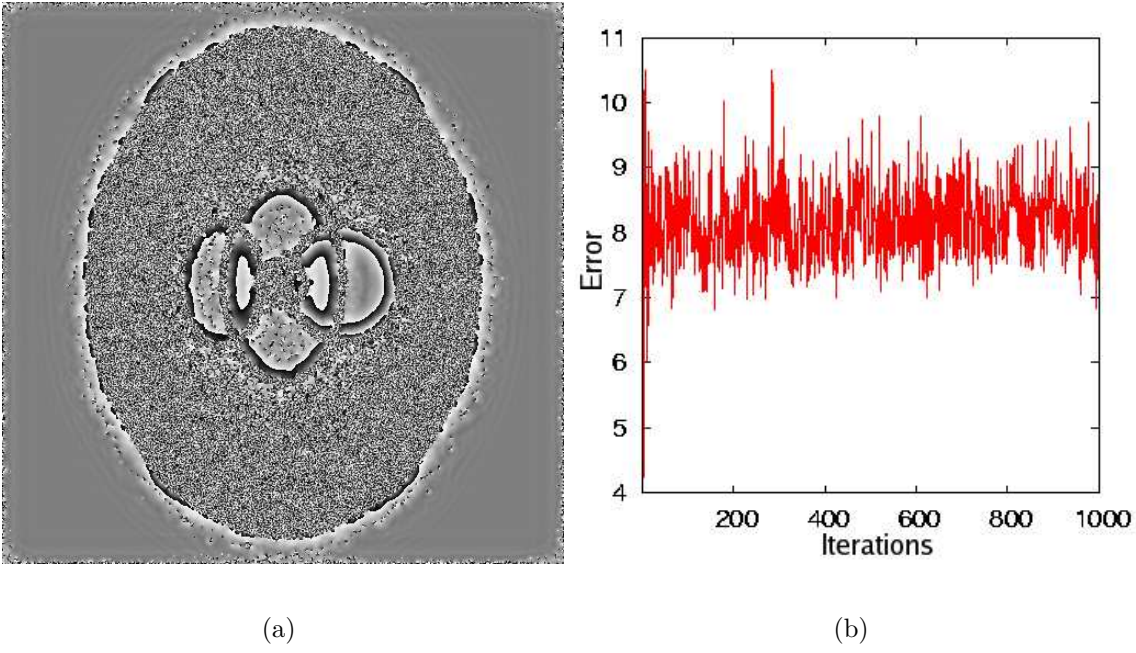


Figure 7.6: Retrieved phase and error evolution plot with algorithm 1 (Section 7.1.5), using the transform domain projection in Fig. 7.2, (a) Retrieved phase and (b) error evolution plot. In (a), the support is visible, albeit fairly uneven, and the outside of the object is approaching zero. Some structure is also visible inside the object, but the interior is mostly noise. The error evolution plot (b) shows no sign of convergence.

to any of the sets (just enforcing one of the constraints would immediately reduce the distance to that set). Instead, the most fruitful direction seems to be to combine two constraints pairwise in a difference map, and cycle through the constraints as in algorithm 3 (Section 7.1.5). Possibly, the difference map could be extended to operate on more than two projections simultaneously. Finally, better adapted projections in either the object or transform domain for this particular problem have not been considered, and could speed up convergence (as is the case in other applications (Elser, 2003)).

Experimental parameters could also be optimized to work with iterative algorithms. Certainly, longer distances could be used, which is indicated by the slow convergence in the low frequencies compared to the higher frequencies in the simulations above, into distance regions where the linearized methods do not seem to operate well. Scanning the illumination across the object to acquire several diffraction patterns from overlapping regions of the object, to increase redundancy and thus convergence of iterative reconstruction, has been considered for the Fraunhofer case (Rodenburg et al., 2007; Thibault et al., 2008). This scheme could possibly be adapted to the Fresnel case, at

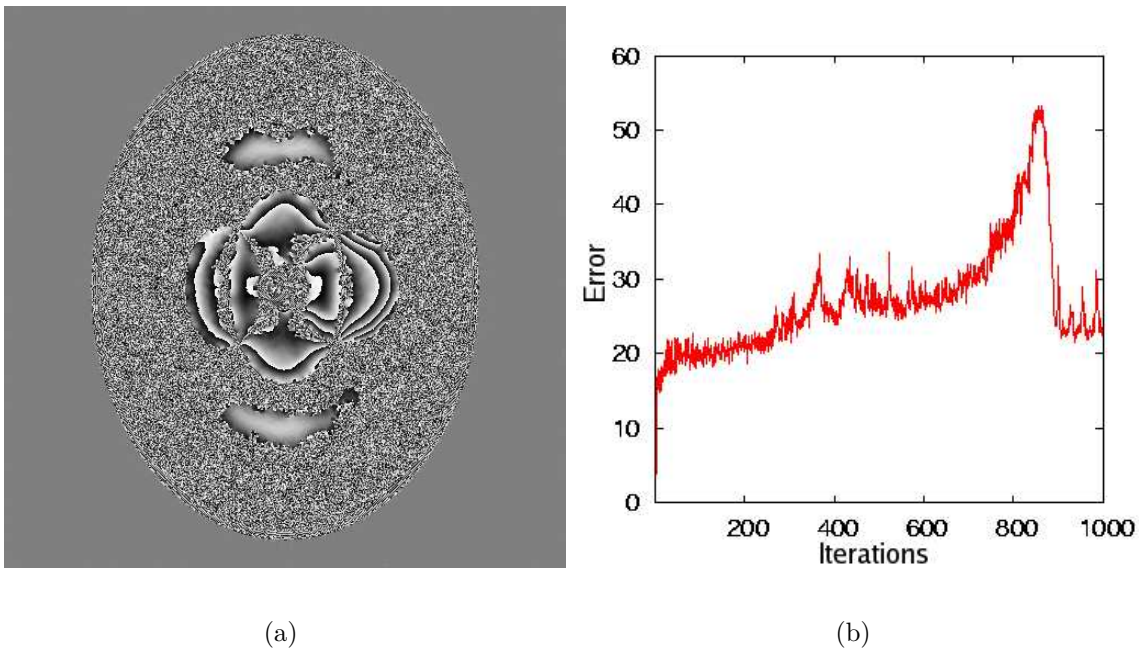


Figure 7.7: Retrieved phase and error plot for algorithm 2 (Section 7.1.5), using the transform domain projection in Fig. 7.3, (a) retrieved phase and (b) error plot. Also here there is hardly any convergence and some structure is reconstructed in the center of the object.

the cost of a more complicated experimental setup.

## 7.2 Linear methods

There might also be room for improvement within the framework of linearized methods. Recent developments have been aimed at unifying the previous models (Wu and Liu, 2003; Gureyev et al., 2004; Guigay et al., 2007) and extending validity to more general, especially strongly absorbing, objects (Paganin et al., 2002; Wu et al., 2005; Gureyev et al., 2006; Guigay et al., 2007). The most recent work in the unifying direction has been to revisit mixed frequency and spatial representations, such as the ambiguity function (Nugent, 2007), as was previously suggested by Guigay (1978). The ambiguity function was used to unify all methods, even the iterative ones (Nugent, 2007). We could see also in Chapter 4 the usefulness of the ambiguity function (Eq. 2.64) as a starting point to derive the linearized phase retrieval algorithms.

The road forward could lie here, with combinations of existing algorithms or new

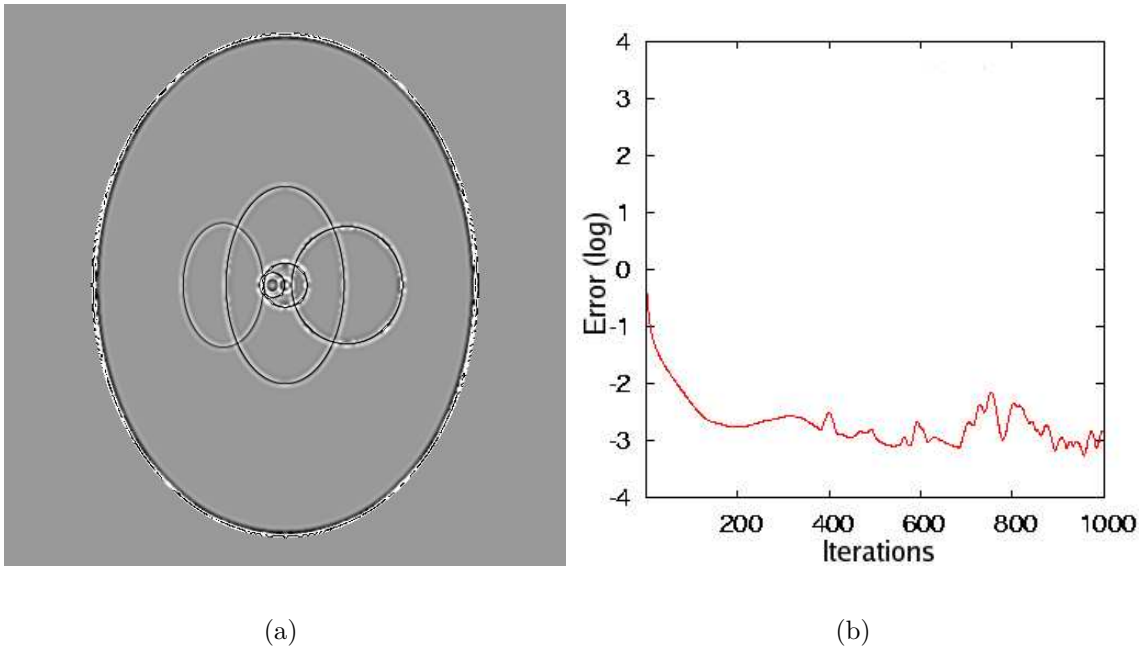


Figure 7.8: Retrieved phase and error plot for algorithm 3 (Section 7.1.5), using the transform domain projection and iteration scheme in Fig. 7.4, (a) retrieved phase and (b) error plot (lin-log scale). Convergence is much stronger and the appearance of the retrieved phase is very different from that of the previous two methods. High frequencies seem well retrieved, but low frequencies seem hardly present.

formulations. Indeed, the ambiguity function was used as the starting point for deriving the mixed approach (Chapter 3), and there could be room for more developments of this type. Similarly, other space/frequency representations could be explored, such as wavelet transform analysis of the Fresnel integral. The work in Section 5.3 should be seen as a step towards this direction.

# Chapter 8

## Conclusion

Phase tomography enhances the sensitivity of computed micro-tomography ( $\mu$ CT) by several orders of magnitude. The main contribution in of this work is the extension of phase retrieval in the Fresnel region to the case of strong absorption. To this effect, we developed a new linearized contrast model that is valid for strong absorption, but is limited to slowly varying objects (Chapter 3), which we dubbed the mixed approach. It generalizes the contrast transfer function (CTF) and transport of intensity equation (TIE), as it approaches them respectively in the limit of weak absorption and short propagation distance. This represents a step towards more general phase retrieval algorithms, valid for wider classes of samples and extended experimental conditions. Previous algorithms either assumed negligible absorption (Cloetens et al., 1999), short propagation distances (Nugent et al., 1996; Gureyev and Nugent, 1996), or both (Bronnikov, 1999). The TIE, CTF, an implementation of the TIE for weak absorption and the mixed approach were evaluated using both simulated and experimental data. The mixed approach was shown to perform best according to the chosen evaluation criteria.

It was seen that phase retrieval from Fresnel diffraction patterns, due to the image formation process, is sensitive to noise in the low frequency range (Chapter 5). Similar artifacts can also be seen in other studies (Groso, Stampanoni, Abela, Schneider, Linga and Müller, 2006; Arhatari et al., 2007). In this work we investigated regularization approaches to solve this problem. Two algorithms were developed, one based on regularization in both the Fourier and wavelet domains (Neelamani et al., 2004), and one based on using the absorption image as prior information on the phase in the low frequency range through using a phase-absorption duality assumption (essentially assuming a homogeneously composed object). The Fourier-wavelet regularized algorithm, while showing promising results on simulated data, could not be satisfactory

## Conclusion

applied to experimental data due to high computational cost and difficulty in choosing the regularization parameters. The regularization based on prior knowledge from the absorption images turned out to be very efficient in alleviating the low frequency artefacts. For this regularization scheme, an automatic parameter selection algorithm based on the L-curve method was developed, which minimizes user time.

Not much is discussed in literature about regularization of phase retrieval. Bronnikov (1999) claims no regularization is necessary, but considers only high frequencies, and states that the influence of the detector is regularizing enough in the high frequencies. Groso, Abela and Stampanoni (2006) implemented a semi-empirical regularization scheme for the TIE in the weak absorption case, which was based on simulated radiographs with different amounts of absorption. Algorithms for homogeneous, weakly absorbing objects have previously been developed (Paganin et al., 2002; Gureyev et al., 2006; Arhatari et al., 2007). The homogeneity was included as a “hard” constraint, that is requiring strict proportionality between absorption and phase, effectively reducing the number of unknowns to one. In our algorithm, information from the absorption image is included as prior knowledge about the phase, and only in the frequency range where information from the radiographs is poor or missing.

The algorithm for homogeneously composed object was shown to be useful in practice. The utility of the proposed algorithm was demonstrated by applying it to experimental data. It was applied to an imaging problem in paleontology (Section 6.1), where in the imaging of a fish bearing fossil it allowed to reveal the first known preserved structure of a brain. In this case, the homogeneous composition assumption was well fulfilled, since the fossil was close to homogeneous. The algorithm was also applied in tissue engineering (Section 6.2). Porous artificial bone scaffolds, grown in vitro with bone cells, were imaged. The reconstructed refractive index distribution allowed to segment and quantify a lowly calcified matrix deposited by the cells. These samples were essentially composed of two phases. Even though the homogeneity assumption was not fulfilled, the algorithm still enabled quantitative analysis of the two phases. Further applications of the algorithm are foreseen, in a wide range of areas, from materials science and paleontology to biological imaging.

There are several directions for further development of phase retrieval algorithms in the Fresnel region (Chapter 7). The most promising seems to be the search for further linearizations, or combination of algorithms through the ambiguity function (Guigay, 1978; Nugent, 2007). Possibilities to find linearized models could also be discovered through other space/frequency representations, e.g. through Wavelet analysis of Fresnel diffraction. Finally, there is a family of non-linear, iterative algorithms in use in

Fraunhofer phase retrieval which, with the appropriate adaptations, either on their own or in combination with linear algorithms, could prove fruitful.

## Conclusion

# References

- Ahlberg, J. H., Nilson, E. N. and Walsh, J. L. (1967), *The theory of splines and their applications*, Academic Press, London.
- Ali, R., Gooding, M., Christlieb, M. and Brady, M. (2008), Advanced phase-based segmentation of multiple cells from brightfield microscopy images, in ‘Proceedings of the 4th IEEE International Symposium on Biomedical Imaging: From Nano to Macro, ISBI 2007.’, pp. 181–184.
- Allen, L. J., McBride, W. and Oxley, M. P. (2004), “Exit wave reconstruction using soft X-rays”, *Opt. Comm.*, Vol. 233, pp. 77–82.
- Allen, L. J. and Oxley, M. P. (2001), “Phase retrieval from series of images obtained by defocus variation”, *Opt. Comm.*, Vol. 199, pp. 65–75.
- Ando, M. and Hosoya, S. (1972), An attempt at X-ray phase-contrast microscopy, in G. Shinoda, K. Kohra and T. Ichinokawa, eds, ‘Proc. 6th Intern. Conf. On Xray Optics and Microanalysis’, Univ. of Tokyo Press, Tokyo, pp. 63–68.
- Andrews, H. C. and Hunt, B. R. (1977), *Digital image restoration*, Prentice-Hall, Englewood Cliffs, NJ.
- Aoki, S., Hoshino, M. and Watanabe, N. (2007), “Application of a Zernike-type phase contrast hard X-ray microscope to microtomography”, *J. X-ray Sci. Technol.*, Vol. 15, pp. 65–72.
- Arhatari, B. D., De Carlo, F. and Peele, A. G. (2007), “Direct quantitative tomographic reconstruction for weakly absorbing homogeneous phase objects”, *Rev. Sci. Instrum.*, Vol. 78, p. 053701.
- Badea, C., Hedlund, L. W. and Johnson, G. A. (2004), “Micro-CT with respiratory and cardiac gating”, *Med. Phys.*, Vol. 31, pp. 3324–3329.

- Bartels, R. H., Beatty, J. C. and Barsky, B. A. (1987), *An introduction to splines for use in computer graphics and geometric modeling*, Morgan Kaufmann Publishers, Los Altos, CA.
- Barty, A., Nugent, K. A., Paganin, D. and Roberts, A. (1998), “Quantitative optical phase microscopy”, *Opt. Lett.*, Vol. 23, pp. 817–819.
- Baruchel, J., Buffière, J., Maire, E., Merle, P. and Peix, G. (2000), *X-Ray Tomography in Material Science*, Hermes Science Publications, Paris.
- Baruchel, J., Buffiere, J. Y., Cloetensa, P., Michiela, M. D., Ferrie, E., Ludwig, W., Maire, E. and Salvo, L. (2006), “Advances in synchrotron radiation microtomography”, *Scripta Mater.*, Vol. 55, pp. 41–46.
- Bauschke, H. H., Combettes, P. L. and Luke, D. R. (2002), “Phase retrieval, error reduction algorithm, and Fienup variants: a view from convex optimization”, *J. Opt. Soc. Am. A*, Vol. 19, pp. 1334–1345.
- Bayat, S., Apostol, L., Boller, E., Brochard, T. and Peyrin, F. (2005), “In vivo imaging of bone micro-architecture in mice with 3D synchrotron radiation microtomography”, *Nucl. Instrum. Meth. A*, Vol. 548, pp. 247–252.
- Beleggia, M., Schofield, M. A., Volkov, V. V. and Zhu, Y. (2004), “On the transport of intensity technique for phase retrieval”, *Ultramicroscopy*, Vol. 102, pp. 37–49.
- Berger, M. J., Hubbell, J. H., Seltzer, S. M., Chang, J., Coursey, J. S., Sukumar, R. and Zucker, D. (1998), ‘XCOM: Photon cross sections database’. Retrieved September 22, 2008 from <http://physics.nist.gov/PhysRefData/Xcom/Text/XCOM.html>.
- Bernhardt, R., Scharnweber, D., Müller, B., Thurner, P., Schliephake, H., Wyss, P., Beckmann, F., Goebbels and Worch, H. (2004), “Comparison of microfocus- and synchrotron X-ray tomography for the analysis of osteointegration around Ti6Al4V-implants”, *Eur. Cell. Mater.*, Vol. 7, pp. 42–51.
- Bernhardt, R., van den Dolder, J., Bierbaum, S., Beutner, R., Scharnweber, D., Jansen, J., Beckmann, F. and Worch, H. (2005), “Osteoconductive modifications of Ti-implants in a goat defect model: characterization of bone growth with SR  $\mu$ CT and histology”, *Biomaterials*, Vol. 26, pp. 3009–3019.
- Bonse, U., ed. (1999), *Developments in X-ray tomography II*, Vol. 3775 of *Proc. of SPIE*, SPIE, Bellingham, WA.

- Bonse, U., ed. (2002), *Developments in X-ray tomography III*, Vol. 4503 of *Proc. of SPIE*, SPIE, Bellingham, WA.
- Bonse, U. and Hart, M. (1965), “An X-ray interferometer”, *Appl. Phys. Lett.*, Vol. 6, pp. 155–156.
- Born, M. and Wolf, E. (1997), *Principles of optics*, 7th edn, Cambridge University Press, Cambridge, United Kingdom.
- Briggs, D. E. G. (2003), “The role of decay and mineralization in the preservation of soft-bodied fossils”, *Ann. Rev. Earth Planet. Sci.*, Vol. 31, pp. 275–301.
- Bronnikov, A. V. (1999), “Reconstruction formulas in phase-contrast tomography”, *Opt. Comm.*, Vol. 171, pp. 239–244.
- Bronnikov, A. V. (2002), “Theory of quantitative phase-contrast computed tomography”, *J. Opt. Soc. Am A*, Vol. 19, pp. 472–480.
- Calderbank, A. R., Daubechies, I., Sweldens, W. and Yeo, B. L. (1998), “Wavelet transforms that map integers to integers”, *Appl. Comp. Harm. Anal.*, Vol. 5, pp. 332–369.
- Cancedda, R., Cedola, A., Giuliani, A., Komlev, V., Lagomarsino, S., Mastrogia-como, M., Peyrin, F. and Rustichelli, F. (2007), “Bulk and interface investigations of scaffolds and tissue-engineered bones by X-ray microtomography and X-ray microdiffraction”, *Biomaterials*, Vol. 28, pp. 2505–2524.
- Chapman, D., Thomlinson, W., Johnston, R. E., Washburn, D., Pisano, E., Gmür, N., Zhong, Z., Menk, R., Arfelli, F. and Sayers, D. (1997), “Diffraction enhanced x-ray imaging”, *Phys. Med. Biol.*, Vol. 42, pp. 2015–2025.
- Chappard, C., Basillais, A., Benhamou, L., Bonassie, A., Brunet-Imbault, B., Bonnet, N. and Peyrin, F. (2006), “Comparison of synchrotron radiation and conventional X-ray microcomputed tomography for assessing trabecular bone microarchitecture of human femoral heads”, *Med. Phys.*, Vol. 33, pp. 3568–3577.
- Chui, C. K. (1997), *Wavelets: A Mathematical Tool for Signal Analysis*, SIAM, Philadelphia.
- Cloetens, P. (1999), Contribution to phase contrast imaging, reconstruction and tomography with hard synchrotron radiation - Principles, implementation and applications, PhD thesis, Vrije Universiteit Brussel.

Cloetens, P., Barrett, R., Baruchel, J., Guigay, J. P. and Schlenker, M. (1996), “Phase objects in synchrotron radiation hard X-ray imaging”, *J. Phys. D.: Appl. Phys.*, Vol. 29, pp. 133–146.

Cloetens, P., Ludwig, W., Baruchel, J., Van Dyck, D., Van Landuyt, J., Guigay, J. P. and Schlenker, M. (1999), “Holotomography: Quantitative phase tomography with micrometer resolution using hard synchrotron radiation X rays”, *Appl. Phys. Lett.*, Vol. 75, pp. 2912–2914.

Cloetens, P., Ludwig, W., Boller, E., Helfen, L., Salvo, L., Mache, R. and Schlenker, M. (2002), “Quantitative phase contrast tomography using coherent synchrotron radiation”, *Proceedings of the SPIE*, Vol. 4503, pp. 82–91.

Cloetens, P., Mache, R., Schlenker, M. and Lerbs-Mache, S. (2006), “Quantitative phase tomography of *Arabidopsis* seeds reveals intercellular void network”, *PNAS*, Vol. 103, pp. 14626–14630.

Cloetens, P., Pateyron-Salomé, M., Buffière, J., Peix, G., Baruchel, J., Peyrin, F. and Schlenker, M. (1997), “Observation of microstructure and damage in materials by phase sensitive radiography and tomography”, *J. Appl. Phys.*, Vol. 81, pp. 5878–5886.

Coates, M. I. (1999), “Endochondral preservation of a Carboniferous Actinopterygian from Lancashire, UK, and the interrelationships of primitive Actinopterygians”, *Phil. Trans. R. Soc. London*, Vol. B354, pp. 435–462.

Coene, W., Janssen, G., Op de Beeck, M. and Van Dyck, D. (1992), “Phase retrieval through focus variation for ultra-resolution in field-emission transmission electron microscopy”, *Phys. Rev. Lett.*, Vol. 69, pp. 3743–3746.

Cormack, A. M. (1963), “Representation of a function by its line integrals, with some radiological applications”, *J. Appl. Phys.*, Vol. 34, p. 2722.

Cowley, J. M. (1995), *Diffraction Physics*, 3rd edn, North-Holland, Amsterdam, The Netherlands.

Daubechies, I. (1992), *Ten lectures on wavelets*, SIAM, Philadelphia, PA.

David, C., Nöhammer, B., Solak, H. H. and Ziegler, E. (2002), “Differential X-ray phase contrast imaging using a shearing interferometer”, *Appl. Phys. Lett.*, Vol. 81, pp. 3287–3289.

- Davis, G. R. and Wong, S. L. (1996), "X-ray microtomography of bones and teeth", *Physiol. Meas.*, Vol. 17, pp. 121–146.
- Davis, T. J., Gao, D., Gureyev, T. E., Stevenson, A. W. and Wilkins, S. W. (1995), "Phase-contrast imaging of weakly absorbing materials using hard X-rays", *Nature*, Vol. 373, pp. 595–598.
- Dejus, R. J. and Sanchez del Rio, M. (1996), "Xop: A graphical user interface for spectral calculations and X-ray optics utilities", *Rev. Sci. Instrum.*, Vol. 67, p. 3356.
- Didier, D. (1995), "The phylogenetic systematics of extant chimaeroid fishes (holocephali, chimaeroidci)", *Amer. Mus. Novitates*, Vol. 3119, pp. 1–86.
- Dominguez, P., Jacobsen, A. G. and Jefferies, R. P. S. (2002), "Paired gill slits in a fossil with a calcite skeleton", *Nature*, Vol. 417, pp. 841–844.
- Donoho, D. L. (1995), "Denoising by soft-thresholding", *IEEE Trans. Inform. Theory*, Vol. 41, pp. 613–627.
- Donoho, D. L. and Johnstone, I. M. (1994), "Ideal spatial adaptation via wavelet shrinkage", *Biometrika*, Vol. 81, pp. 425–455.
- Donoho, D. L. and Johnstone, I. M. (1999), "Asymptotic minimaxity of wavelet estimators with sampled data", *Statist. Sinica*, Vol. 9, pp. 1–32.
- Elser, V. (2003), "Phase retrieval by iterated projections", *J. Opt. Soc. Am. A*, Vol. 20, pp. 40–55.
- Feist, M., Liu, J. and Tafforeau, P. (2005), "New insights into paleozoic charophyte morphology and phylogeny", *Amer. J. Bot.*, Vol. 92, pp. 1152–1160.
- Fienup, J. (1978), "Reconstruction of an object from the modulus of its Fourier transform", *Opt. Lett.*, Vol. 3, pp. 27–29.
- Fienup, J. (1981), "Reconstruction and synthesis applications of an iterative algorithm", *Proc. of SPIE*, Vol. 373, pp. 147–160.
- Fienup, J. R. (1982), "Phase retrieval algorithms: a comparison", *Appl. Opt.*, Vol. 21, pp. 2758–2769.
- Ford, N. L., Nikolov, H. N., Norley, C. J. D., Thornton, M. M., Foster, P. J., Drangova, M. and Holdsworth, D. W. (2005), "Prospective respiratory-gated micro-CT of free breathing rodents", *Med. Phys.*, Vol. 32, pp. 2888–2898.

- Ford, N. L., Thornton, M. M. and Holdsworth, D. W. (2003), “Fundamental image quality limits for microcomputed tomography in small animals”, *Med. Phys.*, Vol. 30, pp. 2869–2877.
- Friis, E., Crane, P., Pedersen, K., Bengtson, S., Donoghue, P., Grimm, G. and Stampanoni, M. (2007), “Phase-contrast X-ray microtomography links cretaceous seeds with gnetales and bennettitales”, *Nature*, Vol. 450, pp. 549–552.
- Gabor, D. (1948), “A new microscopic principle”, *Nature*, Vol. 161, pp. 777–778.
- Gerchberg, R. W. and Saxton, W. O. (1972), “A practical algorithm for the determination of phase from image and diffraction plane pictures”, *Optik*, Vol. 35, pp. 237–246.
- Ghael, S., Sayed, A. M. and Baraniuk, R. G. (1997), Improved wavelet denoising via empirical Wiener filtering, *in* ‘Proc. SPIE, Wavelet applications in signal and image processing V’, Vol. 3169, pp. 389–399.
- Ghiglia, D. C. and Pritt, M. D. (1998), *Two-dimensional phase unwrapping: theory, algorithms, and software*, John Wiley Sons, New York.
- Glazer, P. A., Spencer, U. M., Alkalay, R. N. and Schwardt, J. (2001), “In vivo evaluation of calcium sulfate as a bone graft substitute for lumbar spinal fusion”, *Spine J.*, Vol. 1, pp. 395–401.
- Golub, G. H., Heath, M. and Wahba, G. (1979), “Generalized cross-validation as a method for choosing a good ridge parameter”, *Technometrics*, Vol. 21, pp. 215–223.
- Goodman, J. W. (2005), *Introduction to Fourier optics*, 3rd edn, Roberts, Greenwood Village, CO.
- Goujet, D. (1984), *Les poissons placodermes du Spitsberg*, Cahiers de Paléontologie, Editions du CNRS, Paris.
- Grogan, E. D. and Lund, R. (2004), The origin and relationships of early chondrichthyes, *in* J. Carrier, J. A. Musick and M. Heithaus, eds, ‘The Biology of Sharks and their Relatives’, CRC Press, Boca Raton, FL, pp. 3–31.
- Groso, A., Abela, R. and Stampanoni, M. (2006), “Implementation of a fast method for high resolution phase contrast tomography”, *Opt. Express*, Vol. 14, pp. 8103–8110.
- Groso, A., Stampanoni, M., Abela, R., Schneider, P., Linga, S. and Müller, R. (2006), “Phase contrast tomography: an alternative approach”, *Appl. Phys. Lett.*, Vol. 88, p. 214104.

- Guigay, J. P. (1977), “Fourier transform analysis of Fresnel diffraction patterns and in-line holograms”, *Optik*, Vol. 46, pp. 121–125.
- Guigay, J. P. (1978), “The ambiguity function in diffraction and isoplanatic imaging by partially coherent beams”, *Opt. Comm.*, Vol. 26, pp. 136–138.
- Guigay, J. P., Langer, M., Boistel, R. and Cloetens, P. (2007), “A mixed contrast transfer and transport of intensity approach for phase retrieval in the Fresnel region”, *Opt. Lett.*, Vol. 32, pp. 1617–1619.
- Guinier, A. (1994), *X-ray diffraction in crystals, imperfect crystals and amorphous bodies*, Dover, Minneola, NY.
- Gureyev, T. E. and Nugent, K. A. (1996), “Phase retrieval with the transport-of-intensity equation. ii. orthogonal series solution for nonuniform illumination”, *J. Opt. Soc. Am. A*, Vol. 13, pp. 1670–1682.
- Gureyev, T. E. and Nugent, K. A. (1997), “Rapid quantitative phase imaging using the transport of intensity equation”, *Opt. Commun.*, Vol. 133, pp. 339–346.
- Gureyev, T. E., Paganin, D. M., Myers, G. R., Nesterets, Y. I. and Wilkins, S. W. (2006), “Phase-and-amplitude computer tomography”, *Appl. Phys. Lett.*, Vol. 89, p. 034102.
- Gureyev, T. E., Pogany, A., Paganin, D. M. and Wilkins, S. W. (2004), “Linear algorithms for phase retrieval in the Fresnel region”, *Opt. Comm.*, Vol. 231, pp. 53–70.
- Gureyev, T. E., Raven, C., Snigirev, A., Snigireva, I. and Wilkins, S. W. (1999), “Hard X-ray quantitative non-interferometric phase-contrast microscopy”, *J. Phys. D: Appl. Phys.*, Vol. 32, pp. 563–567.
- Hadamard, J. (1902), “Sur les problèmes aux dérivées partielles et leur signification physique”, *Princeton univ. bull.*, Vol. 13, pp. 49–52.
- Hansen, P. C. (1992), “Analysis of discrete ill-posed problems by means of the L-curve”, *SIAM Rev.*, Vol. 34, pp. 561–580.
- Hansen, P. C. (2001), The L-curve and its use in the numerical treatment of inverse problems, in P. Jonston, ed., ‘Computational Inverse Problems in Electrocardiology’, WIT Press, Southampton, United Kingdom, pp. 119–142.

- Hansen, P. C. and O'Leary, D. P. (1993), "The use of the L-curve in the regularization of discrete ill-posed problems", *SIAM J. Sci. Comput.*, Vol. 14, pp. 1487–1503.
- Henke, B. L., Gullikson, E. M. and Davis, J. C. (1993), "X-ray interactions: photoabsorption, scattering, transmission, and reflection at E=50-30000 eV, Z=1-92", *At. Data Nucl. Data Tab.*, Vol. 54, pp. 181–342.
- Hildebrand, T. and Rüegsegger, P. (1997), "A new method for the model-independent assessment of thickness in three-dimensional images", *J. Microsc.*, Vol. 185, pp. 67–75.
- Ho, S. T. and Hutmacher, D. W. (2006), "A comparison of micro CT with other techniques used in the characterization of scaffolds", *Biomaterials*, Vol. 27, pp. 1362–1376.
- Hounsfield, G. N. (1972), 'A method of and apparatus for examination of a body by radiation such as X-ray or gamma radiatoin', British patent No 1283915.
- Hounsfield, G. N. (1973), "Computerized transverse axial scanning (tomography): Part 1 description of system", *Br. J. Radiol.*, Vol. 46, pp. 1016–1022.
- Hwu, Y., Tsai, W. L., Chang, H. M., Yeh, H. I., Hsu, P. C., Yang, Y. C., Su, Y. T., Tsai, H. L., Chow, G. M., Ho, P. C., Li, S. C., Moser, H. O., Yang, P., Seol, S. K., Kim, C. C., Je, J. H., Stefanekova, E., Gross, A. and Margaritondo, G. (2004), "Imaging cells and tissues with refractive index radiology", *Biophys. J.*, Vol. 87, pp. 4180–4187.
- Ingall, V. N. and Beliaevskaya, E. A. (1995), "X-ray plane-wave topography observation of the phase contrast from a non-crystalline object", *J. Phys. D: Appl. Phys.*, Vol. 28, pp. 2314–2317.
- Janvier, P. (1996), *Early Vertebrates*, Vol. 33 of *Oxford Monographs on Geology and Geophysics*, Clarendon Press, Oxford.
- Jollie, M. (1962), *Chordate Morphology*, Chapman and Hall, London.
- Kak, A. C. and Slaney, M. (1998), *Principles of Computerized Tomographic Imaging*, IEEE Press, New York.
- Kitchen, M. J., Lewis, R. A., Yagi, N., Uesugi, K., Paganin, D., Hooper, S. B., Adams, G., Jureczek, S., Singh, J., Christensen, C. R., Hufton, A. P., Hall, C. J., Cheung,

- K. C. and Pavlov, K. M. (2005), “Phase contrast X-ray imaging of mice and rabbit lungs: a comparative study”, *Br. J. Radiol.*, Vol. 78, pp. 1018–1027.
- Kofron, M. D., Li, X. and Laurencin, C. T. (2004), “Protein- and gene-based tissue engineering in bone repair”, *Curr. Opin. Biotechnol.*, Vol. 15, pp. 399–405.
- Komlev, V. S., Peyrin, F., Mastrogiacomo, M., Cedola, A., Papadimitropoulos, A., Rustichelli, F. and Cancedda, R. (2006), “Kinetics of in vivo bone deposition by bone marrow stromal cells into porous calcium phosphate scaffolds: An X-ray computed microtomography study”, *Tissue Eng.*, Vol. 12, pp. 3449–3454.
- Kotre, C. J. and Birch, I. P. (1999), “Phase contrast enhancement of x-ray mammography: a design study”, *Phys. Med. Biol.*, Vol. 44, pp. 2853–2866.
- Labiche, J.-C., Maton, O., Pascarelli, S., Newton, M. A., Ferre, G. C., Curfs, C., Vaughan, G., Homs, A. and Carreiras, D. F. (2007), “The FReLoN camera as a versatile X-ray detector for time resolved dispersive exafs and diffraction studies of dynamic problems in materials science, chemistry, and catalysis”, *Rev. Sci. Instrum.*, Vol. 78, p. 091301.
- Lak, M., Nraudeau, D., Nel, A., Cloetens, P., Perrichot, V. and Tafforeau, P. (2008), “Phase contrast X-ray synchrotron imaging: Opening access to fossil inclusions in opaque amber”, *Microsc. Microanal.*, Vol. 14, pp. 251–2599.
- Lambert, J., Cantat, I., Delannay, R., Renault, A., Graner, F., Glazier, J. A., Veretennikov, I. and Cloetens, P. (2005), “Extraction of relevant physical parameters from 3D images of foams obtained by X-ray tomography”, *Coll. Surf. A*, Vol. 263, pp. 295–302.
- Langer, M., Cloetens, P., Guigay, J. P. and Peyrin, F. (2008), “Quantitative comparison of direct phase retrieval algorithms in in-line phase tomography”, *Med. Phys.*, Vol. 35, pp. 4556–4566.
- Langer, M., Cloetens, P., Guigay, J. P., Valton, S. and Peyrin, F. (2007), Quantitative evaluation of phase retrieval algorithms in propagation based phase tomography, in ‘Proc. ISBI 2007: 4th IEEE international symposium on biomedical imaging’, pp. 552–555.
- Langer, M., Cloetens, P. and Peyrin, F. (Submitted), “Regularization of phase retrieval with phase-attenuation duality prior for 3D holotomography”, *IEEE Trans. Im. Proc.*

- Langstaff, S., Sayer, M., Smith, T. J. N. and Pugh, S. M. (2001), “Resorbable bio-ceramics based on stabilized calcium phosphates. part ii: evaluation of biological response”, *Biomaterials*, Vol. 22, pp. 135–150.
- Lewis, R. A. (2004), “Medical phase contrast X-ray imaging: current status and future prospects”, *Phys. Med. Biol.*, Vol. 49, pp. 3573–3583.
- Lin, A. S. P., Barrows, T. H., Cartmell, S. H. and Guldberg, R. E. (2003), “Microarchitectural and mechanical characterization of oriented porous polymer scaffolds”, *Biomaterials*, Vol. 24, pp. 481–489.
- Macchiarelli, R., Bondioli, L., Debénath, A., Mazurier, A., Tournepiche, J.-F., Birch, W. and Dean, C. (2006), “How neanderthal molar teeth grew”, *Nature*, Vol. 444, pp. 748–751.
- Maire, E., Buffière, J., Salvo, L., Blandin, J., Ludwig, W. and Létang, J. (2001), “On the application of X-ray microtomography in the field of materials science”, *Adv. Eng. Mater.*, Vol. 3, pp. 539–546.
- Maisey, J. G. (1984), “Chondrichthyan phylogeny: a look at the evidence”, *J. Vert. Paleont.*, Vol. 4, pp. 359–371.
- Maisey, J. G. (2001), A primitive Condrichthyan braincase from the middle Devonian of Bolivia, in P. E. Ahlberg, ed., ‘Major Events in Early Vertebrate Evolution’, Taylor and Francis, London, pp. 263–288.
- Maisey, J. G. (2005), “Braincase of the upper Devonian shark Cladodoides wildungensis (Chondrichthyes, Elasmobranchii), with observations on the braincase in early Chondrichthyans”, *Bull. Amer. Mus. Nat. Hist.*, Vol. 288, pp. 1–103.
- Maisey, J. G. (2007), “The braincase in paleozoic symmoriiform and cladoselachian sharks”, *Bull. Amer. Mus. Nat. Hist.*, Vol. 307, pp. 1–122.
- Mallat, S. (1999), *A wavelet tour of signal processing*, 2nd edn, Academic Press, San Diego, CA.
- Marchesini, S., Chapman, H. N., Hau-Riege, S. P., London, R. A., Szoke, A., Me, H., Howells, M. R., Padmore, H., Rosen, R., Spence, J. C. H. and Weierstall, U. (2003), “Coherent X-ray diffractive imaging: applications and limitations”, *Opt. Express*, Vol. 11, pp. 2344–2353.

- Mastrogiacomo, M., Corsi, A., Francioso, E., Comite, M. D., Monetti, F., Scaglione, S., Favia, A., Crovace, A., Bianco, P. and Cancedda, R. (2006), “Reconstruction of extensive long bone defects in sheep using resorbable bioceramics based on silicon stabilized tricalcium phosphate”, *Tissue Eng.*, Vol. 12, pp. 1261–1273.
- Mastrogiacomo, M., Papadimitropoulos, A., Cedola, A., Peyrin, F., Giannoni, P., Pearce, S., Alini, M., and Guagliardi, C. G. and Cancedda, R. (2007), “Engineering of bone using bone marrow stromal cells and a silicon-stabilized tricalcium phosphate bioceramic: Evidence for a coupling between bone formation and scaffold resorption”, *Biomaterials*, Vol. 28, pp. 1376–1384.
- Mayo, S., Davis, T., Gureyev, T., Miller, P., Paganin, D., Pogany, A., Stevenson, A. and Wilkins, S. (2003), “X-ray phase-contrast microscopy and microtomography”, *Opt. Express*, Vol. 11, pp. 2289–2302.
- Meng, F., Liu, H. and Wu, X. (2007), “An iterative phase retrieval algorithm for in-line X-ray phase imaging”, *Opt. Express*, Vol. 15, pp. 8383–8390.
- Miao, J., Charalambous, P., Kirz, J. and Sayre, D. (1999), “Extending the methodology of X-ray crystallography to allow imaging of micrometre-sized non-crystalline specimens”, *Nature*, Vol. 400, pp. 342–344.
- Michette, A. G. and Buckley, C. J., eds (1993), *J. X-ray Sci. Technol.*, IOP, Bristol, UK.
- Mokso, R. (2006), Development and applications of coherent imaging with improved temporal and spatial resolution, PhD thesis, Université Joseph Fourier, Grenoble, France.
- Momose, A. (2005), “Recent advances in X-ray phase imaging”, *Jpn. J. Appl. Phys.*, Vol. 44, pp. 6355–6367.
- Momose, A. and Fukuda, J. (1995), “Phase-contrast radiographs of nonstained rat cerebellar specimen”, *Med. Phys.*, Vol. 22, pp. 375–379.
- Momose, A., Takeda, T. and Itai, Y. (1995), “Phase-contrast X-ray computed tomography for observing biological specimens and organic materials”, *Rev. Sci. Instrum.*, Vol. 66, pp. 1434–1436.
- Momose, A., Takeda, T., Itai, Y. and Hirano, K. (1996), “Phase-contrast X-ray computed tomography for observing biological soft tissues”, *Nat. Med.*, Vol. 2, pp. 473–475.

- Monnin, P., Bulling, S., Hoszowska, J., Valley, J.-F., Meuli, R. and Verdun, F. R. (2004), “Quantitative characterization of edge enhancement in phase contrast X-ray imaging”, *Med. Phys.*, Vol. 31, pp. 1372–1383.
- Moore, E. H. (1920), “On the reciprocal of the general algebraic matrix”, *Bull. Amer. Math. Soc.*, Vol. 26, pp. 394–395.
- Neelamani, R., Choi, H. and Baraniuk, R. (2004), “ForWaRD: Fourier-wavelet regularized deconvolution for ill-conditioned systems”, *IEEE Trans. Sig. Proc.*, Vol. 52, pp. 418–433.
- Neuhausler, U., Schneider, G., Ludwig, W., Meyer, M. A., Zschech, E. and Hambach, D. (2003), “X-ray microscopy in Zernike phase contrast mode at 4 keV photon energy with 60 nm resolution”, *J. Phys. D: Appl. Phys.*, Vol. 36, pp. A79–A82.
- Neumaier, A. (1998), “Solving ill-conditioned and singular linear systems: a tutorial on regularization”, *SIAM Review*, Vol. 40, pp. 636–666.
- Nugent, K. A. (2007), “X-ray noninterferometric phase imaging: a unified picture”, *J. Opt. Soc. Am. A*, Vol. 24, pp. 536–547.
- Nugent, K., Gureyev, T., Cookson, D., Paganin, D. and Barnea, Z. (1996), “Quantitative phase imaging using hard X rays”, *Phys. Rev. Lett.*, Vol. 77, pp. 2961–2964.
- Nuzzo, S., Peyrin, F., Cloetens, P., Baruchel, J. and Boivin, G. (2002), “Quantification of the degree of mineralization of bone in three dimensions using synchrotron radiation microtomography”, *Med. Phys.*, Vol. 29, pp. 2672–2681.
- Otsu, N. (1979), “A threshold selection method from gray-level histograms”, *IEEE Trans. Sys. Man. Cyber.*, Vol. 9, pp. 62–66.
- Paganin, D. M. (2006), *Coherent X-Ray Optics*, Vol. 6 of *Oxford series on synchrotron radiation*, Oxford University Press, Oxford.
- Paganin, D., Mayo, S. C., Gureyev, T. E., Miller, P. R. and Wilkins, S. W. (2002), “Simultaneous phase and amplitude extraction from a single defocused image of a homogeneous object”, *J. Microsc.*, Vol. 206, pp. 33–40.
- Paganin, D. and Nugent, K. A. (1998), “Noninterferometric phase imaging with partially coherent light”, *Phys. Rev. Lett.*, Vol. 80, pp. 2586–2589.

- Pagot, E., Fiedler, S., Cloetens, P., Bravin, A., Coan, P., Fezzaa, K., Baruchel, J. and Hartwig, J. (2005), “Quantitative comparison between two phase contrast techniques: diffraction enhanced imaging and phase propagation imaging”, *Phys. Med. Biol.*, Vol. 50, pp. 709–724.
- Papadimitropoulos, A., Mastrogiacomo, M., Peyrin, F., Molinari, E., Komlev, V. S., Rustichelli, F. and Cancedda, R. (2007), “Kinetics of in vivo bone deposition by bone marrow stromal cells within a resorbable porous calcium phosphate scaffold: an X-ray computed microtomography study”, *Biotechnol. Bioeng.*, Vol. 98, pp. 271–281.
- Papoulis, A. (1974), “Ambiguity function in Fourier optics”, *J. Opt. Soc. Am.*, Vol. 64, pp. 779–788.
- Patterson, C. (1965), “The phylogeny of the chimaeroids”, *Phil. Trans. R. Soc. London*, Vol. B249, pp. 101–219.
- Penrose, R. (1955), “A generalized inverse for matrices”, *Proc. Cam. Phil. Soc.*, Vol. 51, pp. 406–415.
- Penrose, R. (1956), “On best approximate solution of linear matrix equations”, *Proc. Cam. Phil. Soc.*, Vol. 52, pp. 17–19.
- Pfeiffer, F., Weitkamp, T., Bunk, O. and David, C. (2006), “Phase retrieval and differential phase-contrast imaging with low-brilliance X-ray source”, *Nat. Phys.*, Vol. 2, p. 258.
- Poplin, C. (1974), *Etude de quelques paleoniscides pennsylvaniens du Kansas*, Cahiers de Paléontologie, Editions du CNRS, Paris.
- Rade, L. and Westergren, B. (2004), *Mathematics handbook for science and engineering (BETA)*, 5th edn, Studentlitteratur, Lund, Sweden.
- Reid, J. W., Pietak, A., Sayer, M., Dunfield, D. and Smith, T. (2005), “Phase formation and evolution in the silicon substituted tricalcium phosphate/apatite system”, *Biomaterials*, Vol. 26, pp. 2887–2897.
- Rodenburg, J. M., Hurst, A. C., Cullis, A. G., Dobson, B. R., Pfeiffer, F., Bunk, O., David, C., Jefimovs, K. and Johnson, I. (2007), “Hard-X-ray lensless imaging of extended objects”, *Phys. Rev. Lett.*, Vol. 98, p. 034801.
- Sabatier, P. C. (1985), “Inverse problems - an introduction”, *Inv. Prob.*, Vol. 1.

- Salomé, M., Peyrin, F., Cloetens, P., Odet, C., Laval-Jeantet, A.-M., Baruchel, J. and Spanne, P. (1999), “A synchrotron radiation microtomography system for the analysis of trabecular bone samples”, *Med. Phys.*, Vol. 26, pp. 2194–2204.
- Sanchez del Rio, M. and Dejus, R. J. (2004), Xop 2.1: A new version of the X-ray optics software toolkit, in T. Warwick, ed., ‘Synchrotron Radiation Instrumentation: Eighth International Conference’, Americal Institute of Physics, pp. 784–787.
- Sayer, M., Stratilatov, A. D., Reid, J., Calderin, L., Stott, M. J., Yin, X., MacKenzie, M., Smith, T. J. N., Hendry, J. A. and Langstaff, S. D. (2003), “Structure and composition of silicon-stabilized tricalcium phosphate”, *Biomaterials*, Vol. 24, pp. 369–382.
- Shapiro, D., Thibault, P., Beetz, T., Elser, V., Howells, M., Jacobsen, C., Kirz, J., Lima, E., Miao, H., Neiman, A. M. and Sayre, D. (2005), “Biological imaging by soft X-ray diffraction microscopy”, *PNAS*, Vol. 102, pp. 15343–15346.
- Smith, T. M., Tafforeau, P., Reid, D. J., Grn, R., Eggins, S., Boutakiout, M. and Hublin, J.-J. (2006), “Earliest evidence of modern human life history in North African early *Homo sapiens*”, *PNAS*, Vol. 104, pp. 6128–6133.
- Snigirev, A., Snigireva, I., Kohn, V., Kuznetsov, S. and Schelokov, I. (1995), “On the possibilities of X-ray phase contrast microimaging by coherent high-energy synchrotron radiation”, *Rev. Sci. Instrum.*, Vol. 66, p. 5486.
- Stahl, B. J. (1999), Chondrichthyes III - Holocephali, in H.-P. Schultze, ed., ‘Handbook of paleoichthyology’, Vol. 4, Pfeil, Munich, Germany.
- Stark, H. (1987), *Image recovery: theory and application*, Academic press, London.
- Stensiö, E. (1969), Placodermata, Arthrodires, in J. Piveteau, ed., ‘Traité de Paléontologie’, Vol. 4, Masson, Paris, pp. 71–692.
- Tafforeau, P., Bentaleb, I., Jaeger, J.-J. and Martin, C. (2007), “Nature of laminations and mineralization in rhinoceros enamel using histology and X-ray synchrotron microtomography: potential implications for palaeoenvironmental isotopic studies.”, *Palaeogeogr. Palaeoclimatol. Palaeoecol.*, Vol. 246, pp. 206–227.
- Tafforeau, P., Boistel, R., Boller, E., Bravin, A., Brunet, M., Chaimanee, Y., Cloetens, P., Feist, M., Hozowska, J., Jaeger, J.-J., Kay, R. F., Lazzari, V., Marivaux, L., Nel,

A., Nemoz, C., Thibault, X., Vignaud, P. and Zabler, S. (2006), “Applications of X-ray synchrotron microtomography for non-destructive 3D studies of paleontological specimens”, *Appl. Phys. A*, Vol. 83, pp. 195–202.

Tarantola, A. (1987), *Inverse Problem Theory*, Elsevier, New York.

Teague, M. R. (1982), “Irradiance moments: their propagation and use for unique retrieval of phase”, *J. Opt. Soc. Am.*, Vol. 72, pp. 1199–1209.

Teague, M. R. (1983), “Deterministic phase retrieval: a Green’s function solution”, *J. Opt. Soc. Am.*, Vol. 73, pp. 1434–1441.

Thibault, P., Dierolf, M., Menzel, A., Bunk, O., David, C. and Pfeiffer, F. (2008), “High-resolution scanning X-ray diffraction microscopy”, *Science*, Vol. 321, pp. 379–382.

Thomsen, J. S., Laib, A., Koller, B., Prohaska, S., Mosekilde, L. and Gowin, W. (2005), “Stereological measures of trabecular bone structure: comparison of 3D micro computed tomography with 2D histological sections in human proximal tibial bone biopsies”, *J. Microsc.*, Vol. 218, pp. 171–179.

Tikhonov, A. N. and Arsenin, V. A. (1977), *Solution of ill-posed problems*, Winston, Washington, DC.

Turner, L. D., Dhal, B. B., Hayes, J. P., Nugent, K. A., Paterson, D., Scholten, R. E., Tran, C. Q. and Peele, A. G. (2004), “X-ray phase imaging: Demonstration of extended conditions with homogeneous objects”, *Opt. Express*, Vol. 12, p. 2916.

Vetterli, M. and Herley, C. (1992), “Wavelets and filter banks: Theory and design”, *IEEE Trans. Sig. Proc.*, Vol. 40, pp. 2207–2232.

Wang, Y. (2007), “Intuitive dimensional analyses of the energy and atomic number dependences of the cross sections for radiation interaction with matter”, *Journal of X-Ray Science and Technology*, Vol. 15, pp. 169–175.

Weiss, P., Obadia, L., Magne, D., Bourges, X., Rau, C., Weitkamp, T., Khairoun, I., Bouler, J. M., Chappard, B., Gauthier, O. and Daculsi, G. (2003), “Synchrotron X-ray microtomography (on a micron scale) provides three-dimensional imaging representation of bone ingrowth in calcium phosphate biomaterials”, *Biomaterials*, Vol. 24, pp. 4591–4601.

- Wilkins, S. W., Gureyev, T. E., Gao, D., Pogany, A. and Stevenson, A. W. (1996), "Phase-contrast imaging using polychromatic hard X-rays", *Nature*, Vol. 384, pp. 335–338.
- Wu, X. and Liu, H. (2003), "A general theoretical formalism for X-ray phase contrast imaging", *J. X-Ray Sci. Tech.*, Vol. 11, p. 33.
- Wu, X., Liu, H. and Yan, A. (2005), "X-ray phase-attenuation duality and phase retrieval", *Opt. Lett.*, Vol. 30, pp. 379–381.
- Zabler, S., Cloetens, P., Guigay, J. P., Baruchel, J. and Schlenker, M. (2005), "Optimization of phase contrast imaging using hard X rays", *Rev. Sci. Instrum.*, Vol. 76, pp. 1–7.
- Zabler, S., Riesemeier, H., Fratzl, P. and Zaslansky, P. (2006), "Fresnel-propagated imaging for the study of human tooth dentin by partially coherent X-ray tomography", *Opt. Express*, Vol. 14, pp. 8584–8595.
- Zangerl, R. (1981), Chondrichthyes I - Paleozoic Elasmobranchii, in H.-P. Schultze, ed., 'Handbook of paleoichthyology', Vol. 3A, Pfeil, Munich, Germany.
- Zangerl, R. and Case, G. R. (1973), "Iniopterygia, a new order of Chondrichthyan fishes from the Pennsylvanian of North America", *Fieldiana, Geol. Mem.*, Vol. 6, pp. 1–67.

# Publications

- Guigay, J. P., Langer, M., Boistel, R., and Cloetens, P. (2007), “A mixed contrast transfer and transport of intensity approach for phase retrieval in the Fresnel region”, *Opt. Lett.*, Vol. 32, pp. 1617–1619.
- Langer, M., Cloetens, P., Guigay, J. P., Valton, S. and Peyrin, F. (2007), Quantitative evaluation of phase retrieval algorithms in propagation based phase tomography, in ‘Proc. ISBI 2007: 4th IEEE international symposium on biomedical imaging’, pp. 552–555.
- Langer, M., Cloetens, P., Guigay, J. P., and Peyrin, F. (2008), “Quantitative comparison of direct phase retrieval algorithms in in-line phase tomography”, *Med. Phys.*, Vol. 35, pp. 4556–4566.
- Langer, M., Cloetens, P. and Peyrin, F. (Submitted), “Regularization of phase retrieval with phase-attenuation duality prior for 3D holotomography”, *IEEE Trans. Im. Proc.*
- Langer, M., Cloetens, P. and Peyrin, F. (Submitted), “Fourier-wavelet regularization of phase retrieval in x-ray in-line phase tomography”, *J. Opt. Soc. Am. A*.
- Langer M., Liu, Y., Cancedda, R. and Peyrin, F. (Submitted), “3D SR X-ray holotomography enables study of fibrous tissue in porous scaffolds for tissue engineering”, *J. Microsc.*
- Pradel, A., Langer, M., Maisey, J. G., Geffard-Kuriyama, D., Cloetens, P., Janvier, P. and Tafforeau, P. (Submitted), “Skull and brain of a 300 million-year-old chimaeroid fish revealed by synchrotron holotomography”, *PNAS*.

## Folio Administratif

### Thèse soutenue devant l’Institut National des Sciences Appliquées de Lyon

Nom : LANGER

Date de soutenance : 19 Novembre 2008

Prénom : Max

Titre : Phase Retrieval in the Fresnel Region for Hard X-ray Tomography

Nature : Doctorat

Numéro d’ordre : 2008-ISAL-0094

École doctorale : Électronique, Électrotechnique, Automatique

Spécialité : Images et Systèmes

Cote B.I.U. Lyon :

Classe :

#### Résumé :

The main interest in phase-based X-ray imaging techniques is the increase in sensitivity they offer, which can be as large as three orders of magnitude in the hard X-ray region. If a sufficiently coherent X-ray beam is used, phase contrast is achieved by letting the beam propagate a finite distance in free space after interacting with the object. Such an image is called a Fresnel diffraction pattern. A non-linear relationship exists between the phase shift induced by the object, which is dependent on the 3D complex refractive index distribution, and the diffraction patterns. Phase retrieval consists in using this relationship to estimate the phase shift. The 3D refractive index can then be reconstructed by tomographic reconstruction. Whereas methods based on the hypothesis of short propagation distance or weak objects exist, the aim of this study was to develop, evaluate and apply methods for strongly absorbing objects. In this thesis, a linearized contrast model valid for strongly absorbing but slowly varying objects dubbed the mixed approach, is presented. The mixed approach and previously existing methods are evaluated on simulated and experimental data. Two regularization schemes aiming to counter low frequency noise are developed, one based on wavelets and one based on prior knowledge of the phase shift derived from the absorption. The latter is found more successful and is applied to imaging problems in bone graft tissue engineering and paleontology. Finally, a survey of iterative algorithms for phase retrieval from far-field diffraction patterns and development of three iterative algorithms for the Fresnel diffraction case are presented.

**Mots-clés** : X-ray imaging, tomography, microscopy, phase contrast, phase retrieval, coherent imaging, quantitative imaging, phantoms, synchrotron radiation, tissue engineering, paleontology

#### Laboratoire de Recherches :

Centre de Recherche et d’Applications en Traitement de l’Image et du Signal (CREATIS-LRMN), UMR CNRS 5220, U630 Inserm

**Directeur de Thèse** : Françoise PEYRIN

**Président du Jury** : Rémy PROST

#### Composition du Jury :

Peter CLOETENS (Codirecteur), Laurent DESBAT, Jean-Pierre GUIGAY (Invité), Jérôme IDIER (Rapporteur), Françoise PEYRIN (Directeur), Franz PFEIFFER (Rapporteur), Rémy PROST (Président)